université PARIS-SACLAY

On the entanglement of quasi-particles in a Bose-Einstein Condensate

From Faraday waves to the Dynamical Casimir Effect

De l'intrication de quasi-particules dans un condensat de Bose-Einstein

Des ondes de Faraday à l'effet Casimir dynamique

Thèse de doctorat de l'université Paris-Saclay

École doctorale n°572, Ondes et matière (EDOM)
Spécialité de doctorat : Physique
Graduate School : Physique. Référent : Institut d'Optique

Thèse préparée au **Laboratoire Charles Fabry**
(Université Paris-Saclay, CNRS, Institut d'Optique Graduate School),
sous la direction de **Denis BOIRON**, Professeur des universités,
et le co-encadrement de **Christoph WESTBROOK**, Directeur de recherche.

Thèse soutenue à Palaiseau, le 28 janvier 2025, par

Victor Gondret

Composition du jury

Membres du jury avec voix délibérative

Valentina Parigi Professeure, Sorbonne Université	Présidente
Radu Chicireanu Chargé de Recherche, Université de Lille	Rapporteur
Tommaso Roscilde Maître de Conférence, École Normale Supérieure de Lyon	Rapporteur
Frédéric Chevy Professeur, École Normale Supérieure de Paris	Examinateur
Nicolas Pavloff Professeur, Université Paris-Saclay	Examinateur

Membres du jury sans voix délibérative

Denis Boiron Professeur, Université Paris-Saclay	Directeur de thèse
Christoph Westbrook Directeur de recherche, Université Paris-Saclay	Co-directeur de thèse

THESE DE DOCTORAT
NNT : 2025UPASP005

Contents

Remerciements

Je tiens à remercier tout d'abord mon jury de thèse pour l'intérêt qu'il a porté à mon travail et pour ses remarques pointues lors de ma soutenance. Merci donc à Radu Chicireanu et Tommaso Roscilde pour leur temps précieux qu'ils m'ont accordé en tant que rapporteurs. Merci à Valentina Parigi comme présidente, et Nicolas Pavloff et Frédéric Chevy.

Un immense merci à Denis Boiron, mon directeur de thèse, avec qui j'ai aimé apprendre, du refroidissement atomique à l'optique quantique et que je remercie pour sa gentillesse et sa confiance. J'ai particulièrement été touché par l'investissement de Denis sur la manip' et son soutien pour ses doctorants, que ce soit sur un calcul théorique ou un déboulonnage d'une chambre à vide. Un immense merci également à Chris Westbrook, co-directeur de mes travaux de thèse. Sa vision de la physique et sa façon de présenter nos travaux m'ont beaucoup apporté. Merci pour son travail de l'ombre qui nous a permis d'avancer sans soucis ces quatres années.

Ce travail n'aurait pas été possible sans les artisans journaliers de la manip'. Merci à

Figure 1: L'équipe avec laquelle j'ai travaillé durant ma thèse. De gauche à droite, haut en bas: March Cheneau, Alexandre Dareau, Denis Boiron, Charlie Leprince, Quentin Marolleau, Chris Westbrook et V.G. Sur la seconde photo, Paul Paquiez et Clothilde Lamirault nous ont rejoint. En bas: Amaury Micheli, un collbaorateur théoricien et Rui Dias récemment arrivé.

Alexandre Dareau d'avoir guidé mes premiers pas sur l'expérience et pour la transmission de ses bonnes pratiques qui nous ont guidées par la suite. Merci à Quentin Marolleau, qui par son engouement m'a donné envie de rejoindre l'équipe, et qui (malgré ses mises en garde) m'a donné envie de continuer. En plus des nombreuses discussions, son dynamisme et sa rigueur ont permis à la manip de repartir sur des bases très saines. Ces années au labo auraient été très différentes sans la présence de mon accolyte Charlie Leprince, avec qui j'ai passé toute ma thèse. J'ai adoré travailler à ses côté, et je le remercie pour sa gentillesse, son implication et son enthousiasme (même quand Quentin dit que non, ce n'est pas un BEC). Merci à Clothilde Lamirault pour sa rapide prise en main de la manip, sa détermination et dont le calme dans les situations tendues est impressionant ainsi qu'à Rui Dias pour son abnégation et sa sincérité. Avec Léa Camier, je n'ai pas de doute que ces trois là vont former une belle équipe. PS: désolé pour tous les problèmes qu'il reste à régler sur la manip et que vous ne manquerez pas de débusquer. PPS2: le projet Bell c'est vrai que c'est beau mais je vous promets qu'il y a aussi de la belle physique à faire en simulant l'Univers ;-). Merci aussi à Paul Paquiez pour son travail avec nous.

Je remercie globalement l'ensemble des permanents du groupe Gaz quantique pour leur gestion colégiale du groupe, qui permet d'instaurer une ambiance d'entraide et solidaire entre les équipes. Un merci particulier à Marc Cheneau pour ses conseils lors de la remise sur pied de l'expérience, à David Clément pour sa disponibilité et les discussions autour de l'intrication ou de l'écologie ainsi qu'à la Capitaine Isabelle Bouchoule, pour la régate sous la houle ou les manifs dans la foule. Plus globalement, merci à l'ensemble des membres du groupe pour l'ambiance agréable au sein du labo et plus spécialement à Léa Dubois et Guillaume Thémèze au sein du bureau.

Au sein du laboratoire, je remercie Patrick Georges pour son dévouement, ainsi que l'ensemble des services techniques du laboratoire et du service infrastructure de l'Institut. Un merci particulier à Jean-René Rullier, dont le calme et l'efficacité redoutable sont précieux et Fabien Siffritt pour les nombreux dépannages qui furent cruciaux dans la réalisation de ces travaux.

Un grand merci à nos deux théoriciens de l'équipe COSQUA. Merci à Scott Robertson d'avoir pris le temps de me former et de s'être toujours rendu disponible pour prendre au sérieux mes question naïves. Merci à Amaury Micheli (Mikeli pardon) pour l'ensembre de nos discussions et moments, que ce soit de physique ou autre et avec qui c'est un plaisir de travailler. Merci à Maxime Jacquet pour les nombreuses discussions que nous avons eu, et pour son dynamisme dans le développement de la recherche en gravité analogue.

Un immense merci à ma famille, avec une pensée particulière pour la préparation du pôt et les modifications de présentation de dernière minute. Merci également à tous mes amis pour leur soutien et les moments de qualités partagés. Merci aussi pour leur perspicacité pour relativiser les soirs de loose: "En vrai, t'es sûr qu'il faut que tu refasse des expériences ? À force, je pense tu introduis un biais dans la science." Merci particulièrement aux colocs de La Plata pour ces belles années passées ensamble. Enfin, à Alice, gracias por todo, y vamos!

Résumé (en français)

1. Contexte

Ce travail de thèse revisite une variante de l'instabilité de Faraday en l'interprétant comme une analogie avec l'effet Casimir Dynamique et le préchauffage dans l'univers primordial. En particulier, nous nous intéressons aux effets quantiques lors d'une excitation paramétrique. Cet travail se situe dans le domaine de la théorie quantique des champs en espace-temps courbe (QFTCST), également connu sous le nom de *gravité analogue*. Ce domaine vise à reproduire, dans des expériences de laboratoire, des prédictions de QFTCST dont l'observation directe est impossible. Cela permet également d'utiliser et modifier des outils théoriques intialement développés en relativité générale ou en théorie quantique des champs pour modéliser des systèmes de matière condensée. Ce champs de recherche a été initié par un article fondateur de Unruh (1981) *"Experimental Black-Hole Evaporation"*. L'idée centrale de son approche est d'observer des radiations de Hawking (analogues). Dans sa proposition, l'horizon des trous noirs analogues est défini par l'interface où un écoulement de fluide passe du régime subsonique au régime supersonique. Les photons des trous noirs sont remplacés par des phonons, qui ne peuvent pas remonter le courant lorsque l'écoulement est supersonique, tout comme un photon ne peut s'échapper après avoir traversé l'horizon d'un trou noir.

Depuis 2008, des trous noirs analogues ont été réalisés sur différentes plateformes expérimentales (Jacquet et al., 2020) : des réservoirs d'eau (Rousseaux et al., 2008; Weinfurtner et al., 2011), des fibres optiques (Philbin et al., 2008), des condensats de Bose-Einstein (CBE) (Lahav et al., 2010), des cristaux massifs (Belgiorno et al., 2010), des polaritons en microcavité (Nguyen et al., 2015) ou encore l'hélium superfluide ^{3}He-*B* (Človečko et al., 2019).

Alors que la plupart des expériences cherchent à observer l'intrication des radiations de Hawking émises de façon spontanée (Steinhauer, 2016), d'autres plateformes se sont récemment concentrées sur des modèles analogues de l'inflation, ainsi que sur les phases de préchauffage et de réchauffage de l'Univers primordial.

La cosmologie standard a prédit l'existence du Fond Diffus Cosmologique (CMB, pour Cosmic Background Radiation) et l'expansion de l'univers (loi de Hubble) (Watson, 2000). Avant un moment spécifique appelé découplage (voir Figure 2(a)), l'univers était un plasma chaud et dense composé de photons, d'électrons et de protons, où la lumière était continuellement diffusée par les électrons libres. Au découplage, environ 380 000 ans après le Big Bang, l'univers s'est suffisamment refroidi pour que les électrons et les protons forment des atomes d'hydrogène neutres, permettant ainsi aux photons de voyager librement à travers l'espace. Cet instant a donné naissance à ce que l'on appelle la "surface de dernière diffusion", qui constitue une photo de l'univers au moment du découplage. La lumière issue de ce processus est aujourd'hui observée sous la forme du CMB, qui sert de référence pour comparer les prédictions des modèles cosmologiques aux observations. Malgré le succès de ses prédictions, le modèle standard n'explique pas la remarquable isotropie et homogénéité du CMB à larges

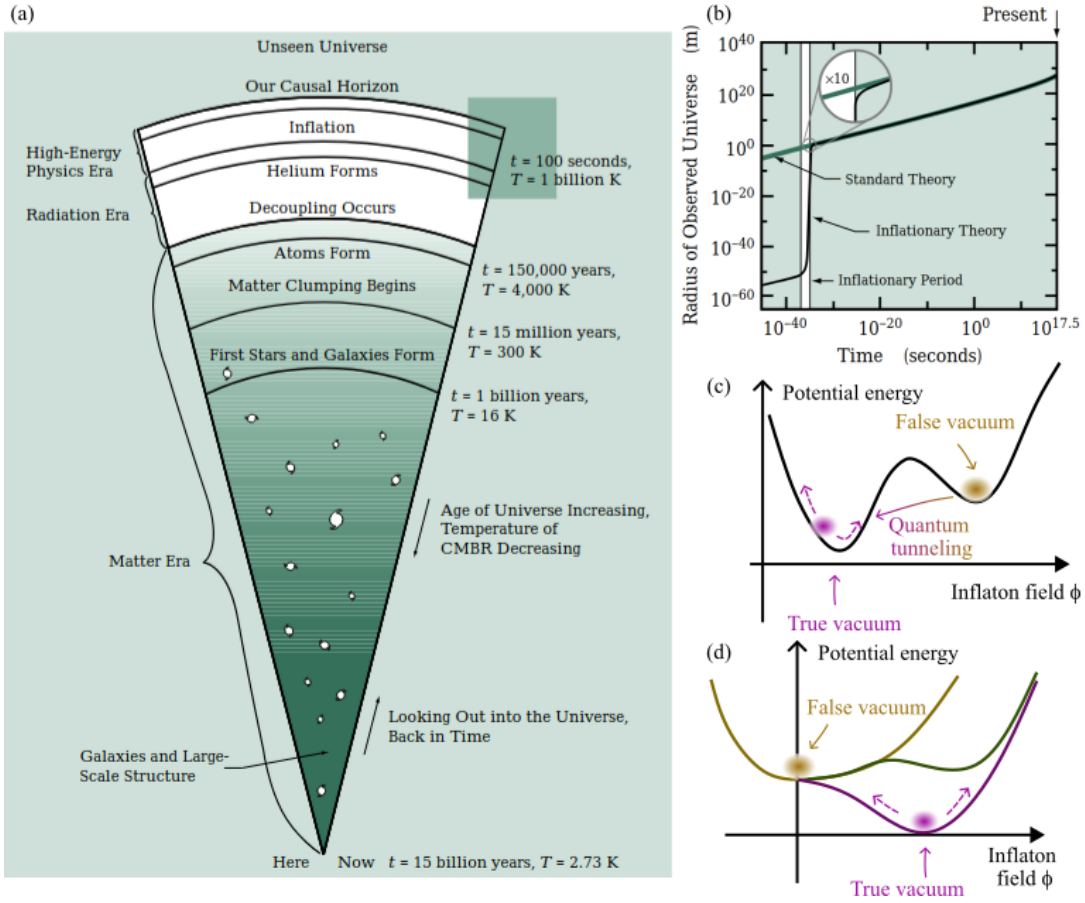

Figure 2: (a) Évolution de notre Univers décrite par le modèle standard. (b) Évolution du rayon de l'Univers actuellement observé, reproduite de Guth (1997). Sans inflation, deux régions opposées du ciel sont causalement séparées, ce qui est contredit par l'apparente uniformité du CMB. (c-d) Deux modèles simple pour étudier la désintégration de l'inflaton. Initialement, le champ est dans un état de faux vide et transit vers un état de vrai vide, dans lequel il commence à osciller, créant des paires de particules sous forme d'états comprimés à deux modes. ©Figures (a-b) de Guth (1997).

échelles (le problème de l'horizon). En particulier, lorsque nous observons deux régions opposées du CMB[1], celles-ci présentent la même température et structure, ce qui implique une connexion causale à un certain moment. La Figure 2(b) montre le rayon de l'univers observable en fonction du temps. Si nous extrapolons l'expansion de l'univers jusqu'au moment du Big Bang, le rayon de l'univers observable aujourd'hui serait trop grand pour que ces régions largement séparées aient jamais été en contact causal. Ce problème de l'horizon, ainsi que d'autres, a motivé l'introduction d'un nouveau champ appelé *inflaton*, qui entraîne une période d'expansion rapide nommée inflation (Guth, 1981; Linde, 1982). Nous voyons sur le graphique que selon la théorie de l'inflation, l'univers observable a, au début, été en contact causal.

La dynamique du champ d'inflaton est décrite comme une transition de phase. Initiale-

[1] En fait, les deux régions n'ont pas besoin d'être opposées pour être causalement déconnectées. Watson (2000) affirme que "toute régions séparées de plus de 2 degrés dans le ciel aujourd'hui aurait été causalement déconnectée au moment du découplage" sans inflation.

ment, ce champ était dans un état appelé “faux vide”. Il a ensuite évolué vers sa valeur de “vrai vide”, libérant une grande quantité d’énergie. Les Figure 2(c) et (d) présentent deux modèles différents de cette transition de phase (Gregory, 2023). Un modèle prévoit un effet tunnel induit par des fluctuations quantiques et/ou thermiques, récemment simulé par Zenesini et al. (2024). L’autre est analogue à une transition de phase du premier ordre. Selon le modèle et la forme du potentiel testé, la dynamique de l’expansion est modifiée. Sa cohérence vis-à-vis des observations du CMB est ensuite vérifiée, ce qui permet de valider le modèle ou de l’affiner.

Une fois l’inflation terminée, l’Univers est froid et vide en raison de cette expansion rapide. Le champ d’inflaton atteint sa valeur minimale mais possède encore une grande énergie potentielle et commence à osciller. Ce champ oscillant se désintègre en particules, “en raison d’une résonance paramétrique large” (Kofman et al., 1994). Cette période de création paramétrique de particules est connue sous le nom de *préchauffage*.
À mesure que le nombre de particules créées augmente, les oscillations de l’inflaton diminuent et la rétroaction des particules avec le champ d’inflaton ne peut plus être négligée. Les particules interagissent et thermalisent : cette période est appelée *réchauffage* (Kofman et al., 1997). Dans cette thèse, nous nous concentrons sur la toute première étape, le préchauffage. Une dynamique de (pré)chauffage analogue a également été étudiée dans un réservoir d’eau, à Nottingham, par Barroso et al. (2022). Je pense que leur conclusion résume bien l’objectif de la QFTCST, qui n’est pas de reproduire exactement la physique de l’inflaton, mais plutôt de démontrer “l’universalité et la robustesse des modèles théoriques abordant la thermalisation dans l’Univers primordial et ses différentes étapes”.
Une fois l’inflation terminée, l’Univers est vide : ce sont les fluctuations du vide qui déclenchent la croissance exponentielle des modes bosoniques (Parentani, 2003). En raison de la conservation de l’impulsion, le vide évolue en un produit d’états comprimés à deux modes d’impulsion opposées $(-k, k)$ (Grishchuk and Sidorov, 1990; Campo and Parentani, 2006). Afin d’observer expérimentalement une amplification paramétrique bosonique depuis le vide, il faut donc un système vide d’excitation donc à température nulle. En effet, lorsque la température n’est pas nulle, le mécanisme d’amplification bosonique est déclenché par les fluctuations thermiques plutôt que par les fluctuations du vide. Parmi les différents systèmes utilisés en gravité analogue, la température extrêmement basse des condensats de Bose-Einstein permet justement d’être sensible aux fluctuations du vide et de révéler des effets quantiques. Bien sûr, la température absolue zéro est inatteignable et il existe donc toujours une infime fraction thermique qui déclenche l’amplification bosonique. Dans ce cas, la population de chaque mode croît selon une loi $(2n_{th} + 1)\sinh^2 Gt$, où n_{th} est la population thermique initiale du mode et G le gain du processus. Le “1” dans $2n_{th} + 1$ témoigne de la contribution des fluctuations du vide dans la croissance de la populatio. Plutôt qu’un état comprimé du vide à deux modes, nous observerons donc un état comprimé *thermique* à deux modes dans notre système. Dans ce cas, le rôle des fluctuations du vide se manifeste dans la non-séparabilité de l’état : la valeur moyenne de $|\langle \hat{a}_k \hat{a}_{-k} \rangle|$ dépasse la population $\langle \hat{a}_k^\dagger \hat{a}_k \rangle$. L’objectif central de ce travail de thèse est donc d’observer qu’une résonance paramétrique des excitations collectives dans un condensat conduit à un état non séparable.

Avec les condensats de Bose-Einstein (CBEs), une modulation soudaine de l’intensité des interactions excite un large éventail de modes de Bogoliubov (Jaskula et al., 2012). De nombreuses expériences ont étudié l’évolution temporelle des corrélations après un quench (changement brutal d’un paramètre du système) : Cheneau et al. (2012) a étudié leur propagation dans un cône de lumière (cône sonore) et Hung et al. (2013) a observé des oscillations de Sakharov. Avec un gaz de Bose unidimensionnel, Schemmer et al. (2018) a tenté de mettre

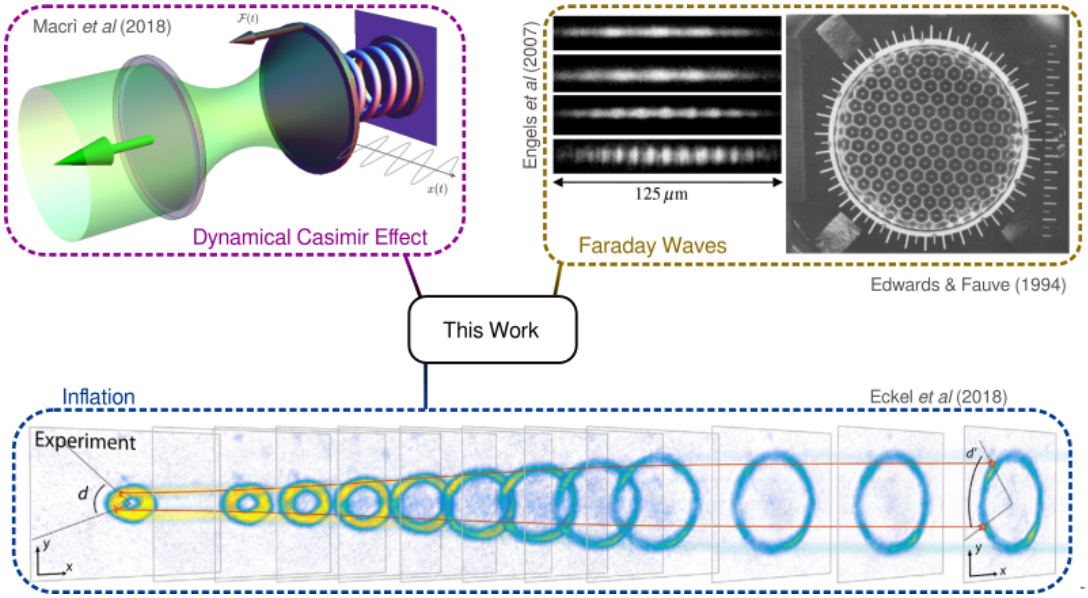

Figure 3: Les différents domaines auxquels cette thèse se rapporte. ©Figures de Macrì et al. (2018), Engels et al. (2007), Edwards and Fauve (1994) et Eckel et al. (2018).

en évidence la compression des phonons de faible k, mais celle-ci a été masquée en raison du potentiel harmonique peu profond. Cependant, des développements technologiques récents permettent désormais d'ingénier des potentiels arbitraires (Gaunt et al., 2013; Corman et al., 2014). En particulier, Eckel et al. (2018) rapporte l'observation du décalage vers le rouge des excitations de grande longueur d'onde dans un condensat en anneau en expansion supersonique. Chen et al. (2021) utilise un potentiel de type boîte plate et une résonance de Feshbach pour effectuer un quench sur un gaz de Bose bidimensionnel et démontrer des corrélations non classiques des quasi-particules créées. Grâce à un microscope quantique 2D, Viermann et al. (2022) exploite une résonance de Feshbach pour ajuster les interactions et utilise leur outil de potentiel arbitraire afin de démontrer la production de particules sur différentes courbures spatiales.

Bien que la résonance paramétrique de l'inflation soit large, celle que nous étudions dans cette thèse ne concerne qu'un seul mode : la fenêtre de résonance en impulsion est relativement étroite. Dans cette perspective, elle est mieux décrite comme une "analogie acoustique de l'effet Casimir dynamique". L'effet Casimir dynamique est en lui-même un domaine de recherche actif (Dodonov, 2010). Il désigne la production de particules due à un paramètre variant de manière non adiabatique. Dans l'étude initiale de Moore (1970), une oscillation rapide de la position d'un miroir de cavité à une fréquence ω crée des photons à partir du vide, dont le vecteur d'onde $k \propto 2\pi/L$ est égal à $\omega/2c$. Ici, c désigne la vitesse de la lumière et L la longueur de la cavité. Cependant, le nombre de photons créés est proportionnel à $(v_m/c)^2$, où v_m est la vitesse du miroir (Lambrecht et al., 1996). Le rapport (v_m/c) est assez défavorable, en particulier dans le contexte du mouvement mécanique. Une alternative consiste à modifier rapidement l'indice optique de la cavité, *i.e.* changer la vitesse de la lumière dans le milieu. Cette technique a permis d'observer la création paramétrique de quasi-particules à partir du vide dans quatre dispositifs différents : des circuits supraconducteurs (Wilson et al., 2011), des jonctions Josephson (Lähteenmäki et al., 2013), une fibre optique modulée spatialement (Vezzoli et al., 2019) et une chaîne d'ions (Wittemer et al., 2019).

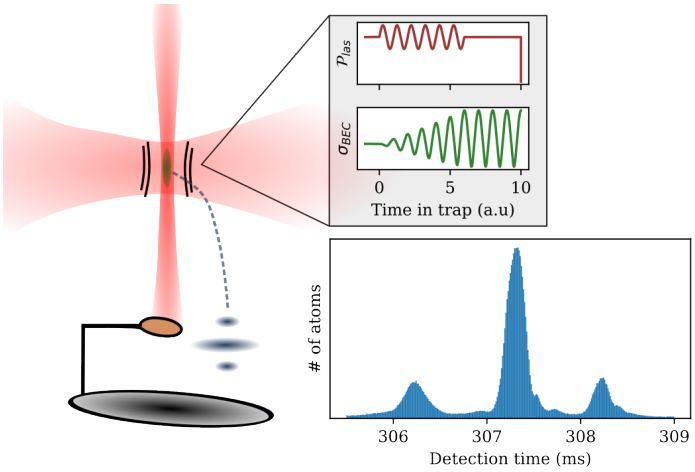

Figure 4: Dispositif expérimental : le CBE allongé verticalement est piégé dans un piège dipolaire croisé. Le laser de piégeage est modulé à deux fois la fréquence du piège avec une faible amplitude pendant quelques périodes (6 périodes pour la courbe rouge en encart). Le CBE est excité dans son mode de respiration: sa largeur oscille à deux fois la fréquence du piège et l'amplitude de cette oscillation augmente avec l'amplitude et la durée de l'excitation laser. La largeur attendue du CBE est montrée dans l'encart avec la courbe verte. Lorsque la modulation du laser s'arrête, le CBE continue d'osciller, et donc d'exciter un mode de Bogoliubov. Une fois le piège éteint, l'excitation collective est transféré en atomes "témoins" qui s'échappent du CBE et sont détéctés. Nous pouvons discriminer ces atomes de ceux du condensat: sur l'image, ils sont de part et d'autre du condensat

Notre dispositif expérimental est le même[2] que celui utilisé par Jaskula et al. (2012) pour démontrer la création paramétrique de phonons dans un CBE dont la densité est modulée. Les auteurs ont mis en évidence une corrélation claire entre les paires de phonons, mais celle-ci n'était pas suffisante pour démontrer la non-séparabilité de l'état. Le protocole pour exciter ces phonons est le suivant : le confinement transverse d'un CBE allongé (forme de cigar) est modulé dans le temps à une fréquence ω. Une telle excitation excite paramétriquement des modes longitudinaux à la fréquence $\omega/2$, un phénomène centenaire connu sous le nom d'ondes de Faraday. De telles excitations paramétriques ont été étudiées avec des gaz quantiques 1D par Engels et al. (2007), Nguyen et al. (2019) et Hernández-Rajkov et al. (2021), ainsi qu'avec un CBE 2D par Liebster et al. (2023). Une expérience plus exotique de type Faraday a été réalisée dans un CBE 1D à deux espèces par Cominotti et al. (2022).

Dans ce travail, nous excitons le mode de respiration transverse d'un CBE en forme de cigar, à deux fois la fréquence du piège (voir l'encart rouge $\mathcal{P}_{las}$ de Figure 4). À cette fréquence spécifique, le CBE entre dans un mode de respiration et sa largeur oscille dans le temps (encart vert σ_{CBE}). Cette oscillation transverse à $2\omega_\perp$ excite une onde de Faraday longitudinale, dont l'énergie est moitié moindre soit à $\omega_\perp$. Lorsque le piège est relâché, les deux modes de phonons sont transférés vers des modes atomiques témoins. Durant le temps de vol de 307 ms, les paquets d'ondes atomiques $(-k, k)$ se séparent du CBE et nous pouvons ainsi discriminer l'impulsion des atomes. Cela est représenté par les deux nuages bleus qui se détachent du CBE sur le schéma de Figure 4. À droite, l'histogramme montre le nombre

[2]Notons tout de fois qu'il ne s'agit pas exactement de la *même* expérience : entre-temps, nous avons changé *quelques* composants (voir le troisième chapitre). Cependant, le grand ralentisseur Zeeman de 4 m est resté le même depuis 30 ans, bien qu'il ait peut-être perdu quelques bobines au fil des doctorants...

d'atomes détectés en fonction du temps : le pic central correspond au CBE et les deux bandes latérales aux pics de phonons.

2. Contenu du manuscrit

Le premier chapitre de cette thèse est une revue de la littérature sur le processus de production de quasi-particules. La première section décrit la fonction d'onde de l'état fondamental du CBE, qui se situe dans le crossover entre le régime en forme de cigare 3D et le régime de champ moyen 1D. Nous introduisons un *ansatz* gaussien pour modéliser le profil transverse du gaz, que nous utilisons tout au long de ce manuscrit. La deuxième section introduit les oscillations collectives, en mettant particulièrement l'accent sur le mode de respiration du CBE. En particulier, nous étudions la réponse du rayon transverse du CBE à un potentiel arbitraire dépendant du temps et proposons un protocole pour mieux contrôler son oscillation. La dernière section introduit la théorie et la transformation de Bogoliubov. Elle passe en revue les principaux progrès théoriques sur le processus de création de paires induit par un hamiltonien dépendant du temps.

Le deuxième chapitre présente la contribution théorique de cette thèse. La première section introduit le formalisme des états gaussiens et la deuxième section passe en revue les critères d'intrication. Notamment, nous introduisons le critère généralisé de Peres-Horodecki permettant d'évaluer la non-séparabilité des états gaussiens. La troisième section se concentre sur deux témoins de corrélation largement utilisés dans les expériences sur les atomes froids : la compression du nombre relatif et la violation de l'inégalité classique de Cauchy-Schwarz. Cette discussion est motivée par notre besoin de mieux comprendre si ces quantités permettent ou non d'évaluer l'intrication des *modes*. La dernière section constitue la principale contribution de ce chapitre. En utilisant les outils introduits dans les première et deuxième sections, nous démontrons qu'il est possible d'évaluer et de quantifier la non-séparabilité des états gaussiens en mesurant les fonctions de corrélation à 2 corps et 4 corps. Lorsque la mesure des corrélations à 4 corps est impossible ou trop bruitée, nous proposons également une borne inférieure sur la fonction de corrélation à 2 corps pour détecter l'intrication. Enfin, nous discutons du domaine d'applicabilité de ce critère ainsi que de sa mise en œuvre expérimentale.

Le troisième chapitre présente l'expérience sur laquelle j'ai travaillé. Nous résumons brièvement les améliorations apportées à l'appareil et décrivons le déroulement de la séquence expérimentale. Les principales descriptions techniques sont laissées en annexe. La troisième section prend un peu plus de temps pour décrire la diffraction de Bragg. Sans entrer trop dans les détails, nous expliquons comment nous façonnons temporellement les impulsions lumineuses de Bragg afin de réaliser des déflecteurs sélectifs et efficaces. Nos capacités expérimentales avec les impulsions de Bragg façonnées dépassent ce qui est décrit dans ce manuscrit et ont conduit à une publication en cours de publication (Leprince et al., 2024). La dernière section discute des propriétés de notre CBE, en s'appuyant sur la description théorique faite dans le premier chapitre.

Le quatrième chapitre décrit notre détecteur, la galette de microcanaux (MCP pour microchannel plate) et les lignes à retard. Ce détecteur original permet de mesurer le temps d'arrivée et la position des atomes individuels. La première section explique comment nous reconstruisons l'impulsion tri-dimensionnelle *in-situ* d'atomes individuels ainsi que le processus de reconstruction. La deuxième section rapporte l'installation d'un écran de protection pour la MCP afin de la protéger du laser vertical, visible dans la Figure 4. La dernière section décrit le processus de mesure du détecteur et discute de ses limitations.

Le cinquième chapitre de cette thèse se concentre sur la dynamique du processus de créa-

tion de quasi-particules. Dans la première section, nous mesurons la relation de dispersion Bogoliubov. La deuxième étudie la création exponentielle de phonons. En particulier, nous mesurons le taux de croissance de la production de quasi-particules et le relions à la prédiction théorique. La différence entre le gain mesuré et la valeur théorique nous permet de déterminer le taux de décroissance des quasi-particules. Bien que ces résultats soient encore préliminaires, ils sont prometteurs et sont comparés aux taux de décroissance théoriques issus de la littérature.

Le sixième chapitre présente le principal résultat expérimental de ce travail. En supposant que l'état est gaussien, nous démontrons la non-séparabilité de l'état de quasi-particules, en nous appuyant sur le travail théorique du deuxième chapitre. La première section rappelle les éléments expérimentaux clés nécessaires pour observer cette non-séparabilité, dans une section "méthode". Les deuxième et troisième sections rapportent la mesure des fonctions de corrélation du deuxième ordre, en utilisant deux approches différentes. Elles donnent des résultats similaires, tant pour les fonctions de corrélation locales que croisées. Dans la dernière section, nous analysons davantage la distribution de Fock de chaque mode pour nous vérifier que nos mesures sont dans le domaine d'applicabilité du critère dintrication dérivé dans le chapitre 2. Nous mesurons également la fonction de corrélation à 4 corps. L'incertitude assez grande sur la mesure nous empêche de caractériser complètement l'état gaussien et son degré d'intrication. Cependant, sur la base de la discussion et des bornes de $g^{(2)}$ dérivées dans le deuxième chapitre, nous évaluons que l'état (gaussien) est intriqué. Nous estimons son degré d'intrication en utilisant la négativité logarithmique. Enfin, nous utilisons une approche autoconsistante pour estimer l'efficacité quantique du détecteur, ce qui nous permet de reconstruire l'état en tenant compte d'une efficacité quantique non unitaire.

Introduction

1. Context

This thesis lies at the intersection of various fields of physics, drawing analogies between the Dynamical Casimir effect and the preheating scenario in the early Universe. In particular, it explores the well-known Faraday wave effect with a particular focus on quantum aspects. It belongs to the so-called field of quantum field theory in curved space-time (QFTCST), also known as *analog gravity*. This field aims to reproduce on table-top experiments systems that behave like unaccessible observables. It also intends to use theoretical tools developed in general relativity or quantum field theory to model condensed matter systems. It was pioneered by a seminal paper by Unruh (1981), titled "Experimental Black-Hole Evaporation". Central to his idea is to observe (analog) Hawking radiations. In such experiments, the horizon of the analog black holes is defined by the interface at which a liquid flow changes from subsonic to supersonic. The photons of the black holes are replaced by the phonons, which cannot go upstream when the water flow is supersonic, as a photon cannot escape once crossed the black hole horizon. Analog black holes were realized since 2008 on various experimental platforms (Jacquet et al., 2020): water-tanks (Rousseaux et al., 2008; Weinfurtner et al., 2011), optical fibers (Philbin et al., 2008), Bose-Einstein condensates (BEC) (Lahav et al., 2010), bulk crystals (Belgiorno et al., 2010), microcavity polaritons (Nguyen et al., 2015) or superfluid ^{3}He-*B* (Človečko et al., 2019). While most of the experiments aim to observe entanglement of spontaneous Hawking radiations (Steinhauer, 2016), other platforms focused more recently on analog model of inflation, on the preheating and reheating stages.

Standard cosmology greatly succeeded in predicting the existence of the Cosmic Background Radiation (CMB) and the universe expansion (Hubbles law) (Watson, 2000). Before a specific time called decoupling (see Figure 5(a)), the universe was a hot, dense plasma of photons, electrons, and protons, where light was continuously scattered by free electrons. At decoupling, about 380,000 years after the Big Bang, the universe cooled enough for electrons and protons to form neutral hydrogen atoms, allowing photons to travel freely through space. This moment created what is called the "last scattering surface", which is a snapshot of the universe at decoupling. The light from this process is now observed as the CMB which is the resource used to compare cosmological models. One of the long-standing problems in cosmology, known as the horizon problem, arises from the observation that the CMB is remarkably isotropic and homogeneous across vast distances. In particular, when we observe two opposite[3] regions in the CMB, they exhibit the same temperature and structure, which implies a causal connection at a time. Figure 5(b) shows the radius of the observable universe as function of time. If we extrapolate the expansion of the universe back to the time of the

[3] In fact the two regions do not need to be opposite to be causally disconnected. Watson (2000) states that "any region separated by more than 2 degrees in the sky today would have been causally disconnected at the time of decoupling".

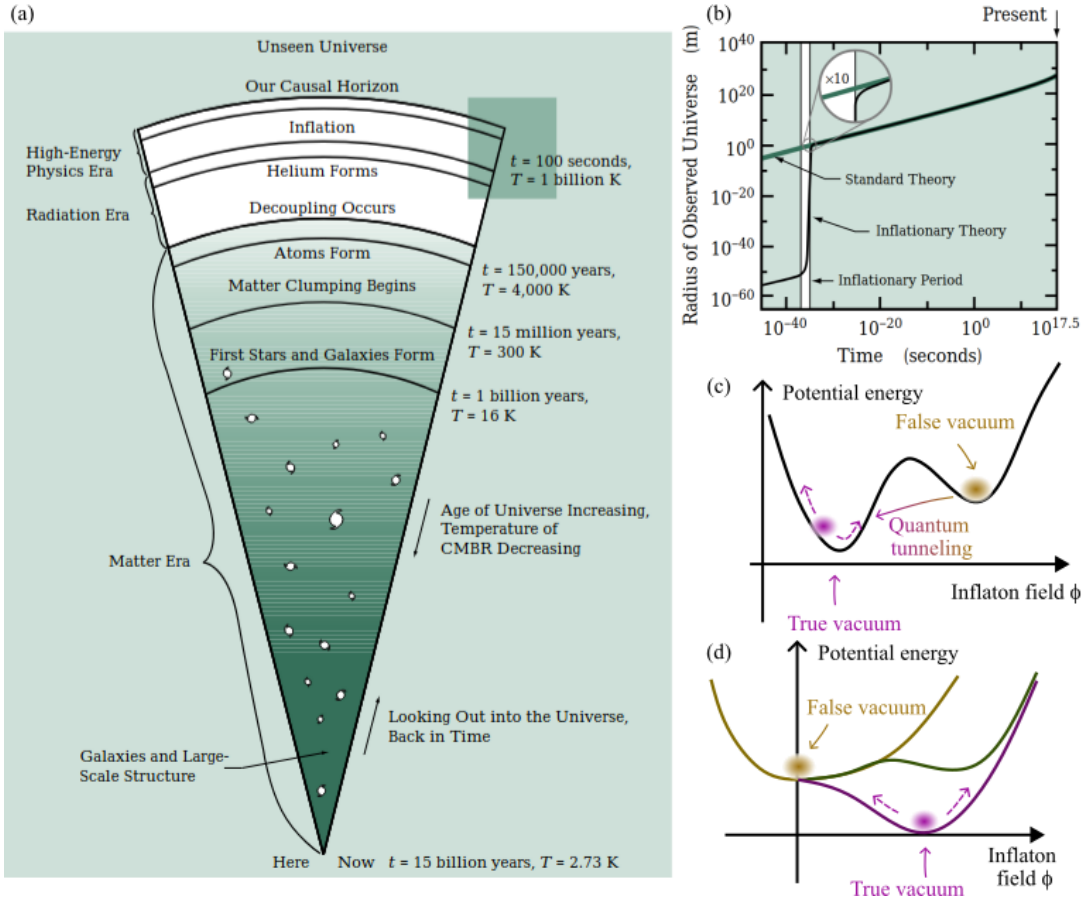

Figure 5: (a) Evolution of our Universe described by the Standard model. (b) Evolution of the radius of the (currently) observed Universe, reproduced from Guth (1997). Without inflation, two opposite regions in the sky are causally separated. (c-d) Two toy models for the decay of the inflaton field. Initially, the field is in the a false vacuum state and later decays into a true vacuum state, in which it starts to oscillates, creating pairs of particles in a product of two-mode squeezed states. ©Figures (a-b) from Guth (1997).

Big Bang, the radius of the observable universe today would be too large for these widely separated regions to have ever been in causal contact. This horizon problem, along with others, motivated the introduction of a new field known as the *inflaton*, which drives a period of rapid expansion called inflation (Guth, 1981; Linde, 1982).

The dynamics of the inflaton field is described as a phase transition: initially, this field was in a state that is referred to as "false vacuum". This field then decayed to its "true vacuum" value, releasing a great amounts of energy. Figure 5(c) and (d) show two different models of this phase transition (Gregory, 2023). One model expects quantum and/or thermal driven tunneling and was recently mimicked by Zenesini et al. (2024). The other one is analogous to a first order phase transition. Depending on the model and the shape of the test potential, the dynamics of the expansion is modified. Its consistency can be verified through CMB observations, which determines the validity of the model, or fine-tunes it.

Once inflation ends, the Universe is cold and empty, due to this rapid expansion. The inflaton field reached its minimum value but has still a large potential energy and starts to oscillate. This oscillating field decays into particles, "due to a broad parametric resonance"

(Kofman et al., 1994). Such period of parametric creation of particles is known as *preheating*. While the number of created particles increases, backreaction with the inflaton field cannot be neglected and the oscillations of the inflaton decrease. Particles interact together and thermalize: this period is referred to as *reheating* (Kofman et al., 1997). In this thesis, we focus on the very first step, the preheating. Analog (p)reheating dynamics was also investigated in tank water, in Nottingham by Barroso et al. (2022). I think that their conclusion summarizes well the goal of QFTCST which is not to exactly reproduce inflaton physics but rather to demonstrate "universality and robustness of theoretical models tackling the thermalization in the Early Universe and its distinct stages".
After inflation the Universe is empty: it is vacuum fluctuations that trigger the exponential growth of bosonic modes (Parentani, 2003). Because of conservation of momentum, the vacuum evolves into a product of two-mode squeezed states in the $(-k, k)$ basis (Grishchuk and Sidorov, 1990; Campo and Parentani, 2006). When the temperature is not zero, bosonic amplification mechanism is triggered by thermal fluctuations rather than vacuum fluctuations. Among analog gravity setups, the extremely low temperature of BECs allows to be sensitive to vacuum fluctuations and to reveal quantum effects. Of course, absolute zero temperature is unreachable therefore there is always a tiny thermal fraction that triggers bosonic amplification: the population grows as $(2n_{th}+1)\sinh^2 Gt$, where n_{th} is the initial thermal population of the mode and G the gain of the process. Without initial thermal population, the mode population grows due to quantum fluctuations. The "1" in $2n_{th}+1$ witnesses this vacuum fluctuation part. Rather than a two-mode squeezed vacuum state, we shall observe a two-mode squeezed *thermal* state in our system. In this case, the role of vacuum fluctuation manifests in the non-separability of the state: the average value of $|\langle \hat{a}_k \hat{a}_{-k} \rangle|$ exceeds the population $\langle \hat{a}_k^\dagger \hat{a}_k \rangle$. Central to this work is therefore to demonstrate that a parametric resonance leads to a non-separable state.

With BECs, quenching the interaction strength excites a broad range of Bogoliubov modes (Jaskula et al., 2012). Many experiments studied the time evolution of the correlations after a quench: Cheneau et al. (2012) studied their spreading within a light-cone (sound-cone) and Hung et al. (2013) observed Sakharov oscillations. With a 1D Bose gas, Schemmer et al. (2018) tried to evidence the squeezing of low k phonons, the latter being masked due to the shallow harmonic potential. However, recent technological developpements allow now to engineer arbitrary potentials (Gaunt et al., 2013; Corman et al., 2014). In particular, Eckel et al. (2018) report on the observation of the redshift of long-wavelength excitations in a supersonically expainding ring condensate. Chen et al. (2021) use a flat box potential and a Feshbach resonance to quench a 2D Bose gas and demonstrate non-classical correlations of the created quasi-particles. With a 2D quantum microsope, Viermann et al. (2022) make use of a Feshbach resonance to tune interactions, using their arbitrary potential tool to demonstrate particle production on different spatial curvatures.

While the parametric resonance of inflation is broad, the one we study in this thesis involves only a single mode: the resonant window in k is quite narrow. From this perspective, it is better described as an "Acoustic analog of the Dynamical Casimir Effect". The Dynamical Casimir effect is in itself already an active field of research (Dodonov, 2010). It refers to the production of particles due to a non-adiabatically changing parameter. Originally,Moore (1970) sudied a fast oscillation of the position of a cavity mirror at ω, which creates photons from vacuum whose wave-vector $k \propto 2\pi/L$ is equal to $\omega/2c$. Here, c refers to the light speed and L to the cavity length. However, the number of created photons scales as $(v_m/c)^2$ where v_m is the speed of the mirror (Lambrecht et al., 1996). The (v_m/c) is a rather unfavorable ratio, especially in the context of mechanical motion. One could instead rapidly change the

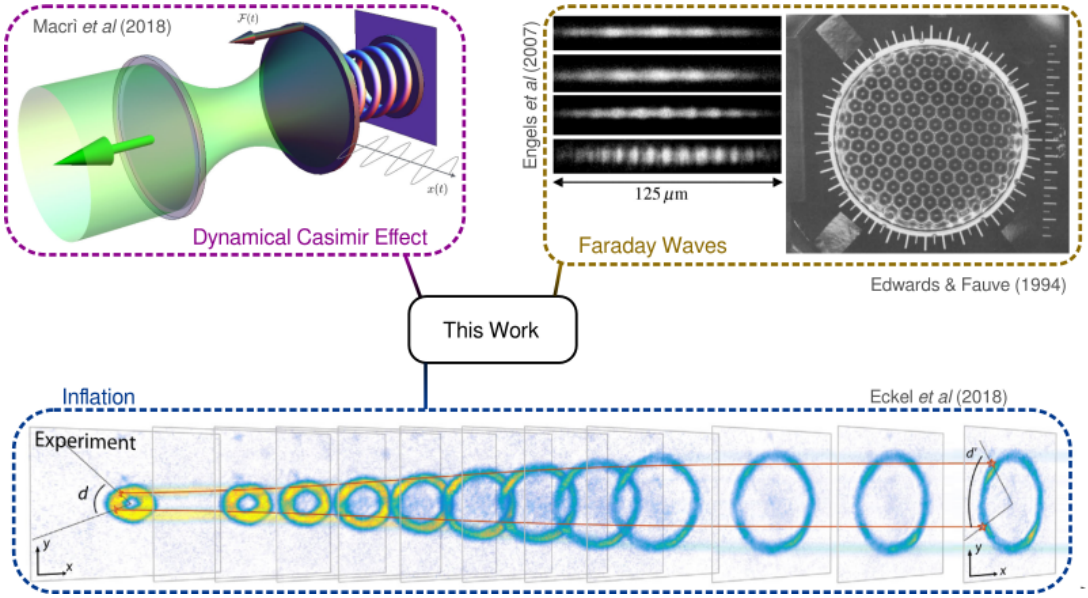

Figure 6: The different fields to which this thesis refers to. ©Figures from Macrì et al. (2018), Engels et al. (2007), Edwards and Fauve (1994) and Eckel et al. (2018).

optical index of the cavity *i.e.* modifying the light speed in the medium. This technique led to the observation of the parametric creation of quasi-particles from vacuum in four different setups, with superconducting circuits (Wilson et al., 2011), Josephson junctions (Lähteenmäki et al., 2013), an optical fiber (Vezzoli et al., 2019) and an ion chain (Wittemer et al., 2019).

Our experimental machine is the same experiment[4] that was used by Jaskula et al. (2012) to demonstrate parametric creation of phonons in a density-modulated BEC. The authors demonstrated a clear correlation between the phonon pairs however the correlation was not sufficient to demonstrate non-separability of the state. The protocol to excite these phonons follows: the highly elongated BEC transverse confinement is time-modulated at frequency ω. Such excitation parametrically excites longitudinal modes at frequency $\omega/2$, a century-year old phenomenon known as Faraday waves. Such parametric excitations were studied with 1D quantum gases by Engels et al. (2007), Nguyen et al. (2019) and Hernández-Rajkov et al. (2021) and a 2D BEC by Liebster et al. (2023). A more exotic Faraday-like experiment was conducted in a two-species 1D BEC by Cominotti et al. (2022).

In this work, we excite the transverse breathing mode of a highly elongated BEC at twice the frequency of the trap (see the red inset $\mathcal{P}_{las}$ of Figure 7). At this specific frequency, the BEC enters a breathing mode and its width oscillates in time (green inset σ_{BEC}). This transverse oscillation at $2\omega_\perp$ excites a longitudinal Faraday wave, whose energy is $\omega_\perp$. When the trap is released, the two phonon modes are transferred to witness atomic modes. During the 307 ms time-of-flight, the $(-k, k)$ atomic wave-packets separate from the BEC. This is represented by the two blue clouds that separate from the BEC on the sketch of Figure 7. On the right, the histogram shows the number of detected atoms as a function of time: the central peak corresponds to the BEC and the two side-bands to the phonon peaks.

[4] Let me emphasize that it is not exactly the "same" experiment: in the meantime, we changed a *few* components (see the third chapter). The large 4m Zeeman slower is however the same since 30 years, even though it might have lossed a few coils per PhD student...

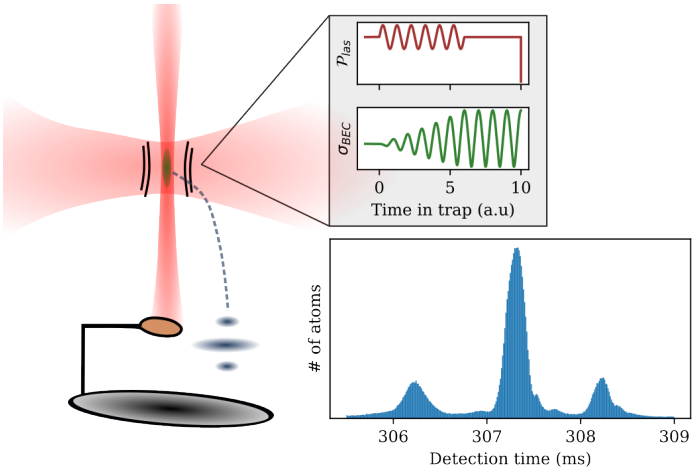

Figure 7: Experimental setup: the vertically elongated BEC is trapped in a cross dipole trap. The trapping laser is modulated at twice the trap frequency with a small amplitude for a few periods (6 periods in the red curve inset). The BEC enters breathing mode, its width oscillates at twice the trap frequency and the amplitude of its oscillation increases with both the amplitude and the excitation duration. The BEC expected width is shown in the inset, with the green curve. When the laser stops modulating, the BEC keeps oscillating, hence keeps exciting one Bogoliubov mode. Once the trap is switched off, the collective excitation is mapped to witness atoms that are detected just before and after the BEC.

2. Content of this manuscript

The first chapter of this thesis is a literature review of the quasi-particle production process. The first section describes the BEC ground state wave-function which is in the crossover between the 3D cigar shaped regime and the 1D mean field regime. We introduce a Gaussian Ansatz to model the gas transverse profile that we use throughout this manuscript. The second section introduces collective oscillations, with a special focus on the BEC breathing mode. In particular, we study the response of the BEC transverse radius to an arbitrary time-dependent potential and propose a protocol to better control its oscillation. The last section introduce Bogoliubov theory and transformation and reviews the major theoretical progresses on pair creation process due to a time dependant Hamiltonian.

The second chapter contains the theoretical contribution of this thesis. The first section introduces Gaussian state formalism and the second reviews entanglement criteria. Notably, we introduce the *bona fide* condition for any Gaussian state and the generalized Peres-Horodecki criterion that assess non-separability of Gaussian states. The third section focuses on two correlation witnesses widely used in cold atoms experiment: relative number squeezing and the classical Cauchy-Schwarz inequality violation. Such discussion is motivated by our need to better understand if these quantities can or cannot assess *mode* entanglement. The last section is the main contribution of this chapter. Using the tools introduced in the first and second section, we demonstrate that we can assess and quantify non-separability of Gaussian states by measuring the 2- and 4-body correlation functions. When the 4-body correlation measurement is not possible or too noisy, we also provide a lower bound on the 2-body correlation function to assess entanglement. We finally discuss the range of applicability of this criterion and its experimental implementation.

The third chapter introduces the BEC machine on which I have been working. We briefly

summarize the upgrades implemented on the apparatus and describe the course of the experimental sequence. Major technical descriptions are left within the appendix. The third section takes a bit more time to describe Bragg diffraction. Without going too much into the details, we describe how we shape Bragg pulses to realize selective and efficient deflectors. Our experimental capabilities with shaped bragg pulses go beyond what is described in this manuscript, and led to a submitted publication (Leprince et al., 2024). The last section discusses the properties of our cigar shaped BEC, relying on the theorical description made in the first chapter.

Fourth chapter describes our detector, the micro-channel plate (MCP) and delay lines. This original detector allows to detect the arrival time and position of individual atoms. The first section explains how we reconstruct the *in-trap* 3D momentum of individual atoms and reconstruction code. The second section reports on the installation of a shield to protect the MCP from the vertical laser, which can be seen in Figure 7. The last section describes the measurement process of the detector and discusses its limitations.

The fifth chapter of this thesis focuses on the dynamics of the quasi-particle creation process. In the first section, we measure the Bogoliubov dispersion relation. The second studies the exponential creation of phonons. In particular, we measure the growth rate of the quasi-particle production and relate it to the theoretical prediction. The difference between the measured gain and the theoretical value allows us to determine the quasi-particle decay rate. While these results are still preliminary, they are promising and are compared with the theoretical decay rates from the literature.

The sixth chapter presents the main experimental result of this work. Assuming the state is Gaussian, we demonstrate non-separability of the quasi-particle state, relying on the theoretical work of the second chapter. The first section recalls the key ingredients that were needed to observe this non-separability, in a "method" section. The second and third sections report the measurement of the second-order correlation functions, using two differents approaches. They yield similar results, both for local and cross correlation functions. In the last section, we further analyse the full-counting statistics of each mode to demonstrate that we are in the applicability domain of the criterion derived in chapter 2. We also measure the 4-body correlation function. The quite large uncertainty on the measurement prevents us to completely characterize the Gaussian state and its degree of entanglement. However, based on the discussion and the $g^{(2)}$ bounds derived in the second chapter, we assess that the (Gaussian) state is entangled. We estimate its degree of entanglement using the logarithmic negativity. Finally, we use a self-consistent approach to estimate the detector's quantum efficiency, which allows us to reconstruct the state accounting for non-unit quantum efficiency.

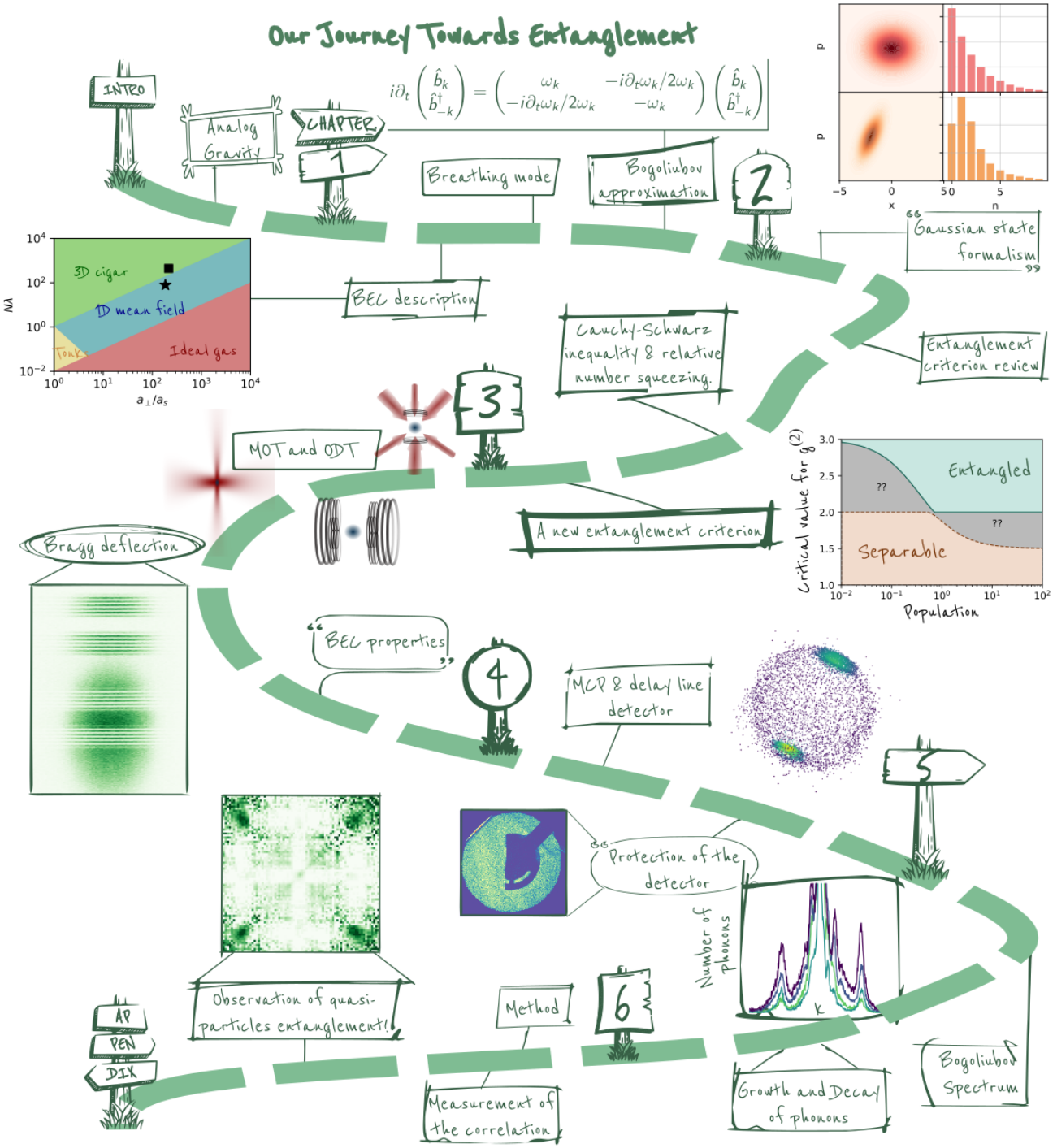

Figure 8: On overview of the journey in this manuscript.

Chapter I

Parametric creation of quasi-particles

Faraday's experiment consists in shaking a fluid vertically at a well-defined frequency. Depending on the viscosity of the fluid and the boundary conditions, a specific pattern appears at the liquid interface. After the proposal of Staliunas et al. (2002) from which we reproduce numerical simulations in Figure 9, Engels et al. (2007) performed similar experiment with a cigar-shape Bose-Einstein condensate. By modulating periodically the transverse potential of the BEC, the authors excite longitudinal collective excitations. In particular, they show that when the frequency of the modulation is ω_d, they excite the collective mode with wave-vector k such that $\omega(k) = \omega_d/2$, where $\omega(k)$ is the BEC dispersion relation. A series of theoretical papers followed this experiment to better model the dispersion relation $\omega(k)$ (Nicolin et al., 2007; Nicolin and Raportaru, 2010; Nicolin, 2011). In their work, the authors use a transverse Ansatz to study an effective 1D Gross-Pitaevskii equation. Linearizing the system for a small perturbation with wave-vector k, they obtain a Mathieu equation for which a Floquet analysis gives access to unstable regions. As for any periodically driven system, it reveals the presence of multiple resonances, at wave-vectors such that $\omega(k) = n\omega_d/2$, where n is an integer. The unstable regions, shown in Figure 9, are referred to as Mathieu tongues due to their shape. With quantum fluids, secondary resonances were observed experimentally by Nguyen et al. (2019) and Hernández-Rajkov et al. (2021).

These Faraday waves can be interpreted microscopically as pairs of Bogoliubov quasi-particles with opposite momenta, k and $-k$. This is our approach in this manuscript: we partition the system in the $(k, -k)$ basis and focus on the non-separability of the two-mode state. This perspective is particularly relevant because, when the trap is turned off, the quasi-particle state maps onto the atomic state, yielding a momentum-entangled source of massive particles. To describe the state entanglement dynamics, we must keep the longitudinal modes quantized. With this approach, our treatment and theoretical description align more closely with other pair-creation mechanisms studied in the literature.

- Four-wave mixing with two colliding Bose-Einstein condensates by Perrin et al. (2007), Kheruntsyan et al. (2012) and Hodgman et al. (2017);
- Collisional de-excitation of a 1D Bose gas by Bücker et al. (2011);
- Four-wave mixing by changing the dispersion relation in an optical lattice by Campbell et al. (2006) and Bonneau et al. (2013);
- Modulation of the interaction strength though a Feshbach resonance by Clark et al. (2017).

We start this chapter by describing the background on which quasi-particles propagate

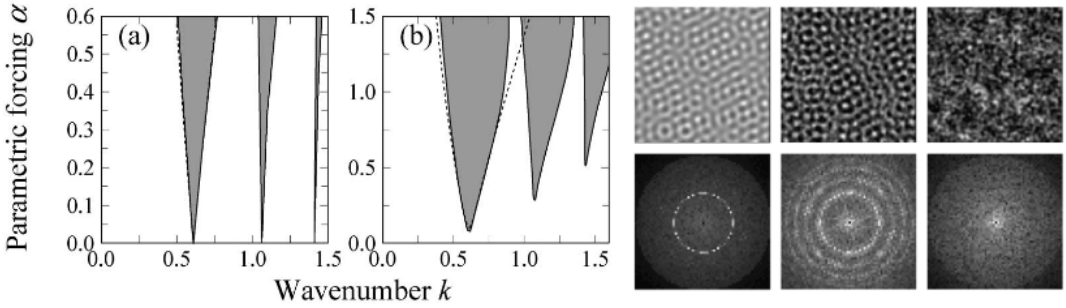

Figure 9: Left: Resonance tongues of the parametric instability, which are typical in parametrically driven systems. The shaded area represents the unstable regions. In panel (a), there is no damping, so all wave-vectors k_n such that $\omega(k_n) = n\omega_d/2$ can be excited, even with very low parametric forcing. In panel (b), a small dissipative term is included. For sufficiently small forcing, only one resonant wavevector $\omega(k_1) = \omega_d/2$ is excited. Right: Simulation snapshots showing the evolution of the Faraday pattern in real space (top) and Fourier space (bottom). ©Figures from Staliunas et al. (2002).

which is the BEC wave-function. In the second section we focus on the transverse dynamics of the BEC when the transverse trap frequency is modulated. The last section is dedicated to the pair creation process: we introduce Bogoliubov transformation and discuss under which conditions the entanglement of the two-mode state can be observed.

What we knew, what is new ? This chapter is mainly a review of the literature. The only contribution is the proposed protocol to better control the oscillations of the BEC radius, in section 2.C.

1. Description of the ground state BEC

In this chapter, we investigate the dynamics of the field $\hat{\Psi}$ describing N bosons of mass m confined in an external potential U. The typical density of our Bose-Einstein condensate is a few 10^{13} at/cm^3 meaning that the typical interparticle distance is 0.5 µm. The typical range of the interatomic forces at play is much lower than this distance, hence we can consider only interactions between two particles (Pitaevskiĭ and Stringari, 2016). The typical length of interaction is given by the scattering length $a_s \sim 7$ nm. We can therefore consider that our gas is weakly interacting. Second, we model the atomic interactions by a contact potential (Dalibard, 2022) so that the Hamiltonian of the bosonic field $\hat{\Psi}(\mathrm{r})$ is

$$\hat{H} = \int d\mathrm{r} \left[\frac{\hbar^2}{2m} \nabla\hat{\Psi}^\dagger \cdot \nabla\hat{\Psi} + U(\mathrm{r})\hat{\Psi}^\dagger\hat{\Psi} + \frac{g}{2}\hat{\Psi}^\dagger\hat{\Psi}^\dagger\hat{\Psi}\hat{\Psi} \right] \tag{1}$$

where the coupling constant is related to the s-wave scattering length $g = 4\pi\hbar^2 a_s/m$. From this many-body hamiltonian (1), we can derive the motion equation for the field, that is then given by the commutator of $\hat{\Psi}$ with the hamiltonian. This leads to the Gross-Pitaevskii equation, derived independently by Gross (1961) and Pitaevskii (1961)

$$i\hbar\partial_t\hat{\Psi} = \left(-\frac{\hbar^2\nabla^2}{2m} + U(r) + g|\hat{\Psi}|^2 \right) \hat{\Psi}(r). \tag{2}$$

In order to derive the ground state wave-function, we replace the field $\hat{\Psi}$ by a classical field Ψ_0, that represents the Bose-Einstein condensate wave-function.

In subsection 1.A, we describe the system and the trap properties, resulting in a highly elongated BEC. We recall the BEC properties in two different one-dimensional regimes. The first one (section 1.B) is the 3D cigar-shaped regime in which the system keeps its 3D features. The second one (section 1.C) is the one-dimensional mean field regime, in which the radial dynamics is frozen. The chemical potential is low compared to the first excited level of the harmonic oscillator. As we shall see, the relation between the sound speed, the chemical potential, the number of atoms and the BEC size are quite different in these two regimes. Our experiment being in between those two regimes, we will use the approach of Gerbier (2004) to describe the system in the crossover regime in section 1.D, using a Gaussian Ansatz for the transverse density profile.

1.A A gas of bosons in an elongated trap

The BEC we consider is cigar-shaped : the trapping frequencies in the transverse directions $\omega_\perp$ are much larger than the longitudinal one ω_z. The aspect ratio $\lambda \equiv \omega_z/\omega_\perp$ is small compared to 1. The transverse frequency is typically of the order of 1 kHz and the longitudinal is typically 30 Hz. The mean field Ψ_0 obeys also the Gross-Pitaevskii equation (2) for which, in the stationary configuration, the time derivative on the left hand-side is replaced by the chemical potential μ_0, that represents the energy per particle, leading to

$$-\frac{\hbar^2}{2m}\nabla^2\Psi_0 + U(\mathrm{r}, z)\Psi_0 + g|\Psi_0|^2\Psi_0 = \mu_0\Psi_0. \tag{3}$$

Note that the stationary Gross-Pitaevskii equation can also be derived from the energy functional of equation (1) by introducing the chemical potential *by hand* as a Lagrange multiplier, as in the chapter II of Dalibard (2024). The first term in this equation is the kinetic energy of the ground state whose contributions result from the confining strength along each axis. The so-called Thomas-Fermi (TF) limit consists of neglecting this term with respect to the interaction term. In this limit, the BEC density has an inverted parabola shape. We are not in this case because the BEC is strongly confined along the transverse direction. We now write the order parameter $\Psi_0 = \sqrt{n_1} f(\tilde{r}, n_1)/a_\perp$, introducing the harmonic oscillator length $a_\perp = \sqrt{\hbar/m\omega_\perp}$ along the transverse direction, the $1D$ density $n_1(z)$ and $\tilde{r} = r/a_\perp$. Even though it is not explicit, we allow the f function to depend on z through the density n_1. We now neglect the kinetic energy along z i.e. we neglect $\partial_z\Psi_0$ compared to the kinetic energy. This is the so-called local density approximation where one solves the Gross-Pitaevskii equation at any position z for a fixed density $n_1(z)$. We then find the solution f that depends on z through n_1. In this case, the stationary Gross-Pitaevskii equation (3) reads

$$\left(-\frac{1}{2}\Delta_{\tilde{r}} + \frac{1}{2}\tilde{r}^2 + 4\pi a_s n_1 f^2\right) f = \frac{\mu_{le}}{\hbar\omega_\perp} f. \tag{4}$$

where $\mu_{le} = \mu_0 - \omega_z^2 z^2/2$ is the local equilibrium chemical potential that fixes the 1D atomic density n_1. The balance between the kinetic energy and the interaction depends on the dimensionless parameter $n_1 a_s$. The density n_1 that drives the transition between those two regimes cannot be approximated by N/a_z where a_z is the harmonic oscillator length along the z direction and N the number of atoms. Indeed, the size of the BEC is much larger than this length. As we shall see, the natural dimensionless number to describe in which regime the gas is

$$\chi := N\frac{a_s a_\perp}{a_z^2} = N\lambda\frac{a_s}{a_\perp}. \tag{5}$$

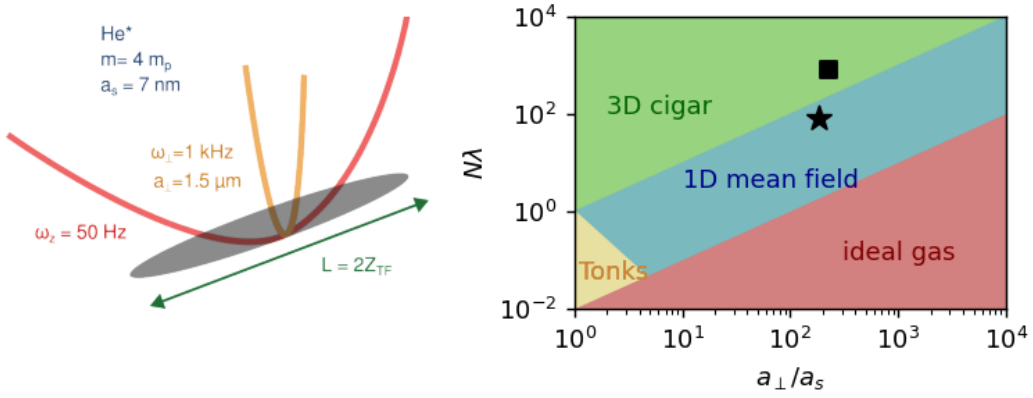

Figure 10: Left: scheme of the system. A cigar-shaped BEC of size L is trapped in a harmonic trap with frequencies 1100 and 50 Hz, trapping frequencies for the crossed-dipole trap BEC. Right: phase diagram in the plane $N\lambda$ and $a_\perp/a$. In the 3D cigar-shaped regime, the system keeps its 3D features which is not the case in the one dimensional mean field regime. The ideal gas region, where the conditions of applicability of the LDA fails, is where the inequality $(Na/a_\perp\sqrt{\lambda})^{1/3} \ll 1$ no longer holds. The value of λ taken was 0.04, which is the typical value for cross dipole trap BECs in our experiment. The black star represents the experiment carried by Jaskula et al. (2012) for which $a_s n_1 \sim 0.2$. The square shows the region where the experiment reported in this manuscript are performed ($a_s n_1 \sim 1$). ©Inspired from Menotti and Stringari (2002).

When this number is large, the product $n_1 a_s$ is large and the behavior of the system can be approximated by neglecting the kinetic energy term : this regime is called the three dimensional cigar regime, or 1D Thomas-Fermi regime. On the opposite, when χ is small compared to one, the kinetic energy can no longer be neglected and one enters in the one dimensional mean field regime. Note that the description we will give of the system in this regime fails when the interparticle distance n_1^{-1} is smaller than the healing length $\xi = (8\pi a_s n_{3D})^{-1/2}$. In this case, the regime enters the so-called Tonks-Girardeau regime. The transition between those two regimes is tuned by the dimensionless parameter $N\lambda a_\perp^2/a_s^2 = \chi a_\perp^3/a_s^3$ (Petrov et al., 2000; Dunjko et al., 2001). Our experiment being far from this regime, we do not aim to describe it and refer the interested reader to Menotti and Stringari (2002) or the chapter 24 of Pitaevskiĭ and Stringari (2016).

1.B The 3D cigar-shaped regime or radial Thomas-Fermi regime

When $a_s n_1 \gg 1$, the kinetic energy is small compared to the interaction strength. Such regime is called the radial Thomas-Fermi regime, or three-dimensional cigar. In this regime, even though the density profile is very anisotropic and elongated, the system keeps its 3D features as its chemical potential is sufficient not to be confined to the first transverse energy level (Pitaevskiĭ and Stringari, 2016). In this regime, we start by writing the transverse profile defined by the function f, at fixed position z i.e. at fixed density n_1. Neglecting the kinetic energy leads to an inverted parabola for the transverse profile

$$|\Psi_0|^2 = \frac{2n_1}{\pi R_\perp^2}\left(1 - \frac{r^2}{R_\perp^2}\right), \qquad R_\perp = 2a_\perp(a_s n_1)^{1/4} \tag{6}$$

and zero where $r > R_\perp$. In this regime, the local equilibrium chemical potential reads

$$\frac{\mu_{le}}{\hbar\omega_\perp} = 2\sqrt{a_s n_1}. \tag{7}$$

In particular, this equation links the chemical potential to the density at the center of the trap. The total number of particles $N = \int n_1$ fixes then the length of the BEC, which is the length at which the density vanishes. Especially, the 1D atomic density takes the form (Menotti and Stringari, 2002)

$$n_1(z) = \frac{1}{16 a_s}\left(15N\lambda\frac{a_s}{a_\perp}\right)^{4/5}\left(1-\frac{z^2}{Z_{3D}^2}\right)^2 \tag{8}$$

where the length of the BEC is given by

$$Z_{3D} = \sqrt{\frac{2\mu_0}{m\omega_z^2}} = \frac{a_z}{\sqrt{\lambda}}\sqrt{\frac{2\mu_0}{\hbar\omega_\perp}} = \frac{a_z}{\sqrt{\lambda}}\left(15N\lambda\frac{a_s}{a_\perp}\right)^{1/5}. \tag{9}$$

Note that this profile is not the same as a 3D Thomas-Fermi profile: the shape is *not* an inverted parabola on the long axis but a square of an inverted parabola. As we will see, this changes the dispersion relation in the fluid compared to the isotropic case. In particular, the speed of sound c_s can be deduced from the thermodynamic relation $mc_s^2 = n_1\partial_{n_1}\mu$ (Pitaevskiĭ and Stringari, 2016). Using equation (7), one obtains at the center of the trap

$$c_s = \frac{\hbar}{m a_\perp}(a n_1)^{1/4} = \sqrt{\mu/2m}. \tag{10}$$

It worth noticing that this result differs from the sound velocity derived in the case of a isotropic harmonic trap by a factor $\sqrt{2}$, the latter being simply given by $mc_s^2 = \mu_0$. This result was derived by Zaremba (1998) after the first measurement of the sound speed in a cigar-shaped BEC by Andrews et al. (1997). The exhibited dependence of the speed of sound on the density did not match the 3D case which motivated a more careful analysis, taking into account the anisotropic profile and leading to this $\sqrt{2}$ factor. Note however that the expression of the total chemical potential in the 3D cigar regime is the same as in the 3D Thomas-Fermi. We have

$$\mu_0 = \frac{\hbar\omega_\perp}{2}\left(15N\lambda\frac{a_s}{a_\perp}\right)^{2/5} = \frac{\hbar\bar{\omega}}{2}\left(15N\frac{a_s}{\bar{a}}\right)^{2/5} \tag{11}$$

where $\bar{\omega}^3 = \omega_x\omega_y\omega_z$ and $\bar{a} = \sqrt{\hbar/m\bar{\omega}}$. The right hand-side of this equation is the expression of the chemical potential in the 3D TF regime.

1.C The 1D mean field regime

When $a_s n_1 \ll 1$, the kinetic energy can no longer be ignored. Neglecting it totally would lead us to recover the Gaussian ground state of the radial harmonic oscillator. At first order, the chemical potential is linear with $a_s n_1$ (Menotti and Stringari, 2002)

$$\frac{\mu}{\hbar\omega_\perp} = 1 + 2a_s n_1 \tag{12}$$

In this regime, we often introduce the effective one-dimensional coupling constant $g_{1D} = 2a_s\hbar\omega_\perp$: the stronger the transverse confinement is, the stronger the interactions are. In this regime, the Thomas-Fermi radius is given by (Dunjko et al., 2001)

$$Z_{1D} = \frac{a_z}{\sqrt{\lambda}}\left(3N\lambda\frac{a_s}{a_\perp}\right)^{1/3} \tag{13}$$

and the density is

$$n_1(z) = \frac{1}{4a_s}\left(3N\lambda\frac{a_s}{a_\perp}\right)^{2/3}\left(1-\frac{z^2}{Z_{1D}^2}\right). \tag{14}$$

The longitudinal profile of the gas exhibits the usual inverted parabola profile. In this regime the sound speed takes the form

$$c_s = \frac{\hbar}{ma_\perp}(2a_s n_1)^{1/2}. \tag{15}$$

1.D BEC in the crossover regime: the Gaussian Ansatz

In our experiment, the typical value of χ is not far from 1, so that we are neither in the TF regime nor in the 1D mean field one. Following Gerbier (2004), we use a Gaussian Ansatz[1] for the radial dependence of the order parameter, characterized by a width σ, that depends on the density n_1. This Ansatz can be justified by the fact that, when there are no interactions $a_s = 0$, the lowest energy level of the gas is just the ground state of the harmonic oscillator, which is Gaussian. In fact when $a_s n_1$ is very large, the transverse TF profile is also well approximated by this approach. With this Ansatz, the atomic density is given by

$$|\Psi_0|^2 = \frac{n_1(z)}{\pi\sigma^2}e^{-r^2/\sigma^2} \tag{16}$$

where $n_1 = \int dr|\Psi_0|^2$ is the 1D density and σ is the width of the trial function that might depend on the location z through the $1D$ density. Within the local density approximation, the spatial derivative of the wave-function along the shallow axis is neglected with respect to the radial derivative. Inserting this Ansatz in the Gross-Pitaevskii equation and integrating over the transverse size leads to

$$\mu = \frac{1}{2}m\omega_\perp^2\sigma^2 + \frac{1+4n_1a_s}{2m\sigma^2}. \tag{17}$$

where μ is the *local equilibrium chemical potential*, which is simply the chemical potential minus the potential dependence along the longitudinal direction e.g. $\mu = \mu_0 - m\omega_z^2 z^2/2$ in the case of a harmonic trapping. In equation (17), we have therefore three unknown quantities that are the density n_1, the width σ and the chemical potential. To express the width as a function of n_1, we simply argue that this width is such that, at n_1 fixed, the local equilibrium potential is minimized. In other words, we find the width σ such that $\partial_\sigma\mu = 0$, at fixed n_1. This leads to

$$\sigma[n_1] = a_\perp(1+4n_1a_s)^{1/4} \tag{18}$$

Here again, we recover the fact that when interactions are turned off, the ground state is simply given by the Gaussian wave-function of the harmonic oscillator. While increasing the interaction strength, the wave-function expands. Inserting the width functional from equation (18) in equation (17), the chemical potential reads

$$\mu[n_1] = \hbar\omega_\perp(1+4a_sn_1)^{1/2}. \tag{19}$$

Here, it must be stressed out that this dependence of the chemical potential with the local equilibrium potential is not specific to the Gaussian Ansatz for the radial profile. This equation

[1] Note other authors proposed different Ansatz to describe a BEC in this cross-over regime. For example, Muñoz Mateo and Delgado (2006) uses a modified radial Thomas-Fermi profile Ansatz. Note also that this Gaussian Ansatz was already studied by Jackson et al. (1998) and Salasnich et al. (2002).

of state was shown to be accurate by Fuchs et al. (2003). The local equilibrium chemical potential is just the chemical potential minus the the trapping potential: one recovers that for a constant trap potential, n_1 no longer depends on z. The chemical potential is then fixed by the total number of atoms that is

$$\begin{aligned} \hbar\omega_\perp(1+4a_s n_1)^{1/2} =& \mu_0 - m\omega_z^2 z^2/2\,, \\ \int n_1 dz =& N. \end{aligned} \tag{20}$$

From this equation, we can deduce the Thomas-Fermi radius $Z_c = L/2$. Its value is no longer given by the point where the right hand-side of equation (20) vanishes but when it takes the value $\hbar\omega_\perp$, that is when $n_1 = 0$. It is therefore given by

$$Z_c^2 = 2\frac{\mu_0 - \hbar\omega}{m\omega_z^2} = \frac{a_z^4}{a_\perp^2}\alpha \quad , \quad \alpha \equiv 2\left(\frac{\mu_0}{\hbar\omega_\perp} - 1\right) \tag{21}$$

where we introduced the dimensionless parameter α as Gerbier (2004). Deep in the Thomas-Fermi regime, this parameter is large but it approaches 0 when going into the 1D mean field regime. Using the α parameter and the TF radius, the density is given by

$$n_1(z) = \frac{\alpha}{16a_s}\left(1 - \frac{z^2}{Z_c^2}\right)\left[\alpha\left(1 - \frac{z^2}{Z_c^2}\right) + 4\right]. \tag{22}$$

and the normalization condition leads to

$$\left(\frac{15Na_s a_\perp}{a_z^2}\right)^2 = (15\chi)^2 = \alpha^3(5+\alpha)^2 \tag{23}$$

where we recover the parameter χ introduced in equation (5). This equation links the chemical potential μ_0, through the quantity α, to the atom number and the trap frequencies. When α is large, the number of atoms is proportional to the chemical potential to the power 5/2, that is what we found in the Thomas-Fermi regime, in equation (11). When α is small, the chemical potential grows linearly with the atom number to the power 2/3, as in the one-dimensional mean field regime. In Figure 11, we extracted a figure from Gerbier (2004) and the appendix of Robertson et al. (2017b) that illustrates that the Gaussian Ansatz well describes the system in the crossover 1D-3D.

The sound speed for the longitudinal excitation is given by $mc^2 = n_1\partial_{n_1}\mu$ hence we have

$$mc_s^2 = a_s n_1 \frac{2\hbar\omega_\perp}{\sqrt{1+4a_s n_1}} = \frac{g}{2\pi\sigma^2}n_1 \equiv g_1 n_1 \tag{24}$$

where we introduced g_1 called the effective one-dimensional coupling constant. Note that in both regimes $a_s n_1 \ll 1$ and $a_s n_1 \gg 1$, we recover the 1D mean field dependence $c \sim \sqrt{2a_s n_1}$ and the 3D Thomas-Fermi relation for which $c \sim (a_s n_1)^{1/4}$. We will also use the healing length ξ, that is

$$\xi = \frac{\hbar}{mc_s} = \sqrt{\frac{\sigma^2}{2a_s n_1}} = a_\perp \frac{(1+4a_s n_1)^{1/4}}{\sqrt{2a_s n_1}} \tag{25}$$

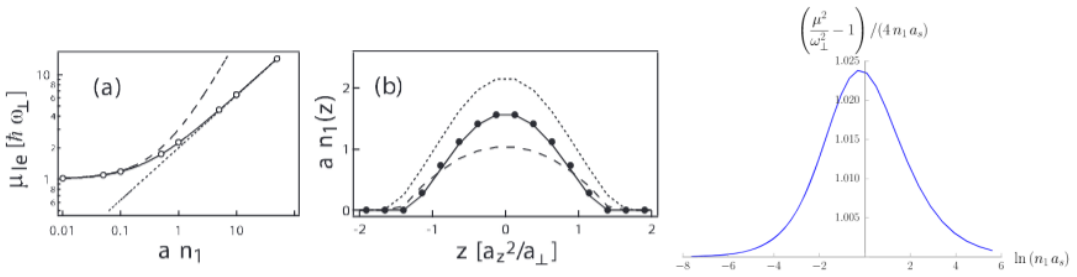

Figure 11: Accuracy of the description of the crossover regime by the Gaussian Ansatz. (a) Local chemical potential as a function of the local density n_1. The circles are numerical calculations from Menotti and Stringari (2002) that should be compared with equation (19). The dotted and dashed lines represent the 3D radial TF and 1D mean field regime limiting case. (b) One dimensional density as a function of z for $\chi = 1$. The circles were obtained from a numerical solution of the Gross-Pitaevskii equation are indistinguishable from the Gaussian Ansatz result (solid line). The dotted and dashed lines give the 3D TF and 1D mean-field profiles, extrapolated to $\chi = 1$ for comparison. Right: difference of the chemical potential computed numerically solving the 3D GPE and the result of equation (19). The quantity that is plotted is exactly 1 in the Gaussian Ansatz, the deviation from this value are deviation of the Gaussian Ansatz to the numerical prediction. It is quite small for all values of $n_1 a_s$, the difference being smaller by a few percents. As expected, on the left, where $a_s n_1 \to 0$, the Gaussian Ansatz is expected to be quite accurate. One can see that the Ansatz is still good even for large values of $n_1 a_s$. The maximum deviation is 0.025 which highlights the fact that the Gaussian approximation is quite accurate. ©Left figure is extracted from Gerbier (2004) and right figure from Robertson et al. (2017b).

1.E The crossover regime: beyond the Gaussian Ansatz

Actually, assuming a Gaussian for the transverse profile is not necessary. Indeed, Robertson et al. (2018) showed that the Gaussian transverse density profile of the cloud is quite different from Gross-Pitaevskii numerics. The idea of their study is to only assume that the radial wavefunction is a certain function of $a_s n_1$. The authors then use thermodynamic relations to constrain this function. For example, the authors assume the thermodynamic relation $\mu[a_s n_1] = \hbar\omega_\perp\sqrt{1+4a_s n_1}$ which was shown to be accurate by Fuchs et al. (2003). I will not repeat the calculation here but go straight to the result, which gives the expression for the sound speed velocity (Micheli, 2024).

$$mc^2 = 2\hbar\omega_\perp a_s n_1 G\left(a_s n_1\right) . \tag{26}$$

where

$$G\left(a_s n_1\right) = \frac{6a_s n_1\sqrt{1+4a_s n_1} - \left(1+4a_s n_1\right)^{3/2} - 1}{6\left(a_s n_1\right)^2} \xrightarrow[a_s n_1 \to 0]{} \frac{1}{\sqrt{1+4a_s n_1}} \tag{27}$$

This generalized result converges to the Gaussian Ansatz in the limit where $a_s n_1$ goes to 0. From the measure of the speed of sound, one can therefore deduce within the Gaussian Ansatz

$$a_s n_1 = \frac{1}{2}\left(\frac{mc^2}{\hbar\omega_\perp}\right)^2\left[1+\sqrt{1+\left(\frac{\hbar\omega_\perp}{mc^2}\right)^2}\right] \tag{28}$$

or the generalized result

$$a_s n_1 = \frac{1}{8}\left\{3 + 9\left(\frac{mc^2}{2\hbar\omega_\perp}\right)^2 + \sqrt{3}\left[-1 + 3\left(\frac{mc^2}{2\hbar\omega_\perp}\right)\right]\sqrt{3 + 2\frac{mc^2}{2\hbar\omega_\perp} + 3\left(\frac{mc^2}{2\hbar\omega_\perp}\right)^2}\right\} \tag{29}$$

Summary In this section, we reviewed the different regime that describe a highly elongated quantum gas. The dimensionless parameter $a_s n_1$, where a_s is the scattering length and n_1 is the 1D density drives the transition between the 1D mean field (frozen transverse dynamics) and the 3D cigar shaped regime. In particular, we showed that assuming the transverse wave-function profile to be Gaussian, we are able to describe the system in the *in between* regime. In the following of this work, we will describe the transverse profile using this Ansatz.

2. Transverse collective oscillation of the BEC

In the last section, we described the ground state properties of the system. We now aim to describe its response to a time-dependent trap. We start in subsection 2.A by briefly recalling central works on collective excitations that followed the first BEC experiments. We end this historical journey with the experiment by Chevy et al. (2002) that observed the un-damped breathing mode. This specific collective mode is the topic of the next section. Within the Gaussian Ansatz, we express the time dependence of the BEC width in subsection 2.B and show that the BEC width dynamics exhibits a resonance at $2\omega_\perp$ *i.e.* twice the frequency of the trap. Subsection 2.C proposes a protocol to force the BEC oscillation at any frequency avoiding the resonance.

2.A Collective excitations in BECs: brief historical perspectives

Collective excitations play a central role in understanding the physical properties of matter. Their applications range from the physics of tsunamis (Kanamori, 1972) to the *theory of superfluidity* (Bogoliubov, 1947) and superconductivity (Bardeen et al., 1957). After the observation of the first Bose-Einstein condensates (Anderson et al., 1995; Davis et al., 1995), the study of collective excitations in Bose gases in harmonic potentials sparked significant interest, both theoretically and experimentally (Jin et al., 1997; Stamper-Kurn et al., 1998). In the last section, we described the ground state of our BEC; we will now examine its collective oscillations. We will continue to assume the temperature is very low, and the gas is weakly interacting. By doing so, we neglect the interaction of our BEC with both the thermal component and quantum depletion (Stringari, 1996). With this approach, the collective excitations of the Bose gas are well described by the time-dependent Gross-Pitaevskii equation.

$$i\hbar\partial_t\Psi_0 = -\frac{\hbar^2}{2m}\nabla^2\Psi_0 + U(\mathrm{r}, z)\Psi_0 + g|\Psi_0|^2\Psi_0. \tag{30}$$

For our purpose of a highly anisotropic trap, the excitation spectrum of a 3D cigar Bose gas was studied, for example, by Stringari (1998) and Fliesser et al. (1997), and the excitations in the crossover between different 1D regimes are discussed by Menotti and Stringari (2002). While we neglected the interaction with the non-condensed gas in equation (30), we can describe the influence of temperature by adding damping to these collective excitations. Damping of a collective excitation ν occurs *via* two channels, called the Landau and Beliaev channels.

- Landau damping refers to the combination of this excitation with another excitation into a third one *i.e.* a thermal excitation ν_{th} with the collective excitation: $\nu_{th} + \nu \rightarrow \nu'$. This damping therefore vanishes at zero temperature. For homogeneous systems, a seminal result was obtained by Hohenberg and Martin (1965), who showed a T^4 scaling. This result was revisited and derived for BECs by Pitaevskii and Stringari (1997) and Vincent Liu (1997). However, it was noted by Fedichev et al. (1998) that the value of the damping rate "drastically depends on the trapping geometry".
- Beliaev damping refers to the decay of a single excitation into two lower-energy excitations *i.e.* $\nu \rightarrow \nu_1 + \nu_2$. This damping occurs at zero temperature, as it was originally derived in this context by Beliaev (1958) before being extended to non-zero temperatures by Popov (1972).

Chevy et al. (2002) reported the observation of an undamped collective oscillation: the breathing mode (monopole mode) of an elongated BEC. In this mode, the transverse radius of the BEC oscillates at $2\omega_\perp$, *i.e.*, twice the transverse trap frequency. The authors showed that the damping of this breathing mode is very low compared to others already reported. They also showed that it is independent of the temperature. This "anomalously small measured damping rate" was numerically and theoretically studied by Jackson and Zaremba (2002). They demonstrated that this was due to an "accidental suppression of Landau damping" for this specific mode (transverse breathing) and geometry (elongated). In the usual derivation of a decay rate, the non-condensed cloud is assumed to be in thermal equilibrium. Here, both the BEC and the thermal cloud oscillate at $2\omega_\perp$ (Castin and Dum, 1996; Kagan et al., 1996), resulting in the suppression of Landau damping. The origin of this damping was already suggested by Pitaevskii and Stringari (1998). In their work, they emphasized that this breathing mode "could produce a parametric instability [...] due to decay into two or more axial excitations," which was further investigated by Kagan and Maksimov (2001). Twenty-five years later, it is the subject of this work.

In order to study entanglement of the longitudinal $(k, -k)$ modes, we will treat the breathing collective oscillation of the BEC classically, while keeping the collective excitations of the gas along the long axis quantized. We will assume the BEC is homogeneous along the z-axis and factor out the transverse profile of the gas

$$\hat{\Psi} = \Psi_0(r,t)[1 + \hat{\phi}(z,t)]. \tag{31}$$

In the following section, we will study the evolution of $\Psi_0(r,t)$ when the trap is modulated. Our approach is a special case of the description of BECs in time-dependent traps by Castin and Dum (1996) and Kagan et al. (1996).

2.B When the laser quenches, it's time to breathe

We therefore factor out the radial dependence of the BEC wave-function (31) and describe the atomic wave-function within the Gaussian Ansatz seen in section 1.D. This choice is justified by the fact that our BEC is neither in the 1D Thomas-Fermi regime nor in the 1D mean field regime. We therefore write the transverse profile as

$$\Psi_0(t,r) = \sqrt{\frac{n_1}{\pi\sigma_0^2}} e^{-r^2/2\sigma_0^2} e^{-i\mu_0 t/\hbar}. \tag{32}$$

The subscript 0 underlines the fact that they are defined at $t = 0$, time at which the trap frequencies are constant and the cloud at equilibrium. Kagan et al. (1996) showed that when

one knows the initial stationary solution, it is possible to build the time-dependent solution from that initial solution (Micheli, 2023)

$$\Psi_0(t,r) = \sqrt{\frac{n_1}{\pi\sigma^2}} e^{-r^2/2\sigma^2} \exp i \left[\frac{mr^2}{2\hbar}\frac{\dot{\sigma}}{\sigma} - \frac{\mu_0}{\hbar}\int^t \frac{\sigma_0^2}{\sigma^2(\tau)} d\tau \right] \tag{33}$$

where the width σ is time-dependent and satisfies the so-called Ermakov-Pinney equation (Leach and Andriopoulos, 2008)

$$\ddot{\sigma} + \omega_\perp^2(t)\sigma = \frac{\sigma_0^4 \omega_{\perp,0}^2}{\sigma^3}. \tag{34}$$

In the following of this section we aim to describe how the width of the BEC responds to a time-dependent trap.

Remark

This non-trivial result was reviewed under an other angle by Robertson et al. (2017b). In the last section 1.D, we derived the (local equilibrium) width σ of the BEC by minimizing the local equilibrium chemical potential. We can therefore see the chemical potential from equation (17) as an effective potential for the width σ

$$V_{eff}(\sigma) = \frac{1}{2}m\omega_\perp^2\sigma^2 + \frac{1+4n_1a_s}{2m\sigma^2}. \tag{35}$$

The dynamics of the width σ in this potential is then simply given by the equation of motion of a classical particle with mass m and position σ

$$m\ddot{\sigma} = -\partial_\sigma V_{eff}(\sigma) = -m\omega_\perp^2\sigma + \frac{1+4n_1a_s}{m\sigma^2} \tag{36}$$

which leads to equation (34) by replacing $1+4n_1a_s$ by the initial width and initial trapping frequency from equation (18).

Knowing the time-dependence of the trap frequency $\omega_\perp$, we can integrate equation (34) over time to access the time-evolution of the BEC transverse density. An example of the response of the BEC width is given in Figure 12. After a quench, the BEC enters a breathing mode and oscillates at twice the frequency of the trap. This was the protocol used in the experiment by Chevy et al. (2002). This oscillation is represented in the upper panel of Figure 12 in which trap frequency was abruptly changed by a factor of $\sqrt{2}$ (left subplot (a)). The BEC width is observed to oscillate at a frequency which is $2^{\pm 1/2} \times 2\omega_{\perp,0}$. On the plot of Figure 12, we see that the frequencies of the two quenches differ by a factor 2. On the lower panel, the trap frequency was modulated periodically at a frequency $2\omega_{\perp,0}$ with a small amplitude A of a few percent for a few periods in order to inject energy in the system. The excitation form is $\omega_\perp^2 = \omega_{\perp,0}^2[1 + A\sin(2\omega_{\perp,0}t)]$ with A = 4-8% during 6 periods. As we excite a system at its resonant frequency, the amplitude of the BEC oscillation grows with the excitation duration. Figure 13 represents the peak-peak amplitude of the width oscillation as a function of the amplitude of the modulation and its duration. It shows that the amplitude of the modulation increases linearly with those parameters.

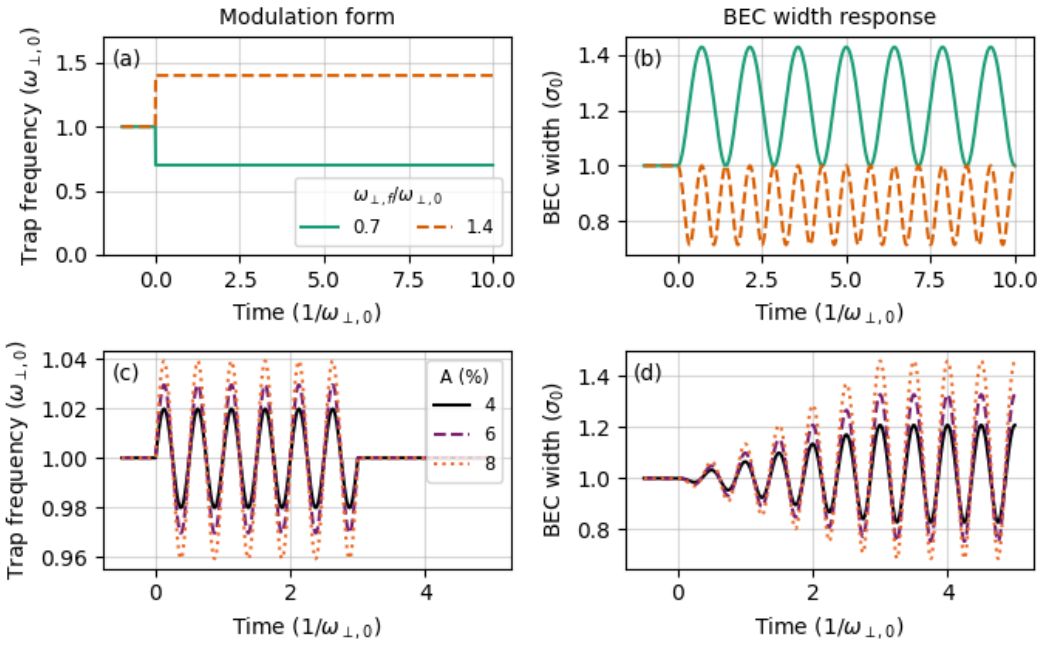

Figure 12: Response of the BEC ground state to different modulation. Time is in units of twice the initial trap frequency $1/2\omega_{\perp,0}$. Upper panels: response of the BEC to a quench. (a) The frequency of the trap is divided (multiplied) by a factor $\sqrt{2}$ on the green solid (orange dash) curve. (b) Response of the BEC width for the two quenches. The BEC width oscillates at twice the final frequency: the orange dashed curve ($\omega_{\perp,f} = \sqrt{2}\omega_{\perp,0}$) frequency is twice the frequency of the solid green line ($\omega_{\perp,f} = \omega_{\perp,0}/\sqrt{2}$). Lower panels: response of the BEC width to a resonant excitation, (c) The trap frequency is modulated with an amplitude A at a frequency $2\omega_{\perp,0}$ that corresponds to the breathing frequency for 6 periods : $\omega_\perp^2 = \omega_{\perp,0}^2[1 + A\sin(2\omega_{\perp,0}t)]$. (d) The BEC width response to the excitation increases exponentially with times. For a modulation of 4%, the BEC width oscillates with an amplitude that is comparable with the quenches of the upper panel.

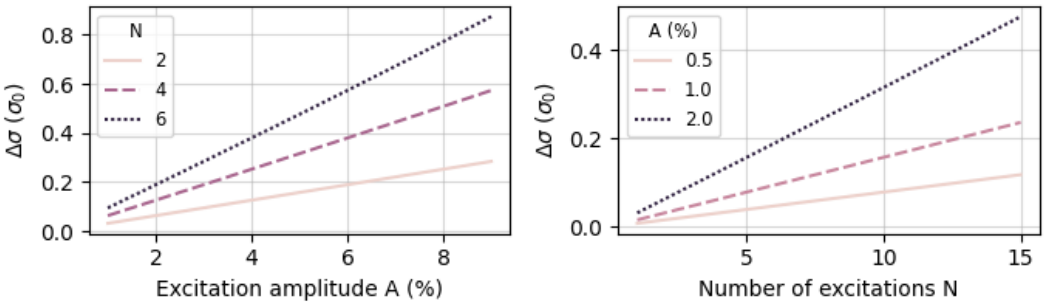

Figure 13: Peak-peak amplitude $\Delta\sigma$ in units of the initial with σ_0 of the final oscillation of he BEC width after a trap modulation $\omega_\perp^2 = \omega_{\perp,0}^2[1 + A\sin(2\omega_{\perp,0}t)]$ for a duration $N = \Delta t\omega_{\perp,0}/\pi$. On the left, $\Delta\sigma$ is plotted as a function of the modulation amplitude A and on the right as a function of the modulation duration. We observe that $\Delta\sigma$ increases linearly with both parameters.

2.C Forcing oscillations of the BEC width: Let gentleness my strong enforcement be

We can also explore the time-dependent response of the BEC width to an excitation at a non-resonant frequency, ω_d. To achieve this, we continuously modulate the transverse trap at frequency ω_d rather than halting after a certain number of oscillations. We would like to find a way to force the BEC to oscillate at the driving frequency ω_d.
Protocol: A first way to excite the system is to modulate the trap frequency at $t = 0$ at the frequency ω_d, *i.e.* with the function

$$\omega_\perp^2 = \omega_{\perp,0}^2[1 + A\sin(\omega_d t)H(t)] \tag{37}$$

where $H(t)$ denotes the Heaviside step function, defined as zero for $t < 0$ and one for $t > 0$. A second possibility is to rise slowly the modulation frequency, for example with a hyperbolic tangent function as

$$\omega_\perp^2(t) = \omega_{\perp,0}^2[1 + A\sin(\omega_d t)(1 + \tanh[t/\tau])/2]. \tag{38}$$

Results: The time dependent form of those two excitation functions are represented on the first row of Figure 14. The first column represents the "brutal" modulation in equation (37), the second one the "sweet" excitation in equation (38), for which the modulation is raised adiabatically (with respect to $2\omega_{\perp,0}$). The modulation frequency chosen here is $\omega_d = 3\omega_{\perp,0}$. The second row depicts the time evolution of the width of the BEC $\sigma(t)$. In the case of a brutal modulation (left), the BEC width response does not look like a sine function and exhibits two harmonics. In the case of a sweet modulation, the width response seems much nicer (right). To confirm this intuition, one can look at the third row that represents the Fourier transform $\tilde{\sigma}$ of the BEC width $\sigma(t)$. The Fourier transform is computed between $6\omega_{\perp,0}$ and $20\omega_{\perp,0}$ so that the response is in the steady state regime. On the Fourier spectrum, the green and red vertical lines with transparent shading represents respectively the driving frequency ω_d and the natural frequency $2\omega_{\perp,0}$. The brutal modulation response presents two peaks: one at the resonant frequency $2\omega_{\perp,0}$ and the second one at the driving frequency ω_d. In the case of the "sweet" modulation, we observe only one peak, located at the driving frequency ω_d.

Conclusion We conclude that, at the excitation frequency $3\omega_{\perp,0}$, the response of the BEC follows well the "sweet" modulation function (38). This allows us to control the oscillation frequency of the BEC i.e. we control the collective excitation. That said, this was checked for a particular excitation frequency. This study could be scaled up to examine other excitation frequencies.

Protocol: To better check the robustness of the sweet modulation approach, we numerically solve the time evolution of the width of the BEC, $\sigma(t)$. We solve it for various frequencies ω_d, both for the brutal modulation (37) and the gentle modulation (38). Once $\sigma(t)$ is known, we compute its Fourier transform, $\tilde{\sigma}$ in the steady state regime.
Results: The spectrum depicted in Figure 15 illustrates the Fourier components $\tilde{\sigma}(\omega)$ of the BEC width response. The color scale denotes the magnitude $|\tilde{\sigma}(\omega)|$ of the Fourier components, shown along the y-axis. The x-axis represents the driving frequency ω_d. Frequencies are given in units of the initial trapping frequency $\omega_{\perp,0}$. The Fourier amplitude is normalized so that the maximal Fourier component is 1: each column of the map is normalized. This allows us to see for each driving frequency ω_d what the main frequencies (bluer) are in the

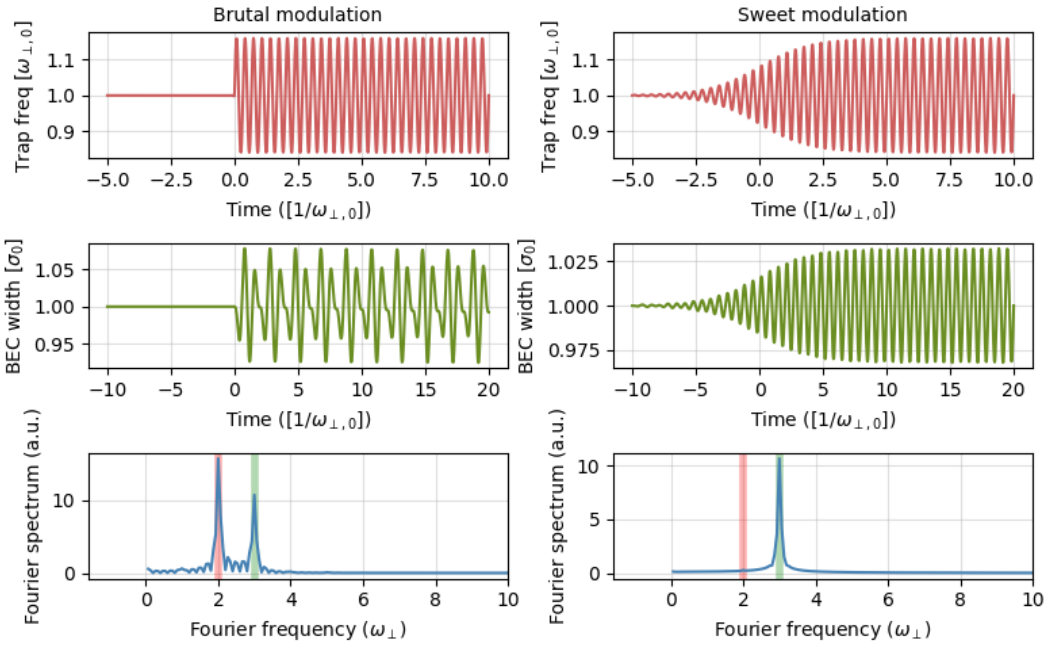

Figure 14: Response of the BEC width to two different excitation profiles with a driving frequency of $3\omega_{\perp,0}$. The left column matches the *brutal* excitation (37) and the right column the *sweet excitation* (38). The first row represents the trap frequency profile, which is experimentally realized by changing the laser power of the trap. On the left, the excitation starts at $t = 0$ brutally while the excitation is adiabatically tuned ($\tau = 2/\omega_{\perp,0}$) on the right column. The second row represents the time dependent response of the BEC width. The left subplot exhibits a non-sinusoidal behavior while the right one seems *proper*. The last row depicts the Fourier transform of the width response in steady state regime (*i.e.* for $t\omega_{\perp,0} > 6$). The red are highlights the breathing mode frequency and the green area the driving frequency. The brutal modulation exhibits two peaks: one at the resonance frequency and one at the driving frequency while the sweet modulation has only one frequency. For this figure, the amplitude of the modulation is A = 8%.

BEC width response. If the BEC oscillates exactly at the driving frequency ω_d, one would observe a stronger signal on the diagonal, as the Fourier transform of the BEC width would exhibit a peak only at $\omega = \omega_d$.

The right panel of Figure 15 is easier to interpret: we observe a strong signal on the diagonal, which means that the main frequency of the system is the driving frequency. The only exceptions are at $1\omega_{\perp,0}$ and $2\omega_{\perp,0}$.

The left panel is a bit more chaotic. For low driving frequencies ω, that is, on the left of the graph, the system follows the driving frequency: the Fourier transform $\tilde{\sigma}$ is well-peaked on the diagonal. When the driving frequency is greater than $\omega_{\perp,0}$, the main component of $\tilde{\sigma}$ is no longer the driving frequency but the resonant frequency $2\omega_{\perp,0}$. The system is oscillating at its natural frequency. We can interpret this as the oscillation at $2\omega_{\perp,0}$ being due to the energy injected at $t = 0$, when the frequency of modulation is not yet defined. When the modulation is applied smoothly, the system is better controlled and keeps oscillating at the driving frequency[2]. The conclusion of this subsection leaves no doubt: the softer, the better.

[2]Before attempting this adiabatically raised modulation, I initially attempted a more sophisticated approach. I

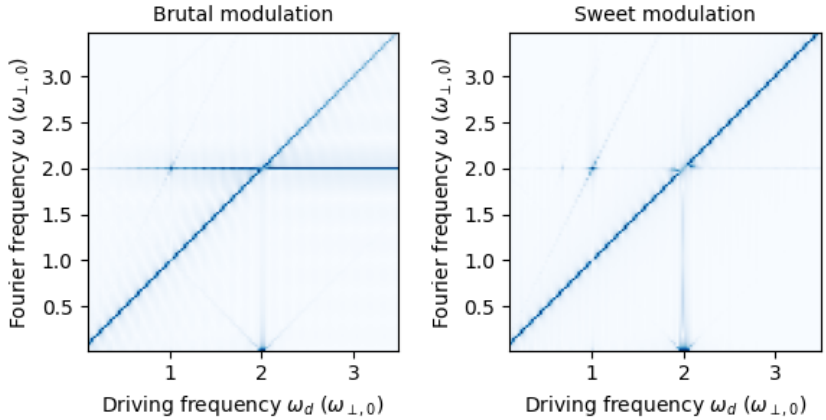

Figure 15: Spectrum of the BEC width $\tilde{\sigma}(\omega)$ response to a modulation at frequency ω_d, on the x-axis. The vertical axis represents the Fourier frequency of the function $\tilde{\sigma}(\omega)$ whose amplitude is proportional to the colorscale. A bluer color represents a higher amplitude of the Fourier component. When the transverse trap is modulated with a *brutal modulation* given by equation (37), the system does not follow perfectly the driving frequency but tends to oscillate at its own natural frequency $2\omega_{\perp,0}$. This is shown by the strong horizontal blue line. When the modulation is gently switched on (right plot), with the excitation given by equation (38), the unwanted oscillation at $2\omega_{\perp,0}$ is suppressed. For this image, $A = 5\%$ and $\tau = 2/\omega_{\perp,0}$. The duration of the modulation is $80/2\omega_{\perp,0}$ and the Fourier transform is computed at late time *i.e.* for $t > 60/2\omega_{\perp,0}$

This is why we titled it with Orlando's line "*Let gentleness my strong enforcement be.*", *As you Like It*, Shakespeare.

Summary This section showed, using the Gaussian Ansatz, that a quench or a small variation of the transverse trap frequency causes the BEC to oscillate at twice the frequency of the trap: that is, the breathing mode. We then proposed a protocol to force the BEC to oscillate at any frequency.

aimed to engineer a modulation $\omega^2_{\perp,0}$ so that its response $\sigma(t)$ would oscillate at frequency ω_d. Let f be a function representing this targeted width, behaving like a constant plus a small modulation at frequency ω_d, for instance. By utilizing equation (34), one can designed the modulation function $\omega^2_\perp \propto 1/f^4 - \ddot{f}/f$ so that the solution σ of (34) would converge to f. However, the results from this method proved no better than those depicted in Figure 15 when the modulation was turned on adiabatically, and it performed even worse results near the resonance. The simpler being the better, I preferred to stick with the smooth approach.

3. Parametric creation of quasi-particles in a BEC

In the last section, we studied the time dependence of the ground state of the BEC when it is time-modulated. In particular, we showed that, in our regime, we can model the transverse profile of the BEC by a Gaussian function of width σ. We found that using the right modulation profile of the trap frequency, we are able to induce oscillations at frequency ω_d of the transverse width. In first approximation, it means that the 1D coupling oscillates at ω_d. As we shall see, such modulation excites well-defined opposite momentum modes.

3.A Bogoliubov-de Gennes equation

Following Robertson et al. (2017b), we decompose the field as

$$\hat{\Psi} = \Psi_0(r,t)\left(1+\hat{\phi}(z,t)\right) \tag{39}$$

where $|\hat{\phi}|^2$ is small compared to 1. Here we treat the BEC as a c-number and not a quantum operator: this is one of Bogoliubov's approximations (Bogoliubov, 1947). We now insert the field (39) in the many-body Hamiltonian (1). After integrating over the radial profile, we can write the effective one-dimensional Hamiltonian for $\hat{\phi}$ (Micheli, 2023)

$$\hat{\mathcal{H}}'_{1D} = \int_0^L dz \left[\frac{\hbar^2}{2m}\nabla\hat{\phi}^\dagger\cdot\nabla\hat{\phi} + g_1 n_1\hat{\phi}^\dagger\hat{\phi} + \frac{g_1 n_1}{2}\left(\hat{\phi}^2+\hat{\phi}^{\dagger 2}+\hat{\phi}^{\dagger 2}\hat{\phi}+\hat{\phi}^\dagger\hat{\phi}^2+\hat{\phi}^{\dagger 2}\hat{\phi}^2\right)\right] \tag{40}$$

where $g_1 = g/2\pi\sigma^2$ is the effective one-dimensional coupling constant that could (and will) depend on time. In this equation, we removed the BEC mean field contribution, this is why we added a prime to the Hamiltonian (see the second chapter of Dalibard (2022)). Following Robertson et al. (2017b), we assume periodic boundary conditions and assume the condensate is homogeneous along z. This means that k is a good quantum number. We decompose the field $\hat{\phi}$ in Fourier modes:

$$\hat{\phi} = \frac{1}{\sqrt{N}}\sum_{k\in 2\pi\mathbb{Z}^*/L}\hat{\phi}_k e^{ikz} \tag{41}$$

where the $\hat{\phi}_k$ is the annihilation operator for an atom with momentum k. These operators satisfy the canonical commutation relations $[\hat{\phi}_k,\hat{\phi}^\dagger_{k'}] = \delta_{k,k'}$ and $[\hat{\phi}_k,\hat{\phi}_{k'}] = 0$. The $k=0$ mode is removed as it corresponds to the BEC mode.

The (second) Bogoliubov approximation (Bogoliubov, 1947) consists in neglecting the interaction terms involving more than two atoms from the non-condensed part. In equation (40), we only keep terms that are second order or less in $\hat{\phi}$: the Hamiltonian is of second order. In particular, this means that the equations of motion are linear. Such approximation requires the interaction strength not to be large and the number of non-condensed atoms to be negligible, with respect to the number of condensed particles. Indeed, the BEC is treated as an infinite reservoir of particles *i.e.* a true coherent state. From this second order Hamiltonian, we derive the equation of motion for the field $\hat{\phi}_k$ and $\hat{\phi}^\dagger_k$, called the Bogoliubov-de Gennes equation

$$i\hbar\partial_t\begin{pmatrix}\hat{\phi}_k\\ \hat{\phi}^\dagger_{-k}\end{pmatrix} = \begin{pmatrix}\frac{\hbar^2k^2}{2m}+g_1n_1 & g_1n_1\\ -g_1n_1 & -\frac{\hbar^2k^2}{2m}-g_1n_1\end{pmatrix}\begin{pmatrix}\hat{\phi}_k\\ \hat{\phi}^\dagger_{-k}\end{pmatrix}. \tag{42}$$

3.B Bogoliubov transformation

The Bogoliubov-de Gennes equation that we derived is not straightforward to solve as it mixes two different modes $\hat{\phi}_k$ and $\hat{\phi}^\dagger_{-k}$. The general idea of Bogoliubov transformation is to find a basis $(\hat{b}_k, \hat{b}^\dagger_k, \hat{b}_{-k}, \hat{b}^\dagger_{-k})$ such that the Hamiltonian can be written as a sum of $\hat{b}^\dagger_q \hat{b}_q$ terms[3]. The Bogoliubov transformation maps the atom operator $\hat{\phi}_k$ to the collective excitation operator $\hat{b}_k$, also called quasi-particle operator. This transformation is given by

$$\begin{pmatrix} \hat{\phi}_k \\ \hat{\phi}^\dagger_{-k} \end{pmatrix} := \begin{pmatrix} u_k & v_k \\ v_k & u_k \end{pmatrix} \begin{pmatrix} \hat{b}_k \\ \hat{b}^\dagger_{-k} \end{pmatrix}. \tag{43}$$

This transformation must preserve the bosonic commutation rules: $[\hat{b}_k, \hat{b}_{k'}] = \delta_{k,k'}$. It is called a symplectic transformation that satisfies $|u_k|^2 - |v_k|^2 = 1$. The u_k and v_k coefficients are given by

$$u_k,\, v_k = \pm\sqrt{\frac{\hbar^2 k^2/2m + g_1 n_1}{2\hbar\omega_k} \pm \frac{1}{2}} \tag{44}$$

where

$$\hbar\omega_k = \sqrt{2 g_1 n_1 \frac{\hbar^2 k^2}{2m} + \left(\frac{\hbar^2 k^2}{2m}\right)^2} \tag{45}$$

is the energy associated to each quasi-particle mode k. Here, we recall that $g_1 n_1 = m c_s^2$ so that replacing it in Eq. (45), we recover the usual form commonly used in the literature for the dispersion relation. In this quasi-particle basis, the Bogoliubov-de Gennes equation is given by

$$i\partial_t \begin{pmatrix} \hat{b}_k \\ \hat{b}^\dagger_{-k} \end{pmatrix} = \begin{pmatrix} \omega_k & -i\partial_t \omega_k / 2\omega_k \\ -i\partial_t \omega_k / 2\omega_k & -\omega_k \end{pmatrix} \begin{pmatrix} \hat{b}_k \\ \hat{b}^\dagger_{-k} \end{pmatrix}. \tag{46}$$

Dispersion relation

The energy of a quasi-particle at momentum k is $\hbar\omega_k$, defined in Eq. (45). This dispersion can be probed using Bragg diffraction. It was measured by Steinhauer et al. (2002) and is reproduced in Figure 16.

- At low momentum k, the energy is linear $\omega_k = c_s|k|$, where the sound speed is $c_s = \sqrt{g_1 n_1/m}$. This part of the dispersion relation is called the phonon branch.
- At high momentum, the dispersion relation is quadratic and shifted with an offset $g_1 n_1/m$. This part is called the particle-like branch.

The healing length $\xi = \hbar/mc_s$ represents the boundary between phonon-like and particle-like excitations. In this work, we excite quasi-particles with $k \lesssim \xi^{-1}$, which are not strictly phonons. These have been referred to as such in the literature. Although I have attempted to replace the term with "quasi-particles," I occasionally retain the "phonon" terminology.

[3] This can be found in the fourth chapter of Pitaevskiĭ and Stringari (2016), the second of Dalibard (2022) or Castin (2001) for example.

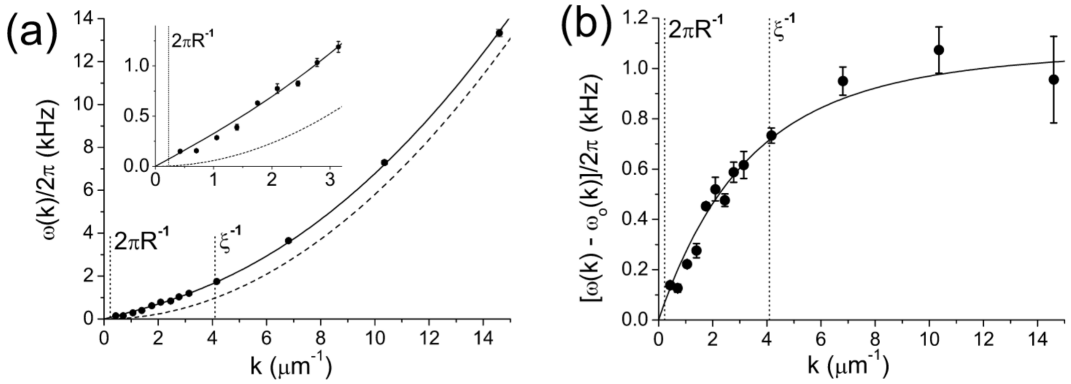

Figure 16: The Bogoliubov dispersion relation measured with Bragg diffraction. Left: dispersion relation of a BEC probed with Bragg diffraction. Solid line is equation (45) in the LDA approximation and the dashed line is the the free-particle spectrum. The inset is a zoom at low k: the dispersion relation is indeed linear. Right: as left but the free particle energy $\hbar^2k^2/2m$ was subtracted. The constant value at high k is a signature of the mean field shift g_1n_1/m. ©Figure from Steinhauer et al. (2002).

What about a non-homogeneous gas ? When the gas is not uniform, the dispersion relation (45) is no longer exact. When the trapping is harmonic, the dispersion relation can be derived within the local density approximation. In the 3D Thomas-Fermi regime, the sound speed c_s depends then on the momentum, ranging from $0.68\sqrt{\mu/m}$ for low k to $0.76\sqrt{\mu/m}$ for large k[4] (Zambelli et al., 2000). The solid line in Figure 16 takes into account this LDA approximation.

A Bogoliubov transformation creates particles from vacuum

We first consider the case where ω_k is time-independent: the time evolution of $\hat{b}_k$ and $\hat{b}^\dagger_{-k}$ are uncorrelated. The quasi-particles behave as a gas of non-interacting bosons and their number distribution follows the Bose-Einstein statistics

$$\langle \hat{b}^\dagger_k \hat{b}_k \rangle = \frac{1}{e^{\hbar\omega_k/k_BT} - 1}. \tag{47}$$

We now turn to the case where the interaction $mc_s^2 = g_1n_1$ is time-dependent: it is characterized by the interaction constant $g_1^{(in)}$ for $t \to -\infty$ and $g_1^{(out)}$ for $t \to +\infty$. This interaction constant defines the speed of sound c_s, which we will use to define the system's basis. For a given mode k, both the Bogoliubov coefficient and the mode energy $\hbar\omega_k$ depend on c_s. This means, in particular, that the ground state of the system changes with c_s. The mapping of the system from the *in* basis to the *out* basis depends on the rate of change of c_s.

Adiabatic change: If the interaction constant changes slowly with respect to the phonon frequency ω_k, that is $\partial_t\omega_k/\omega_k \ll \omega_k$, the system will adiabatically follow the ground state defined by each phonon basis. In particular, if we assume the system is initially at zero temperature in the ground state $|0_{(in)}\rangle$, it means that the system will adiabatically follow the ground state and be mapped to $|0_{(out)}\rangle$.

[4] This result agrees and extends the sound speed value in an anisotropic BEC derived by Zaremba (1998) and that we discussed in section 1.B: the factor $1/\sqrt{2} \sim 0.7$ is somehow a mean of the low k sound speed value and the high k value.

Sudden change: If the interaction constant changes suddenly from the phonon point of view, the ground state of the initial state is projected onto the new phonon basis. This means that at $t = 0^+$, the state of the system is the ground vacuum state of the *in* basis evaluated in the *out* basis.

$$n_k^{(out)} = \langle 0_{(in)}| \hat{b}_k^{\dagger(out)} \hat{b}_k^{(out)} |0_{(in)}\rangle \tag{48}$$

If we introduce (u'_k, v'_k) the Bogoliubov coefficients[5] that map the *in* basis to the *out* basis, we find that

$$n_k^{(out)} = (|u'_k|^2 + |v'_k|^2)\, \langle \hat{b}_k^{\dagger(in)} \hat{b}_k^{(in)} \rangle + |v'_k|^2 \tag{49}$$

where the initial number of quasi-particles $n_k^{(in)} = \langle \hat{b}_k^{\dagger(in)} \hat{b}_k^{(in)} \rangle$ is given by equation (47). However now, even if the initial population vanishes (zero temperature), the mean number of phonons in the out basis is not zero: particles were created out of vacuum. The vacuum of the *in* basis is different from that of the *out* basis hence projecting one onto the other results in particle creation. Experimentally, this can be done by abruptly turning off the interactions. In this case, the initial state of the system, expressed in the phonon basis, is projected onto the atom basis $\hat{\psi}_k$. For this specific transformation, the coefficients (u'_k, v'_k) in Eq. (49) are simply the Bogoliubov coefficients (u_k, v_k) given in Eq. (44). The non-condensed part of the atoms, that is the second part of Eq. (49), is called *quantum depletion*. It is composed of pairs of $(k, -k)$ entangled atoms that were recently observed by Tenart et al. (2021). On the other hand, the first term of Eq. (49) is called the *thermal depletion*.

In the following, we will rapidly change the interaction strength (with respect to ω_k) but keep describing the system in the phonon basis.

3.C Controlling and observing non-separability of phonons in a 1D Bose gas

This section reviews the theoretical advances that have been made the past ten years to control and observe non-separability of phonons in a 1D Bose gas.

Parametric creation of phonons

Experimentally, we do not have a direct control of the interaction strength $g_1 = g/2\pi\sigma^2$ (hence the sound speed $mc_s^2 = g_1 n_1$). We rather control indirectly the width of the BEC σ through the transverse trapping frequency. Although we do not have the ability to change it abruptly, we can (theoretically) force its oscillation at any frequency, see section 2.C. This means in particular that $\omega_k(t)$, defined in Eq. (45), can be computed from the evolution of mc_s^2 through the one of σ. Starting from an initial thermal state at time t_{in}, the evolution of the phonon operator is determined by the Bogoliubov-de Gennes equation (46). The evolution of these operators is given by the following system (Busch et al., 2014)

$$\begin{pmatrix} \hat{b}_k(t) \\ \hat{b}^\dagger_{-k}(t) \end{pmatrix} = \begin{pmatrix} \alpha_k(t) e^{-i\int_{t_{in}}^t \omega_k dt'} & \beta_k^\star(t) e^{-i\int_{t_{in}}^t \omega_k dt'} \\ \beta_k(t) e^{i\int_{t_{in}}^t \omega_k dt'} & \alpha_k^\star(t) e^{i\int_{t_{in}}^t \omega_k dt'} \end{pmatrix} \begin{pmatrix} \hat{b}_k(t_{in}) \\ \hat{b}^\dagger_{-k}(t_{in}) \end{pmatrix} \tag{50}$$

[5] The Bogoliubov coefficients associated to this change of basis are related to the usual Bogoliubov coefficients (44) of the *in* and *out* base $u'_k = u_k^{(in)} u_k^{(out)} - v_k^{(in)} v_k^{(out)}$ and $v'_k = v_k^{(in)} u_k^{(out)} - u_k^{(in)} v_k^{(out)}$.

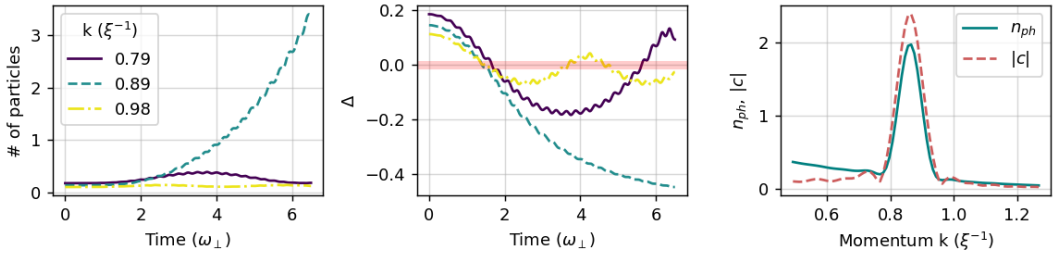

Figure 17: Evolution of the number of phonons (52) (left) and the entanglement witness Δ (54) (middle) according to equation (50) as a function of time. Right: number of phonons $n_{\pm k}$ (52) and correlation $|c_k|$ (53) as a function of the phonon speed. When the dashed red correlation curve lies above the occupation green solid curve, the state is entangled. The parametric excitation consists of 4 oscillations of the trapping frequency with a 3% amplitude at resonance and an additional 9 breathing periods. The initial temperature is $k_B T = 0.7 m c_s^2$ and the driving frequency is the breathing frequency.

where $\alpha_k(t_{in}) = 1$ and $\beta_k(t_{in}) = 0$ and their time evolution is given by

$$\begin{aligned} \dot{\alpha}_k &= \frac{\dot{\omega}_k}{2\omega_k} \beta_k e^{2i\int_{t_{in}}^{t} \omega_k dt'} \\ \dot{\beta}_k &= \frac{\dot{\omega}_k}{2\omega_k} \alpha_k e^{-2i\int_{t_{in}}^{t} \omega_k dt'} . \end{aligned} \tag{51}$$

When mc_s^2 is constant, so are α_k and β_k. The phonon operators $\hat{b}_k$ and $\hat{b}_{-k}^\dagger$ are decoupled and oscillate with opposite frequency $\pm\omega_k$. When mc_s changes, it mixes these two modes with opposite frequency: quasi-particles are produced. We assume the initial state is thermal so that the correlation between the opposite momentum modes vanishes *i.e.* $\langle \hat{b}_k(t_{in}) \hat{b}_{k-}(t_{in}) \rangle = 0$. The number of quasi-particles at k is given by

$$n_k = \langle \hat{b}_k^\dagger \hat{b}_k \rangle = |\beta_k|^2 + n_{th}^{(in)} \left(|\alpha_k|^2 + |\beta_k|^2 \right) \tag{52}$$

where the time dependence of α_k and β_k was omitted to simplify notation. The time variation of the sound speed acts as a two-mode squeezer and here again, particles are produced from vacuum. When the initial state is thermal, it is not only the vacuum fluctuations that seed the final state but also the thermal fluctuations: the final state is a two-mode squeezed thermal state. The correlation between the two modes $(k, -k)$ is given by

$$c_k := \langle \hat{b}_k \hat{b}_{-k} \rangle = \alpha_k \beta_k^\star + 2\alpha_k \beta_k^\star n_{th}^{(in)} . \tag{53}$$

We finally introduce $\Delta := n_k - |c_k|$, whose negativity assesses non-separability of the state[6] (Campo and Parentani, 2005)

$$\Delta = -(|\alpha_k| - |\beta_k|)|\beta_k| + n_{th}^{(in)} (|\alpha_k| - |\beta_k|)^2 . \tag{54}$$

An example of parametric creation of phonons is shown in Figure 17 for a gas with initial temperature $k_B T = 0.7 m c_s^2$. Here, the excitation frequency is twice the trap frequency: at the breathing mode. On the left panel is plotted the number of phonons as a function of time, for

[6] We will go through the details of entanglement and entanglement witnesses in the next section.

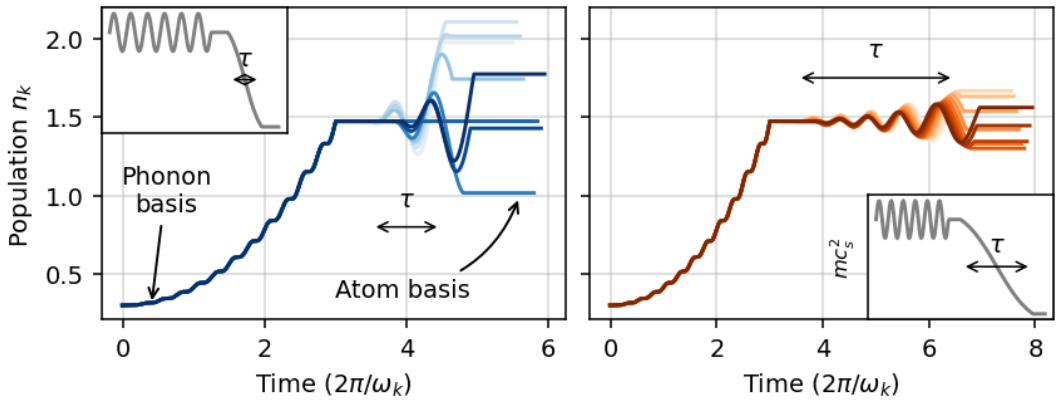

Figure 18: Quasi-particle population with momentum k as a function of time. The interaction strength is modulated at frequency $\omega_d = 2\omega_k$ to produce quasi-particles and then switch off on a duration τ after a delay t'. Different curves refer to different delays t' that range over one period, in the quasi-particle frequency units $\omega_k/2\pi$. On the left panel, $\tau = 2\pi/\omega_k$ and on the right, $\tau = 3 \cdot 2\pi/\omega_k$.

different modes k. We observe an exponential creation of phonons for the mode $k = 0.89\xi^{-1}$ while the two others are not resonant with the amplification process. The middle panel shows the evolution of Δ, whose negativity assesses non-separability of the state. For the resonant mode, the entanglement increases with time *i.e.* with the squeezing parameter. On the right panel is shown the number of $(k, -k)$ phonons $n_{\pm k}$ (52) and their correlation $|c_k|$ (53) after the total duration. We observe that the process is resonant for narrow mode bandwidth around a resonant mode k_{res}, which is determined by the oscillation frequency of the BEC width Ω: it is the mode for which $\omega(k_{res}) = \Omega/2$ where ω is the dispersion relation.

Process efficiency and resonant wave-vector

Busch et al. (2014) show that two dimensionless numbers mainly govern the efficiency of the creation process. Assuming the speed of sound is modulated with an amplitude a at frequency ω_d, the production of phonons with momentum k is governed by the number of oscillations N and the resonance parameter R_k

$$R_k := \frac{4}{a\omega_d}(2\omega_k - \omega_d). \tag{55}$$

The phonon creation process is exponential if $|R| < 1$. In fact, this resonance parameter is simply the first resonance tong at half the driving frequency, without damping term.

Measuring in the phonon basis

Measurements will be experimentally performed after a time-of-flight: atoms are measured rather than collective excitations. As we saw in section 3.B, the phonon vacuum corresponds to pairs of entangled atoms: the "atom" basis is related to the "phonon" basis by a Bogoliubov transformation. In this work, we aim to measure the phonon state which means that the mapping from the phonon basis to the atom basis should be adiabatic.

To better illustrate this phenomenon, we use our theoretical model and modulate the sound speed mc_s^2 as follows:

- For $t \in [0, 6\pi/\omega_k]$, we modulate the sound speed at frequency $\omega_d = 2\omega_k$. This means we excite the quasi-particles during 6 periods. During this stage, we expect to parametrically excite quasi-particles with momentum k.
- For $t \in [6\pi/\omega_k, 6\pi/\omega_k + t']$, we keep the sound speed constant. During this stage, the Bogoliubov modes evolve with their relative phase at $\pm\omega_k$. We will vary t' over one period, in units of the phonon frequency.
- At $t = 6\pi/\omega_k + t'$, we switch off interactions with a tanh profile, on a typical duration τ. When the value of $mc_s^2 = 0$, this means that there are no interactionsphonons anymore and the quasi-particle basis corresponds to the atomic basis. Depending on the value of τ, the mapping from the initial quasi-particle basis onto the atom basis can be adiabatic ($\tau \gg \omega_k^{-1}$) or instantaneous ($\tau \ll \omega_k^{-1}$).

The insets of Figure 18 shows the evolution of mc_s^2. At all times, we follow the number of quasi-particles with momentum k in the eigenbasis of the system defined by mc_s^2. We show in Figure 18 this population as a function of time for two values of τ: short on the left and longer on the right. When there are interactions (left of the plot), the eigenbasis of the system is the Bogoliubov quasi-particle basis. Once interactions are switched off (right of the plot), the natural basis of the system is the atomic basis.

The different curves in each subplot of Figure 18 refer to different values of t' over 1 period (in phonon frequency unit $2\pi/\omega_k$). After the modulation, the number of quasi-particles is 1.5. However depending on the delay t', we observe that the final number of atoms with momentum k varies: the final plateau of each curve is different. We also observe that the difference between the curves of the left subplot are greater than the one of the right subplot.

In fact, the final number of atoms with momentum k oscillates as a function of t' with frequency $2\omega_k$. This oscillation is shown in the inset of Figure 19. To understand the origin of this oscillation, we evaluate the number of particles in the atom basis just after the modulation

$$\begin{aligned} n_k = \langle \hat{\phi}_k^\dagger \hat{\phi}_k \rangle = |u_k|^2 \langle \hat{b}_k^\dagger \hat{b}_k \rangle + |v_k|^2 \langle \hat{b}_{-k}^\dagger \hat{b}_{-k} \rangle + |v_k|^2 \\ u_k v_k^\star \langle \hat{b}_{-k} \hat{b}_k \rangle + v_k u_k^\star \langle \hat{b}_{-k}^\dagger \hat{b}_k^\dagger \rangle \,. \end{aligned} \tag{56}$$

Here u_k and v_k refers to the Bogoliubov coefficients between the atomic basis and the eigen-quasi-particles basis defined in Eq. (44). In equation (56), the first line is the same as Eq. (49). However, in the previous scenario, the second line was zero due to the absence of correlation. Here, we squeezed the two modes during 6 periods hence this term is not zero. The terms $\langle \hat{b}_{-k} \hat{b}_k \rangle$ and $\langle \hat{b}_{-k}^\dagger \hat{b}_k^\dagger \rangle$ interfere constructively and destructively with frequency $2\omega_k$. When the mapping from the quasi-particle basis to the atom basis is adiabatic, the Bogoliubov coefficients of this transformation are $u_k = 1$ and $v_k = 0$. The oscillation is suppressed and one measures the "right" number of quasi-particles. The quality of this mapping depends on τ *i.e.* the adiabaticity of the transformation.

To further study this simple model, we show in Figure 19, the final atomic population as a function of the switch off duration. The solid line shows the mean and the shaded area the amplitude of the oscillation with respect to t'. In the limit $\tau \to \infty$, the mapping from the quasi-particle basis to the atom basis is perfect, and the number of atoms matches the phonon number. To have a good mapping of the quasi-particle basis to the atom basis, the interactions must be switched off on a timescale which is larger than the typical quasi-particle timescale $2\pi/\omega_k$. On the right panel of Figure 19, we show the average and amplitude of the oscillation of Δ, the entanglement criterion.

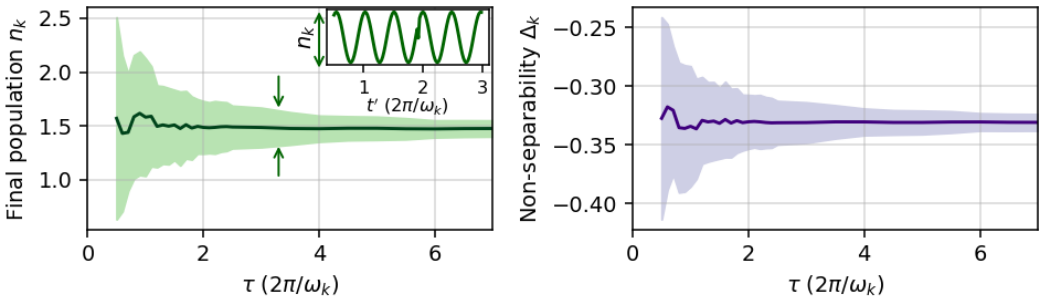

Figure 19: Asymptotic value of the population n_k and the non-separability criterion Δ_k in the atom basis. Solid line is the means of the state and the shaded region shows the amplitude of the oscillations as a function of τ.

The transverse expansion of the cloud: an adiabatic mapping "for free"?

In the experiment, the interactions are not switched off instantaneously. Even though the trap is opened abruptly, the cloud expands as $\sigma_0\sqrt{1+\omega_\perp^2 t^2}$. This means that the density (hence the sound speed) decrease as $1/(1+\omega_\perp^2 t^2)$. In the context of Bragg diffraction, Tozzo and Dalfovo (2004) studied how a collective excitation is mapped to an atom. In their work, they show that a collective excitation is mapped to a "witness" atom for wave-vector k so that $ka_\perp > 0.5$[7]. We see here that the natural transverse expansion of the cloud adiabatically maps the quasi-particle basis *for free* for sufficiently large momentum ($\omega_k > \omega_\perp$).

This problem was further studied by Robertson et al. (2017b), also focusing on the transfer of the non-separability of the state. For quasi-particle at momentum $k \sim \xi^{-1}$, the authors found that abruptly switching off the trap is not adiabatic enough. While they advocate for an adiabatic opening as slow as the experiment will allow, they show that switching off the trap in a time $\tau \sim 1.5\omega_\perp^{-1}$ adequately reduces the effect of this change of basis.

Phonon-phonon interactions: a phenomenological decay rate

The Bogoliubov-de Gennes model that we described does not take into account the damping of the quasi-particles. The influence of a damping was studied by Busch et al. (2014). To model it, the authors use a phenomenological damping rate $\Gamma_k \ll \omega_k$ which decreases n_k and c_k by $\Gamma_k \mathrm{d}t$ during $\mathrm{d}t$. Main conclusions of their model follow.

- A large value of Γ_k can prevent the state to be nonseparable.
- With their model, a non-zero Γ_k cannot explain the disappearance of entanglement once established. In other words, if the gain of the process is sufficiently large and turns the state to a non-separable state, the state cannot become nonseparable because of Γ_k. This is due to the fact that both the correlation c_k and the population n_2 decrease at the same rate Γ_k.
- However, the authors introduce the notion of entanglement *visibility* to explain that a sufficiently large value of Γ_k can prevent the measurement of the non-separability of the state.

A good example to illustrate this notion of visibility is to consider a two-mode squeezed

[7] We have $k\xi = ka_\perp (1+4a_s n_1)^{1/4}/\sqrt{2a_s n_1} \sim ka_\perp$ in our case.

thermal state. The population n and correlation c of such state can be written as

$$n_k = 2n_{th} + (2n_{th} + 1)\sinh^2 r, \qquad c_k = (2n_{th} + 1)\sinh r \cosh r \tag{57}$$

where r is the squeezing parameter and n_{th} the initial thermal population. This state is entangled if and only if the squeezing parameter is sufficiently large *i.e.* if $e^{2r} > 1 + 2n_{th}$. If we measure the normalized second order correlation function of this state, we have

$$g^{(2)}_{k,-k} = 1 + \frac{|c_k|^2}{n_k^2}. \tag{58}$$

If the state is entangled, $g^{(2)} > 2$. However, if both c_k and n_k are too large, one could have that $n_k < |c_k|$ without being able to resolve it. The correlation function approaches 2, and it might not be possible to distinguish whether it is above or below 2.

The decay rate introduced by Busch et al. (2014) was phenomenological. However, recently, Micheli and Robertson (2022) derived an analytical formula for the decay rate of Bogoliubov quasi-particles in a quasi-BEC. They test the validity of their analytical formula comparing it to numerical simulations and found a good agreement in the particle-like branch ($k\xi > 2$). We will further discuss this decay rate in the fifth chapter, section 2.D, when we will measure the growth rate of the phonon occupation. The value of their decay rate validates *a posteriori* the weak dissipation $\Gamma_k \ll \omega_k$ hypothesis of Busch et al. (2014).

Decoherence and beyond Bogoliubov effect

As we said, the decay rate does not capture decoherence processes: it cannot turn an entangled state to a separable state. In fact, within the Bogoliubov-de Gennes approach, the interactions between longitudinal phonons are not taken into account. In our model, the number of created quasi-particles increases exponentially. At some point, their number cannot be negligible with respect to the number of condensed particles, and we expect the Bogoliubov approximation to break-down, because of quasi-particles interaction. Moreover, the back-reaction of these phonons on the BEC is also neglected within the Bogoliubov approach: the BEC is treated as a classical field hence an infinite reservoir. Such approximation is no longer valid when number of created quasi-particles is large. To investigate such effects, numerical simulations were conducted by Robertson et al. (2018). Interaction between phonons are taken into account by solving an effective 1D Gross-Pitaevskii equation using the truncated Wigner approximation (TWA). To evaluate the back-reaction of the phonons on the amplitude of the oscillation, the authors use a self-consistent method. The energy associated to the oscillation of the BEC width σ is evaluated using an effective potential for σ that we wrote in Eq. (35). The decrease of the BEC oscillation is computed arguing that the total energy (longitudinal phonons + BEC oscillations) is conserved. Note the damping of this BEC oscillation due to quasi-particle creation and its treatment is similar to the damping of the inflaton field.

This thesis manuscript focuses however on the early times and on the non-separability effects. We are thus more interested in the decoherence effects shown in Figure 20, for which the back reaction of the phonon occupation can be neglected, according to the authors. In this figure, reproduced from Robertson et al. (2018), the second order correlation function is plotted as a function of the momentum k. Each curve represents $g^{(2)}_{k,-k}$ at different times from early (top left panel) to late times (bottom right).

Initially, the state is at thermal equilibrium. After just a few oscillations of the BEC width, the state $(k, -k)$, for which $ka_\perp \sim 1$ becomes non-separable (black dashed-dotted curve) and

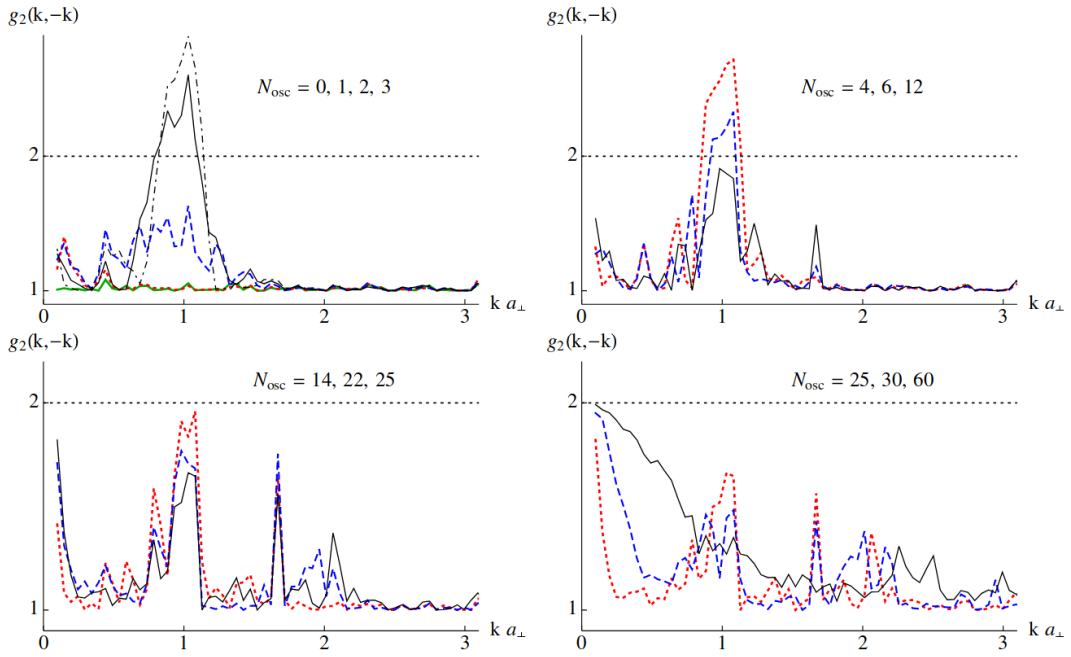

Figure 20: Normalized second order correlation function as a function of k, in unit of the transverse oscillator length $a_\perp$. In each plot, the curves are time-ordered as follows: (solid green), dotted red, dashed blue, solid black, (dot-dashed black). ©Figure from Robertson et al. (2018)

entanglement last for some oscillation. Starting from 12 oscillations, the entanglement visibility is lost, but the authors do not expect the state to be non-separable. With these numerics, the authors argue that the loss of visibility is due to the method used to compute $g^{(2)}$ (they perform a moving average of $g^{(2)}$ over neighbors k). They checked that it is not decoherence effects that are responsible for this decrease. The authors explained that it is after $\sim$ 17 oscillations that non-linearities play a role and are responsible for the effective loss of non-separability.

Figure 21 shows even more clearly how entanglement can be masked when measured using $g^{(2)}$. Here, we show the second order correlation function of the resonant modes $(k_{res}, -k_{res})$ as a function of time. The 1D parameter of the gas is $a_s n_1 = 1.25$ and the temperature of $k_B T/mc_s^2 = 0.91$. The amplitude of the modulation of g_1 is 0.2 in panel (a) and 0.5 for panel (b). Yellow circles are independent numerical simulations using the TWA. For clarity, the error bars are not shown, but they are of same order of the dispersion of the points. Solid red line is the prediction of Bogoliubov theory without dissipation while the dashed dotted blue curve takes into account the damping rate of Micheli and Robertson (2022).

We see that the points from the TWA go slightly above 2, but this deviation is not very significant. On the right of panel (b), we also see that the TWA numerics deviate from 2 at late time. On this panel, a small window exists between 2 and 4 oscillations where entanglement can be revealed.

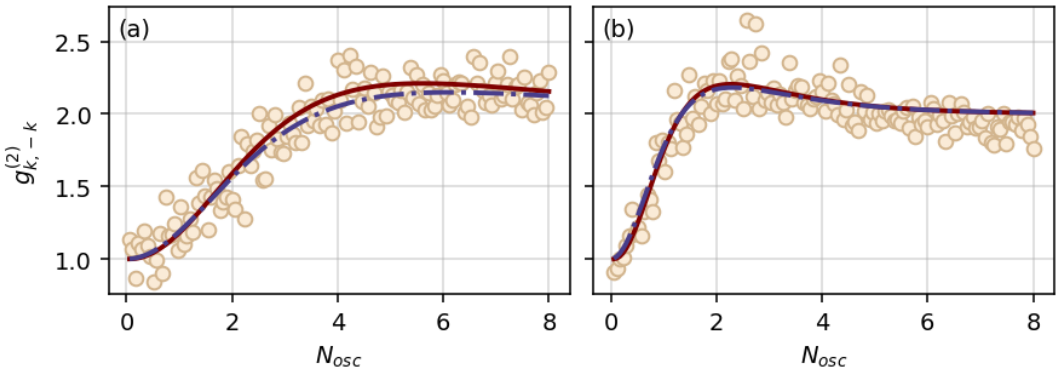

Figure 21: The normalized second order correlation function of the resonant mode as a function of time for a modulation amplitude of 0.2 (panel a) and 0.5 (panel b). ©Courtesy of Amaury Micheli.

Summary In this section, we use the Bogoliubov approximation to derive the Bogoliubov-de Gennes equation that model the pair creation process. Such an approximation treats the BEC as a classical field and neglects quasi-particles interaction. We also introduce Bogoliubov transformations that allow, when the system is stationary, to treat Bogoliubov quasi-particles as independent harmonic oscillators. When the interaction strength oscillates at frequency ω_d, opposite momentum modes with wave-vector k_{res} are squeezed. We observe an exponential creation of quasi-particles at k_{res} such that $\omega(k_{res}) = \omega_d/2$, a well studied mechanism known as a Faraday wave. When the temperature is low enough, the modes $(k, -k)$ are expected to be non-separable. However, detecting such entanglement can be non-trivial, even though the state is strongly non-separable.

Chapter II

Quantifying entanglement of two-mode Gaussian states

Central to this thesis is the detection of entanglement. In the last chapter, we introduced $\Delta_k = \sqrt{n_k n_{-k}} - |\langle \hat{a}_k \hat{a}_{-k} \rangle|$ and explained that negativity of this quantity assesses entanglement. In the experiment, we do not have access to the anomalous correlation term $\langle \hat{a}_k \hat{a}_{-k} \rangle$: this quantity does not conserve the number of particles. On the other hand, we measure any N-body correlation function. When the state is Gaussian, the measurement of these correlation functions can be expanded as a sum of two-field correlation functions. The theory we used to describe our system involves time-dependant second order in creation and annihilation operator Hamiltonian that preserves Gaussianity of the state. Here we therefore discuss how to probe entanglement of *Gaussian* states with a single particle detector (or at least a detector that can resolve many-body correlation functions). In particular, if the Gaussian two-mode state is centered, the normalized two-body correlation function is given by

$$g^{(2)}_{k,-k} = \frac{\langle \hat{a}^\dagger_k \hat{a}^\dagger_{-k} \hat{a}_k \hat{a}_{-k} \rangle}{n_k n_{-k}} = 1 + \frac{|\langle \hat{a}_k \hat{a}_{-k} \rangle|^2}{n_k n_{-k}} + \frac{|\langle \hat{a}^\dagger_k \hat{a}_{-k} \rangle|^2}{n_k n_{-k}} \tag{59}$$

which was expanded using Wick theorem. If we assume that the last term in this equation is zero, it means that the second order correlation function is in one-to-one correspondence with the measurement of the pure correlation term $|\langle \hat{a}_k \hat{a}_{-k} \rangle|$. This chapter aims to discuss such assumption. In fact, we will show that this assumption might not be needed to detect entanglement. We also aim to discuss other correlation witnesses that have been used to claim entanglement: the violation of the classical Cauchy-Schwarz inequality and the observation of relative number squeezing. For our discussion, we will use Gaussian state formalism.

The first section of this chapter will be devoted to the introduction to the Gaussian state formalism, which is a convenient toolbox to describe our state (Cerf et al., 2007). We will then devote a section to entanglement, starting with a discussion on the difference between *mode entanglement* and *particle entanglement*. We will define the PPT criterion and its generalization by Simon, the logarithmic negativity and other entanglement witnesses. The third section is devoted to relative number squeezing and the Cauchy-Schwarz inequality. Those two quantities quantify correlations (entanglement?) and are widely used within the community. We aim here to investigate under which conditions they can assess mode entanglement. The last section of this chapter is devoted to the application of the generalized PPT criterion for thermal Gaussian states. Central to our journey, we demonstrate that the measurement of the second and fourth order correlation functions allow one not only to assess entanglement but also to quantify it.

What we knew, what is new ? The first and second sections of this chapter are a literature review: we introduce Gaussian states and some entanglement criteria/witnesses. The third part of this work discusses the notion of particle and mode entanglement, as well as the range of applicability of the classical Cauchy-Schwarz inequality and relative number squeezing. It does not contain "new" contributions and the discussion might seem trivial; however I did not find in the literature a clear explanation why those quantities could or could not witness mode entanglement. In that sense, the discussion is original. The last section is the major theoretical contribution of this thesis. It demonstrates how 2- and 4-body correlation functions can be used to quantify the entanglement of thermal Gaussian states.

1. Gaussian states

The theoretical study of Gaussian states is abundant in the literature: their general and mathematically rigorous introduction is beyond the scope of this thesis. In this section, I introduce the key properties of two-mode Gaussian states. Subsection 1.A recalls some key properties of the density matrix operator and subsection 1.B the Wigner function. Subsection 1.C introduces the Gaussian state formalism which will be used in the rest of this chapter, especially the second section and the fourth one, which are the main theoretical results from this work. Subsections 1.D and 1.E recalls usual single mode and two-mode states and transformations. The last subsections present usual states and transformations. Subsection 1.F provides references to compute the N-mode probability distribution of Gaussian states.

1.A Density matrix of a quantum state

In this first subsection, we review key properties of the density operator $\hat{\rho}$ that we will use throughout this chapter. We will use the properties required by a density operator to derive bounds on the covariance matrix of a Gaussian state.

Definition - Density matrix
The density operator $\hat{\rho}$ defines a quantum state. It must be a Hermitian operator, positive semi-definite[a] with trace 1.

[a] A positive-definite matrix $\boldsymbol{M}$ is such that for any non-zero vector x, the real quantity $\boldsymbol{x}^\intercal \boldsymbol{M}\boldsymbol{x}$ is strictly positive. A positive semi-definite matrix requires just positivity of this quantity (it allows zero value).

In particular, if a matrix $\hat{\rho}$ has a negative eigenvalue, it cannot represent a quantum state. A pure state can be written as $\hat{\rho} = |\psi\rangle\langle\psi|$: it is a projector. The purity of an arbitrary quantum state is $p = \mathrm{Tr}(\hat{\rho}^2)$. It is 1 for a pure state and smaller than 1 for mixed states.

Definition - Expectation value of an operator
The expectation value of any operator $\hat{A}$ is given by

$$\langle \hat{A} \rangle_{\hat{\rho}} = \mathrm{Tr}(\hat{\rho}\hat{A}) = \langle \hat{A} \rangle \tag{60}$$

where we will omit the bracket subscript $\hat{\rho}$ in the following.

Theorem - Cauchy-Schwarz inequality
Because the density matrix of a quantum state is semipositive definite, it implies that for any operator $\hat{A}$ and $\hat{B}$, it is always true that the following Cauchy-Schwarz inequality is satisfied (Horn and Mathias, 1990; Robertson, 2021)

$$|\mathrm{Tr}(\hat{\rho}\hat{A}^\dagger\hat{B})|^2 = |\langle\hat{A}^\dagger\hat{B}\rangle|^2 \leq \langle\hat{A}^\dagger\hat{A}\rangle\langle\hat{B}^\dagger\hat{B}\rangle \tag{61}$$

Note that this inequality is **always true** and is never violated. As we shall see after, the so-called "violation of the classical Cauchy-Schwarz inequality" as an entanglement witness is different from this inequality. It refers to the violation of the latter *normally ordered* inequality.

1.B The Wigner function

The Wigner function $W(x,p)$, introduced by Wigner (1932), represents the quasiprobability distributions of the state in the phase space (x,p).

Definition - Wigner function
The Wigner function of a state $\hat{\rho}$ is defined as (Leonhardt, 2010)

$$W(x,p) = \frac{1}{2\pi}\int e^{ipy/\hbar}\langle x - y/2|\hat{\rho}|x + y/2\rangle\,\mathrm{d}y. \tag{62}$$

Remark - The Wigner function: a quasiprobability distribution function
The Wigner function is quasiprobability function as its integral over x (resp p) gives the probability distribution of the state in p (resp x)

$$\begin{aligned}\langle x|\hat{\rho}|x\rangle &= \int W(x,p)\mathrm{d}p\\ \langle p|\hat{\rho}|p\rangle &= \int W(x,p)\mathrm{d}x\end{aligned} \tag{63}$$

and is often referred to as a quasi-probability distribution. The reason is that the projection along any axis (x,p) gives the probability distribution along this axis. Wigner functions can be measured using homodyne detection measurement as proposed by Vogel and Risken (1989). The first experimental measurement of a Wigner function was realized a few years later by Smithey et al. (1993), who measured the vacuum state $|0\rangle$ and a squeezed vacuum state[1]. Their experimental measurement is reproduced in the first subplot of Figure 22. After this pioneering measurement, more and more complex states were measured: Lvovsky et al. (2001), Ourjoumtsev et al. (2006a), and Cooper et al. (2013) respectively measured the one, two, and three photon Fock states before producing and measuring cat states (Ourjoumtsev et al., 2006b) [2].

What is the Wigner function of the vacuum ? The Wigner function definition (62) involves the wave-function of the vacuum state that can be deduced by the definition of the annihilation

[1] Note also the measurement of the Wigner function of an atomic wave after a double-slit by Kurtsiefer et al. (1997) with... metastable helium atoms!

[2] For a review of the "Production and applications of non-Gaussian quantum states of light", see Lvovsky et al. (2020).

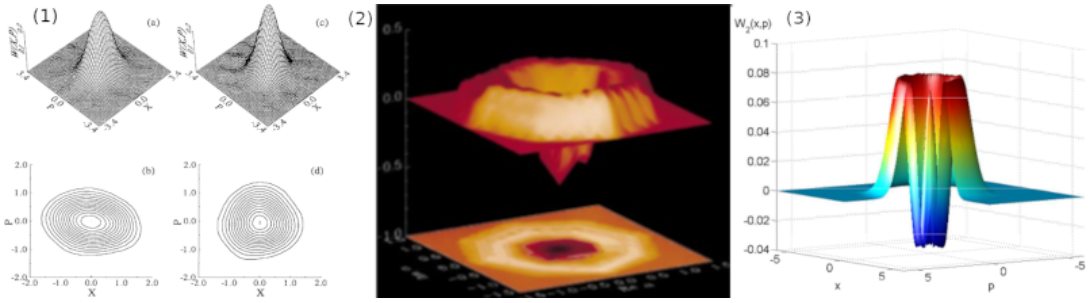

Figure 22: Wigner function reconstructed from experimental data. Sub-figure (1) represents the first measured Wigner distribution by Smithey et al. (1993) of a squeezed state (left, a-c) and of a vacuum state (right, b-d). The squeezed state is elliptical (squeezed in the X quadrature) compared to the vacuum state whose shape is circular. Sub-figure (2): Wigner distribution of a Be^+ ion in the Fock state $|1\rangle$ measured by Leibfried et al. (1996) and (3) of free-propagating photons in the Fock state $|2\rangle$ by Ourjoumtsev et al. (2006a). The Wigner functions of (1) are Gaussian while (2) and (3) are obviously not Gaussian. The negative value taken by the Wigner function is a signature of the quantumness of the state, that cannot be mimic by any classical-like state. ©Figure from Smithey et al. (1993), Leibfried et al. (1996) and Ourjoumtsev (2007).

$\hat{a} = (\hat{x} + i\hat{p})/\sqrt{2}$ operator. Indeed, the action of the latter on the vacuum gives 0 and noting that $\hat{p} = i\partial_x$ in the x representation, the vacuum wave-function $\psi_0(x)$ satisfies $(x + \partial_x)\psi_0 = 0$, *i.e.* it is Gaussian. Inserting ψ_0 in equation (62) leads to the Wigner distribution of the vacuum state

$$W_0(x, p) = \frac{1}{\pi} \exp\left(-x^2 - p^2\right) \tag{64}$$

that is Gaussian. As we shall see, Gaussian states are transformed into other Gaussian states by second order transformations, hence their simple Wigner function simplifies their study. In fact, the Wigner function of a state is just a way to describe this state, and we can recover the expectation value of any operator from its Wigner function. To do so, we need to introduce the Weyl transform of an operator.

Definition - Weyl transform
The Weyl transform of an operator $\hat{A}$ is defined by (Weyl, 1950)

$$\tilde{A}(x, p) = \int e^{-iyp/\hbar} \langle x + y/2| \hat{A} |x - y/2\rangle \tag{65}$$

where the similarity with the definition of the Wigner (62) appears clearly. Here, we expressed the operator $\hat{A}$ in the x basis but it is possible also to express it in the p basis, simply by flipping the role of x and p and the sign in the exponential (Case, 2008). The average value of any operator $\hat{A}$ over a state $\hat{\rho}$ is then given by the phase-space integral of the product of the Wigner function W_ρ of this state and the Weyl transform of the operator $\hat{A}$

$$\langle \hat{A} \rangle = \int W_\rho(x, p)\tilde{A}(x, p)\mathrm{d}x\mathrm{d}p. \tag{66}$$

For example, the Weyl transform of the projector $|x\rangle \langle x|$ is simply x. An other example is the

Weyl transform of the projector on the Fock basis $|j\rangle\langle j|$ (Leonhardt, 2010)

$$W_j(x,p) = \frac{(-1)^j}{\pi} e^{-x^2-p^2} \mathcal{L}_j(2x^2+2p^2) \tag{67}$$

where $\mathcal{L}_j$ are the Laguerre polynomials.

1.C Gaussian states

Hamiltonians of second order in creation and annihilation operators are central in physics. It is for example the case of the BCS[3] model for superconductivity or the Bogoliubov theory discussed in the last chapter (see Section 3.A). A Gaussian state that evolves under such Hamiltonian remains Gaussian. The vacuum, thermal states and coherent states are Gaussian: this means that the evolution of those states under second order hamiltonians are also Gaussian. This motivated the detailed study of *Gaussian states* and the description of their evolution.

Gaussian states are only defined by their first and second moment: a state of N Gaussian modes is characterized by its first moment vector $\boldsymbol{\mu}$ and its covariance matrix $\boldsymbol{\sigma}$, defined in (68). The size of the vector is $2N$ and the covariance matrix is $N \times N$. However, because of the canonical commutation rules and the Heisenberg uncertainty relation, this matrix belongs to the so-called symplectic group $Sp(2N,\mathbb{R})$ with size $N(2N+1)$ (Arvind et al., 1995). The Gaussian state formalism is therefore quite practical as it avoids working with an infinite Hilbert space (for example the Fock basis $\{|n\rangle\}$) but rather with $N(2N+3)$ parameters (degree of freedom for the covariance matrix and the mean vector).

Literature references This section is an aggregate of many references. Among them, the comprehensive description of Gaussian states offered in the book by Serafini (2017) was highly utilized. The *Analog Gravity in Benasque* lecture notes by Brady (2023) were also fundamental in my comprehension of Gaussian formulism. In the same vein but more concise, the review articles by Weedbrook et al. (2012), Adesso et al. (2014), and Braunstein and van Loock (2005) provide a really good overview of the literature. I also used and recommend the pedagogical article by Case (2008), which introduces *Wigner functions and Weyl transforms for pedestrians*. Note finally the excellent note by Brask (2022) that summarizes well the topic. From a mathematical perspective, the review article by Arvind et al. (1995) provides a complete and rigorous overview of the key properties of the real symplectic group.
For shorter references, many articles provide nice summaries. Among them, Serafini et al. (2004a) and Pirandola et al. (2009) introduce well the progress made in the early 2000s. The article by Brady et al. (2022) pedagogically introduces symplectic circuits as a tool to model multi-mode scattering events in analog gravity. Martin et al. (2023) focuses on the comparison of entanglement criteria and derives analytic expressions for the effective squeezing parameter and purity for a noisy or lossy two-mode squeezed thermal state.

In the following, we will group the canonical operator as $\hat{\boldsymbol{r}} = (\hat{x}_1, \hat{p}_1, ..., \hat{x}_N, \hat{p}_N)$, with a special focus on $N = 2$-mode systems. Here, $\hat{x}$ and $\hat{p}$ are related to the creation and annihilation

[3] BCS stands for Bardeen–Cooper–Schrieffer, the three scientists that devlopped the "Microscopic Theory of Superconductivity" (Bardeen et al., 1957).

operators $\hat{a}_j = (\hat{x}_j + i\hat{p}_j)/\sqrt{2}$. The first moment vector and the covariance matrix of the state read (Serafini, 2017)

$$\mu_i = \langle \hat{r}_i \rangle \quad ; \quad \sigma_{i,j} = \langle \{\Delta\hat{r}_i, \Delta\hat{r}_j\} \rangle \tag{68}$$

where $\Delta\hat{r}_i = \hat{r}_i - \langle \hat{r}_i \rangle$ and the Poissonian bracket $\{,\}$ was used as a shortcut to define the anti-commutator $\{\hat{A}, \hat{B}\} := \hat{A}\hat{B} + \hat{B}\hat{A}$. Note that in the community, the definition of the covariance matrix differs depending on the value of $\hbar$: here we follow the notation of Serafini (2017), but one should be careful when using formulae from the literature. As explained in the introduction of the arxiv version of Weedbrook et al. (2012), "there is no consensus about the value of the variance of the vacuum, with common choices being either 1/4 ($\hbar = 1/2$), 1/2 ($\hbar = 1$) or 1". This means that depending on the notation, the covariance matrix might be defined with a factor $1/2$. Throughout this chapter, we have in particular

- $\hbar = 1$,
- $\hat{a}_j = (\hat{x}_j + i\hat{p}_j)/\sqrt{2}$
- $\sigma_{i,j} = \langle \{\Delta\hat{r}_i, \Delta\hat{r}_j\} \rangle$.

With these conventions, the Wigner function of a Gaussian state is simply given by (Brady, 2023)

$$W(\boldsymbol{r}) = \frac{1}{\pi^N \sqrt{\mathrm{Det}[\boldsymbol{\sigma}]}} \exp\left[-(\boldsymbol{r}-\boldsymbol{\mu})^\intercal \boldsymbol{\sigma}^{-1} (\boldsymbol{r}-\boldsymbol{\mu})\right]. \tag{69}$$

and the bosonic commutation relations are

$$\left[\hat{r}_i, \hat{r}_j\right] = i\Omega_{i,j} \quad , \quad \boldsymbol{\Omega} = \bigoplus_{k=1}^{N} \boldsymbol{\Omega}_1 = \begin{pmatrix} \boldsymbol{\Omega}_1 & & \\ & \ddots & \\ & & \boldsymbol{\Omega}_1 \end{pmatrix} \quad , \quad \boldsymbol{\Omega}_1 = \begin{pmatrix} 0 & 1 \\ -1 & 0 \end{pmatrix}, \tag{70}$$

where $\boldsymbol{\Omega}$ is called the (N-mode) symplectic form. A Gaussian transformation is a quantum transformation that preserves Gaussianity of the state. Simon et al. (1987) showed that Gaussian unitary transformations can be written as a combination of a displacement $\boldsymbol{d} \in \mathbb{R}^4$ and a symplectic transformation $\boldsymbol{S} \in \mathcal{S}p(2N, \mathbb{R})$. The mean and the covariance matrix of the state is thus transformed as

$$\boldsymbol{\mu} \to \boldsymbol{S}\boldsymbol{\mu} + \boldsymbol{d}, \qquad \boldsymbol{\sigma} \to \boldsymbol{S}\boldsymbol{\sigma}\boldsymbol{S}^\intercal. \tag{71}$$

Definition - Symplectic group and transformations
The group of the real symplectic matrices $\mathcal{S}p(2N, \mathbb{R})$ is defined as the real matrices of size $2N \times 2N$ that satisfy (Arvind et al., 1995)

$$\boldsymbol{S}\boldsymbol{\Omega}\boldsymbol{S}^\intercal = \boldsymbol{\Omega} \tag{72}$$

As we shall see, we can bring the covariance matrix to a normal form (which is diagonal, see Williamson decomposition) using symplectic transformations.

Not all symmetric matrices can represent a quantum state. Indeed, a quantum state must respect the canonical commutation relations and be semi-positive definite. Simon et al. (1994) showed that those two conditions can be recast in the following compact form, called the Schrödinger-Robertson inequality or the *bona fide* condition.

Theorem - Schrödinger-Robertson inequality or bona fide condition
Any covariance matrix $\boldsymbol{\sigma}$ that represents a positive bosonic quantum state must respect the following *bona fide* condition

$$\boldsymbol{\sigma} + i\boldsymbol{\Omega} \geq 0. \tag{73}$$

The purity p of the state can also be computed from the covariance matrix

$$p = \mathrm{Tr}(\hat{\rho}^2) = \frac{1}{\sqrt{\det\boldsymbol{\sigma}}} \tag{74}$$

When $p = 1$, the state is pure, and it is said *mixed* when $p < 1$.

It is possible to decompose the covariance matrix on *normal modes*, that is a basis in which the system is split into N decoupled degrees of freedom. Such a transform is often referred as Williamson decomposition.

Theorem - Williamson decomposition
Williamson (1936) showed that, for any symmetric positive-definite matrix $\boldsymbol{\sigma}$, there exists a symplectic transformation $\boldsymbol{S} \in \mathcal{S}p(2N, \mathbb{R})$ such that

$$\boldsymbol{\sigma} = \boldsymbol{S} \bigoplus_{j=1}^{N} \begin{pmatrix} \nu_j & 0 \\ 0 & \nu_j \end{pmatrix} \boldsymbol{S}^\intercal \tag{75}$$

where $\nu_j > 0$ are the *symplectic eigenvalues* of $\boldsymbol{\sigma}$.

Note here that the matrix is not diagonalized in the sense that it is not a change of basis *i.e.* $\boldsymbol{S}^{-1} \neq \boldsymbol{S}^\intercal$. Furthermore, the *bona fide* condition (73) applied to the normal mode decomposed covariance matrix $\boldsymbol{\nu}$ implies

$$\boldsymbol{\nu} + i\boldsymbol{\Omega} = \bigoplus_{j=1}^{N} \begin{pmatrix} \nu_j & i \\ -i & \nu_j \end{pmatrix} \geq 0 \tag{76}$$

and therefore that *all symplectic eigenvalues of the covariance matrix of a quantum state must be greater than 1.*

For a two-mode Gaussian state $\hat{\rho}_{AB}$ whose covariance matrix is

$$\boldsymbol{\sigma} = \begin{pmatrix} \boldsymbol{A} & \boldsymbol{C} \\ \boldsymbol{C}^\intercal & \boldsymbol{B} \end{pmatrix} \tag{77}$$

the Williamson form is $\nu_- \mathbb{I}_2 \oplus \nu_+ \mathbb{I}_2$ where the symplectic spectrum was shown by Serafini et al. (2004b) to be given by

$$\nu_\pm = \sqrt{\frac{\Delta \pm \sqrt{\Delta^2 - 4\det\boldsymbol{\sigma}}}{2}} \qquad \Delta := \det\boldsymbol{A} + \det\boldsymbol{B} + 2\det\boldsymbol{C}. \tag{78}$$

In terms of those quantities, the *bona fide* condition (73) can be rewritten as (Pirandola et al., 2009)

$$\boldsymbol{\sigma} > 0 \qquad \det\boldsymbol{\sigma} \geq 1 \qquad \Delta \leq 1 + \det\boldsymbol{\sigma} \tag{79}$$

Last but not least, Brask (2022) provides us that by tracing out the system to focus on a single mode, we can assess the properties of the local displacement and covariance matrix. The following statement is extracted from his paper:

Property	Hilbert space $\mathcal{H}$	Phase space Γ
dimension	∞	$2N$
structure	$\bigotimes$	$\bigoplus$
description	ρ	$\boldsymbol{d}$, $\boldsymbol{\sigma}$
bona fide	$\rho \geq 0$	$\boldsymbol{\sigma} + i\boldsymbol{\Omega} \geq 0$
unitary operations	$\{\widehat{U} : \widehat{U}^\dagger \widehat{U} = \widehat{\mathbb{I}}\}$ $\rho \mapsto \widehat{U}\rho\widehat{U}^\dagger$	$\{\boldsymbol{S} : \boldsymbol{S\Omega S}^\mathsf{T} = \boldsymbol{\Omega}\}$ $\boldsymbol{d} \mapsto \boldsymbol{Sd}$, $\boldsymbol{\sigma} \mapsto \boldsymbol{S\sigma S}^\mathsf{T}$
spectra	$\widehat{U}^\dagger\rho\widehat{U} = \mathrm{diag}\{\lambda_j\}_{j=1}^{\infty}$ $0 \leq \lambda_j \leq 1$	$\boldsymbol{S}^\mathsf{T}\boldsymbol{\sigma S} = \mathrm{diag}\{(\nu_k, \nu_k)\}_{k=1}^{N}$ $1 \leq \nu_k < +\infty$
pure states	$\lambda_i = 1$, $\lambda_{j\neq i} = 0$	$\nu_k = 1$, $\forall\, k = 1, \ldots, N$
purity	$\mathrm{Tr}\rho^2 = \sum_j \lambda_j^2$	$1/\sqrt{\det \boldsymbol{\sigma}} = \prod_k \nu_k^{-1}$

Figure 23: Schematic comparison between Hilbert space and phase space pictures for N - mode Gaussian states. ©Table from Adesso et al. (2014)

Theorem - Tracing out
For the two-mode Gaussian state $\hat{\rho}_{AB}$ with mean vector $(\boldsymbol{r}_A, \boldsymbol{r}_B)$ and covariance matrix (77), the reduced state $\hat{\rho}_A$ (respectively $\hat{\rho}_B$) of subsystem A (resp. B) is also Gaussian with displacement $\boldsymbol{r}_A$ and covariance matrix $\boldsymbol{A}$ (resp. $\boldsymbol{r}_B$ and $\boldsymbol{B}$).

1.D Single mode Gaussian states and single mode transformations

The expression of usual Gaussian operations can be found in many reviews article and text-books, see Weedbrook et al. (2012) for example. They can be divided into *passive* and *active* transformations. Passive transformations preserve the value of $\mathrm{Tr}(\boldsymbol{\sigma})$, *i.e.* they preserve the mean energy of the system while *active* transformations do not preserve it. The interested reader might refer to Adesso et al. (2014) for a more mathematical description of the difference between passive and active transformations.

The vacuum state: the covariance matrix of the vacuum is the identity, and it is centered on the origin of the phase space ($\boldsymbol{r} = 0$).

$$\boldsymbol{\mu} = (0, 0) \qquad \boldsymbol{\sigma} = \mathbb{I}_2 \qquad \hat{\rho}_{vac} = |0\rangle\langle 0| \tag{80}$$

Coherent states: the covariance matrix of a coherent state (displaced vacuum state) is also the identity but is not centered on the phase space origin.

$$\hat{D}(\alpha) = \exp(\alpha\hat{a}^\dagger - \alpha^*\hat{a}) \quad \Longleftrightarrow \quad \boldsymbol{\mu} \to \sqrt{2}(\Re(\alpha), \Im(\alpha)) + \boldsymbol{\mu} \tag{81}$$

leaving the covariance matrix unchanged. If the average population of a coherent state is $\bar{n}$, a coherent state lies on a circle in the phase space of radius $\sqrt{2\bar{n}} = \sqrt{2}|\alpha|$

$$\boldsymbol{\mu} = \sqrt{2\bar{n}}(\cos\theta, \sin\theta) \qquad \boldsymbol{\sigma} = \mathbb{I}_2 \qquad |\alpha\rangle = \exp\left(-|\alpha|^2/2\right)\sum_i \frac{\alpha^i}{\sqrt{i!}}|i\rangle \tag{82}$$

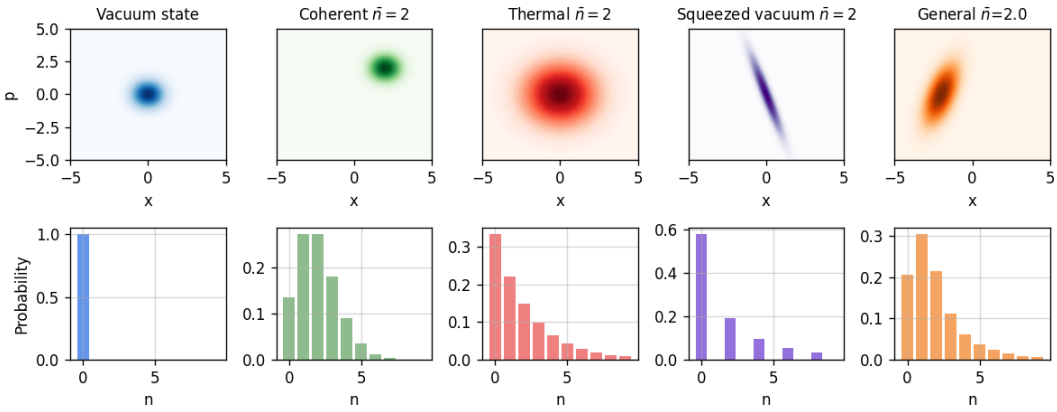

Figure 24: Wigner function (top raw) and photon number distribution (second raw) of one mode Gaussian states. From left to right: the vacuum state has 0 mean population while the coherent state, the thermal state and the single-mode squeezed vacuum state were chosen so that their mean population is 2. The last column represents a general squeezed ($r = 0.5$), rotated ($-\pi/5$) and displaced ($\bar{x} = -2$) Gaussian state with purity $p = 0.5 < 1$. The mean photon population is also 2. ©The photon number distribution were computed using the Walrus library (Gupt et al., 2019).

Thermal states: thermal states are not pure states, their purity is $p = 1/(2\bar{n}+1)$ where $\bar{n}$ is the mean photon population. They are centered on the phase space origin, but their covariance matrix is the identity multiplied by $2\bar{n}+1$

$$\boldsymbol{\mu} = (0,0) \qquad \boldsymbol{\sigma} = (2\bar{n}+1)\mathbb{I}_2 \qquad \hat{\rho}_{th}(\bar{n}) = \sum_i \frac{\bar{n}^i}{(\bar{n}+1)^{i+1}} |i\rangle\langle i| \tag{83}$$

Single-mode squeezed states: A single mode squeezing operator is an active transformation and is parametrized by the squeezing parameter r

$$\hat{S} = \exp\left[r(\hat{a}^2 - \hat{a}^{\dagger 2})/2\right] \quad \leftrightarrow \quad \boldsymbol{S}(r) = \begin{pmatrix} e^{-r} & 0 \\ 0 & e^{r} \end{pmatrix} \tag{84}$$

generates a squeezed vacuum state when acting on the vacuum (Yuen, 1976)

$$\boldsymbol{\mu} = (0,0) \qquad \boldsymbol{\sigma} = \boldsymbol{S}(2r) \qquad \hat{\rho}_0(r) = \frac{1}{\sqrt{\cosh r}} \sum_i \frac{\sqrt{(2i)!}}{2^i\, i!} \tanh r^i\, |2i\rangle\langle 2i| \tag{85}$$

Phase shift: a single mode rotation by an angle $\varphi/2$ in phase space is a passive transformation and reads

$$\hat{U} = \exp(i\varphi \hat{a}_i^\dagger \hat{a}_i) \quad \leftrightarrow \quad \boldsymbol{R}(\varphi) = \begin{pmatrix} \cos\varphi/2 & -\sin\varphi/2 \\ \sin\varphi/2 & \cos\varphi/2 \end{pmatrix} \tag{86}$$

General one-mode Gaussian state: Any pure Gaussian state can be generated with squeezing, rotation and displacement operators acting on the vacuum, *i.e* one can characterize any one mode Gaussian state with four numbers $(\bar{x}, \bar{p}, \varphi, r)$. The most general form for a (non necessary pure) Gaussian state is therefore the following

$$\boldsymbol{\mu} = (\bar{x}, \bar{p}) \qquad \boldsymbol{\sigma} = \frac{1}{p}\boldsymbol{R}(\varphi)\boldsymbol{S}(2r)\boldsymbol{R}^\intercal(\varphi) \tag{87}$$

where p is the purity of the single mode state $p = 1/\sqrt{\det\boldsymbol{\sigma}}$.

Noise and loss channels: the usual way to take into account the non-unit efficiency of detectors is by mixing the state on a beam-splitter with the environment. For pure loss channels, the environment is simply the vacuum. The action of a pure loss channel parametrized by η *i.e.* the efficiency of the detector, is given by (Barbosa et al., 2011)

$$\boldsymbol{\mu}' = \sqrt{\eta}\boldsymbol{\mu} \qquad \boldsymbol{\sigma}' = \eta\boldsymbol{\sigma} + (1-\eta)\mathbb{I}_2 \tag{88}$$

Noisy channels can also be parametrized by a noise parameter, often noted Δ that changes the covariance matrix according to (Martin et al., 2023)

$$\boldsymbol{\sigma}' = \boldsymbol{\sigma} + \Delta\mathbb{I}_2 \tag{89}$$

1.E Two-mode Gaussian states and transformations

Thermal state: a two-mode thermal Gaussian state can be parametrized by two different thermal occupation $\bar{n}_1$ and $\bar{n}_2$. Its covariance matrix is given by

$$\boldsymbol{\mu} = (0,0,0,0) \qquad \boldsymbol{\sigma} = \begin{pmatrix} (2\bar{n}_1+1)\mathbb{I}_2 & 0 \\ 0 & (2\bar{n}_2+1)\mathbb{I}_2 \end{pmatrix} \tag{90}$$

and the purity of this state is $p^{-1} = (2\bar{n}_1+1)(2\bar{n}_2+1)$.

Beam-Splitter: is a transformation that mixes the two modes and is quite useful to model an interferometer with Gaussian states. It writes (Brady et al., 2022)

$$\boldsymbol{S}_{BS}(\theta) = \begin{pmatrix} \cos\theta & 0 & \sin\theta & 0 \\ 0 & \cos\theta & 0 & \sin\theta \\ -\sin\theta & 0 & \cos\theta & 0 \\ 0 & -\sin\theta & 0 & \cos\theta \end{pmatrix} \tag{91}$$

Noises and pure losses: each subsystem might undergo different pure loss channel. In this case, the covariance matrix is transformed as (Barbosa et al., 2011)

$$\boldsymbol{\mu}' = \boldsymbol{L}\boldsymbol{\mu} \qquad \boldsymbol{\sigma}' = \boldsymbol{L}(\boldsymbol{\sigma}\mathbb{I}_4)\boldsymbol{L} + \mathbb{I}_4, \qquad \boldsymbol{L} = \begin{pmatrix} \sqrt{\eta}_1\mathbb{I}_2 & 0 \\ 0 & \sqrt{\eta}_2\mathbb{I}_2 \end{pmatrix} \tag{92}$$

The same could apply for noisy channels, see Serafini et al. (2004a) for which one can define the noise on channel 1 and the noise on channel 2, particularly relevant in the frame of quantum information to take into account the transmission channel.

Two-mode squeezed state: a two-mode squeezer is defined by a squeezing parameter r

$$\hat{S}_2(r) = \exp[r(\hat{a}\hat{b} - \hat{a}^\dagger\hat{b}^\dagger)/2] \quad \leftrightarrow \quad \boldsymbol{S}(r) = \begin{pmatrix} \cosh r\mathbb{I}_2 & \sinh r\boldsymbol{\sigma}_z \\ \sinh r\boldsymbol{\sigma}_z & \cosh r\mathbb{I}_2 \end{pmatrix} \tag{93}$$

where $\boldsymbol{\sigma_z}$ is the Pauli matrix diag(1,-1). When the two-mode squeezing operator acts on the vacuum, one obtains a two-mode squeezed vacuum state

$$|\text{TMSv}\rangle\,(r) = \sqrt{1-\tanh^2 r}\sum_i (\tanh r)^i\,|i,i\rangle \tag{94}$$

whose covariance matrix reads

$$\boldsymbol{\sigma}_{\text{TMSv}}(r) = \begin{pmatrix} \cosh 2r\mathbb{I}_2 & \sinh 2r\boldsymbol{\sigma}_z \\ \sinh 2r\boldsymbol{\sigma}_z & \cosh 2r\mathbb{I}_2 \end{pmatrix}. \tag{95}$$

The variance of the quadrature difference or sum vanishes in the limit $r \to \infty$ as

$$V(\hat{x}_a - \hat{x}_b) = V(\hat{p}_a + \hat{p}_b) \propto e^{-2r}. \tag{96}$$

This state is often referred as an EPR state, for Einstein-Podolski-Rosen because it exhibits perfect correlations between subsystem a and b. In experiments however, one never deals with zero temperature systems and the temperature of the environment must be taken into account. A thermal squeezed state is therefore a thermal state (91) that has been squeezed (93)

$$\boldsymbol{\sigma}_{\text{TMSth}} = \boldsymbol{S}\boldsymbol{\sigma}_{\text{th}}\boldsymbol{S}^{\intercal} = (1 + 2n_e)\boldsymbol{\sigma}_{\text{TMSv}}(r) \tag{97}$$

where n_e is the temperature environment that we take equal for the two subsystems for simplicity.

1.F Joint probability distribution

The covariance matrix defines the state entirely. In principle, it is possible to obtain the probability distribution of the particle number $\mathcal{P}(n, m)$, namely the probability of having n particles in mode A and m particles in mode B. In practice, projecting a Gaussian state onto the Fock space is not trivial. *A priori*, this distribution can be computed from the Weyl transform of the Fock basis projectors $|i\rangle\langle i|$, as given in equation (67). For our system, it reads

$$\mathcal{P}(n, m) \propto \int \mathrm{d}\boldsymbol{r}\ W_n(r_1, r_2) W_m(r_3, r_4) e^{-\sum_{i,j}(r_i - \mu_i)\sigma_{ij}^{-1}(r_j - \mu_j)} \tag{98}$$

which is neither analytical nor easy to evaluate. In fact, the analytical expression for the joint photon-number distribution was first derived for a displaced but pure two-mode squeezed state by Caves et al. (1991). For a mixed state, Dodonov et al. (1994a) started by deriving the photon distribution for a single-mode state. Finally, Dodonov et al. (1994b) extended this result to a general N-mode Gaussian mixed state of light. The latter formula involves "diagonal multidimensional Hermite polynomials" (Berkowitz and Garner, 1970; Kok and Braunstein, 2001). Fortunately, this has been implemented in a Python package named The Walrus by Gupt et al. (2019). Also, note the existence of Qugit, a Python package to simulate the evolution of Gaussian states developed by Brandão et al. (2022), but it does not currently implement the routine to obtain the joint particle distribution.

Summary This section introduced Gaussian states, that can be fully characterized by their first and second moment, the covariance matrix (68). Any covariance matrix that represents a quantum state must satisfy a *bona fide* condition, the Schrödinger-Robertson inequality (73). It requires its (symplectic) eigenvalues to be reater than 1. This inequality is fundamental in the next sections, to assess the non-separability of Gaussian states.

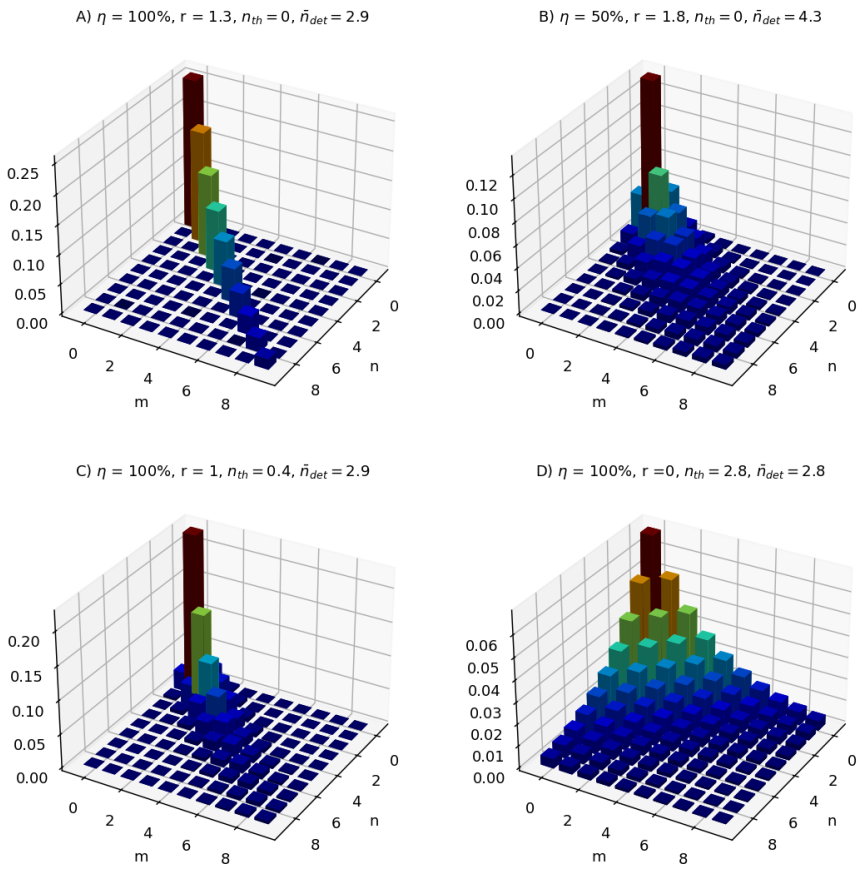

Figure 25: Joint probability distributions of different two-mode Gaussian states. A) Two-mode squeezed vacuum state with squeezing parameter $r = 1.3$ and detected with a 100% efficiency detector. A pure TMSv has non zero elements on the diagonal and 0 elsewhere. B) Two-mode squeezed vacuum state detected with a detector that has 50% efficiency: the distribution exhibits non-diagonal elements. C) Two-mode squeezed ($r = 1$) thermal ($n_{th}^{in} = 0.4$) state. The initial thermal population broadens the diagonal distribution. D) Two-mode thermal state ($n_{th} = 2.8$) with no correlations. This state is completely symmetric and exhibits no correlations at all. ©Distributions obtained using the Walrus library (Gupt et al., 2019).

2. Entanglement criteria review

The word "entanglement" was introduced by Schrödinger (1935) as "not *one* but rather *the* characteristic trait of quantum mechanics". Experimental observation of entanglement was then made possible through the violation of a Bell inequality, introduced by Bell (1964) and reformulated by Clauser et al. (1969) as the CHSH inequality. Such inequality paved the way towards the observation of entanglement with experimental systems by Clauser (1974) and Aspect (Aspect et al., 1981, 1982b,a), leading to the so-called first and second quantum

revolution (Dowling and Milburn, 2003).

For pure states, there is an equivalence between entanglement and a violation of a Bell inequality (Gisin, 1991; Gisin and Peres, 1992). If we consider non-pure states (*mixed* state), this is no longer true. For example, there are states that can be used for teleportation (and are thus entangled) but do not violate a Bell inequality (Popescu, 1994). For mixed state, Werner (1989) introduced the notion of "non-separability" to refer to entangled states: entanglement and non-separability are thus synonyms.

The following of this section focuses on entanglement criteria and witnesses. In the subsection 2.A, we define entanglement from the non-separability definition of Werner (1989). We then define the widely used PPT (Positive Partial Transpose) criterion and its generalization for Gaussian states (gPPT) in subsection 2.B. This part is central as the fourth section of this chapter relies on it. Subsection 2.C introduces the logarithmic negativity (LN) as an entanglement quantifier. We then briefly review in part 2.D other criteria and witnesses that are commonly used in work related to this thesis.

2.A Separability definition

The definition of separable states is due to Werner (1989): "*A state of a composite quantum system is called classically correlated if it can be approximated by convex combinations of product states, and Einstein-Podolsky-Rosen correlated otherwise*".

> **Definition - Separability**
> Considering a bipartite system of two modes 1 and 2, a quantum state describing it is separable if and only if it can be expressed in the form
>
> $$\hat{\rho} = \sum_j p_j \hat{\rho}_{j1} \otimes \hat{\rho}_{j2} \tag{99}$$
>
> where $p_j \geq 0$, $\hat{\rho}_{j1}$ and $\hat{\rho}_{j2}$ are the density matrices of subsystem 1 and 2. Any non-separable quantum state is entangled.

For example, the density matrix of an uncorrelated two-mode thermal state is $\hat{\rho} = \hat{\rho}_{th,1} \otimes \hat{\rho}_{th,2}$ where $\hat{\rho}_{th}$ is the density matrix of a thermal state (83).

Furthermore, following Gühne and Tóth (2009), we make the distinction between an entanglement criterion which is a necessary and sufficient condition for the (non) separability of the state, and an entanglement witness which only assesses that, above a threshold, the state is non-separable. It is often reported that entanglement depends on the partition *i.e.* the subsystem we are considering. In this work, as we aim to measure particles in the $(k, -k)$ basis, the partition is clear, and we will refer to the entanglement between those two modes. Note also that it was reported by Sperling et al. (2019) the existence of a family of quantum states that is "entangled for arbitrary mode decompositions", invalidating my previous statement. The state they consider is such that it is a "superposition of nonparallel and non-orthogonal modes".

$$|\Psi\rangle = \frac{\sqrt{2}\,|2,0\rangle + \lambda\,|1,1\rangle}{\sqrt{2+|\lambda|^2}} \tag{100}$$

where $\lambda \neq 0$. This state is highly non-Gaussian and is beyond the discussion of this thesis. Indeed, as we saw, a Gaussian state can always be diagonalized by Williamson's theorem which means that, in this partition, the modes are separable.

From the separability definition, it is obvious that a fock state $|\Psi_{TF}\rangle = |n, n\rangle$ is *not* entangled while a two-mode squeezed state is. The Fock state is not entangled in the sense that the *modes* k and $-k$ are not entangled. However, it is known that a Fock state enables one to achieve Heisenberg-limited interferometry measurement (Sahota and Quesada, 2015). It was also shown to outperform the (mode entangled) two-mode squeezed state in many configurations (Marolleau et al., 2024). For some authors, this *apparent lack of non-classicality* results from second quantization *hiding* entanglement. As pedagogically introduced by Morris et al. (2020), in first quantization, the $|1_e, 1_f\rangle$ state, in which we have one particle in state e and one particle in state f, is written

$$|\psi_{TF}\rangle = \frac{|f\rangle_1 |e\rangle_2 + |e\rangle_1 |f\rangle_2}{\sqrt{2}}. \tag{101}$$

Here, this state seems entangled because we labeled by 1 and 2 the indistinguishable particles and symmetrized the state. Such entanglement arising from particle exchange symmetrization is a nonsense for other authors and there are not yet a consensus on its nature (Köhnke et al., 2021). This paradox led therefore to the development of many definitions of entanglement (Modi et al., 2012) or new approaches to write states (Compagno et al., 2018), as reviewed by Benatti et al. (2020). Correlations arising from particle exchange symmetry are for example referred to by Morris et al. (2020) as "particle entanglement". Even though particle entanglement was shown to be "a useful and consistent resource", in the following, we will focus on mode entanglement *i.e.* states that do not satisfy equation (99) unless otherwise stated.

2.B The positive partial transpose criterion

Definition for arbitrary quantum state

In a pioneering work, Peres (1996) derived "a simple algebraic test, which is a necessary condition" for the separability of the state. This necessary condition was shown to be also sufficient for a 2x2 or 2x3 system by Horodecki et al. (1996) but not for 2x4 or 3x3 states by Horodecki (1997). Here, nxm refers to the size of the Hilbert space of each system. For example, the 2x3 refers to entanglement between a subsystem of size two and another one of size 3 (a spin 1/2 and spin 1). The criterion consists in checking if the partial transpose of the density matrix is positive or not. Writing the density matrix as $\rho_{m\mu,n\nu}$ such that latin indices refer to sub-system 1 and greek indices to sub-system 2. We define the partial transpose operation as

$$(\rho_{m\mu,n\nu})^{\mathsf{T}_2} := \rho_{m\nu,n\mu} \tag{102}$$

which only exchanged the greek indices of the later matrix i.e. transposed the subsystem 2.

> **Theorem - PPT criterion**
> The partial transpose of a density matrix of a separable state is positive. If the system is a 2x2 or 2x3 system, if the partial transpose of the state is positive, the state is separable.

Proof. For a separable density operator, the partial transpose operation is given by

$$\hat{\rho} = \sum_j p_j \hat{\rho}_{j1} \otimes \hat{\rho}_{j2} \quad \leftrightarrow \quad \hat{\rho}^{\mathsf{T}_2} = \sum_j p_j \hat{\rho}_{j1} \otimes \hat{\rho}_{j2}^{\mathsf{T}} \tag{103}$$

The matrices $\hat{\rho}_{j2}^{\mathsf{T}}$ are non-negative matrices with unit trace: they are legitimate density matrices for a quantum state. This implies that the density matrix $\hat{\rho}^{\mathsf{T}_2}$ is also a legitimate density matrix. The proof for the necessary condition can be found in Horodecki et al. (1996).

□

Simon says: it is entangled !

The PPT criterion is not *a priori* a criterion for a two-mode continuous variable system as it is a $\infty \times \infty$ system (and $\infty > 3$). However, Simon (2000) and Duan et al. (2000) showed that this entanglement witness is an entanglement criterion, that is a sufficient and necessary condition. This criterion is therefore often referred as GPH criterion, for Generalized Peres-Horodecki or gPPT for generalized PPT criterion. In the following, we keep the same notations as the one we used in the last section and we write

$$\boldsymbol{r} = \begin{pmatrix} x_1 \\ p_1 \\ x_2 \\ p_2 \end{pmatrix} \quad , \quad \boldsymbol{\sigma} = \begin{pmatrix} \boldsymbol{A} & \boldsymbol{C} \\ \boldsymbol{C}^\intercal & \boldsymbol{B} \end{pmatrix} \tag{104}$$

where the matrix $\boldsymbol{A}$ describes subsystem 1, $\boldsymbol{B}$ subsystem 2 and $\boldsymbol{C}$ the correlation between the two modes. With this notation, Simon (2000) showed the *bona fide* condition (73) can be recast in a simple inequality[4]

Theorem - Bona fide condition by Simon
The covariance matrix $\boldsymbol{\sigma}$ of a quantum state written as in equation (104) must respect the *bona fide* condition (73) $\boldsymbol{\sigma} + i\boldsymbol{\Omega} > 0$ that writes

$$\begin{aligned} \det[\boldsymbol{A}] + \det[\boldsymbol{B}] \leq \det[\boldsymbol{A}]\det[\boldsymbol{B}] + (1 - \det[\boldsymbol{C}])^2 \\ - \mathrm{Tr}\left(\boldsymbol{A}\boldsymbol{\Omega}_1\boldsymbol{C}\boldsymbol{\Omega}_1\boldsymbol{B}\boldsymbol{\Omega}_1\boldsymbol{C}^\intercal\boldsymbol{\Omega}_1\right). \end{aligned} \tag{105}$$

The PPT criterion requires the density matrix of the partial transposed state not to be positive to ensure entanglement. For a Gaussian state, this means that the covariance matrix does not respect the *bona fide* condition (105). How does the covariance matrix change under the partial transpose operation? Here again, Simon (2000) provides a remarkable interpretation of the partial transpose operation, interpreting it as "*a mirror reflection in the Wigner phase space*". Formally, under a partial transpose operation, the Wigner distribution is transformed as

$$W(x_1, p_1, x_2, p_2)^{\intercal_2} = W(x_1, p_1, x_2, -p_2) \tag{106}$$

In terms of matrices, the partial transpose corresponds therefore to multiplication by $\boldsymbol{\Lambda} = \mathrm{diag}(1, 1, 1, -1)$. The covariance matrix of the partially transposed state reads therefore

$$(\boldsymbol{\sigma})^{\intercal_2} = \boldsymbol{\Lambda}\boldsymbol{\sigma}\boldsymbol{\Lambda} = \begin{pmatrix} \boldsymbol{A} & \boldsymbol{C}\sigma_z \\ (\boldsymbol{C}\sigma_z)^\intercal & \sigma_z\boldsymbol{B}\sigma_z \end{pmatrix} \tag{107}$$

where σ_z is the third Pauli matrix diag(1,-1). PPT criterion states that a state is separable if and only if its partial transpose is positive. When plugging the covariance matrix of the partially transposed state, in the *bona fide* condition (105), it justs flips the sign of the term det$C$. Last but not least, Simon (2000) demonstrates that the generalized PPT criterion is not only sufficient but also necessary.

[4] When comparing inequality (105) to the one derived by Simon (2000), there is a factor 1/4 that differs which is due to the covariance matrix definition (1/2 factor).

Theorem - gPPT criterion by Simon
A Gaussian quantum state is separable if and only if $\mathcal{P}_- \geq 0$ where

$$\begin{aligned}\mathcal{P}_- :=& \det\boldsymbol{A}\det\boldsymbol{B} + (1 - |\det[\boldsymbol{C}]|)^2 - \det\boldsymbol{A} - \det\boldsymbol{B} \\ &- \mathrm{Tr}\left(\boldsymbol{A}\boldsymbol{\Omega}_1\boldsymbol{C}\boldsymbol{\Omega}_1\boldsymbol{B}\boldsymbol{\Omega}_1\boldsymbol{C}^\intercal\boldsymbol{\Omega}_1\right)\end{aligned} \tag{108}$$

The difference between Eq. (105) and (108) lies in the absolute value $|\det[\boldsymbol{C}]|$. Especially, any non-separable Gaussian state must respect the *bona fide* condition (105) while violating (108). In some sense, there is only a little place for entanglement.

Remark - Entanglement depends on the partition basis
Here, the quantity $\mathcal{P}_-$ depends on local symplectic invariants, which do not change under *local* transformation. However, we saw in the last section 1.C with Williamson decomposition (75) that it is always possible to decompose the covariance matrix on normal modes, that is a basis in which the state is made of two independent modes. It highlights the fact that entanglement depends on the basis, the choice of the partition. In a different basis, a two-mode squeezed state is simply two one-mode squeezed states. In this work, the partition is clear: subsystem A refers mode $-k$ and subsystem B to mode k.

Note that our discussion here relies on Gaussian states: the gPPT criterion derived is no longer necessary for non-Gaussian states.

2.C Logarithmic negativity

Deeply connected to the PPT criterion is the so-called logarithmic negativity (LN). It was shown by Vidal and Werner (2002) to be a faithfull measure of entanglement because "it does not increase under local manipulations of the system". This is particularly relevant in the frame of quantum communication (Plenio and Virmani, 2005) in which the theory of entanglement tries to understand "how well mixed quantum states can be converted to pure maximally entangled states and vice versa, by means of "free" physical operations that do not increase entanglement" (Wang and Wilde, 2020). This criterion is equivalent to the PPT criterion hence it is an entanglement *criterion* for bipartite quantum states. Also, LN was shown to be an entanglement monotone (Plenio, 2005) *i.e.* it can be used to *measure* entanglement and not only assess it. Starting from a thermal state, LN increases with the squeezing parameter while it decreases with the noise. In this regard, it enables one to identify in a physical process what causes entanglement, what destroys it and how much (Brady et al., 2022).

Theorem - Logarithmic negativity criterion
The logarithmic negativity, defined as

$$E_{\mathcal{N}}(\hat{\rho}) := \log_2 ||\hat{\rho}^{\intercal_2}||_1 \quad , \quad ||\hat{A}||_1 := \mathrm{tr}(\sqrt{\hat{A}^\dagger\hat{A}}) \tag{109}$$

that is the logarithm of the trace norm of the partial transpose of the density matrix[a] is an entanglement witness.

[a] Here $^{\intercal_2}$ refers to the partial transpose operation over sub-system 2.

Proof. The trace norm of an operator is the sum of the absolute value of its eigenvalues. For any quantum state $\hat{\rho}$, the sum of its eigenvalues is 1 and since it is semi-positive, that is all its

eigenvalues are positive or zero, the sum of the norm of its eigenvalues is also 1. Mathematically, if we write the eigenvalues of $\hat{\rho}$ as ν_i, we have

$$\begin{matrix}\mathrm{Tr}(\hat{\rho}) = 1 \\ \hat{\rho} \geq 0\end{matrix} \quad \rightarrow \quad \begin{matrix}\sum_i \nu_i = 1 \\ \forall i,\ \nu_i \geq 0\end{matrix} \quad \rightarrow \quad \sum_i |\nu_i| = 1 \tag{110}$$

If the partial transposed state $\hat{\rho}^{\intercal 2}$ is not positive, it has a negative eigenvalue. The partial transpose operation preserves the trace, therefore the sum of the eigenvalues of $\hat{\rho}^{\intercal 2}$ is also 1. However, this means that the sum of the absolute value of the eigenvalues is larger than 1. Therefore, the logarithmic negativity of this quantity is positive.

$$\begin{matrix}\mathrm{Tr}(\hat{\rho}^{\intercal 2}) = 1 \\ \hat{\rho}^{\intercal 2} \geq 0\end{matrix} \quad \rightarrow \quad \begin{matrix}\sum_i \tilde{\nu}_i = 1 \\ \exists i,\ \nu_i < 0\end{matrix} \quad \rightarrow \quad \sum_i |\nu_i| > 1 \quad \rightarrow \quad E_{\mathcal{N}}(\hat{\rho}) > 0 \tag{111}$$

□

For Gaussian states, the logarithmic negativity can be easily computed from the covariance matrix.

Theorem - Logarithmic negativity for a two-mode Gaussian states
For a Gaussian state, Adesso et al. (2004) showed that the smallest eigenvalue of the partial transpose of the covariance matrix $\tilde{\nu}_\pm$ "completely qualifies and quantifies the quantum entanglement of a Gaussian state $\boldsymbol{\sigma}$". The logarithmic negativity is

$$E_{\mathcal{N}}(\boldsymbol{\sigma}) = \max\left[0, -\log_2 \tilde{\nu}_-\right], \qquad \tilde{\nu}_\pm = \sqrt{\frac{\tilde{\Delta} \pm \sqrt{\tilde{\Delta}^2 - 4\det\boldsymbol{\sigma}}}{2}} \tag{112}$$

where $\tilde{\Delta} := \det(\boldsymbol{A}) + \det(\boldsymbol{B}) - 2\det(\boldsymbol{C})$ is a local symplectic invariant of the (partial transposed) covariance matrix.

The state is entangled if and only if $\tilde{\nu}_- \geq 1$ or equivalently $\tilde{\Delta} \leq 1 + \det\boldsymbol{\sigma}$.
Note that the *bona fide* condition for $\boldsymbol{\sigma}$ implies also that $\Delta \leq 1 + \det\boldsymbol{\sigma}$ (see equation (79))

For a two-mode squeezed vacuum state, the logarithmic negativity is given by

$$E_{\mathcal{N}}\left[|\mathrm{TMSv}\rangle\,(r)\right] = \frac{2r}{\log 2} \tag{113}$$

i.e. the logarithmic negativity increases with the squeezing parameter. We recover the fact that this state is always entangled for positive r. For a two-mode thermal state with initial population n_e (97), the logarithmic negativity is given by (Brady et al., 2022)

$$E_{\mathcal{N}} = \max\left(0, -\log_2\left((1+2n_e)e^{-2r}\right)\right) \tag{114}$$

which shows that LN increases with squeezing and decreases with the temperature environment. Entanglement vanishes if $1 + 2n_e > e^{2r}$. Given that the number of noise quanta is given by the Bose-Einstein distribution $n_e = 1/(e^{\omega/T_e} - 1)$, it is often introduced the *squeezing temperature* that is the temperature that satisfies

$$n_s = \frac{1}{e^{\omega/T_s} - 1}, \qquad n_s = \sinh^2 r. \tag{115}$$

The state is entangled if the environment temperature is lower than twice the squeezing temperature (Brady, 2023)

$$T_e < 2T_s. \tag{116}$$

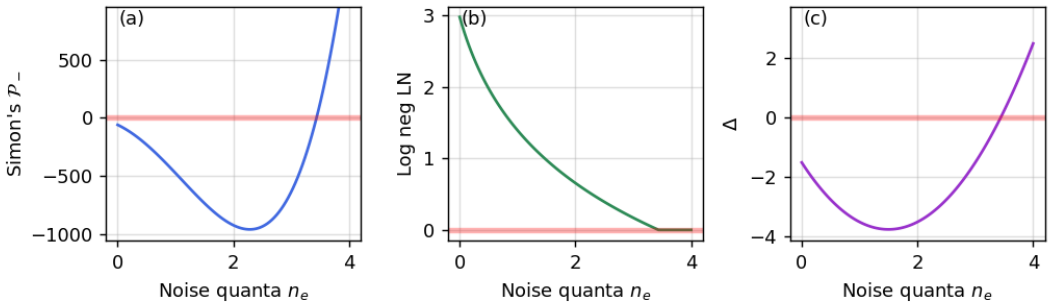

Figure 26: Variation of entanglement witnesses as a function of the environment noise. (a) Quantity $\mathcal{P}_-$ from Simon (2000) defined in equation (108), which is negative for entangled states. (b) Logarithmic negativity (109) and (c) the quantity Δ that will be described in the next section. This figure exhibits quite well the fact that the logarithmic negativity is an entanglement monotone and therefore a good quantifier of entanglement compared to the two other criteria. ©Figure inspired from Brady et al. (2022).

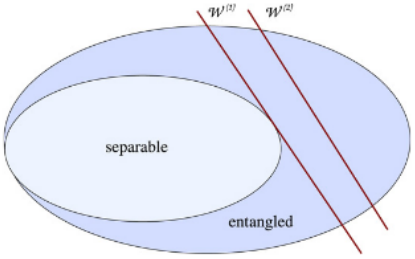

Figure 27: Schematic picture of the set of all states and the set of separable states as nested convex sets and two witnesses, $W^{(1)}$ and $W^{(2)}$. The red lines represent the hyperplanes where the witnesses fail to detect entanglement. Obviously, the first witness is finer than the second one. ©Figure from Gühne and Tóth (2009).

2.D Other (non-hermitian) entanglement witnesses

Since not all quantum states are Gaussian, other entanglement witnesses were derived to better capture entanglement. Much work focus on reviewing the existing entanglement criteria and witnesses. For a complete review, the interested reader might refer to the work by Horodecki et al. (2009) or Gühne and Tóth (2009). In this subsection, we focus on the Campo-Parentani criterion and its generalizations.

This criterion enables one to assess the separability of the state under some hypothesis. It seems that it was first introduced by Campo and Parentani (2005) when studying the mode decoherence to "describe the primordial fluctuations in inflationary scenarios".

Theorem - Campo-Parentani criterion - Δ criterion
Defining $\Delta = \langle \hat{n}_1 \rangle \langle \hat{n}_2 \rangle - |\langle \hat{a}_1 \hat{a}_2 \rangle|^2$ and assuming $\langle \hat{a}_1 \hat{a}_1 \rangle = \langle \hat{a}_2 \hat{a}_2 \rangle = 0$ and $\langle \hat{a}_1^\dagger \hat{a}_2 \rangle = 0$, a centered Gaussian state is entangled if and only if

$$\Delta < 0. \tag{117}$$

The proof for this criterion can be found in the appendix of Busch et al. (2014), but it will be

a special case of the criterion we will derive in section 4.E. Note that when the nullity of the condition listed above is not fulfilled, Δ is still an entanglement witness (Adamek et al., 2013). Indeed, it was shown by Hillery and Zubairy (2006) that

Theorem - Hillery-Zubairy witness
For any positive integer m and n, a separable state must satisfy the condition

$$\langle \hat{a}_1^m \hat{a}_2^n \rangle \leq \sqrt{\langle (\hat{a}_1^\dagger)^m \hat{a}_1^m \rangle \langle (\hat{a}_2^\dagger)^n \hat{a}_2^n \rangle} \tag{118}$$

The proof of this witness can be found in Hillery and Zubairy (2006) or in Adamek et al. (2013). Note also that the Hillery-Zubairy entanglement witness is a special case of the two-mode entanglement criterion defined by Shchukin and Vogel (2005).

Theorem - Shchukin-Vogel criterion
A quantum state is separable if and only if all the determinants

$$D_N = \begin{vmatrix} 1 & \langle \hat{a}_1 \rangle & \langle \hat{a}_1^\dagger \rangle & \langle \hat{a}_2^\dagger \rangle & \langle \hat{a}_2 \rangle & \dots \\ \langle \hat{a}_1^\dagger \rangle & \langle \hat{a}_1^\dagger \hat{a}_1 \rangle & \langle \hat{a}_1^{\dagger 2} \rangle & \langle \hat{a}_1^\dagger \hat{a}_2^\dagger \rangle & \langle \hat{a}_1^\dagger \hat{a}_2 \rangle & \dots \\ \langle \hat{a}_1 \rangle & \langle \hat{a}_1^2 \rangle & \langle \hat{a}_1^\dagger \hat{a}_1 \rangle & \langle \hat{a}_1 \hat{a}_2^\dagger \rangle & \langle \hat{a}_1 \hat{a}_2 \rangle & \dots \\ \langle \hat{a}_2 \rangle & \langle \hat{a}_1 \hat{a}_2 \rangle & \langle \hat{a}_1^\dagger \hat{a}_2 \rangle & \langle \hat{a}_2^\dagger \hat{a}_2 \rangle & \langle \hat{a}_2^2 \rangle & \dots \\ \langle \hat{a}_2^\dagger \rangle & \langle \hat{a}_2^\dagger \hat{a}_1 \rangle & \langle \hat{a}_2^\dagger \hat{a}_1^\dagger \rangle & \langle \hat{a}_2^{\dagger 2} \rangle & \langle \hat{a}_2 \hat{a}_2^\dagger \rangle & \dots \\ \vdots & \vdots & \vdots & \vdots & \vdots & \ddots \end{vmatrix} \tag{119}$$

are nonnegative that is

$$\forall N : \; D_N \geq 0. \tag{120}$$

This formulation is quite powerful as Simon's criterion is now a special case of this criterion, namely, it requires the D_5 determinant to be negative.

Remark - Other entanglement witnesses from the covariance matrix
Even when a state is not Gaussian, the covariance matrix elements of the quantum state can be used to find the *finest* witness. For example, Hyllus and Eisert (2006) developed an open source numerical routine to provide the user the best entanglement witness to look at given the covariance matrix of the bipartite state. More recently, Gessner et al. (2017) introduced a "multi-mode squeezing coefficient to characterize entanglement in N-particle CV system" from the covariance matrix, that applies also for non-Gaussian states. Zhang et al. (2021) also reported a "hierarchy of sufficient and necessary conditions for the PPT" of bipartite quantum states.

Summary In this section, we first defined entanglement and explain that, although there is a consensus on the notion of mode entanglement, it is still not the case for particle entanglement. Focussing now on mode entanglement, we defined the Positive Partial Transpose operation and showed that it is an entanglement witness. In the case of 2x2 and 2x3 system, this witness is a criterion *i.e.* it is not only sufficient but also necessary. This statement holds for two-mode Gaussian states. We then introduced the logarithmic negativity as a faithful entanglement quantifier. It is defined for any quantum state, but we gave its expression for a two-mode Gaussian state. In the last section, we introduce the Campo-Parentani criterion noted Δ. It allows one to assess Gaussian state entanglement under some hypotheses. We also saw that this quantity is still an entanglement witness relaxing some of those assumptions, as shown by Hillery and Zubairy.
However, the witnesses we introduced are either not hermitian operators or they require the measurement of the full density matrix. In other words, they cannot be measured with our single particle detector. In the next section, we will introduce two quantities, the normalized variance and the Cauchy-Schwarz ratio. They are hermitian and can be measured using a single particle detector: can they witness mode entanglement ?

3. On the Cauchy-Schwarz inequality and the normalized variance

We consider here the violation Cauchy-Schwarz inequality and the normalized variance as "witness candidates". They are particularly interesting because they have sparked much debate and controversy within the community. We discuss the range of applicability of these criteria and check numerically if they can be considered as entanglement witnesses or not.

3.A Relative number squeezing

Definition - Normalized number difference - normalized variance - relative number squeezing
We define the normalized relative number variance between two modes ξ as

$$\xi^2 := \frac{\langle \Delta\hat{n}^2 \rangle - \langle \Delta\hat{n} \rangle^2}{\langle \hat{n}_1 + \hat{n}_2 \rangle} \tag{121}$$

where $\Delta\hat{n} := \hat{n}_1 - \hat{n}_2$ is the number difference operator. When the normalized variance of a state drops below 1, we will say that such a state exhibits a sub-shot-noise variance or is relative number squeezed.

Indeed, in (121), the numerator is the relative number variance and the denominator is the sum of the population. If we consider a two-mode squeezed state $|\Psi\rangle \sim \sum_i \alpha^i |i\rangle_k |i\rangle_{-k}$, its normalized variance ξ is null and if the detector has an efficiency η, the normalized variance will be equal to $1 - \eta$.

Remark - Poissonian and thermal distribution.
The number variance of a state that exhibits single-mode Poissonian statistics p (coherent state) and a thermal statistics th (thermal state) are

$$\begin{aligned} \langle \hat{n}_p^2 \rangle - \langle \hat{n}_p \rangle^2 &= n_p, \\ \langle \hat{n}_{th}^2 \rangle - \langle \hat{n}_{th} \rangle^2 &= n_{th}^2 + n_{th}. \end{aligned} \tag{122}$$

where n_p and n_{th} refer to the mean of the distribution. This means in particular that the normalized number difference between two incoherent modes with the same mean population and Poissonian or thermal statistics are

$$\xi_{p,\,\text{incoh}} = 1, \qquad \xi_{th,\,\text{incoh}} = 1 + n_{th}. \tag{123}$$

In the 2000s, many BECs experiments reported the observation of number squeezing in BECs (Orzel et al., 2001; Gerbier et al., 2006). Among them, Estève et al. (2008) split a BEC in a double well and resolve the atom number in each well to demonstrate sub-shot-noise variance (121). In the case of spin squeezing, experiments rapidly demonstrated useful entanglement by showing phase sensitivity greater than the standard quantum limit (Gross et al., 2010; Lücke et al., 2011). A few years later, the same authors reported entanglement between two spatially separated atomic modes was (Lange et al., 2018; Fadel et al., 2018; Kunkel et al., 2018).

Other authors observed relative number squeezing between two momentum modes (Jaskula et al., 2010; Bücker et al., 2011). In their work, they do not claim entanglement which is quite understandable as a system of massive entangled particles is precisely the original EPR paradox. For those systems, a violation of Bell inequalities has not yet been observed, even thought promising experiment paved the way (Dussarrat et al., 2017; Thomas et al., 2022). In response to this observation and possible conclusions on entanglement, Finke et al. (2016) designed a classical model with the same physics at play, for which they observed sub-Poissonian variance. In their work, authors highlight the fact that the observation of sub-shot noise variance is not a proof of entanglement. In the next section, we will numerically test under what circumstances normalized variance and Cauchy-Schwarz inequalities fail to be faithful entanglement witnesses.

3.B Classical Cauchy-Schwarz inequality violation: a mode entanglement witness ?

Definition - Cauchy-Schwarz ratio
We define the Cauchy-Schwarz ratio $C_{\mathcal{S}}$ as (Walls and Milburn, 2008)

$$C_{\mathcal{S}} := \frac{\mathcal{G}_{12}}{\sqrt{\mathcal{G}_{11}\mathcal{G}_{22}}}, \qquad \mathcal{G}_{ij} := \langle : \hat{n}_i \hat{n}_j : \rangle \tag{124}$$

where the two dots ":" within the braket refers to normal order operators (Castin, 2011). Observation of $C_{\mathcal{S}} > 1$ will be referred to as violation of the classical Cauchy-Schwarz inequality.

Remark - On the importance of normal ordering
Without the normal ordering on the denominator of the Cauchy-Schwarz ratio, we always have

$$\langle \hat{n}_1 \hat{n}_2 \rangle < \sqrt{\langle \hat{n}_1^2 \rangle \langle \hat{n}_2^2 \rangle} \tag{125}$$

because of the *real* Cauchy-Schwarz inequality (61). Violation of the classical Cauchy-Schwarz inequality is only permitted by the fact that $\langle : \hat{n}_1^2 : \rangle = \langle \hat{n}_1^2 \rangle - \langle \hat{n}_1 \rangle$ *i.e.* by commutation rules. This is why we refer to $C_S > 1$ as a violation of the *classical* Cauchy-Schwarz inequality.

In quantum optics, the violation of the classical Cauchy-Schwarz inequality is recognized as a signature of the quantumness of the system (Reid and Walls, 1986). However, experimental observation of violation of the Cauchy-Schwarz inequality in cold atom experiments (Kheruntsyan et al., 2012; Steinhauer, 2014, 2016) led to many criticisms concerning the conclusion on the non-separability of the state. Using Wick's theorem[5] and assuming $\langle \hat{a}_i^2 \rangle = \langle (\hat{a}_i^\dagger)^2 \rangle = 0$,

$$\begin{aligned} \mathcal{G}_{12} &= n_1 n_2 + |\langle \hat{a}_1 \hat{a}_2 \rangle|^2 + |\langle \hat{a}_1 \hat{a}_2^\dagger \rangle|^2, \\ \mathcal{G}_{11} &= 2n_1^2, \\ \mathcal{G}_{22} &= 2n_2^2, \end{aligned} \tag{126}$$

so that the Cauchy-Schwarz ratio reads

$$C_S = \frac{1}{2}\left(1 + \frac{|\langle \hat{a}_1 \hat{a}_2 \rangle|^2}{n_1 n_2} + \frac{|\langle \hat{a}_1 \hat{a}_2^\dagger \rangle|^2}{n_1 n_2}\right). \tag{127}$$

If one assumes that the last term in this equation is null, observing $C_S > 1$ implies $|\langle \hat{a}_1 \hat{a}_2 \rangle|^2 > n_1 n_2$ which implies entanglement. This is the proposal of Steinhauer (2015) and De Nova et al. (2014). However, violation of the classical Cauchy-Schwarz inequality cannot be considered as an unambiguous proof for mode entanglement because of the above assumption. This is for example discussed by Nova et al. (2015).

Another drawback was pinpointed by Finke et al. (2016). When measuring the atom number through the intensity of a fluorescence signal, one has access to the intensity of the signal I_j. Averaging this intensity over realizations gives the mean atom number $\langle \hat{n}_j \rangle = \bar{I}_j$ after proper calibration. Here the bar means average over many realizations. When one evaluates the Cauchy-Schwarz ratio, the denominator is therefore defined as $\bar{I}_j^2 - \bar{I}_j$ which means that the bosonic commutation rules are put *by hand*. As underlined in the remark above, it is this subtraction and the commutation rules that allows one to witness $C_S > 1$.

Remark - Link between relative number squeezing and the classical Cauchy-Schwarz inequality
Under the same hypothesis we have made, we can link the Cauchy-Schwarz ratio and the relative number squeezing

$$\xi^2 = 1 + 2\sqrt{\mathcal{G}_1 \mathcal{G}_2}\frac{1 - C_S}{n_1 + n_2} + \frac{n_1^2 + n_2^2 - 2n_1 n_2}{n_1 + n_2}, \tag{128}$$

[5] Wick's theorem will be defined in the next section 4.A.

which emphasizes that

1. when the populations are equal, relative number squeezing and the classical Cauchy-Schwarz violation are equivalent,
2. when the populations are different, the term on the right is positive: it is possible to observe a violation of the classical Cauchy-Schwarz inequality but not relative number squeezing. In other words, relative number squeezing is in this case harder to observe[a],
3. $C_S \leq 1/\max(n_1, n_2)$, which is required by the *real* Cauchy-Schwarz inequality (61), implies that we do have $\xi^2 > 0$.

[a] This is only true because we assume we have a centered Gaussian state for which Wick's theorem applies. In other words, relative number squeezing is harder to observe only when the statistics are thermal, i.e. $\langle \hat{n}^2 \rangle = 2n^2 + n$. It is not the case for a displaced state *i.e.* a coherent state.

Conclusion: We can link a violation of the classical Cauchy-Schwarz inequality and mode entanglement when

1. the state is Gaussian,
2. the state is centered $\langle \hat{a}_i \rangle = \langle \hat{a}_i^\dagger \rangle = 0$,
3. each thermal mode is not squeezed: $\langle \hat{a}_i^2 \rangle = \langle (\hat{a}_i^\dagger)^2 \rangle = 0$,
4. the coherence between the terms is zero $\langle \hat{a}_1 \hat{a}_2^\dagger \rangle = 0$,

3.C Cauchy-Schwarz inequality and particle entanglement

As we saw, only strict assumptions allow one to link the classical Cauchy-Schwarz inequality violation and mode entanglement. A different route is suggested by other authors, assuming the so-called superselection rule (SSR).

Definition - Superselection rule
The superselection rule (Wick et al., 1952) is that a state of massive bosons cannot have a fluctuating number of particles. It must be diagonal in the total number operator basis $\hat{N}$ *i.e.* $[\hat{\rho}, \hat{N}] = 0$. This implies that the most general quantum state for a system of identical bosonic particles (photons or atoms) can only be of the form (Dalton et al., 2017)

$$\hat{\rho} = \sum_{N=0}^{\infty} \sum_{\phi} P_{\phi,N} \left|\phi_N\right\rangle \left\langle\phi_N\right|, \qquad \left|\phi_N\right\rangle = \sum_i C_i^N \left|N\, i\right\rangle \tag{129}$$

where $|\phi_N\rangle$ is a quantum superposition of states $|N\, i\rangle$, labelled by i, which involves exactly N particles.

Theorem - Cauchy-Schwarz violation witness
Both for a system with a fixed or fluctuating number of particles, it was shown by Wasak et al. (2014) that defining two (arbitrarily chosen) regions X_a and X_b and defining

$$\mathcal{G}^{(2)}_{ij} := \int_{X_i} \mathrm{d}r \int_{X_j} \mathrm{d}r' \, \langle \hat{\Psi}^\dagger(r)\hat{\Psi}^\dagger(r')\hat{\Psi}(r)\hat{\Psi}(r')\rangle \tag{130}$$

and

$$C_{\mathcal{S}} := \frac{\mathcal{G}^{(2)}_{ab}}{\sqrt{\mathcal{G}^{(2)}_{aa}\mathcal{G}^{(2)}_{bb}}}, \tag{131}$$

violation of $C_{\mathcal{S}} \leq 1$ implies *particle* entanglement.

The proof for this witness can be found in the previous reference. It relies on SSRs. Note that a twin-Fock state does violate this criterion: it is therefore particle entangled as we discussed in the previous section (Killoran et al., 2014). As the second order correlation function decreases when the population decreases, the Cauchy-Schwarz ratio converges to 1 when the number of particles increases. This is in contradiction with the potential utility of the state: the bigger the twin-Fock state is, the more useful the state is for interferometry measurement. In this sense, the quantity $C_{\mathcal{S}}$ does not increase with the usefulness of the state (Wasak et al., 2016).

3.D Numerical test to check mode entanglement

In this section, we come back to mode entanglement. We saw that the Cauchy-Schwarz inequality and the normalized variance are faithful mode entanglement witnesses under (some) hypotheses. Here, we would like to relax the hypothesis that the coherence term $\langle \hat{a}_1 \hat{a}_2^\dagger \rangle$ is null and check numerically if this relaxation prevents C_S from being a faithful entanglement witness. Our procedure is the following and is summarized in Figure 28 (a). We represent the space of separable and non-separable states with different projections (x and y axis) and we plot the hyperplane of three different witnesses (C_S,ξ and Δ). Our goal is to push entanglement witnesses to their limit. Importantly, an entanglement witness can fail to detect entanglement but must never falsely claim that a state is entangled when it is not. Somehow, a (faithful) entanglement witness has sworn to the (holy) entanglement criterion (judge) that it will never lie. Geometrically, this means that the hyperplane defined by an entanglement witness must never cut the separable region.

In Figure 28, we focus on relative simple quantum states : two-mode squeezed on a thermal seed or on a single mode squeezed thermal state. In Figure 29, we push forward and test Gaussian states that I did not build from a physical process (I do not have a protocol to create them). Still they exist and should be considered.

Description: the blue color-scale represents the logarithmic negativity *i.e.* it quantifies entanglement. The bluer, the more entangled. The white region filled with grey dots is the region where lie separable states. The separable region is split from the entanglement region by the solid black curve that is the gPPT criterion. The dashed-dotted pink curve is the Δ quantity from the Campo-Parentani witness. The dashed blue and orange dotted curves represent respectively the Cauchy-Schwarz ratio (131) and the normalized variance (124).

On the three panels represented in Figure 28, we do not observe any witness curve in the separable region. This means that, so far, the possible entanglement witnesses cannot be rejected.

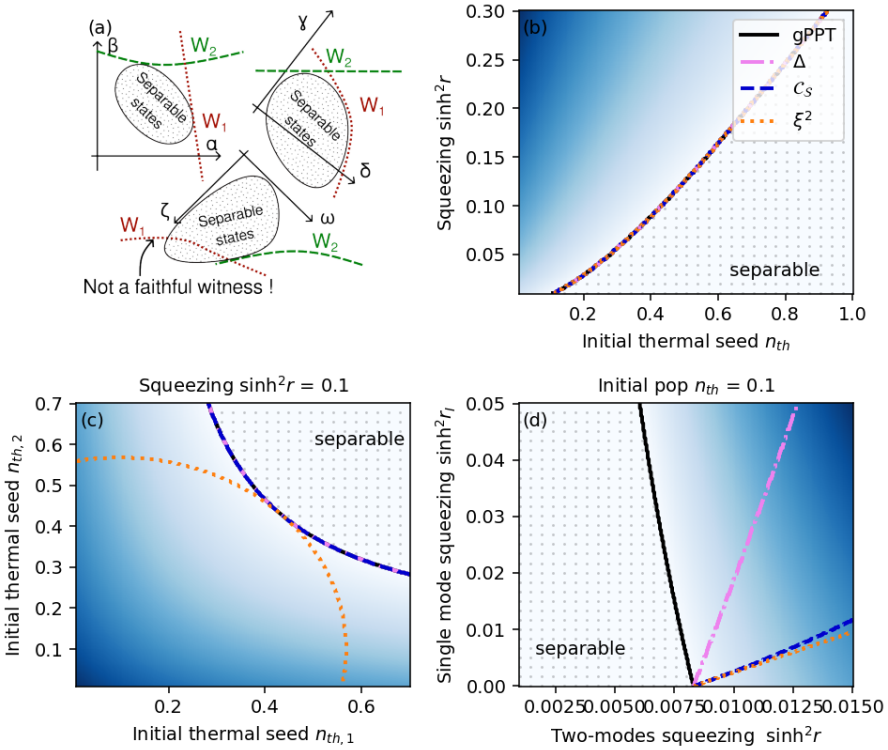

Figure 28: (a) Scheme of our procedure: we project the space of separable states along different directions and make sure entanglement witnesses never cut this space. (b-d) Comparison of the accuracy and faithfulness of entanglement witnesses. White region with grey dots is the separable region, surrounded by the gPPT criterion (solid black). On (c), the normalized variance (orange dotted) fails more often than the other to detect entanglement. On (d) all witnesses are not really sensitive to detect entanglement. However, witnesses do not enter the separable space: they do not lie and cannot be rejected.

On the y-axis of the panel (b) lies the squeezing parameter and the initial thermal seed on the x-axis. On this panel, all curves lie on the PPT curve, which means that the witnesses are all correct and accurate. On the panel (c), the two-mode squeezing parameter r is fixed, however the initial thermal seed is changed and is different for each mode: the thermal seed is the same only on the diagonal. Here, the normalized variance is much less accurate as it fails to detect entanglement when the population between the two modes strongly differs. This is what we remarked from equation (128): the normalized variance is less accurate when there is population imbalance between the two modes. The last plot was used as a benchmark to probe the robustness of the witnesses. On the y-axis lies the strength r_I of the single-mode squeezer that was applied to mode 1, while the x-axis represents the two-mode squeezing parameter (applied after the one mode squeezing operation). Here, all witnesses fail to detect entanglement accurately, but none of them lies in the separable region. Note that in the last panel, $|\langle \hat{a}_1 \hat{a}_2^\dagger \rangle| \neq 0$ which means that remarkably, while the Cauchy-Schwarz ratio fails to detect entanglement, it does not lie.

To push the limit of the Cauchy-Schwarz bounds, we now focus on states where $|\langle \hat{a}_1 \hat{a}_2^\dagger \rangle| \neq 0$. In Figure 29, we work with a mean number of particles: 0.2 on the left subplot and 2.2 on the right subplot (taken equal for both modes) and change the correlation between

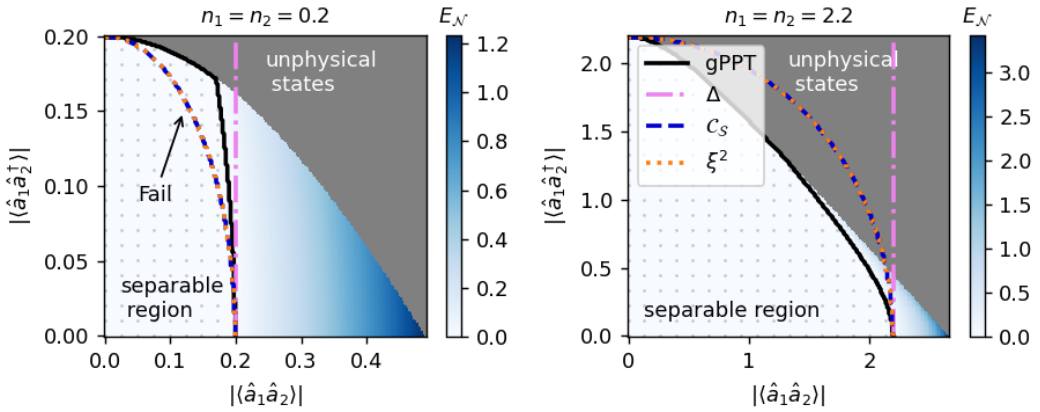

Figure 29: Failure of the Cauchy-Schwarz ratio $C_\mathcal{S}$ (dashed blue) and the normalized variance ξ (dotted orange) to reliably witness entanglement. For these plots, the population was kept constant ($n = 0.2$ on the left and $n = 2.2$ on the right) while the correlation between the modes was changed, namely $|\langle \hat{a}_1 \hat{a}_2 \rangle|$ on the x axis and $|\langle \hat{a}_1 \hat{a}_2^\dagger \rangle|$ on the y axis. Depending on the value of these operators, the state can be separable (on the left) or entangled (on the right).

the modes: $|\langle \hat{a}_1 \hat{a}_2 \rangle|$ on the x-axis and $|\langle \hat{a}_1 \hat{a}_2^\dagger \rangle|$ on the y-axis. These values are bounded: the grey region on the plot corresponds to an unphysical region where the Gaussian state does not satisfy the *bona fide* condition (105). The witnesses were prolonged in this region, but this does not mean they should be rejected. Here again, the gPPT criterion splits the space in two: separable states lie on the left, and entangled states lie on the right of the map.

On the left panel, the normalized variance and the Cauchy-Schwarz ratio lines are inside the separable region. This is problematic because it means they incorrectly identify a non-entangled state as entangled. In this sense, they *cannot be considered as mode entanglement witnesses when we relax the* $|\langle \hat{a}_1 \hat{a}_2^\dagger \rangle| \neq 0$ *hypothesis*. However, when the population is greater, we observe that they do not *lie* anymore: they are inside the entangled region. This is a taste of the next section: we will demonstrate that $C_\mathcal{S}$ is a faithful entanglement witness for sufficiently large population.

On the other hand, the Campo-Parentani witness Δ is represented by the (vertical) dashed-dotted pink line and lies entirely in the entangled region. It is not surprising as Δ was (mathematically) demonstrated to be a faithful entanglement witness. Here we observe again that it misses detecting the entanglement of some states, even if this region is small. This is expected, as one of the conditions for it to be a criterion is when $|\langle \hat{a}_1 \hat{a}_2^\dagger \rangle| \neq 0$.

Summary In this section, we defined and studied the normalized variance and the Cauchy-Schwarz ratio $C_\mathcal{S}$. The latter was shown to be a particle entanglement witness, and we showed that under some assumptions, it is also a mode entanglement witness. However, once one of the assumptions was relaxed ($|\langle \hat{a}_1 \hat{a}_2^\dagger \rangle| \neq 0$), the Cauchy-Schwarz ratio incorrectly identified a separable state as entangled, making it impossible to rely on with certainty. When the population was higher, we observed that they no longer lie in the separable region. Could they be more reliable in this case? As we shall see, for sufficiently high populations, they are: this will be the topic of the next section. Indeed, as Chris uses to say:
"But there's got to be something, I mean, it's hard to beat the shot noise!"

4. Assessing the degree of entanglement of thermal Gaussian states with 2- and 4-body correlation functions

In this section, we explain how the second order correlation function can be used to witness entanglement and separability. We also show that if one has access to the fourth order correlation function, it is possible to assess the non-separability of the state. In other words, we show that the measurement of the populations and the second and fourth order correlation functions provides an entanglement **criterion** for thermal Gaussian states. Finally, we show that this measure gives access to the symplectic spectrum of the state and therefore quantifying entanglement, using the logarithmic negativity for example.

4.A What information can correlation functions say about the covariance matrix ?

Theorem - Wick-Isserlis theorem
For a Gaussian state with zero mean, the expectation value of any operator reads (Wick, 1950; Isserlis, 1918)

$$\langle \hat{b}_1 \hat{b}_2 ... \hat{b}_N \rangle = \sum_{\text{binary contractions}} \langle \hat{b}_1 \hat{b}_\alpha \rangle \langle \hat{b}_\beta \hat{b}_\gamma \rangle ... \langle \hat{b}_\zeta \hat{b}_\omega \rangle \tag{132}$$

and is zero if the number of operators is odd.

The proof for this theorem and a nice discussion on its non applicability for the BEC condensed mode can be found in Castin (2011). In particular, the Wick theorem under this form *only applies to zero mean Gaussian states* and therefore not for coherent states (displaced vacuum states). With a micro-channel plate, we measure the mode occupancy and any n order correlation functions. We also measure the *normal ordered field operators*[6] in the sense of Glauber (1963b). Especially, we have access to the mode population and the second order correlation functions

$$n_i := \langle \hat{a}_i^\dagger \hat{a}_i \rangle , \qquad g_{ij}^{(2)} := \frac{\langle \hat{a}_i^\dagger \hat{a}_j^\dagger \hat{a}_i \hat{a}_j \rangle}{\langle \hat{a}_i^\dagger \hat{a}_i \rangle \langle \hat{a}_j^\dagger \hat{a}_j \rangle}. \tag{133}$$

We now assume the state has zero mean, *i.e.* we do not treat the $k = 0$ condensed mode. With that assumption, we introduce the following (complex) quantities

$$\alpha_i := \langle \hat{a}_i^2 \rangle \qquad c := \langle \hat{a}_1 \hat{a}_2 \rangle \qquad d := \langle \hat{a}_1 \hat{a}_2^\dagger \rangle . \tag{134}$$

Those quantities fully determine the covariance matrix which reads

$$\boldsymbol{A} = \begin{pmatrix} 2n_1 + 1 + 2\mathcal{R}(\alpha_1) & 2\mathcal{I}(\alpha_1) \\ 2\mathcal{I}(\alpha_1) & 2n_1 + 1 - 2\mathcal{R}(\alpha_1) \end{pmatrix}$$

$$\boldsymbol{\sigma} = \begin{pmatrix} \boldsymbol{A} & \boldsymbol{C} \\ \boldsymbol{C}^\intercal & \boldsymbol{B} \end{pmatrix} \qquad \boldsymbol{B} = \begin{pmatrix} 2n_2 + 1 + 2\mathcal{R}(\alpha_2) & 2\mathcal{I}(\alpha_2) \\ 2\mathcal{I}(\alpha_2) & 2n_1 + 1 - 2\mathcal{R}(\alpha_2) \end{pmatrix} \tag{135}$$

$$\boldsymbol{C} = \begin{pmatrix} 2\mathcal{R}(c+d) & 2\mathcal{I}(c-d) \\ 2\mathcal{I}(c+d) & 2\mathcal{R}(-c+d) \end{pmatrix},$$

[6] We describe the measure with a micro-channel plate reproducing Glauber's work in the fourth chapter.

where $\mathcal{I}(x)$ and $\mathcal{R}(x)$ refers to the imaginary and real parts of x. Using Wick expansion, one can show that the second order correlation functions is

$$g_{ii}^{(2)} = 2 + \frac{|\alpha_i|^2}{|n_i|^2}. \tag{136}$$

In other words, if one finds that the second order correlation function is two, this implies that $\alpha_i = 0$. In the following, we will assume this is the case. This assumption is motivated by the fact that it is what we expect from the Hamiltonian seen in the first chapter. It is also observed experimentally: it was reported in different configurations (but still with the same physics at play) by other authors (Dall et al., 2013; Perrier et al., 2019; Hercé et al., 2023). This assumption greatly simplifies the covariance matrix which reads

$$\begin{gathered} \boldsymbol{A} = (2n_1 + 1)\mathbb{I}_2 \qquad \boldsymbol{B} = (2n_2 + 1)\mathbb{I}_2 \\ \boldsymbol{C} = \begin{pmatrix} 2\mathcal{R}(c+d) & 2\mathcal{I}(c-d) \\ 2\mathcal{I}(c+d) & 2\mathcal{R}(-c+d) \end{pmatrix}. \end{gathered} \tag{137}$$

We can now consider the second-order cross correlation function

$$g_{12}^{(2)} = \frac{n_1 n_2 + |c|^2 + |d|^2}{n_1 n_2}. \tag{138}$$

If we *assume* $d = \langle \hat{a}_1 \hat{a}_2^\dagger \rangle = 0$, *i.e* that we directly measure the pure correlation term $|c|$, an observation of $g_{12}^{(2)} > 2$ implies entanglement. The $d = 0$ assumption implies we exactly measure Δ: this is the Campo-Parentani criterion, defined in section 2.D. In section 4.B, we relax the $d = 0$ assumption and show that that the second order correlation function still witnesses entanglement.

4.B The second order correlation function to probe non-separability

As introduced in the first section, because $\hat{\rho}$ is positive definite, the Cauchy-Schwarz inequality (61) implies that $\forall \hat{A}, \hat{B}$, $|\langle \hat{A}^\dagger \hat{B} \rangle|^2 \leq \langle \hat{A}^\dagger \hat{A} \rangle \langle \hat{B}^\dagger \hat{B} \rangle$. We can use this inequality with $\hat{a}_1$ and $\hat{a}_2$ to show that (Robertson, 2021)

$$\begin{aligned} |d|^2 = |\langle \hat{a}_1 \hat{a}_2^\dagger \rangle|^2 &\leq n_1 n_2 \\ |c|^2 = |\langle \hat{a}_1 \hat{a}_2 \rangle|^2 &\leq n_1 n_2 + n_1 \\ &\leq n_1 n_2 + n_2. \end{aligned} \tag{139}$$

We can express the modulus of c as a function of the second order correlation function (138)

$$|c|^2 = (g_{12}^{(2)} - 1) n_1 n_2 - |d|^2 \tag{140}$$

From the Cauchy-Schwarz inequality (139), we have $|d|^2 < n_1 n_2$ which means that

$$|c|^2 \geq (g_{12}^{(2)} - 2) n_1 n_2 \tag{141}$$

If $g^{(2)} > 3$, this means that $|c|^2 > n_1 n_2$ and therefore that the state is entangled. As a conclusion, $g^{(2)} > 3$ implies entanglement. This bound is however really constraining: for an ideal two-mode squeezed vacuum state, the second order correlation function is $2 + 1/n$ where n is the population of one mode. Therefore, this $g^{(2)} > 3$ bound allows us to witness entanglement only for low population *i.e.* for $n < 1$.

The defect of this entanglement witness is due to the fact that the increase we took for $|d|$ is the highest possible: $n_1 n_2$. We also assumed that a non-zero value of d cannot participate in the non-separability. We now find a more constraining bound on $|d|$ to derive the following "$g^{(2)}$ entanglement witness".

Theorem - g2 entanglement witness

Assuming that the state is Gaussian with zero mean ($\langle \hat{a}_i \rangle = 0$) and that $|\hat{a}_1^2| = |\hat{a}_2^2| = 0$[a] the two-mode state 1-2 is entangled if $g_{12}^{(2)}$ is slightly above 2. In particular,

- if $n_1 n_2 \geq 1/2$, then $g_{12}^{(2)} > 2$ is a sufficient condition,
- if $n_1 n_2 < 1/2$, the threshold for $g_{12}^{(2)}$ is shifted and the sufficient condition for non-separability reads

$$g_{12}^{(2)} > 2 + \frac{1/2 - n_1 n_2}{2n_1 n_2 + n_1 + n_2 + 1/2} \,. \tag{142}$$

[a] Here again I want to stress that this is not only an assumption: it can be checked experimentally.

Proof. As we assumed the state is Gaussian, the gPPT criterion assesses the non-separability of the state. It is entangled if and only if Simon's quantity $\mathcal{P}_-$ defined in equation (108) is negative (Simon, 2000). In our case, this quantity reads

$$\begin{aligned} \mathcal{P}_- = 16\Big[&(1+n_1)(1+n_2)(n_1 n_2 - |d|^2 - |c|^2) \\ &+ \left(\frac{1}{2} - n_1 n_2\right)\left(|d|^2 + |c|^2\right) \\ &+ (|c|^2 - |d|^2)^2 - \frac{1}{2}\big||c|^2 - |d|^2\big|\Big]. \end{aligned} \tag{143}$$

In this expression, we grouped the terms involving the sum $|d|^2 + |c|^2$: they are known through the value of $g_{12}^{(2)} = 1 + (|c|^2 + |d|^2)/n_1 n_2$. The *a priori* unknown quantity is the difference $|c|^2 - |d|^2$. This proof consists of showing that this value is bounded and that it cannot be arbitrarily large: this quantity cannot change too much the sign of $\mathcal{P}_-$.
As stated in equation (139), the value of $|c|^2$ and $|d|^2$ are bounded by $n_1 n_2 + n_1$ and $n_1 n_2$. Here we consider that $n_1 \leq n_2$ without loss of generality, not to make the discussion more cumbersome. We can therefore define δ such that

$$\big||c|^2 - |d|^2\big| := \delta n_1 n_2, \qquad \delta \in \Big[0, 1 + \frac{1}{n_2}\Big]. \tag{144}$$

With that notation, the entanglement criterion $\mathcal{P}_-$ reads

$$\begin{aligned} \mathcal{P}_- = 16 n_1 n_2\Big[&(1+n_1)(1+n_2)(2 - g_{12}^{(2)}) \\ &+ \left(\frac{1}{2} - n_1 n_2\right)\left(g_{12}^{(2)} - 1\right) \\ &+ \delta\left(n_1 n_2 \delta - \frac{1}{2}\right)\Big]. \end{aligned} \tag{145}$$

Assume the sum of the first line is negative: the state is entangled if the last term $\delta(n_1 n_2 \delta - 1/2)$ is not too large. The question we are interested in here is: what is the highest value of

$\delta(n_1n_2\delta - 1/2)$ so that $\mathcal{P}_-$ is negative without it and positive when taking it into account. We look for an upper bound for $\delta(n_1n_2\delta - 1/2)$.

We first prove that we can take $\delta \leq 1$ by absurdity. Let's assume a state is such that $\mathcal{P}_- \geq 0$ and $\delta > 1$. The latter condition implies from (144) that either $|c|^2 > n_1n_2$ or $|d|^2 > n_1n_2$. This second possibility is impossible because of the Cauchy-Schwarz inequality (139). We therefore must have that $|c|^2 > n_1n_2$. This last inequality implies that the state is entangled as it is the Hillery-Zubairy witness. Inequality $\mathcal{P}_-$ is not only sufficient but necessary for entanglement: it must therefore be negative. We conclude that it is not possible to have a state for which $\delta > 1$ and $\mathcal{P}_- \geq 0$ and we can restrict our analysis to $\delta \in [0, 1]$.

The maximum of the quantity $\delta(n_1n_2\delta - 1/2)$ depends on the population. We are therefore left to distinguish two cases, depending on the population n_1n_2.

If $n_1n_2 < 1/2$, the last parenthesis of equation (145) is always negative thus an upper bound for $\mathcal{P}_-$ is obtained for $\delta = 0$. Negativity of the first two lines *implies* negativity of $\mathcal{P}_-$ and therefore non-separability. A bit of algebra leads then to the critical value in equation (142) for the second order correlation function $g^{(2)}_{12}$ to ensure non-separability.

If $n_1n_2 > 1/2$, this last term might increase $\mathcal{P}_-$ and we must consider the case where it could be maximal, that is when $\delta = 1$. When doing so, the two last lines simplify and factorize as

$$\begin{aligned}\mathcal{P}_- \leq 16n_1n_2\Bigg[&(1+n_1)(1+n_2)\left(2 - g^{(2)}_{12}\right)\\ &+\left(n_1n_2 - \frac{1}{2}\right)\left(2 - g^{(2)}_{12}\right)\Bigg].\end{aligned} \tag{146}$$

We see that we have a positive term that is multiplied by $2 - g^{(2)}_{12}$. We conclude that in this case, $g^{(2)}_{12} > 2$ implies non-separability.

□

In Figure 30, we represented the threshold value for $g^{(2)}$ given by equation (142). This threshold reaches 3 in the limit of vanishing population: we recover the threshold discussed in the introduction.

Consequence on the Cauchy-Schwarz inequality The shift of the $g^{(2)}$ non-separability bound shifts as well the Cauchy-Schwarz ratio C_S bound. For a population larger than 0.7, the observation of $C_S \geq 1$ does not need to assume anymore the vanishing coherence of the $\langle \hat{a}_1\hat{a}_2^\dagger \rangle$ term. For a lower population, the bound of the non-separability threshold is just increased as half of equation (142) *i.e.* the bound for C_S shifts from 1 to 1.5.

4.C The second order correlation function to probe separability

We can also take advantage that $\mathcal{P}_-$ is an entanglement criterion to derive a bound for $g^{(2)}_{12}$ to ensure separability of the state. The derivation will exactly follow the proof of the $g^{(2)}$ non-separability witness, but this time in finding decrease for δ so that $\mathcal{P}_s$ is positive.

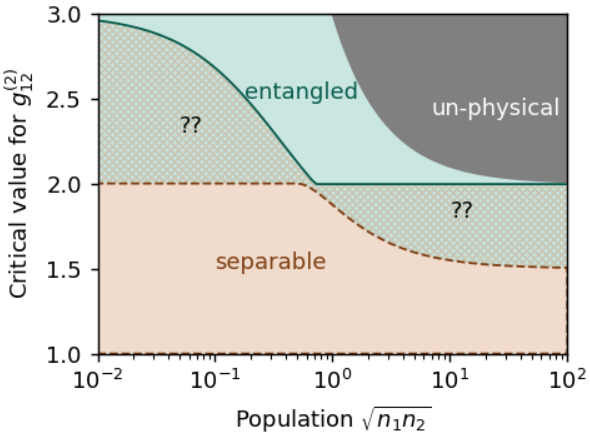

Figure 30: Critical value for the second order correlation function to assess non-separability and separability of the bipartite state 1-2. The maroon dashed curve corresponds to the separability witness: any state lying below this curve is separable. The solid green curve and the area above represents a region where states are entangled. In between these two curves, it is not possible to assess the separability of the state using only the population in each modes and the second order correlation function. The un-physical limit corresponds to a value of $g^{(2)}$ greater than the one of a two-mode squeezed state. It is $2 + 1/n$ where n is the mode population.

Theorem - g2 maximal bound for separability

Assuming that the state is Gaussian and that $\langle \hat{a}_i \rangle = \langle \hat{a}_i^2 \rangle = 0$, the two-mode state 1-2 is separable if $g_{12}^{(2)}$ is slightly below 2. Especially,

- if $n_1 n_2 \leq 1/4$, then $g_{12}^{(2)} < 2$ is a sufficient condition,
- if $n_1 n_2 \geq 1/4$, the threshold for $g_{12}^{(2)}$ is shifted and the sufficient condition for separability reads

$$g_{12}^{(2)} < 2 - \frac{(1 - 4n_1 n_2)^2}{8n_1 n_2 (1 + 2n_1)(1 + 2n_2)} \,. \tag{147}$$

which asymptotically reaches 1.5.

Proof. The proof follows the same recipe as the one for the $g^{(2)}$ entanglement witness. The difference is that we now look for a lower bound for $\mathcal{P}_-$. The minimum of the $\mathcal{P}_-$ polynomial is reached for $\delta = 1/4n_1 n_2$. The value for the separability lower bound is bounded by 2, which is the value when $d = 0$. As a result, δ is bounded by 1. We are therefore left with the following values for δ:

- if $n_1 n_2 \leq 1/4$, the lower bound for the gPPT criterion is obtained by replacing δ by 1 in equation (145) which leads immediately to the critical value of 2 for $g_{12}^{(2)}$.
- if $n_1 n_2 \geq 1/4$, the minimum is reached for $\delta = 1/4n_1 n_2$. Inserting this value in equation (145) leads after some algebra to the critical value for the second order correlation function given by equation (147).

□

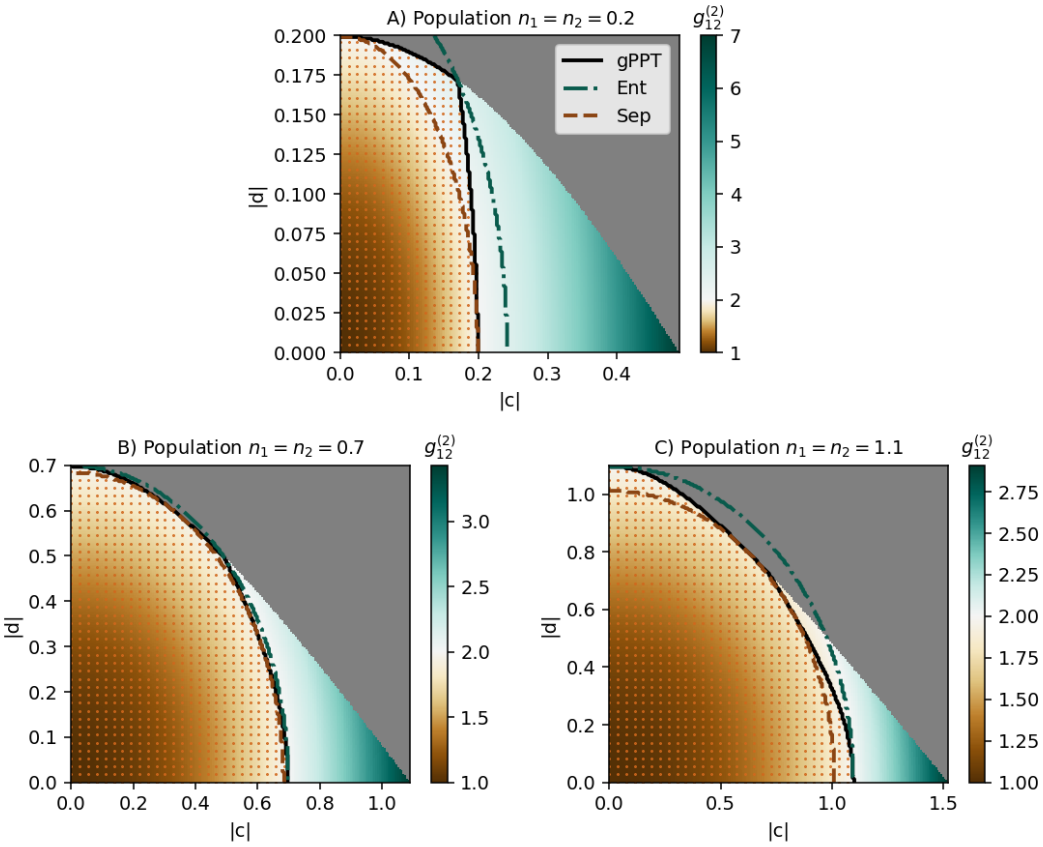

Figure 31: Colormap of $g^{(2)}$ for Gaussian states in the (c, d) plane for different mean population (see title). The grey region represents unphysical Gaussian states. Black solid curve is the gPPT criterion, brown dashed line the $g^{(2)}$ separable witness threshold and the blue dashed-dotted curve is the non-separability witness threshold.

4.D Graphical resolution of the $g^{(2)}$ witness

Figure 31 provides a graphical illustration of the separable and non-separable bounds. We represent the second order correlation function on the (c, d) map at fixed population. The color encodes the value of $g^{(2)}$ and the solid black curve is the gPPT criterion. On the left of the figure lie separable states and on the right entangled states. The grey region represents unphysical states. The form of the $g^{(2)}$ curves (solid dashed green and dashed brown) drawn gives a glimpse of the behavior of iso-$g^{(2)}$ curves on this plan. We can interpret the different regimes (small and high populations) in terms of convexity of the gPPT curve in the $(|c|, |d|)$ plane, and compare it to the convexity of the iso-$g^{(2)}$ curves. When the population is low (top panel), the iso-$g^{(2)}$ curves are more convex than the gPPT curve. As a result, the threshold value of $g^{(2)}$ to certify entanglement is given by the value of $g^{(2)}$ at the top corner, for which $d \neq 0$. For higher population - bottom right panel C - we observe that the gPPT curve is more convex than the iso-$g^{(2)}$. It is therefore the value at the bottom of the graph that fixes the minimum value for $g^{(2)}$. In this case, entanglement is certified by $g^{(2)} > 2$.

4.E Second and fourth order correlation function as an entanglement criterion

It was proposed by Clément (2022) to use the fourth order correlation function to retrieve more information and assess the (non)-separability of the state. The cross four-body normalized correlation function is given by

$$\begin{aligned} g_{12}^{(4)} &\equiv \frac{\langle : (\hat{a}_1^\dagger \hat{a}_1)^2 (\hat{a}_2^\dagger \hat{a}_2)^2 : \rangle}{\langle \hat{a}_1^\dagger \hat{a}_1 \rangle^2 \langle \hat{a}_2^\dagger \hat{a}_2 \rangle^2} \\ &= 4\left[1 + \frac{\left(|d|^2 + |c|^2\right)^2}{n_1^2 n_2^2} + 4\frac{|c|^2 + |d|^2}{n_1 n_2} + 2\frac{|d|^2|c|^2}{n_1^2 n_2^2}\right]. \end{aligned} \tag{148}$$

Surprisingly, it involves non-only the sum of the square modulus of c and d but also their product, which might allow one to access both values. Having information about the individual values for $|c|^2$ and $|d|^2$ would therefore allow us to completely characterize the separability of the state. While powerful, this method might not be relevant for photonic experiments: measuring the fourth order correlation function requires the use of two beam-splitters combined with four single photon avalanche photo-diodes that are quite expansive. In this case, a complete tomography of the state seems more appropriate. However, this might be relevant for atom counting experiments in which one can often count precisely several particles per mode while measuring the full tomography of the state is less common.

Definition - The Bona fide function

As we saw in the first section, any Gaussian state must respect the *bona fide* condition (105). In our particular case where a state is characterized by its mean population (n_1, n_2) and its correlation (c, d). It is therefore practical to define the following function

$$\begin{aligned} \mathcal{P}_+(n_1, n_2, c, d) =& (1+n_1)(1+n_2)(n_1 n_2 - |c|^2 - |d|^2) \\ &+ \left(\frac{1}{2} - n_1 n_2\right)\left(|d|^2 + |c|^2\right) \\ &+ (|c|^2 - |d|^2)^2 - \frac{1}{2}\left(|d|^2 - |c|^2\right). \end{aligned} \tag{149}$$

Any Gaussian state whose covariance matrix is of the form (135) must satisfy $\mathcal{P}_+(n_1, n_2, c, d) \geq 0$.

A couple of remarks that will help in understanding the $g^{(2)}/g^{(4)}$ criterion. First, note the difference between $\mathcal{P}_-$ defined in eq. (143) and $\mathcal{P}_+$ in (149): the absolute value in the third line disappears. This means that an entangled quantum state will exhibit $\mathcal{P}_+ \geq 0$ while having $\mathcal{P}_- < 0$. Second, note that $\mathcal{P}_- \leq \mathcal{P}_+$. As a result, if a state is entangled, it implies that $|c| > |d|$. The three conditions $\mathcal{P}_- < 0$, $|c| < |d|$ and $\mathcal{P}_+ \geq 0$ are incompatible: as discussed by Simon (2000), a entangled quantum state must have $\det C < 0$.

We now prove the following theorem.

Theorem - g2 and g4 criterion
Assuming that the state is Gaussian and that $\langle \hat{a}_i \rangle = \langle \hat{a}_i^2 \rangle = 0$, the measure of the population of each mode as well as the second and fourth order correlation functions $g^{(2)}$ and $g^{(4)}$ provide an entanglement criterion. We define

$$\beta_{\pm}^2 = \frac{n_1 n_2}{2}\left[g_{12}^{(2)} - 1 \pm \sqrt{2 + 8\left(g_{12}^{(2)} - 1\right) + 3\left(g_{12}^{(2)} - 1\right)^2 - \frac{g_{12}^{(4)}}{2}}\right]. \tag{150}$$

The state is entangled if and only if $\mathcal{P}_+(n_1, n_2, \beta_-, \beta_+) < 0$. In particular, if the state is non-separable, it is then characterized by

$$|\langle \hat{a}_1 \hat{a}_2 \rangle| = \beta_+ \qquad |\langle \hat{a}_1 \hat{a}_2^\dagger \rangle| = \beta_-. \tag{151}$$

Proof. From the $g^{(4)}$ expression in equation (148), the fourth order correlation function involves not only the sum $|d|^2 + |c|^2$ but also the product $|d|^2|c|^2$. We can therefore obtain the value of $|c|$ and $|d|$, using $g^{(2)}$ and $g^{(4)}$ through the system

$$\begin{aligned} |c|^2|d|^2 &= \frac{n_1^2 n_2^2}{2}\left[\frac{g_{12}^{(4)}}{4} - \left(g_{12}^{(2)} - 1\right)^2 - 1 - 4\left(g_{12}^{(2)} - 1\right)\right] \\ |c|^2 + |d|^2 &= n_1 n_2\left(g_{12}^{(2)} - 1\right). \end{aligned} \tag{152}$$

This system has *a priori* two indiscernible solutions for $|c|$ and $|d|$, and we introduce the following quantity

$$\beta_{\pm}^2 = \frac{n_1 n_2}{2}\left[g_{12}^{(2)} - 1 \pm \sqrt{2 + 8\left(g_{12}^{(2)} - 1\right) + 3\left(g_{12}^{(2)} - 1\right)^2 - \frac{g_{12}^{(4)}}{2}}\right]. \tag{153}$$

There are two possible candidates for the value of (c, d) that are (β_+, β_-) and (β_-, β_+). The outcome of our measurement is therefore either the (family of) quantum states characterized by $(n_1, n_2, \beta_+, \beta_-)$ or the one characterized by $(n_1, n_2, \beta_-, \beta_+)$. Here, the term that come first in the parenthesis refer to the value of c and the one that comes after to the value of d. I added "family" in parentheses because our measurement does not completely characterize the state: we do not measure the phase of c and d. However, for thermal states, the phase does not appear in the *bona fide* condition and in the measure of the entanglement[7]. This is why I will drop the absolute value of c and d to lighten the notations.

Before accepting one candidate, we must check that it is physically acceptable, *i.e.* that it satisfies the *bona fide* condition (105). In our case, it writes using the quantity $\mathcal{P}_+(n_1, n_2, c, d)$ we defined above, in equation (149). Last but not least, we remark that each solution is the partial transpose of the other:

$$\hat{\rho}^{TB}_{(n_1, n_2, \beta_+, \beta_-)} = \hat{\rho}_{(n_1, n_2, \beta_-, \beta_+)}. \tag{154}$$

To clarify, let's distinguish between the different scenarios. Because $\beta_+ > \beta_-$, we have that $\mathcal{P}_+(n_1, n_2, \beta_+, \beta_-) \geq \mathcal{P}_+(n_1, n_2, \beta_-, \beta_+)$, which makes only three cases to distinguish.

[7] Note that this is no longer true if the covariance matrix of subsystem A or subsystem B is not diagonal, *i.e.* if $\langle \hat{a}_i^2 \rangle \neq 0$.

- If $\mathcal{P}_+(n_1, n_2, \beta_-, \beta_+) \geq 0$. We cannot distinguish between the two states: they both respect the *bona fide* condition. However, we know the state is separable because the partial transpose of this state does respect the *bona fide* condition.
- If $\mathcal{P}_+(n_1, n_2, \beta_+, \beta_-) \geq 0$ and $\mathcal{P}_+(n_1, n_2, \beta_-, \beta_+) < 0$. It means that the only solution is the state defined by $|c| = \beta_+$ and $|d| = \beta_-$. The density matrix of its partial transposed is also negative, which means the state is entangled.
- If both $\mathcal{P}_+$ and $\mathcal{P}_-$ are negative, there are no solutions. Either the state is non-Gaussian or one of the hypothesis is not satisfied (the state is slightly displaced or not purely thermal).

The last option is impossible with our hypothesis: it means that the sign of $\mathcal{P}_+(n_1, n_2, \beta_-, \beta_+)$ completely determines the separability of the state, which ends the demonstration.

□

Quantifying entanglement

Some authors discussed the need to better quantify entanglement rather than just a yes/no answer (Isoard et al., 2021). Here we briefly explain that with our method, we have access to all the symplectic invariants that allows us to compute the logarithmic negativity, and therefore to quantify entanglement[8]. From the values of $(g^{(2)}, g^{(4)})$, we compute $\beta_\pm$. Using the $g^{(2)}/g^{(4)}$ criterion, we know that:

- Either the state is separable, which means that the logarithmic negativity is null: $E_\mathcal{N} = 0$.
- Or the state is entangled and is characterized by $|c| = \beta_+$ and $|d| = \beta_-$. We therefore have the values of all the local symplectic invariants of the partially transposed covariance matrix: $\det\boldsymbol{A}$, $\det\boldsymbol{B}$, $\det\boldsymbol{C}$, and $\det\boldsymbol{\sigma}$. We can compute the value of its smallest eigenvalue $\tilde{\nu}_-$ using eq. (112) and, consequently, the logarithmic negativity $E_\mathcal{N}(\boldsymbol{\sigma}) = -\log_2 \tilde{\nu}_-$.

Relating the $g^{(2)}/g^{(4)}$ criterion to the $g^{(2)}$ witness

In the proof of the $g^{(2)}$ theorem, we wrote the expression of $\beta_\pm$ in Eq. (153). This quantity is the value of $|c|^2$ and $|d|^2$ hence $\beta_\pm$ must be real and positive. This implies that the fourth order correlation function is bounded from above so that $\beta_\pm \in \mathbb{R}$

$$g_{12}^{(4)} \leq 16 g_{12}^{(2)} + 6\left(g_{12}^{(2)} - 1\right)^2 - 12. \tag{155}$$

and from below to ensure $\beta_- \geq 0$

$$g_{12}^{(4)} \geq 16 g_{12}^{(2)} + 4\left(g_{12}^{(2)} - 1\right)^2 - 12 \tag{156}$$

The two later conditions are needed to ensure that $\beta_\pm$ exists. A deviation from of these bounds would imply that either the state is non-Gaussian state or the local correlation is not exactly 2[9], which invalidates expression (148) for the fourth order correlation function.

Because of these bounds, it is better to parametrize the fourth order correlation function with $\theta \in [0, 1]$ so that we can write the fourth order correlation function as

$$g_{12}^{(4)} = 16 g_{12}^{(2)} + 4\left(g_{12}^{(2)} - 1\right)^2 - 12 + \left(g_{12}^{(2)} - 1\right)^2 \times 2\theta \tag{157}$$

[8] Note that the symplectic spectrum also allows to compute another entanglement quantifier, the Quantum Discord, see Adesso and Datta (2010) for example.

[9] This is because we used the fact that $g_{11}^{(2)} = g_{22}^{(2)} = 2$ to derive the equation on $g_{12}^{(4)}$.

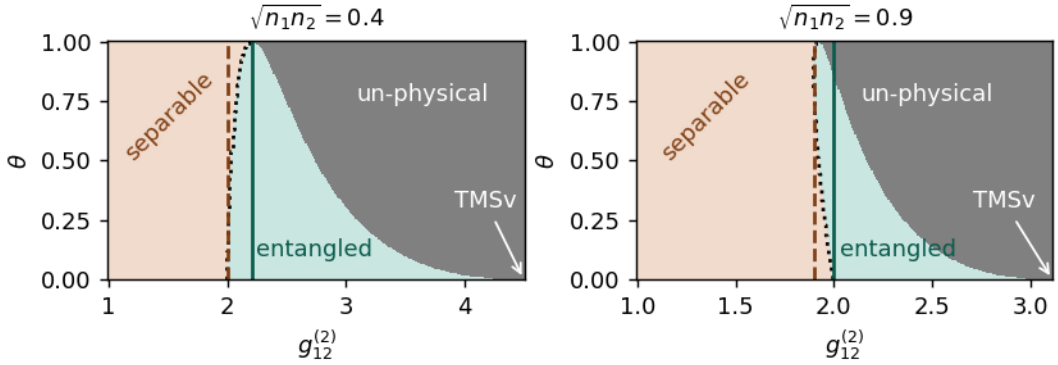

Figure 32: Entanglement 2D plane of the state for a state with an average population of 0.4 (left) and 0.9 (right). On the x-axis lies the second order correlation function and on the y axis the θ parameter defined in eq (157). The separable and non-separable regions are split by the gPPT criterion (dotted black line). The solid green (dashed brown) vertical line represents the entanglement (separable) $g^{(2)}$ threshold. The un-physical region is shown in grey.

so that the $\beta_\pm$ is given by

$$\beta_\pm^2 = n_1 n_2 (g_{12}^{(2)} - 1) \frac{1 \pm \sqrt{1-\theta}}{2}. \tag{158}$$

When $\theta = 0$, that is when the fourth order correlation function takes its minimum value, this implies that either c or d is null. On the opposite, when the fourth order correlation function takes its maximum value, this means that $|c| = |d|$. We now fix the value of the population to 0.4 and 0.9 to study in Figure 32 the entanglement in the $(g^{(2)}, \theta)$ plane. First we observe there are still un-physical regions on these maps. Indeed, the bounds on $g^{(4)}$ that we derived are just algebraic bounds that imply consistency of our reasoning. They do not take into account the *bona fide* condition. The grey regions in Figure 32 is a consequence of this *bona fide* condition. It emphasizes that the bounds on $g^{(4)}$ are stricter. In fact, it is these stricter bounds that permitted us to derive the $g^{(2)}$ bound to witness entanglement.

As previously, we need to discriminate the case where the population is higher than 0.7 or smaller.

- When $n_1 n_2 < 0.5$ (left subplot of Figure 32), the $g^{(2)}$ threshold to assess entanglement is higher than 2. For a 0.4 population it is 2.21. Second, we know also that for such low population, a second order correlation function below 2 implies separability of the state. Those two lines are respectively sketched on the plane as solid and dashed vertical lines. In the tight region where the $g^{(2)}$ witness is not sufficient, the fourth order correlation function gives the answer. We represented the border between the two regions with a dotted black line. In this case (low population)e, we see that at fixed $g^{(2)}$ a lower θ ables one to jump from the separable region to the entangled region. This means that the value of $|d|$ must be as small as possible. In this case, $|d|$ does not contribute to the bi-partite entanglement.
- When $n_1 n_2 > 0.5$, (right subplot of Figure 32), the $g^{(2)}$ threshold to assess entanglement equal to 2. The reasoning here is different from the previous one: a higher value of θ, *i.e.* a higher value of $g^{(4)}$ ables to pass from the separable to the entangled region. In this case, $|d|$ contributes to the non-separability.

When $g^{(2)}$ lies above the non-separability threshold (142), θ cannot take any value in the $[0, 1]$ interval. It is bounded from above by the un-physical region. As the second correlation function increases, it goes to 0 and vanishes in the limiting case where $g^{(2)} = 2+1/n$: this corresponds to a pure two-mode squeezed vacuum state. In this case, the fourth order correlation function must take its lower value.

4.F Finite efficiency effects

So far, I have not discussed the effect of pure losses, which might be significant given that a micro-channel plate has a rather small detection efficiency (approximately 50%, see the fourth chapter's section 3.D). As we saw in section 1.E, losses are represented by a beam splitter with transmittance $\sqrt{\eta}$ that mixes each mode with the vacuum, where η is the efficiency of the detector.

It must be emphasized that a beam splitter, being a passive transformation, cannot produce entanglement (Weedbrook et al., 2012). Consequently, if the state after the beam splitter is entangled, the state before it must also be entangled. In our case, we are interested in determining whether the state before the detector is entangled, and therefore, we need to correct for the effects of finite efficiency. For thermal states, the effect of non-perfect detection efficiency results in multiplying n_1, n_2, $|c|$, and $|d|$ by η.

How losses affect entanglement depends strongly on the nature of the entanglement: it is known for example that a two-mode squeezed thermal state remains entangled after a pure loss channel (Scheel et al., 2001). In general, any state that violates the Campo-Parentani witness Δ before a pure loss channel remains non-separable after (simply because Δ is proportional to the detection efficiency hence it does not change its sign). Some other states are however more fragile. In the literature, Barbosa et al. (2011) divide states in three categories : *robust*, *partially robust* and *fragile* states, showing that the effect of losses is not trivial.

In this manuscript, we are interested in the physics before the detector, eventually by removing it influence[10].

Taking into account losses on the $g^{(2)}$ witness

The threshold on $g^{(2)}$ depends on the population, hence the detection efficiency. The measure of the second order correlation function does not depend on losses while the measured population does. This means that if we measure a population n_{det}, we should compare the criterion to the threshold value for n_{det}/η, where η is the detector efficiency. Geometrically, this corresponds to a shift to the right on the x axis of Figure 30. One could say that taking into account efficiency facilitate the probe of entanglement: but I would answer that a pure loss channel does reduce entanglement and can even destroy it.

For a two-mode squeezed vacuum state, the second order non-normalized correlation function is $G_{12}^{(2)} = 2n_0^2 + n_0$ where n_0 is the number of particles in the state. After detection, we measure the same value of the normalized correlation function, but we measure a population $n_{det} = \eta n_0$. This means that the non-normalized correlation function reads $G_{12}^{(2)} = 2n_{det}^2 + n_{det}/n_0$. If we define the correlation strength as $G_{12}^{(2)} - n_1 n_2$, this means that the initial correlation of the state is n_0 while the measured one is only ηn_0: a pure loss channel decreases the correlation.

[10] This is not the case for example of people that want to distribute quantum states across long distances. In their case, they want to quantify entanglement after fiber transmission.

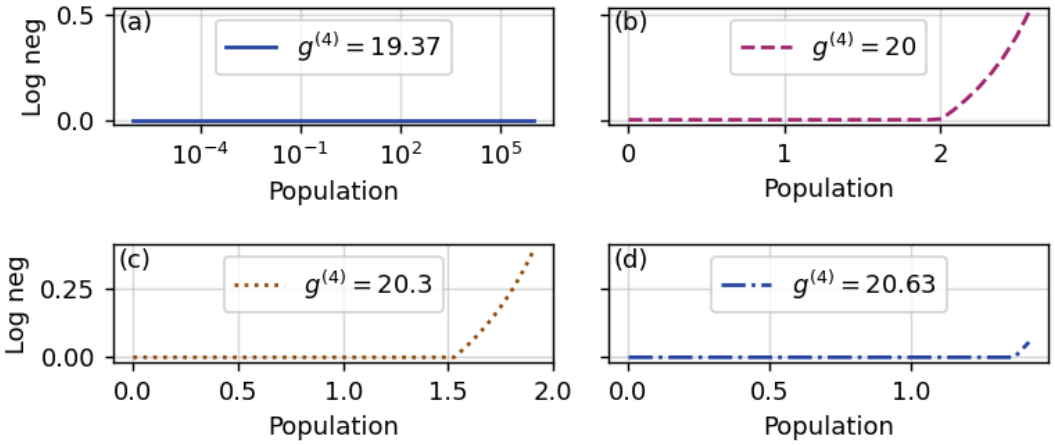

Figure 33: Logarithmic negativity of the state as a function of the population for a fixed value of $g^{(2)} = 1.8$ and $g^{(4)}$ (see legend). The state is entangled when the logarithmic negativity is strictly positive. At fixed value of $(g^{(2)}, g^{(4)})$, the population cannot be arbitrary large: the length of the curve of each panel (see the span of the x-axis) is different.

Taking into account losses on the $g^{(2)}/g^{(4)}$ criterion

The effect of losses on the $g^{(2)}/g^{(4)}$ criterion is more subtle than for the $g^{(2)}$ witness. Note however that the measurement of both correlation functions do not depend on the efficiency of the detector. In the general case, as for the other witness, taking into account the efficiency can be necessary to reveal entanglement. As I did not find a simple way to illustrate the dependance of the criterion with the efficiency, I will just provide an example.

Let's assume we measure $g^{(2)} = 1.8$. To ensure $\beta_{\pm} \in \mathbb{R}^{+}$, the fourth order correlation function must lie in the interval $[19.36, 20.64]$[11]. On Figure 33, we consider the case where we measured 19.37 (top left), 20 (top right), 20.3 (bottom left) and 20.63 (bottom right). Each plot represents the logarithmic negativity of the state as a function of the population. As in the $g^{(2)}$ entanglement witness, when correcting the measured population, we shift on the curve, and we might reveal entanglement. Note however that for a fixed value of the fourth order correlation function, the population cannot be too large. The x-axis reflects the population of the state that is compatible with $(g^{(2)}, g^{(4)})$: the x-axis of each subplot is different. The limiting case is when $g^{(4)}$ goes to its minimal value which means that $\beta_{-} = 0$ (top left). In this case either c or d is null, and the state is never entangled (but is always physical) as $g^{(2)} = 1.8 < 2$.

We now assume we measure a population of 0.8, with a 50% efficiency detector: the population of the state is therefore 1.6. According to the $g^{(2)}$ entanglement witness, this means that we are in the question mark zone of Figure 30. The fourth order correlation function measurement will give us the answer.

- Case where $g^{(4)} = 19.37$: with such low fourth order correlation function, this means that c or d is small and that no matter the population of the state, the state is (almost) never entangled. In the limit where $g^{(4)}$ takes it smaller value, this also mean that the population of the state can be arbitrary large (in this plot, we restricted the population to 10^5 but it is not the limit). Here we can safely say that the state is separable: we cannot

[11] As an experimentalist, I must say that this is interval (frightfully) small.

distinguish c and d.

- Case where $g^{(4)} = 20$: the fourth order correlation function is now higher, which means that c and d are closer, still quite different. Here we observe that for such correlation, a state big enough (population larger than 2) would be entangled. For a population of 1.6, the logarithmic negativity is zero here which means the state is separable.
- Case where $g^{(4)} = 20.3$: with a higher value of the fourth order correlation function, the population threshold for non-separability shifts. If the population of the state is 0.8, the state is separable while for a population of 1.6, it ise entangled. Here we see that the pure loss channel of the detector destroyed the entanglement. If one takes it into account, this means that the state before the detector (the one we want to characterize) is entangled.
- Case where $g^{(4)} = 20.63$: the value of $g^{(4)}$ approaches its highest value which means that $|c| \sim |d|$. The population cannot be arbitrary large here and it is not possible for a state to exhibits this correlation and to have a population higher than 1.4.

We therefore saw that the measurement of the fourth order correlation function allows to distinguish the problematic cases where the $g^{(2)}$ witness cannot. However, this function lies in a rather small interval which might be difficult to resolve experimentally.

4.G Conclusion

In this section, we showed that it is possible to demonstrate the entanglement of thermal Gaussian states with 2- and 4-body correlation functions. In this sense, our reasoning is in line with Schweigler et al. (2017), who characterize their system via correlation functions. They showed a deviation of the fourth order correlation function from its connected part. To make a long story short, they emphasize a non-Gaussian state using $g^{(4)}$. Our work is somehow a complement as we use $g^{(4)}$ to assess the non-separability of the *Gaussian* state.

Other theoretical works suggested different strategies to assess and quantify entanglement in analog gravity setups. Finazzi and Carusotto (2014) proposed an experimental scheme to measure all the terms of the covariance matrix. The idea is to measure the state by coupling it to a cavity and measuring the photon field at the output. This work was motivated by the system set up by Brennecke et al. (2008). This is also the stance taken by Finke et al. (2016), who propose to measure "additional observables, including noncommuting ones, e.g., density and phase fluctuations."

In the case of a stationary field[12], the measurement of the density-density correlation function was shown by Robertson et al. (2017b) to be sufficient to assess the non-separability of the state. This correlation function oscillates in time, and the non-separability criterion lies in its amplitude. In this case, the "noncommuting" paradox was solved elegantly: if the density perturbations $\delta\hat{n}_{-k}(t)$ and $\delta\hat{n}_k(t)$ commute, it is not the case for $\delta\hat{n}_{-k}(t)$ and $\delta\hat{n}_k(t')$ *i.e.* at different times. To measure the amplitude of the oscillation, one needs to measure the density-density correlation at different times, hence noncommuting observables.

Here, in line with Robertson et al. (2017a), our claim is that we do not need to measure noncommuting observables to establish the non-separability of thermal Gaussian states. However, it must be clearly stated that there are drawbacks to our reasoning: we *assume* the state to be Gaussian. It is this fundamental assumption that allows us to derive such a simple entanglement witness. Without measuring the Wigner function of the state, this assumption is hard (impossible) to prove experimentally. One would need to show that *all* correlation functions

[12] One can think of a squeezing Hamiltonian that could be turned on and off for a given amount of time. It is the case for example for Hawking radiation in an inhomogeneous fluid.

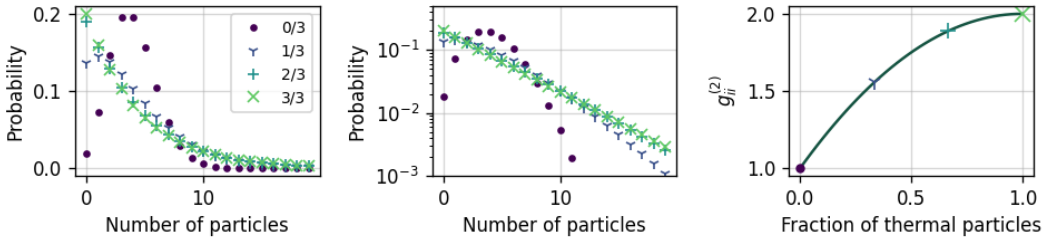

Figure 34: Left: Probability distribution of coherent (violet dots) versus thermal (green crosses) states with a fixed mean number of particles of 4. Each symbol and color represent a different combination of the displacement (coherent part) and width (thermal part) of the Gaussian Wigner function, ranging from a relative fraction of thermal state of zero (purple dots, fully coherent state) to 1 (green crosses, fully thermal state). Middle: same as on the left but with a logarithmic y-scale. Right: second-order correlation function as a function of the fraction of thermal particles. The symbols of the left subplots are also shown on this plot.

have vanishing non-connected contributions. Such a hypothesis can, however, be checked for consistency within the error bars and the range accessible by the experiment.

Still assuming a centered Gaussian function, we also considered un-squeezed thermal states, *i.e.*, states whose local second-order correlation functions (136) are equal to 2. If this is not observed experimentally (or assumed), the consequences are the following:

- It invalidates the $g^{(2)}$ witness. Indeed, the expression of the quantity $\mathcal{P}_-$ that we wrote in (143) is no longer correct. It will now contain a non-trivial dependence on both the amplitude and the phase $\langle \hat{a}_i \rangle^2$. With a single-particle detector, this amplitude can be measured but not the phase. This means that one must write $\mathcal{P}_-$ from scratch, maximize it with respect to the unknown phase, and bound it with respect to the coherence term $|d|$.
- It invalidates the expression of the fourth-order correlation function (148) that contains these terms. For example, one term is $\langle (\hat{a}_1^\dagger)^2 \rangle \langle (\hat{a}_2^\dagger)^2 \rangle \langle \hat{a}_1 \hat{a}_2 \rangle^2$, which contains the relative phase between the covariance matrix terms.

Physical meaning of $\langle \hat{a}_i^2 \rangle \neq 0$ A thermal state for which $\langle \hat{a}_i^2 \rangle \neq 0$ is a *squeezed thermal state*. In the context of analog gravity, it is for example proposed by Agullo et al. (2022) to send squeezed thermal light on an optical analog to a white-black hole pair. They show that the entanglement generated by the analog black-hole horizon was enhanced hence easier to detect.

Another assumption of this work should be emphasized: we assumed working with *thermal* Gaussian states, *i.e.*, states with zero mean. Finke et al. (2016) set up a classical (wave) model that mimics the correlation (variance and Cauchy-Schwarz) observed in experiments. The probability distribution of each mode can, in principle, discriminate between a coherent state and a thermal state, and therefore the probability distribution of a displaced thermal state. In Figure 34, we represent the probability distribution of four states with a mean number of particles of 4. We parametrize those states by the thermal fraction (see legend), setting the displacement to keep the number of particles fixed. The fully coherent state (0/3) is represented in purple dots and the fully thermal state in green crosses (3/3). In between, states are thermal

displaced states. The middle subplot is the same as the left one with a logarithmic y-scale. In these two plots, it is easy to distinguish a fully coherent state from a thermal state. However, the difference between a state that is mostly thermal but with still a bit of coherence (2/3 of thermal population, "+" symbols) is not very different from a state that is fully thermal ("x" symbols): the two curves overlap, and we cannot distinguish one from the other. On the right subplot of Figure 34, the second-order correlation function is shown as a function of the fraction of thermal particles. As expected, it ranges from 1, the value for a fully coherent state, to 2 for a fully thermal state. The imperceptible difference between the two "most thermal" states of the right subplot (2/3 and 1 in the legend) is more visible. The second-order correlation function is a better witness to ensure the state is thermal. This is not surprising: rare events (number of particles larger than 20) are not represented on Figure 34 but have a strong weight on the calculation of the second-order correlation function.

Summary In this section, we showed that it is possible to probe the non-separability of a zero-mean thermal Gaussian state. Measuring both the fourth and second order correlation function allows to completely quantify entanglement. The measurement of the second order correlation function can be sufficient to only witness non-separability. As a result, the classical Cauchy-Schwarz threshold is shifted depending on the population of the state if the nullity of the coherence term between the mode is not assumed. We finally discussed the drawbacks of this result that only applies for purely thermal Gaussian states.

Chapter III

Bose-Einstein condensation of metastable Helium

This chapter goes through the -not that - fast production of a Bose-Einstein condensate with metastable helium. The first section briefly reviews the cooling procedure towards a magnetic trap. We start by introducing the atomic properties of helium (Sec. 1.A) and our source of metastable helium (Sec 1.B). We then describe in section 1.C our magneto-optical trap, that is transferred into a cloverleaf magnetic trap (Sec. 1.D). The second section describes the optical dipole trap loading in section 2.A and evaporation ramp in section 2.C. We finally report on the highly improved stability of the BEC loading in section 2.D, which is a key ingredient to measure opposite momentum correlations. The third section introduces Bragg diffraction. This lattice was set up to realize an atomic interferometer (Lopes et al., 2015; Dussarrat et al., 2017) and we use in section 3.D the recent technological developments to perform a momentum selective deflector by shaping the Bragg impulsion. The fourth section is dedicated to the description of the BEC properties by three methods: time-of-flight expansion in section 4.A, the speed of the parametrically excited sidebands in section 4.B and the Bragg spectroscopy of the BEC in section 4.C.

What we knew, what is new ? The metastable helium experiment I worked on during my thesis is the oldest French BEC still in activity: it needed a facelift to get back on tracks. All the lasers used in this work were changed (cooling, Raman/Bragg and dipole trap). The sequencer was also changed: the details of its operation are left in the appendix. This replacement and the writing of all the driver took a non-negligible time of this work. The watercooling pipes of the room were also changed, and we faced vacuum issues during months. One led us to replace the metastable helium source. Some work was done on the optical setup but no major change. I also worked on the shaping of the laser pulses to realize a momentum selective atomic interferometer, but this project was mainly investigated and developed by Charlie Leprince (2024), who was a PhD student with whom I worked on the experiment for my entire PhD thesis. A publication is in preparation on these results (Leprince et al., 2024).

1. From helium to a magneto-optical trap of metastable helium

1.A Atomic properties

Spectroscopy

The experimental work in this manuscript focuses on the use of one atomic species: ^{4}He. A nice property of helium is the existence of a *metastable* state 2^3S_1[1] often also noted He*, with a 2-hour lifetime (Hodgman et al., 2009). A nice feature of this 2^3S_1 state, which I will refer to in the manuscript as the ground state, is its high internal energy. It is sufficiently high to tear out an electron from a metallic plate. We can therefore detect it electronically : we will go through the detection scheme in the next chapter. As one can see in Figure 35, the internal structure of helium is quite simple which makes it a great candidate to test quantum electrodynamics calculations and extracting fundamental constants. This is for example the research topic in the LaserLab Amsterdam group van der Werf et al. (2023) or The CREMA Collaboration et al. (2023).
In our experiment, we only use the $2^3S_1 - 2^3P_2$ transition to perform the laser cooling, and we use the $2^3S_1 - 2^3P_0$ transition for the Raman transfer and the Bragg diffraction laser.

Collisions and losses

Atom losses can occur in three ways:

1. One-body collisions: $He^* + X \rightarrow He + X^+ + e^-$ or $HeX^+ + e^-$ namely a collision with an atom of the background gas. As our vacuum gauge cannot measure less than 10^{-10} mbar, we use the atom cloud to check the vacuum : its lifetime is expected be to be around 40s in the magnetic trap.

2. Two-body Penning collisions: $2He^* \rightarrow He_2^+ + e^-$ or $He + He^+ + e^-$. They are characterized by a rate β which depends on the polarizability. The unpolarized loss rate is 10^{-10} cm^3/s while it is decreased by four orders of magnitude when atoms are polarized as expected by Shlyapnikov et al. (1994) and measured by Nowak et al. (2000) and later by Seidelin et al. (2004). This makes it possible to condense metastable helium, for which the density is around 10^{13} at/cm^3 with a 1 s lifetime (Robert et al., 2001). The interested reader will find a much more detailed discussion of Penning losses in the first chapter of Browaeys (1999). As we shall see in the next subsection, two-body losses are enhanced in the presence of resonant light hence it is very important to seal off the optical table in order to prevent resonant light from entering the science chamber.

3. Three-body collisions are associated with the decay rate of 3×10^{-27}cm^6/s and was computed and measured by the two previous references. As long as the density does

[1] Let me say a few words about the Russell-Saunders notation to label the electronic levels. The convention used in this manuscript is $n^{2S+1}L_j$ where n ; S is the spin which can take only two values since helium has two electrons. For parahelium, S is null and both electrons have opposite spins $|\uparrow\downarrow\rangle$ while S is 1 for orthohelium $|\uparrow\uparrow\rangle$. L is the total orbital angular momentum vector for all electrons, with spectroscopic notation S for single, P for principal, D for diffuse and F for fundamental. J is the total angular momentum vector for all electrons, which satisfies J = S + L. Its value must therefore range between $|L - S|$ and $L + S$. The three later letters label a *level* while specifying the magnetic quantum number m_j will pinpoint the *state*. m_J can take $2J + 1$ values, ranging from $-J$ to J.

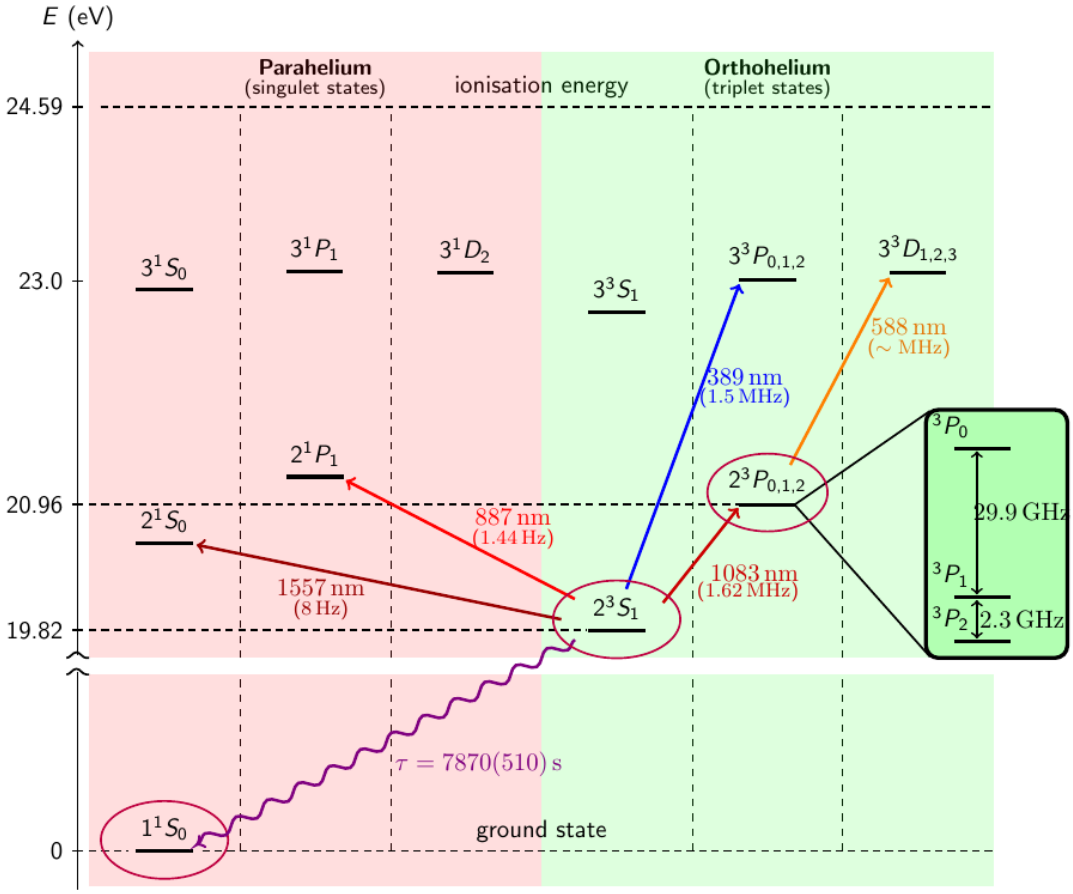

Figure 35: The left hand-side of the figure gives some energy levels of helium. Atoms are excited with a plasma discharge from the fundamental state 1^1S_0 to the metastable state 2^3S_1, to which we refer to as the *fundamental* state. Indeed, its decay time to the true fundamental state is much larger than an experiment cycle. The transition we work with is the $2^3P_{0,1,2}$ transition around 1083 nm. The transition between 2^3S_1 and 2^3P_2 is used to cool down atoms and the transition with 2^3P_0 to perform Raman and Bragg transitions. ©Figure from Marolleau (2022).

not exceed 10^{13} at/cm^3, this loss can be neglected. This is no longer the case for a Bose-Einstein condensate.

Elastic collisions are characterized by the scattering length $a = 7.512(5)$ nm precisely measured by Moal et al. (2006). Note that, sadly, helium does not have any Feshbach resonances.

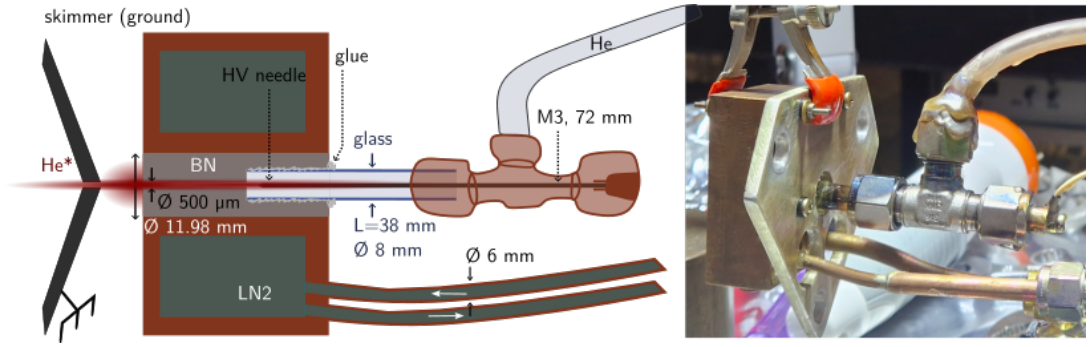

Figure 36: Left: Scheme of the source, inspired from Rooijakkers et al. (1996). A strong electric field is apply between the metallic needle and the skimmer. Helium is guided to the discharge location, through a plastic pipe, connected to the other part of the source with a swagelock connector. The glass tube makes sure the discharge occurs between the needle and the skimmer and not any other part of the vacuum chamber and is glued to the boron nitride cylinder. Helium atoms are then guided through the 500 µm hole in the liquid nitrogen cooled boron nitride. The nitrogen cooling decreases the atom speed from 2.6 to 1.2 km/s. One can understand with this scheme that the source is quite a fragile part of the experiment as a quite heavy metallic part pushes a 1 mm thick glass tube, itself glued to the boron nitride. Right: photo of the source taken in December 2022 that matches the left scheme. The connection between the plastic helium pipe and the source was changed after it burned due to discharges in the helium pipe. I would like to point that the large pile of disgusting glue is no longer present. The interested reader can refer to the technical appendix for more details about the source changes.

1.B Design of the metastable helium source

The first step of the experiment is to create a plasma of helium to excite a fraction of the gas to the metastable state 2^3S_1. This is done in a first vacuum chamber ($1.7 \cdot 10^{-7}/2.5 \cdot 10^{-5}$ mbar without/with helium) with the scheme describe in Figure 36. A helium plasma is created using a strong electric field between a metallic needle (in black and attached to the swagelok connector in Figure 36) and the skimmer (on the left). Out of the total number of atoms leaving the discharge, only a fraction of $10^{-5} - 10^{-4}$ are in the metastable state: this source is therefore not very bright (Vassen et al., 2012). Furthermore, atoms that escape the discharge have a large speed of 2.6 km/s. Such speed would require a Zeeman slower of 7 m! Right after the discharge, the atoms must pass into a boron nitride cylinder cooled down with liquid nitrogen. The cylinder hole is sufficiently small to ensure atoms collide to the wall and are cooled down. During my PhD, we had to replace the source twice: I therefore provide much more details about its installation in the appendix.

This source of metastable helium is not very convenient: it must be cooled with liquid nitrogen. We use a bottle per day which costs now 10 k€ per year and prevents us to let the experiment running during the night. Wang et al. (2021) reported optical excitation of ^{81}Kr with UV lamps. However, the energy required for krypton is 10 eV (120 nm), smaller than the one for helium (20 eV, 60 nm)[2].

[2]Note also that Zheng-Tian Lu reported they spent 3 years working on the different UV lamps in order to optimize the excitation.

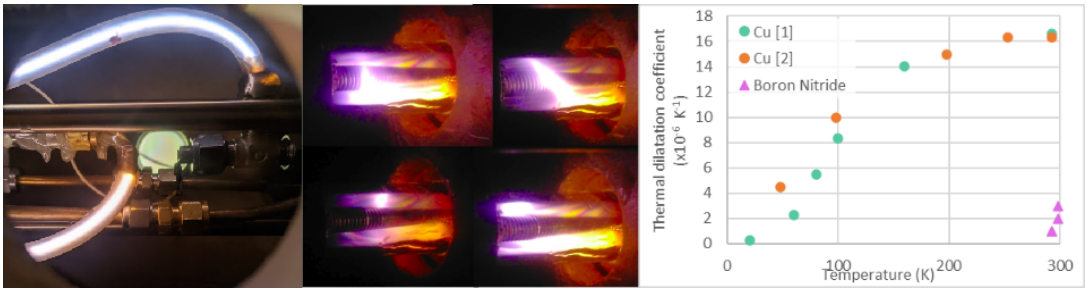

Figure 37: The left picture was taken in February 2024 when the source was not discharging anymore with the skimmer but with the flange (inside the plastic tube that brings helium). Middle: photos taken on January, 20th of 2023 after installing a new source. After some days, the source was much less bright because the discharge charred the glass, giving it a black hue. The right plot represents the thermal dilatation coefficient of copper and boron nitride as a function of temperature. For the copper, ref [1] refers to Gassot et al. (1999) and [2] to UltimHeat (1962) while boron nitride coefficients were extracted from various sellers websites, which provide information for high temperatures only (above 25 °C). One can show that a 12 mm copper diameter at room temperature decreases by 0.03 mm when cooled at 77 K and the retraction of boron nitride can be neglected regarding the copper one.

1.C Magneto-optical trap

Transverse molasses and Zeeman slower

The quite divergent atom flux that escapes from the source at roughly 1.3 km/s is then collimated with a 1.8Γ red-detuned transverse molasses[3] that increases the He* intensity flux by a factor of 10-20 (Labeyrie et al., 1999). At this point, the atomic flux enters the Zeeman slower for which the maximal deceleration that can be achieved is given by $a_{max} = \Gamma h/2m\lambda$ where Γ and λ are the linewidth and wavelength of the transition. The minimum length L_{min} of the Zeeman slower depends then only on the speed of the atomic jet $L_{min} = v_{jet}^2/2a_{max}$. With the 2^3P transition, the maximal deceleration is $4.7 \cdot 10^5 m/s^2$ which corresponds to a minimal Zeeman slower length of 1.5 m for a nitrogen cooled flux of helium[4].

[3]The transverse molasses beams are elliptical with waist 49mm×11mm with roughly 90 mW per beam. As the actual setup is not highly stable, it was proposed a scheme on the 22/03/2021 to change it.

[4]Using the 3^3P transition at 389 nm would increase a lot the maximum deceleration and keeping the same Zeeman length, it would allow the cooling of the source with water rather than liquid nitrogen. Indeed, when cooling atoms with water rather than liquid nitrogen, Labeyrie (1998) measured $1950 \pm 500 m/s$ atomic speed at the exit of the source, which could be slowed down using our 2.3 m Zeeman slower. Sadly, the 2^3S-3^3P transition is not close. A MOT of helium with a 389 nm laser was previously realized by Tychkov et al. (2004). They took advantage of a 389 nm laser to increase the density, but they still used the 1083 nm transition in order to obtain larger loading rate.

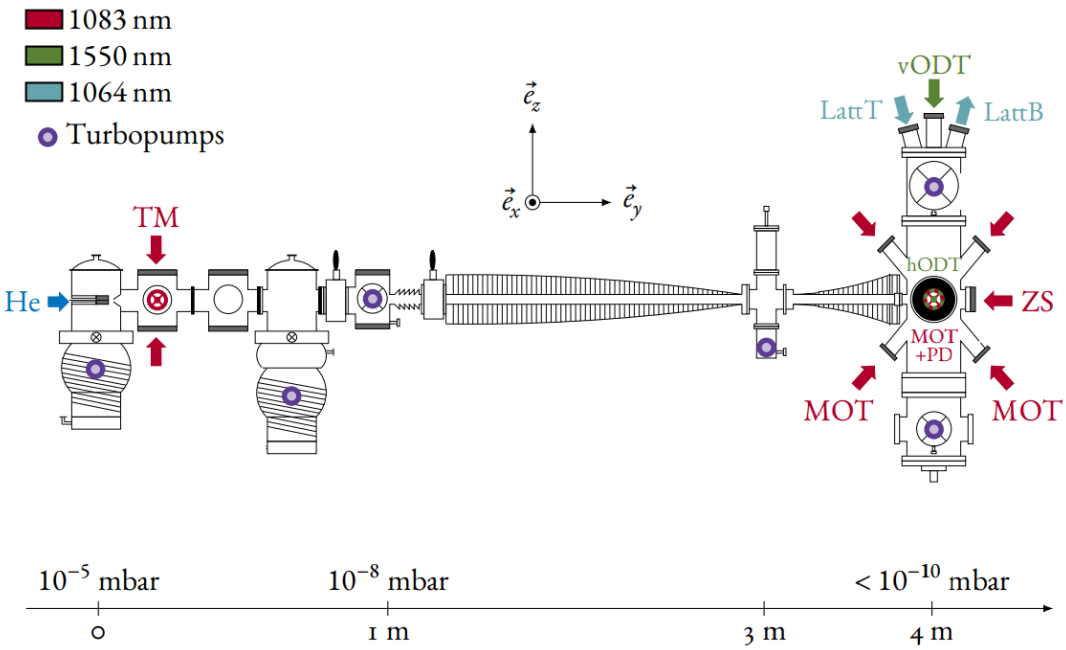

Figure 38: Experimental apparatus. The source of metastable helium atom describe in Figure 36 is located on the left. As the outgoing atom flux is quite divergent, a 2D transverse molasses (TM) deflects it so that a reasonable fraction of the atoms reaches the science chamber, after the 3 m long Zeeman slower (ZS). The cooling steps are performed in the science chamber on the right. The different beams we use are represented by the three different colors. The vertical dipole trap (green) enters from the top window while the 1064nm pair creation lattice (blue) enters from bottom and top windows at 7 degrees from the vertical direction. ©Figure from Marolleau (2022).

Compressed magneto-optical trap and optical molasses

The Magneto-Optical Trap (MOT) is loaded during 1.5 s with three retro-reflected -38Γ red-detuned lasers[5]. In a MOT, atoms are unpolarized hence one would expect Penning losses characterized by a rate coefficient of 10^{-10} cm^3/s. However, a rate of 10^{-7}cm^3/s was reported by Bardou et al. (1992), underlying light-assisted collisions. The closer to resonance the light is, the higher the population of the excited state. The Penning collision rate between two atoms in the fundamental state is much lower than when one of them is in an excited state. This means that inelastic collision are enhanced in the presence of resonant light. In order to keep the loss rate low, one needs to keep the excited population low so that the MOT laser should be as red detuned as possible (Browaeys et al., 2000). The interested reader should refer to Browaeys (1999) for more complete and detailed explanation of the light-assisted collision. Typically, $3(2)\times10^8$ are loaded, this number being deduced from a camera recently calibrated by Lamirault (2023).

At the end of the MOT, we ramp the frequency closer to resonance and decrease the intensity of the laser to increase the density of the cloud, whose temperature is approximately 200 µK at this stage. We finally perform an optical molasses in which the cloud temperature

[5]The waist of the MOT beams are 20.2(5) mm (26/11/2021) and the available power is roughly 35 mW at 100 MHz (16/01/24 for the AOM double pass efficiency). The first QControl MOT was obtained on the 22/04/2021 with the old laser diode and on the 01/07/2021 with the new cooling laser.

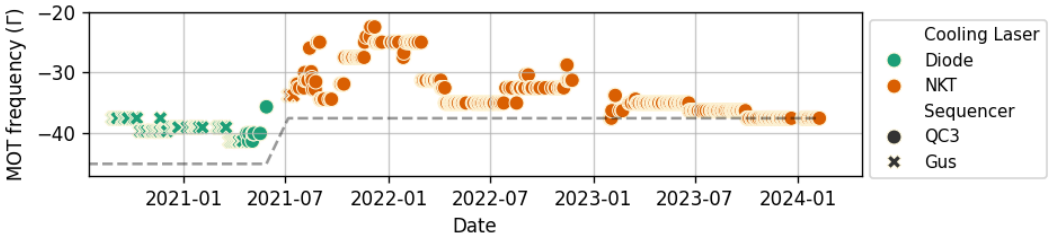

Figure 39: Drift of the optimal MOT frequency from 2020 to 2024, in units of the linewidth Γ of the transition (1.6 MHz). The shape of the markers represent the laser we used and the color the sequencer. The grey dash line represents the greatest frequency difference that we can achieve because of the acousto-optic modulator minimal frequency (80 MHz). When we changed the laser, we switched the laser frequency from 2×116 MHz to 2×110 MHz to have more power during the imaging. Indeed, it is the same AOM that produces MOT and imaging beams and its efficiency decreases rapidly between 110 and 120 MHz.

decreases towards 60 µK, that should be compared to the 40 µK Doppler temperature for helium[6].

During my work at the laboratory, we had anomalous stability issues : on winter 2020, we were not even able to have a proper MOT on a daily basis. We decided at this point to change many possible instability sources on the experiment, starting with the cooling laser and the sequencer. The cooling laser was a 2 MHz diode that was replaced by a NKT Photonics *Koheras ADJUSTIK – single-frequency fiber lasers* with a linewidth smaller than 20 kHz. After this change, there was no observed increase in the absolute number of atoms, but the stability of the experiment was highly improved. Concerning the sequencer, we replaced the home-made sequencer named *gus* by a brand new Adwin Pro II sequencer together with the QControl3 program to control it. The details about the program are left within the appendix, sections 2.A-2.D. Figure 39 represents the daily used MOT frequency: I think it provides a glimpse of the time it took us to converge toward a stable situation regarding the MOT parameters. As mentioned earlier, the further we are from resonance, the larger the number of atoms. The detuning from resonance is larger at the bottom of the graph and the gray dashed line represents the maximal detuning accessible on our setup. This maximal detuning was not chosen higher because it is a trade-off between two usages of the same AOM (that is used both for imaging the cloud and the MOT).

1.D Magnetic Trap

After the optical molasses, a magnetic trap is turned on (Nowak et al., 2000). Atoms being unpolarized during the MOT, they are pumped towards the trapped magnetic sub-level $m_j = 1$ by a short and intense σ^+ polarized laser pulse. The trap geometry is a Ioffe-Pritchard type trap hence we have the ability to set the minimum value of the magnetic field called the bias B_0 (minimum value of the field) as well as the curvature. This allows to realize a Bose-Einstein condensate in a magnetic trap (Robert, 2001).

[6]Contrary to other species such as alkaline-earth atoms, helium does not exhibit sub-Doppler cooling therefore it is a nice toy model to highlight the 3D Doppler theory (Dalibard, 2015). This was studied a few years ago by Chang et al. (2014) with the other metastable helium machine of the group.

Remark - Technical remark
The electrical currents used to produce the magnetic trap are quite high: 200 A. Therefore, the diodes and IGBTs[a] must be water-cooled. They are connected to the cold water circuit that is common to the entire laboratory. On some days, the pressure at the entrance of our lab is too low to allow us to cool properly[b]. This motivated us to switch our cooling circuit from series to parallel to increase the water flux, which sadly did not help as expected. The magnetic coils must also be cooled: they are cooled with a dedicated chiller that was installed in 2023. More details and measurements about the water-cooling of the experiment are provided in the appendix section 3.C.

[a] The IGBTs, Insulated-Gate Bipolar Transistors, allow switching off suddenly the magnetic trap and the diodes protect the current power supplies.

[b] This cooling issue is quite annoying, and I never found its origin. Some days, we observe that the pressure drops suddenly. When sending e-mails to the laboratory, no one reported a change in their measurement/procedure and the water pressure at the top of the building was each time reported "normal" by the infrastructure service.

The magnetic trap cooling in our experiment has been extensively reviewed recently by Marolleau (2022); hence I will not dwell on the subject. At each step of the cooling, the trap is compressed by decreasing the bias. The two cooling steps consist of:

- 1D Doppler cooling: a 1D retro-reflected beam is applied on the cloud along its elongated direction. This step lasts 0.6 seconds with low power close to resonance (Schmidt et al., 2003). We obtain $2(1) \times 10^8$ atoms at 130(10) µK.
- RF evaporation: A radio-frequency wave un-traps the hotter atoms from the trap (Browaeys et al., 2001). The final value of the RF frequency fixes the depth of the trap and hence the temperature of the cloud. Typically, to load a dipole trap, we get a 43(3) µK cloud with $5(3) \times 10^7$ atoms.

Summary We are able to cool down 5×10^7 helium atoms to a few dozen µK using a 1.5 s magneto-optical trap and a 2.2 s magnetic trap.

2. Bose-Einstein condensation in an optical dipole trap

2.A Optical dipole trap

For the past few years, the dipole trap has not been very cooperative in our experiment. It started back in 2017 when the team chose to change the dipole trap laser to use more power and be able to load a hotter cloud for stability reasons. It was decided to buy a 30 W laser from Keopsys[7]. Sadly, after many delays, the new laser never delivered the expected power and was restrained to 20 W. During my thesis, it broke three times[8], and we finally bought a new one from the IPG company[9].

[7] Continuous 1550 nm 30 W Erbium laser sold under reference CEFL-TERA.

[8] Note however that the customer service of Keopsys was really quick to repair the product the two times I asked for.

[9] Model No ELR-30-1550-LP, serial PL2241259 delivers indeed 30 W at 1550.584 nm with 0.226 nm. The beam diameter ($1/e^2$) is 3.632 mm with a far field divergence full angle of 0.54 mrad. Beam quality is $M^2 = 1.02$, laser is linearly polarized with 21.1 dB polarization extinction ratio. The output power was measured to be 30 W. The laser was bought 27.5 k€ and surprisingly, the price we paid was the same as the one on the 2016 quote. The command was passed on July, 11th and the product arrived on September, 07th 2022, which is quite fast.

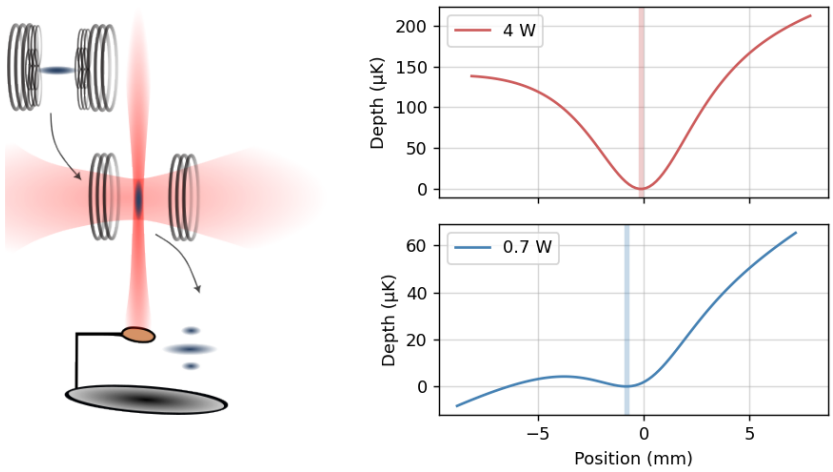

Figure 40: Left: Dipole trap setup: the vertical beam has a waist of 40.5(2) µm and the horizontal 109 µm. The vertical dipole trap hits the protective shield on the MCP not do damage it. The Raman transfer kicks the atoms so that they do not hit the protective copper plate. Right: depth of the dipole trap as a function of the vertical position for 4W (top) and 0.7 W (bottom). The shaded vertical line represents the minimum of the trap, that shifts when the power changes.

However, when the dipole trap laser works, it works... on fire ! Indeed, the vertical beam arm hits (and heats) the micro-channel plate that burned... twice ! To overcome this issue, we placed a shield on the top of the MCP that reflects back the laser. This requires therefore to deflect the cloud when the trap is released so that the MCP detects the atoms. This is done during the Raman transfer. An entire section is dedicated to this shield installation on the chapter dedicated to the MCP.

The dipole trap is formed of two arms: one vertical and one horizontal. The vertical trap has a waist of 40.5(2) µm and the horizontal waist is 108(2) µm[10] (Partridge et al., 2010). The dipole trap is loaded from a 45 µK magnetic trap: only 10% of the atoms are trapped (3×10^6). We use 4 W, which means the initial depth of the trap is 140 µK. Once loaded, the temperature of the trapped cloud is 20(2) µK, still above the condensation temperature of 3 µK. We therefore need to decrease the height of the trap. The latter is fixed on the vertical axis: the depth of the trap is a trade-off between the laser power and the gravity gradient.

On the right of Figure 40 is shown the depth of the trap as a function of the vertical position for a 4 W laser (top) and a 0.7 W laser (bottom). When the power decreases, the depth of the trap decreases, but the center of the trap changes too: this is represented by the shaded vertical line on the figure. As we will see in subsection 2.C, the evaporation ramp must be smooth enough not to push the cloud.

[10]The measurement of the vertical waist using 3 techniques is explained in the appendix. The horizontal beam waist was also measured, in agreement with the value reported by Perrier (2020).

2.B Raman transfer

As mentioned earlier, the atoms must be polarized to decrease the inelastic collision rate and obtain a Bose-Einstein condensate. Since these atoms are sensitive to magnetic fields, they are deflected by residual magnetic fields during their 308 ms time-of-flight towards the MCP. Therefore, we need to transfer them to the $m_j = 0$ state when the trap is switched off. This internal state transfer is achieved using two laser beams in a Raman configuration that induces a two-photon transition. The laser is blue-detuned (600 MHz) from the $2^3S_1 - 2^3P_0$ transition, with one beam being σ^- polarized and the other being π polarized[11]. Since the two lasers do not co-propagate, they impart a velocity kick to the atoms of $2h/\lambda m \sin\theta = 42.5$ mm/s. This allows us to deflect the cloud during its free fall so that it does not hit the MCP[12]: after a 307 ms time of flight, the atoms are shifted by 11.5 mm, as shown in Figure 41. Note that Van Der Beek et al. (2020) used a similar trick to install a vertical lattice on their setup: they displaced their MCP from the center and kicked the cloud during its free fall with a magnetic field pusher rather than a laser pulse.

The Raman transition consists of a short and intense laser pulse[13] of 13 µs that transfers 97(2)% of the cloud. This duration is chosen so that the number of remaining atoms in the $m = 1$ state is minimal on Rabi oscillation on the right subplot of Figure 41.

2.C Dipole trap evaporation ramp

Once the dipole trap is loaded, the power of the laser is decreased to perform the last evaporation ramp. In order to obtain a BEC, one must decrease the trap potential in order to keep the elastic collision rate high (so that the evaporation ramp is efficient) while having a low inelastic collision rate. In practice, the ramp duration is 1.3 seconds and the ramp parameters have an impact on the atom number of the final BEC.
The trapping laser is vertical; hence, when the power of the trap decreases, the position of the minimum shifts due to gravity. Depending on the dynamics of the ramp, the position of this minimum exhibits different trajectories. For an exponential power ramp, we characterize the ramp time-dependence as a function of the decay rate α:

$$\mathcal{P}_{las}(t) = \mathcal{P}_{min} + (\mathcal{P}_{max} - \mathcal{P}_{min}) \frac{e^{-\alpha t/\Delta t} - e^{-\alpha}}{1 - e^{-\alpha}} \tag{159}$$

where $\mathcal{P}_{max/min}$ is the power of the laser and Δt the duration of the ramp. The evaporation ramp of the laser power is shown on the left panel of Figure 42. When $\alpha = 1$, the ramp is a straight line (solid pink curve) and when α is higher, the power is more exponentially damped (dashed dotted green).
On the right panel of Figure 42 is shown the position of the minimum of the trap of the center of the cloud as a function of time. The $\alpha = 1$ solid pink curve exhibits a sharp angle at the end of the evaporation ramp. This means that the velocity of the minimum of the trap is not

[11] The Raman 1 σ^- polarized beam waist is 2.5-2.9 mm and the Raman 2 π polarized 4-4.7 mm (measured on the 29/03/2023). The Raman 1 being linearly polarized, its intensity should be twice the intensity of the Raman 2 beam. This means that, roughly, beam power should be the same.

[12] This kick configuration was installed after the second hole appeared on the MCP, in January 2020. Note however that there is a small angle along the vertical direction of the two beams, resulting in (not so) small momentum transfer downward of 5 mm/s. A measure can be found on the 02/07/2024.

[13] This π pulse is used since September 2023. Before, the Raman transfer was performed using a frequency ramp that adiabatically transferred the atom from the $m_j = 1$ to the $m_j = 0$ state, that is called a Landau-Zener transition (Zener and Fowler, 1932).

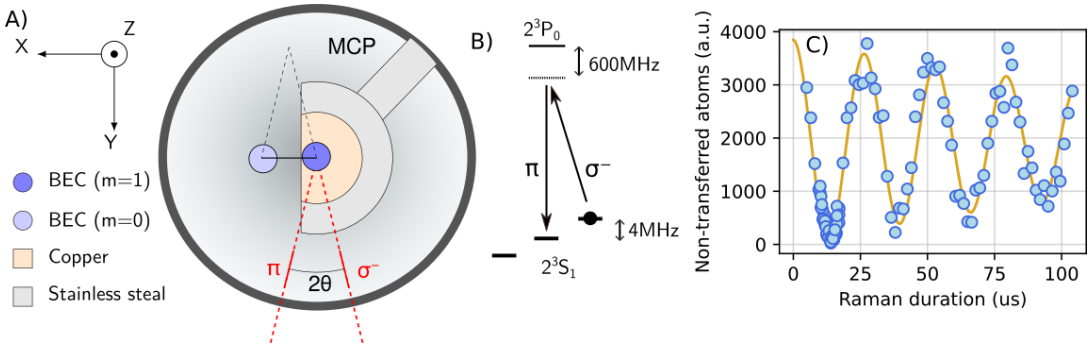

Figure 41: Raman transfer of the atoms. A & B) Scheme of the experimental Raman setup. Two beams σ^- and π polarized transfer the atoms from the $m = 1$ state to the magnetically insensitive $m = 0$ state. During this transfer, the atoms are kicked to the side of the MCP that is not covered by the shield. C) Rabi oscillation: the non-transferred atoms are sensitive to residual magnetic fields in the vacuum chamber. The cloud is deformed and most of the atoms do not hit the MCP. Only a small fraction of them is detected. The cloud is also so stretched that this $m = 1$ cloud does not saturate the MCP, which is not the case of the m=0 BEC. This makes it possible to count precisely the number of remaining atoms in the m=1 state as a function of the laser pulse duration. The latter should be short and intense to avoid velocity selection on the x-axis. Indeed, the damping of the oscillation is due to the different resonant frequency for each momentum. On the graph, the higher number of points around the first minimum allows for precisely determining the duration that transfers the most atoms. ©Left scheme from Leprince (2024).

continuous, which might induce an oscillation of the cloud. On the opposite, the $\alpha = 8$ dashed dotted green curve is smoother.

In order to ensure that the evaporation ramp does not induce any oscillation of the cloud, we perform the following experiment. We fix the value of the evaporation ramp to 1.2 s and perform the evaporation ramp (159) with $\alpha = 1$ (respectively $\alpha = 8$). We then scan the hold time in the trap after the evaporation ramp, from 500 to 600 ms. The arrival time of the cloud on the detector is proportional to the in-trap velocity of the cloud at the moment the cloud is released. If the evaporation ramp induces an oscillation of the cloud, the arrival time of the cloud should exhibit an oscillation too. The arrival time of the BEC as a function of the hold time in the trap is shown in the inset of the left panel of Figure 42, as pink circles for $\alpha = 1$ and green squares for $\alpha = 8$. We observe a strong oscillation of the cloud when $\alpha = 1$, while for the $\alpha = 8$ case, if the oscillation still exists, it is indiscernible from the shot-to-shot variations.

2.D Stability of the BEC

The estimation of the stability of the dipole trap is the following. We produce roughly one or two hundreds BECs and record the arrival time of each BEC. We define the stability of the BEC as the standard deviation of the arrival time distribution. For a single vertical dipole trap, Bonneau (2011) reported a stability of 100 µs, which corresponds to 1 mm/s in *in-trap* velocity. This value should be compared to the size (in speed) of the Bogoliubov wave-function: roughly 0.5(2) mm/s. It means that the shot-to-shot instabilities prevent one from measuring cross-correlations. In the appendix and sixth chapter, section 1.C, we show that instabilities can lead to spurious correlation. This poor value is one of the reason that pushed the team to install a

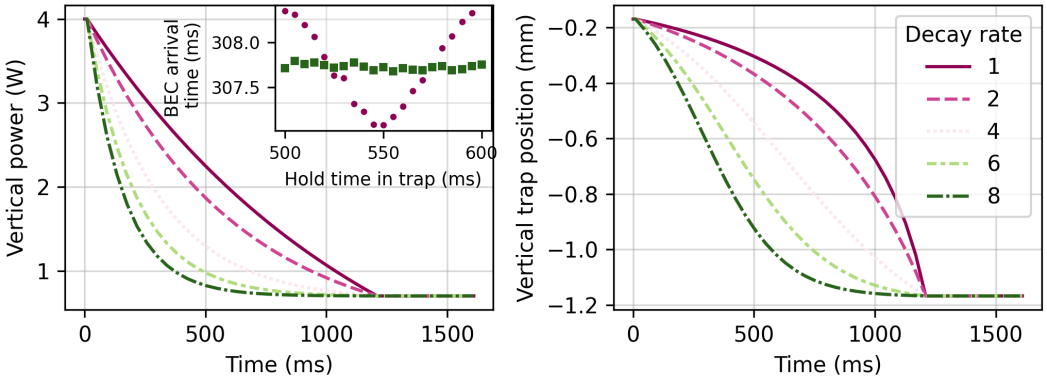

Figure 42: Comparison of different evaporation ramp. Left: exponential decrease of the laser power as a function of time according to equation (159). Each curve corresponds to a different decay rate, from $\alpha = 1$ in solid pink to $\alpha = 8$ in dashed-dotted green. The legend is shown on the right panel and is common to both plots. The right subplot represents the position of the minimum of the trap *i.e.* the trajectories of the center of mass of the cloud. For low values of α, the trajectory exhibits a sharp angle at the end of the evaporation, causing oscillations of the cloud. This behavior can be observed on the inset of the left panel which represent the arrival time of the BEC on the detector as a function of the hold time in the trap. For $\alpha = 1$, the cloud oscillates at the trap frequency while this oscillation seems suppressed for $\alpha = 8$.

second laser beam to work in a cross dipole trap[14]. The stability in this new crossed dipole trap was then improved to 40 µs (0.4 mm/s) (Lopes, 2014). More recently, the value of 30 µs (0.3 mm/s) was achieved (Marolleau, 2022). Here we report a stability of 10(5) µs[15], which corresponds to 0.10(5) mm/s in speed. Such improvement is due to the adiabatic extinction of the magnetic trap when we transfer it to the dipole trap, a good optical alignment between all lasers and the shape of the evaporation ramp. The stability in the single dipole trap was highly improved: from 100 µs, it reached 10(5) µs hence the same stability as the crossed dipole trap. The fact that the laser power available is higher than in 2012 might also help as we load a much hotter trap: we are less sensitive to the fluctuations of the magnetic trap position.

Remark - Technical note
An oscilloscope was added to one of the MCP channel with a low pass filter to register the analog signal. This allows to precisely measure the arrival time of the BEC and recenter the arrival time of different cycles to further improve the resolution from the shot-to-shot fluctuations.

Summary We are able to obtain a Bose-Einstein condensate in a crossed dipole trap in approximately 9 seconds. By optimizing the evaporation ramp, we reduced the shot-to-shot fluctuations of the BEC arrival time fluctuations to 0.01 ms. Such stability is a key ingredient to study opposite momentum correlations.

[14] This change also permitted to have a trap in many configurations, from the 1D regime to the 3D one. The description of the BEC and its properties will be done later.

[15] The stability along x and y was measured to be 1.3 and 1 mm/s respectively. Experiment performed on the 23/05/2024.

3. Bragg diffraction

As we shall see in the next chapter, when an atom enters a channel of the detector, it triggers an electronic cascade. However, it takes a few milliseconds for the channel to re-charge back and be able to detect another atom. In our case, the BEC and the pairs are separated by approximately 1 ms. If the atom of the pair that arrives first is unaffected by the saturation, this is not the case of the one that arrives after the BEC. The solution would be to remove the BEC, or to kick it upwards so that it arrives after the pairs. This section introduces Bragg diffraction which will allows us to do so.

The pulse-shaping techniques reported here were initially developed to realize a 2-particle 4-modes interferometer to perform a Bell test using massive particles entangled in momentum (Leprince et al., 2024). In this work, we take advantage of this state-of-the-art atomic interferometer to simply "kick-off" the BEC outside the region of interest. I participated in the experimental implementation and characterization of this set-up, but this project was mainly investigated by Leprince (2024), to which the interested reader is referred for further details.

3.A Introduction

Consider an atom illuminated by two lasers 1 and 2, characterized by their electric field E_j their frequency ω_j, with a relative half-angle that we note θ_B. As illustrated in Figure 43, the two lasers interfere and create a periodic potential along the vertical direction z. The two lasers are detuned by $\delta\omega_{las} = \omega_1 - \omega_2$, creating a standing light wave that scatters atoms.

Bragg diffraction can be seen as a two-photon process where the atoms absorb one photon from a laser and re-emits it in a stimulated way into the second one (Martin et al., 1988). This interpretation is easily understood with the scheme on the right panel of Figure 43. The atom absorbs a photon from one laser (labeled 1, yellow) and re-emits it in the second laser (labeled 2, red). When the lasers do not co-propagate but have an angle $2\theta_B$, the atom is kicked by a momentum $k_b = 2\frac{2\pi}{\lambda}\sin\theta_B$.

On the experiment, the Bragg speed was measured to be $v_b = \hbar k_b/m$=49.58(3) mm/s. The corresponding wavevector is k_b=3.145(2) µm^{-1} and the associated recoil frequency is $\omega_b = \hbar k_b^2/2m$ is 12.41(3) kHz. The lattice is not perfectly aligned on the vertical direction but experiences a (relatively) small angle along x of 0.08(3)° and 0.04(2)° along y.

Formally, the dipole atom-light interaction is characterized by the Rabi frequency $\hbar\Omega_j := -\langle g|\hat{\mathrm{d}}\cdot\mathrm{E}|e\rangle$. Here, $\hat{\mathrm{d}}$ represents the reduced atomic dipole of the transition $g \longrightarrow e$ between the ground state 2^3S_1 and the excited state 2^3P_0. When the lasers are far detuned from resonance, the population of the excited level can be neglected[16]. The Hamiltonian of the system can then be written using the two-photon Rabi frequency

$$\Omega_R = \frac{\Omega_1\Omega_2^\star}{2\Delta} \tag{160}$$

and the Bragg wavevector $k_b = 2\frac{2\pi}{\lambda}\sin\theta_B$. As we shall see, the Rabi frequency Ω_R plays a central role in determining the different regimes of the light-matter interaction. The laser beam waists are sufficiently large (4 mm) compared to the cloud (200 µm) to assume that the Rabi frequency does not depend on space. For a non-interacting gas, the Hamiltonian that drives the transition is (Leprince, 2024)

$$\hat{\mathcal{H}} = \frac{\hat{P}^2}{2m} - \frac{\hbar|\Omega_R|}{2}\left(e^{ik_b\hat{z}-i\phi(t)} + e^{-ik_b\hat{z}+i\phi(t)}\right) \tag{161}$$

[16]The full derivation of the adiabatic elimination of the excited state can be found in Perrier (2020).

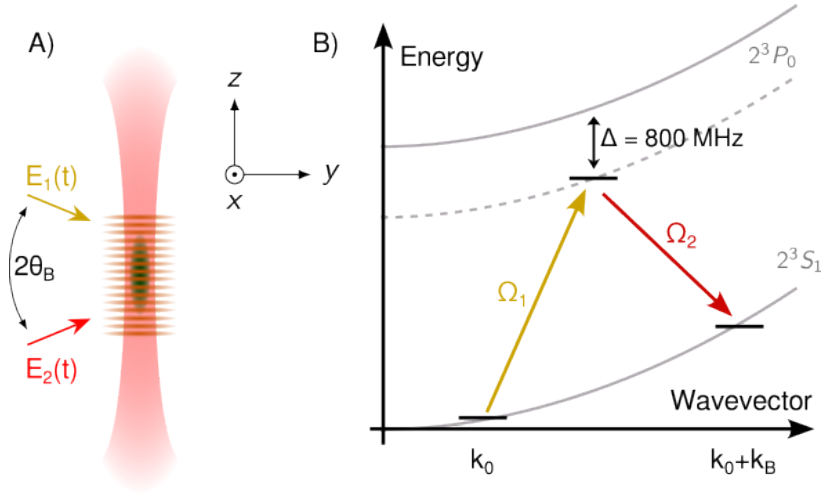

Figure 43: A) Experimental scheme of the laser setup. Two lasers with a 2.8 mm waist interfere at the position of the cloud, creating a standing wave whose speed is set by the frequency difference between the two. The lattice interfringe is 2 µm, that is much smaller than the size of the BEC wave-function which is typically a hundred of µm. B) Illustration of the two-photon process. The two π polarized lasers are detuned from the 2^3P_0 level by Δ=800 MHz.

where $\phi(t) = \delta\omega_{las}t + \varphi$ is the phase difference between the lasers at $z = 0$. Here, $e^{\pm ik_b\hat{z}}$ are translation operators that couple momentum states $e^{\pm ik_b\hat{z}}\,|p\rangle = |p \pm \hbar k_b\rangle$.

3.B Resonant two-photon transfer

First, *a priori*, the Hamiltonian (161) couples an infinite number of momentum states $\{|p + n\hbar k_b\rangle\}_{n\in Z}$. In practice, if the value of the Rabi frequency, that defines the coupling strength, is low enough, we can restrict the analysis to a two level system $\{|p\rangle, |p + \hbar k_b\rangle\}$. Such hypothesis requires the Rabi frequency to be much smaller than the recoil frequency. Leprince (2024) showed numerically that a factor of 4 is enough to suppress the influence of the other levels. He also discusses other regime for which other levels must be taken into account (Béguin et al., 2022). In this work, we will use low enough Rabi frequencies (lower than 3 kHz) so that we couple only two different momentum classes.

Second, by tuning the frequency difference between the two lasers, one can tune the velocity classes that are resonant with the momentum transfer. In order to couple momentum class $|p\rangle$ with $|p + \hbar k_b\rangle$, the frequency difference of the lasers must be

$$\delta\omega_{las}(p) = \frac{k_b}{2m}\,(\hbar k_b - 2p) \tag{162}$$

Figure 44 shows the atomic momentum distribution after the Bragg pulse for a non-resonant detuning (left) and a resonant one (right). The right panel of the figure represents the number of transferred atoms as a function of the laser detuning. At fixed laser detuning $\delta\omega_{las}$, the momentum class that is resonant with the two-photon process is the one for which p satisfies equation (162). The BEC initial state is $|p = 0\rangle$: it is therefore resonant with the two-photon process for $\delta\omega_{las} = \pm\hbar k_b^2/2m$. In the case of a positive detuning, the BEC is transferred to the $|p = +\hbar k_b\rangle$. If the detuning is negative, the atoms are coherently transferred to the $|-\hbar k_b\rangle$ state. Still, if the detuning is not exactly the one given by (162), a transfer can still happen. To

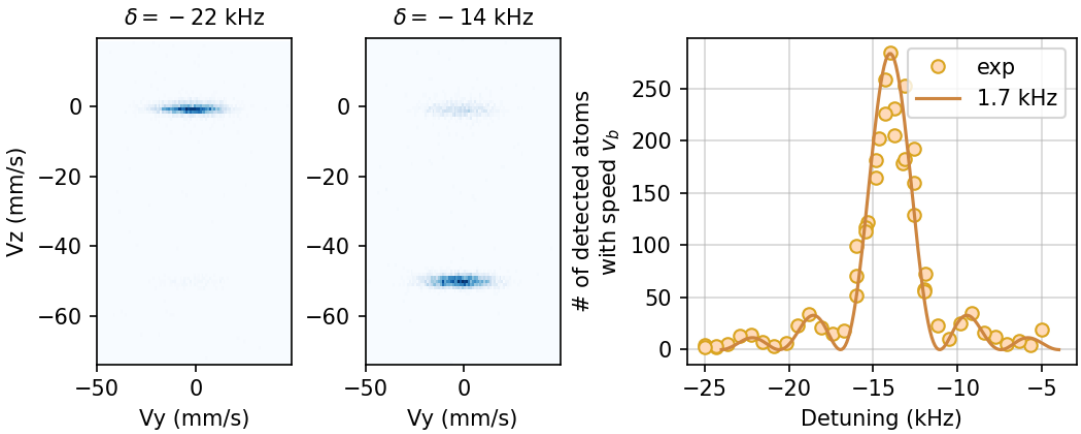

Figure 44: Left: Density of the momentum distribution of the cloud after the Bragg transition. The colorscale represents the atomic density, the darker being the denser. On the first picture, the frequency difference is not set to address the $v_z = 0$ BEC mode. On the second picture, the detuning is resonant with the BEC mode and the zero momentum mode has been transferred to $-v_b = -50$ mm/s. Right: number of detected atoms as a function of the laser detuning. Each dot is the number of atoms for a single realization. We clearly observe that the resonance is around -14 kHz. The solid line is the expected transfer efficiency for a 1.7 kHz π-pulse who's height has been adjusted. ©Theoretical profile courtesy of Ch. Leprince.

estimate it, we write the detuning as

$$\delta = \delta\omega_{las} - \frac{k_b}{2m}(\hbar k_b - 2p) \tag{163}$$

When $\delta = 0$, the process is at resonance. However if $\delta \neq 0$, the transfer might occur if the Rabi frequency is large enough, that is if $\delta/\Omega_R < 1$. Note however that the transfer will be less efficient and oscillate faster. This off-resonance process explains why the resonance curve on Figure 44 is not a Dirac function: its width is given by the Rabi frequency.

3.C Rabi oscillations: chi va piano, va sano e va lontano

As we saw, the characteristic frequency for the two-photon transfer is the Rabi frequency Ω_R (160). When the laser difference frequency is at resonance with one mode k, atoms coherently transfer between states $|k\rangle$ and $|k + k_b\rangle$ with frequency Ω_R. When the momentum class is not perfectly at resonance, that is δ defined by equation (163) is not exactly zero, the oscillation frequency between the two classes and the transfer efficiency is lower. The probability $\mathcal{P}$ for an atom to be transferred reads

$$\mathcal{P}(t) = \frac{\Omega_R}{\Omega}\sin^2(\Omega t/2), \qquad \Omega = \sqrt{\Omega_R^2 + \delta^2}. \tag{164}$$

This is illustrated by the left panel of Figure 45 in which the coherent oscillation of two momentum classes is represented. The blue circles represent the oscillation of the resonant class while the red squares represent those of an off-resonant class speed. Off-resonant momentum classes oscillate faster with a smaller amplitude which is expected from equation (164). Experimentally, the oscillation frequency of the resonant class gives access to the Rabi frequency (and therefore the intensity of the beams). From Figure 45, we measure the value of 1.21(2) kHz.

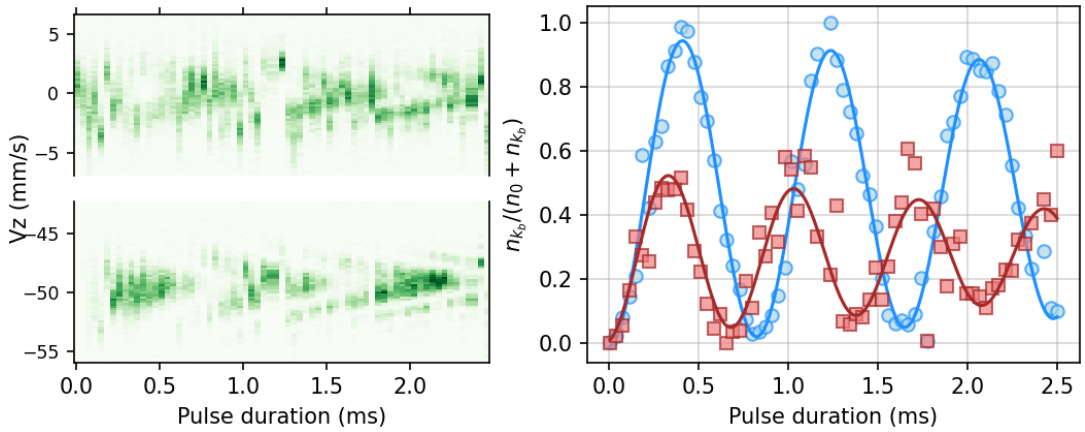

Figure 45: Left: Number of transferred atoms from the BEC $k = 0$ mode to the $k = -k_b$ mode. Here the resonant frequency is -14 kHz. Right: ratio of the transferred population between two momentum modes as a function of time. The blue circles represent the oscillation of the resonant $k = 0$ momentum class while the red squares represent an off resonant velocity class centered at 1.5 mm/s (which represents a 0.8 kHz detuning). The resonant class oscillates at 1.21(2) kHz, which gives the Rabi frequency. The off resonant class oscillates at 1.42(2) kHz, which is consistent with the expected oscillation frequency (164). We observe a damping of the Rabi oscillation for which the typical decay time is 12(5) ms. ®Data taken on the 24/04/23.

This coherent Rabi oscillation illustrates also the possibility to deflect an atomic beam, by lightening the cloud for a duration $t = \pi/\Omega_R$. Such pulse is called a π-pulse and a *mirror* or *deflector*. It is also possible to transfer atoms with a 1/2 probability and therefore to realize a *beam-splitter* with a $\pi/2$ light pulse (Berman and Bian, 1997). In the next subsection, we will optimize this π-pulse to only deflect the BEC.

Equation (164) does not take into account the obvious damping of the oscillation observed on Figure 45. This damping has two origins. The first one is due to the integration volume. Each individual momentum class $|p\rangle$ oscillates at its own frequency given by equation (164), where $\delta \propto k_b p/m$. Physically, we need to define the size of the mode $|0\rangle$ and the mode $|-k_b\rangle$: they cannot be infinitely thin. This choice of integration volume is a trade-off between the noise (the smaller the volume, the smaller the population) and the dephasing. For a volume Δv, the frequency difference will be $k_b \Delta v$. In our configuration and for a $\Delta v = 1$ mm/s which is the one of Figure 45, the frequency difference is 500 Hz.

Another contributing factor is the spontaneous emission. With the intensity that is used to produce Figure 45, Leprince (2024) estimated the spontaneous decay time to 22 ms. This value is consistent with the one we observe[17].

[17]Note that I am writing this paragraph after Eric Cornell's talk at the ICAP24 conference, where he reported the observation of an astonishing coherence time of 8 seconds (Wang et al., 2024). Afterward, he mentioned that "because the theoretical coherence time is 20 seconds, [his] students should not be satisfied until they would have reached it". Nevertheless, here we only aim to get rid of the BEC, hence a coherence time of a few tens of ms is clearly enough.

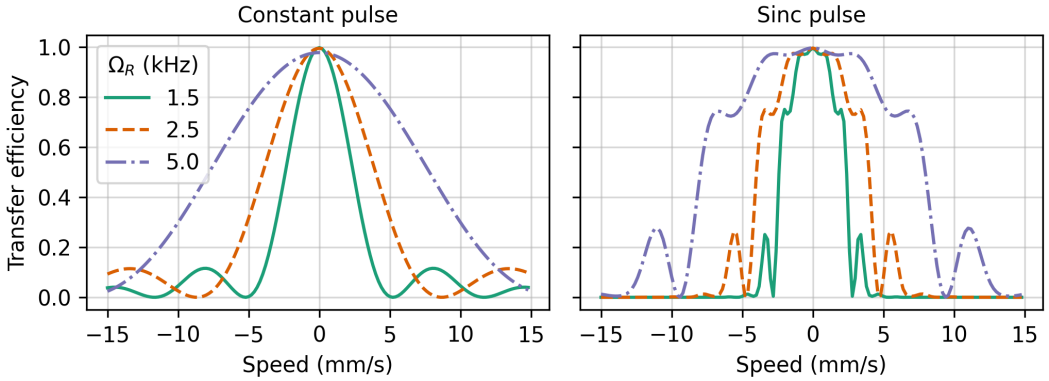

Figure 46: Left: reflectivity profile of constant light pulse for different Rabi frequencies $\Omega_R = 1.5$ kHz (solid green), 2.5 kHz (dashed orange) and 5 kHz (dashed dotted violet). Right: reflectivity profile for sinc shaped pulses with the same mean Rabi frequency. The color and styles corresponds to the one of the left panel. ©Code courtesy of Ch. Leprince.

3.D Mirror, Mirror on the wall, who's the fairest of them all?

In the next chapter, section 3.C, we show that the BEC saturates the detector which degrades the observation of the second pair. We therefore aim to transfer the BEC $v = 0$ mm/s peak while keeping the $v = \pm 10$ mm/s pairs untouched. From now on, we will therefore use pure deflector (π-pulses, or mirror) and study which Rabi frequency allows us to only deflect the BEC. To characterize the reflectivity properties, we will use the notion of reflectivity profile, which gives the probability to deflect each momentum class. The reflectivity profile for different Rabi frequencies is shown on the left panel of Figure 46. One can see that the smaller the Rabi frequency (the longer the light pulse), the smaller the width in momentum of the Bragg deflector. The reflectivity profile of the smallest Rabi frequency (1.5 kHz) has a good width to transfer entirely the BEC. However, it exhibits small wings: the reflectivity is not null for the ± 10 mm/s velocity class. This means that we would also deflect the pairs which is, of course, not what we look for.

A Fourier-like analogy offers a good picture to optimize the reflectivity profile. Even though it is not totally correct, one can think of the reflectivity profile in momentum (hence in detuning) to be the Fourier transform of the light pulse (in time). For the constant pulses we considered so far (the laser intensity is constant), the reflectivity profile looks like a cardinal sine, whose width is fixed by the duration of the pulse.

With that analogy in mind, it is therefore natural to think of a time-dependent Rabi frequency whose shape could be a cardinal sine so that the reflectivity profile is a square. This is what we realized experimentally. However, a cardinal sine is negative while the intensity of a laser field cannot be negative. To overcome this issue, we time modulate the intensity of the field as the absolute value of the cardinal sine. The sign of the cardinal sine is then defined by detuning the phase of one laser by π each time the sinc is negative. Here again, more details about the experimental scheme are provided in Leprince (2024). Even though the instantaneous Rabi frequency $\Omega_R(t)$ now depends on t, we can still define an average Rabi frequency $\bar{\Omega}_R$. This quantity defines the intensity and phase profile of the lasers, hence the width of the reflectivity profile of the pulse. We therefore use the following profile for the Rabi frequency:

$$\Omega_R(t) = \bar{\Omega}_R \mathrm{sinc}\left[\bar{\Omega}_R(t - T/2)\right] \tag{165}$$

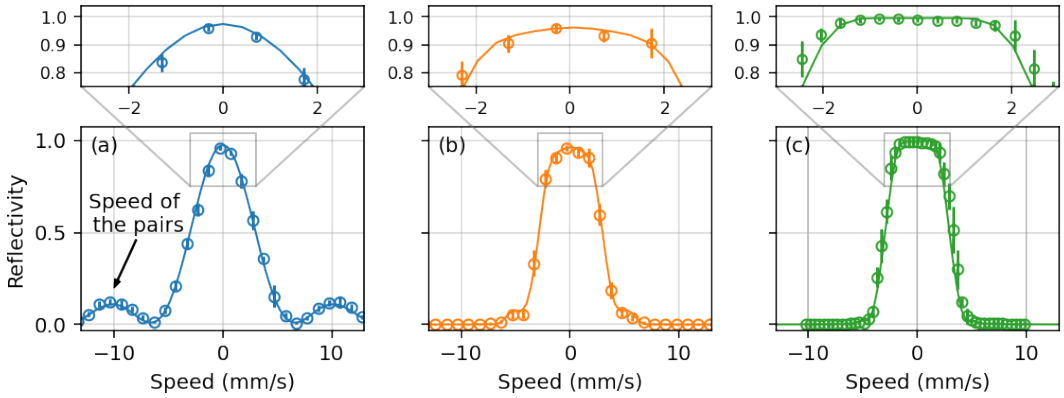

Figure 47: Reflectivity profile of different pulse shapes. (a) constant Rabi frequency, (b) sinc shape and (c) reburp. Circles show experimental measurement and lines are the theoretical curve, with no fit parameter. ®July & August 24. ©Theoretical profile courtesy of Ch. Leprince.

where $\bar{\Omega}_R$ is the "equivalent" Rabi frequency and T the duration of the pulse, the laser intensity being null elsewhere. Here, the equivalent Rabi frequency $\bar{\Omega}_R$ is the Rabi frequency of the equivalent constant π pulse that corresponds to this sinc-shaped pulse. Note we also introduced another parameter, which is the duration of the pulse T. It must be greater than $2\pi/\bar{\Omega}_R$ so that the Rabi frequency is sometimes negative. The duration is typically 2 ms for the reflectivity profile shown in Figure 46. On the right panel, we see that the wings of the reflectivity profile around ±10 mm/s are removed for the 1.5 and 2.5 kHz Rabi frequencies, compared to the constant pulse scenario. This means we can safely remove the BEC while keeping the pairs. We also observe on Figure 46 that the reflectivity profile is flatter at the center and its edges are sharper.

One can see, however, that the reflectivity profile of the sinc pulse is not a perfect square-like function. This is because our Fourier analogy is not accurate when the transferred population becomes larger than typically 10%. More exotic, yet still analytical, pulse shapes were developed and recently implemented in our experiment. Figure 47 shows the measurement of the reflectivity profile for different pulses. Panel (a) and (b) are constant and sinc type pulses with a 1.88 kHz Rabi frequency. Panel (c) represents the reflectivity profile of a so-called *reburp* pulse[18] (McDonald and Warren, 1991; Geen and Freeman, 1991; Luo et al., 2016). Markers represent the experimental points and the solid line the theoretical profile with no adjustable parameter. The small bounces visible on the reflectivity profile of Figure 46 are suppressed due to the integration volume δV_z. We clearly see here that the reflectivity profile is null at ± 10 mm/s for the *sinc* and *reburp* pulses. This means that we can definitely remove a major part of the BEC while keeping the sidebands untouched.

[18] The name *rRE-BURP* stands for Refocusing Band-Selective Pulse with Uniform Response and Phase. It is defined in terms of a Fourier series as $\Omega_{\mathrm{R}}(t) = \Omega_{\mathrm{M}}\left[A_0 + \sum_{n=1} A_n \cos(n\Omega_{\mathrm{S}} t)\right]$ for $0 \leq t \leq 2\pi/\Omega_{\mathrm{S}}$, where $\Omega_{\mathrm{S}} = 2A_0\Omega_{\mathrm{M}}$ and the A_n coefficients, experimentally implemented up to the 15th order.

Summary This section introduces Bragg diffraction as a tool to get rid of the saturation of the BEC. By shaping the lasers intensity and the phase difference between them, we are able to realize sharp deflectors to remove the BEC without affecting the pairs.

4. Measuring the BEC properties

The main disadvantage of our experiment is our inability to measure precisely the atom number in the BEC. This is due to the saturation of the detector, that we discuss in the next chapter, especially section 3.C. Second, we detect the BEC after a 307 ms time-of-flight hence we cannot measure the in-situ size of the cloud. It is worth emphasizing that knowing the properties of the BEC is fundamental to compare with theory. In this subsection, we use three different methods to recover the properties of our gas. In part 4.A, we measure the size of the BEC after the 307 ms time-of-flight and assess its *in-situ* properties from the evolution of the wave-function. In subsection 4.B, we recover the speed of sound measuring the momentum of the two-sidebands excited at parametric resonance. In subsection 4.C, we probe the *in-situ* mean field using the Bragg beams we introduced in the last section. This section re-uses the notations and the description of the BEC introduced in the first chapter, section 1.A.

4.A From its size after a time-of-flight

Castin-Dum expansion

When the trapping frequencies are known, the *in situ* measurement of one of the Thomas-Fermi radius allows one to recover all the gas properties. In our setup, we do not have access to the *in situ* density due to a poor optical resolution. We therefore measure the size of the BEC after a 307 ms time-of-flight, the time during which atoms fall onto the detector. Castin and Dum (1996) showed that, within the Thomas-Fermi approximation, the initial wave-function Ψ_0 expands as

$$\Psi_0(r,z,t) \propto \Psi_0(\frac{r}{\lambda_\perp(t)}, \frac{z}{\lambda_z(t)}, 0) \tag{166}$$

where, at zeroth and second order in $\omega_z/\omega_\perp$, the evolution of the scale factors are

$$\begin{aligned} \lambda_\perp(t) =& \sqrt{1+\omega_\perp^2 t^2} \\ \lambda_z(t) =& 1 + \frac{\omega_z^2}{\omega_\perp^2}\left(\omega_\perp t \arctan\omega_\perp t - \ln\sqrt{1+(\omega_\perp t)^2}\right). \end{aligned} \tag{167}$$

Protocol and results

We produce a typical BEC in a cross dipole trap with frequencies of $\omega_\perp/2\pi$ =1050(50) Hz and $\omega_z/2\pi$ =30(5) Hz. To measure the transverse radius, we use the reconstructed data along the Y direction. We fit the histogram for each shot with a Gaussian function and an inverted parabola, as shown on the right panel of Figure 48. Equation (167) links the measured radius to the *in trap* one. From the Gaussian width $\sigma_\perp^{gaus}$, we recover the BEC properties described in the Gaussian Ansatz description and from the Thomas-Fermi radius, we recover the properties of the BEC in the 3D cigar-shape regime. In both regimes, the radial profile depends on the longitudinal position. Here we are integrating over the longitudinal axis: the measured

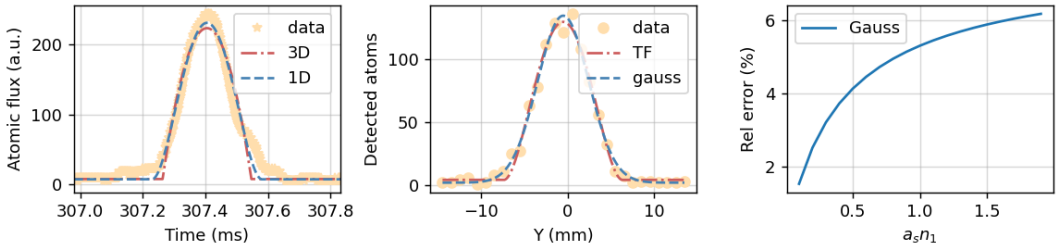

Figure 48: Fit of the density profile of the BEC after a time of flight. Left: the density profile is recorded with an oscilloscope plugged directly on the MCP. The density profile is adjusted with an inverted parabola (dashed blue) and an inverted parabola squared (dashed dotted red). Middle: Fit of the transverse density profile using a Thomas-Fermi profile (dashed dotted red) or a Gaussian (dashed blue). The left panel is a single shot signal and the middle is averaged over 15 realizations. Experiment realized on the 11/04/2024. Right: relative difference between the radius of the integrated profile and of the transverse profile at $z = 0$. The integrated profile is smaller up to a few percents. This is not so negligible as thermodynamics quantities scale with the radius to the power 4-5.

Table III.1: Bose-Einstein Condensate properties derived from the measurement of the size of the cloud after a 307 ms time of flight. The estimation of the errors takes into account of the 1000 measurements and the errors on the trap frequencies. Each line uses a different fit. The first one the Thomas-Fermi radius along the elongated direction Z_{3D} given by equation (8). The second line is the transverse Thomas-Fermi radius fitted using equation (6). The last line is derived using the width from the Gaussian Ansatz (16). ®April, 11th of 2024.

Measure	μ (kHz)	$a_s n_1$	Nat (10^3)	L (μm)	R(μm)
Z_{3D}	1.8(6)	0.7(2)	12(9)	200(20)	2(1)
$R_\perp^{TF}$	1.95(9)	0.95(5)	15(2)	200(10)	2.7(3)
$\sigma_\perp^{gaus}$	2.0(2)	0.7(3)	10(4)	150(40)	2.2(5)

transverse size is therefore smaller. Right panel of Figure 48 shows the relative difference between both profiles as a function of $a_s n_1$. Even though the difference is about 5%, this uncertainty changes the BEC properties of the order of the statistical uncertainties that are reported here. This can be understood by the fact that $a_s n_1$ varies as the fourth power of the widths in the Gaussian Ansatz.

In the vertical direction (time), one has to make sure that the BEC does not saturate the detector. The atomic flux is recorded with an oscilloscope to prevent the saturation of the electronics and a Bragg deflector was used that prevent the MCP channel saturation. Because we do not observe phase fluctuations, the BEC properties are recovered assuming that we are in the 3D cigar shaped regime or the Gaussian Ansatz. The measurement is performed over 1000 shots and the uncertainties are a combination of statistical dispersion and the measured uncertainty on the trap frequencies.

Note however that this method has a severe drawback: when we turn off the trap, the Raman transition changes the atomic state for $m = 1$ to $m = 0$. This changes the scattering length from 7 to 5 nm (Lopes, 2014).

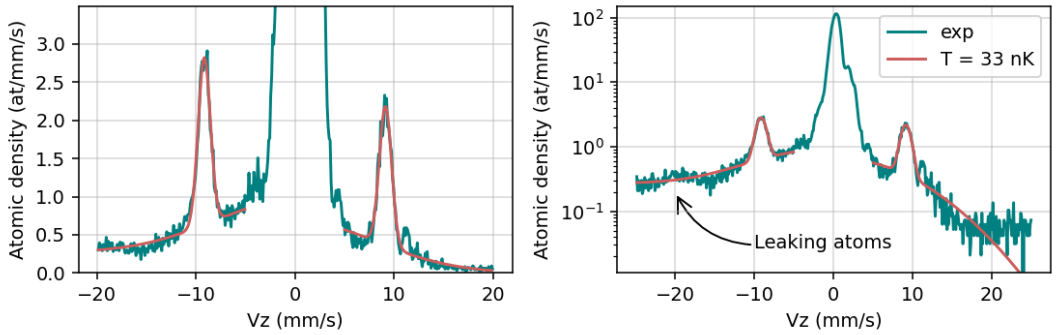

Figure 49: Fit (red) of the $\pm k_{ph}$ momentum distribution (green). The fit function is a double Gaussian function to which is added a thermal part (zero centered Gaussian) and a Heaviside function that ables one to take into account the leakage phenomenon.

4.B From the quasi-particle excitations

Method

The speed of sound can also be measured by changing the trap frequency so that the BEC enters into a breathing mode at $2\omega_\perp$. It excites two Bogoliubov modes $(\omega_\perp, \pm k_{ph})$. Repeating the experiment enables to distinguish clearly and fit the phonon peaks. The relation between the momentum k_{ph} and the excitation energy $\hbar\omega_\perp$ is given by the Bogoliubov dispersion relation, characterized by the sound speed

$$c_s = \frac{1}{k_{ph}}\sqrt{\omega_\perp^2 - \left(\frac{\hbar k_{ph}^2}{2m}\right)^2}. \tag{168}$$

The speed of sound gives then the value of $a_s n_1$ (at the center of the trap) which completely characterized the gas properties.
The center of the peaks are fitted using a double Gaussian (one for each peak) to which we add another large and zero centered Gaussian to take into account the temperature. We finally add a Heaviside step function to take into account the leaking atoms' phenomenon. To obtain low temperatures, the trap final's depth is quite small, and we observe that atoms continuously leak from the trap. This can be seen on the asymmetry of the density profile in Figure 49: the negative side of the momentum distribution (atoms that arrive first on the detector) has an offset, which is not the case of the positive one.

Results

We measure the speed difference between the two excitations to be 9.1(1) mm/s from which we deduce a speed of sound of 10.5(6). From the speed of sound, one can recover the properties of the gas in the different regime. Results are given in Table III.2. The different descriptions do not give the same result, but this is expected as they are valid in different range. With all descriptions, the $a_s n_1$ parameter is not far from 1 which means the gas is neither in the 3D Thomas-Fermi cigar nor in the 1D mean field regime. The Gaussian Ansatz yields $a_s n_1 = 1.3(1)$ and the generalized crossover $a_s n_1 = 1.0(1)$: the difference is not huge regarding the error bars. The number of atoms is therefore around $15 - 20 \cdot 10^3$ and the BEC length is a bit lower than 200 µm. The temperature of the gas is measured to be 30 nK and it should be compared to $mc^2/k_B = 53(6)$ nK.

Table III.2: Bose-Einstein Condensate properties derived from the speed of sound value for the different theories (chemical potential, 1D density, atom number and BEC length). The trap properties were 30(5) Hz along the vertical direction and 1.05(5) kHz in the transverse plane. The phonons were excited at resonance with a momentum of 9.1(1) mm/s, which gives a speed of sound of 10.5(6) mm/s. The measured temperature was 30 nK that should be compared to the chemical potential minus its zero point energy that is $mc^2 = 53(6)$ µK . Dataset taken on the 11th, April of 2024 (051).

Theory	µ (kHz)	$a_s n_1$	Nat (10^3)	L (µm)
3D cigar	2.2(2)	1.1(1)	19(3)	200(10)
1D mean field	2.2(2)	0.5(1)	8(1)	160(30)
Gaussian Ansatz	2.6(2)	1.3(1)	21(3)	190(50)
Generalized crossover	2.3(2)	1.0(1)	14(2)	170(30)

4.C By measuring the *in situ* mean field

Expected mean-field shift on the quasi-particle branch

The two Bragg laser beams that we use to deflect the BEC can also be used *in* the trap. In this scenario, the description we gave of the laser-matter interaction is no longer correct: the atomic interactions must be taken into account. In fact, this two-photon process was widely used to probe the properties of the BEC. The first spectroscopy of a Bose-Einstein condensate was realized by Stenger et al. (1999). Authors observed a shift of the resonance frequency compared to the dilute case that is due to the interactions: the resonance shift gives access to the chemical potential, both in the particle and the phonon branches (Stamper-Kurn et al., 1999). The k-dependance of this resonance shift was then used by Steinhauer et al. (2002) to measure the excitation dispersion relation. The width of this Bragg resonance was also used by Richard et al. (2003) to probe the coherence length in a really elongated BEC. Here we aim to use the line-shift of the resonance to measure the chemical potential hence the atom number.

Our configuration, that we introduced in the apparatus chapter, is sketched on the inset of Figure 50: the Bragg wave-vector is 3 µm^{-1} while the healing length is a typically less than 1 µm[19]. This means that the probed excitation lies on the particle branch. When the gas does not interact, the resonance to transfer the BEC mode $|p = 0\rangle$ is ν_0 and is fixed by the Doppler shift $h\nu_0 = \hbar^2 k_b^2/2m$. For an interacting BEC, there is an additional line-shift which is due to the interactions. On the particle-like branch, Stamper-Kurn et al. (2001) showed its expression is given by

$$\Delta\nu = \nu - \nu_0 = g\,\langle\hat{n}\rangle_{BEC} = \frac{1}{N}\int g n^2(\mathrm{r})\mathrm{dr}. \tag{169}$$

The frequency difference is given by the product of the interaction constant time the atomic density evaluated in the ground state of the system: the BEC. Within the Thomas-Fermi regime, this integral is

$$\Delta\nu_{TF} = \frac{4\mu}{7h} \tag{170}$$

[19]The sound speed we measure is typically 11 mm/s and the Bragg velocity is 50 mm/s. We have therefore $k_b\xi \sim 5$, where ξ is the healing length of the BEC.

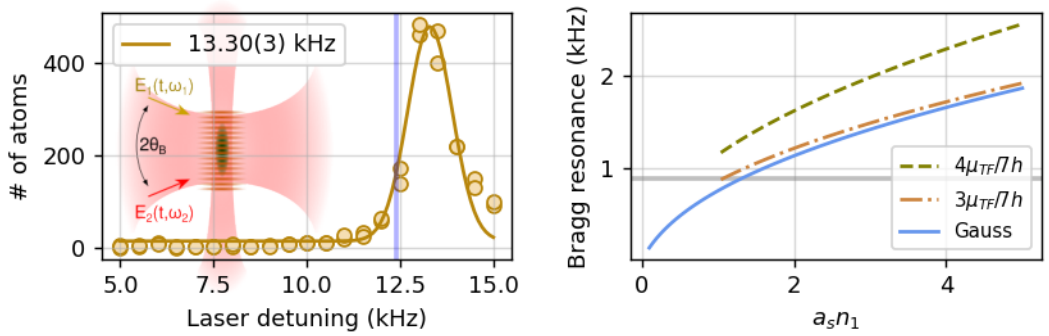

Figure 50: Left: Number of diffracted atoms as a function of the detuning between the two laser beams. The circle are experimental points on a single shot and the solid line is a Gaussian fit centers on 13.3 kHz. The uncertainty is associated to the fit uncertainty. The vertical blue line indicates the expected value for a non-interacting gas. Right: expected mean field detuning as a function of the $a_s n_1$ parameter. In the Thomas Fermi regime, the chemical potential is given by $2\hbar\omega_\perp\sqrt{a_s n_1}$ and the detuning is expected to be $4\mu/7h$ (green dashed line). The dashed-dotted red line is proportional the $3\mu/7h$ detuning expected by the 1D calculation (171). The solid line is the numerical integration of the expected detuning in the Gaussian regime (172). The horizontal grey line is the measured detuning from the left panel that intersects the Gaussian line at $a_s n_1 = 1.3$.

and this linear dependence was shown to be accurate by Stenger et al. (1999).

Result: The spectroscopy resonance is shown on the left panel of Figure 50. On the y axis lies the number of diffracted atoms as a function of the laser detuning. The Doppler shift at 12.41(3) kHz is represented with the blue vertical line. We fit the resonance with a Gaussian curve centered at 13.30(3) kHz. This corresponds to a shift of $\Delta\nu$=0.89 kHz. From equation (170), we deduce that the chemical potential is 1.6 kHz.

Conclusion: In equation (170), we described the gas in the Thomas-Fermi approximation. Such hypothesis should be *a posteriori* checked. In the 3D cigar-shape regime, the chemical potential is linked to $a_s n_1$ taken at the center of the trap through $\mu = 2\hbar\omega_\perp\sqrt{a_s n_1}$. The Thomas-Fermi approximation is valid for $a_s n_1 \gg 1$. The transverse trap frequency is 1 kHz, hence $a_s n_1 = 0.9$. For such low density, the Thomas-Fermi approximation is expected to break down.

History repeats: 3D is not 1D

Our situation here looks like what happened in the late 90's, when the sound speed measured by Andrews et al. (1997) was lower by a factor $\sqrt{2}$ than the expected. To explain such difference, Zaremba (1998) averaged the density over the transverse axis of the elongated BEC to derive the speed of sound of the one-dimensional excitations. The transversely integrated density being of course smaller than the peak density, the effective 1D speed of sound is smaller (Pitaevskiĭ and Stringari, 2016). In the Thomas-Fermi approximation, the local excitation energy $mc^2(\mathrm{r}) = gn(\mathrm{r})$. For an axial excitation in an elongated system we have $g_1 n_1 = mc_s^2$. It makes sense therefore to evaluate integral (169) using the one dimensional density n_1 and the effective 1D coupling constant.

$$h\Delta\nu' = \frac{1}{N}\int g_1 n_1^2(z)\mathrm{d}z \tag{171}$$

where $g_1 n_1 = mc_s^2$, and c_s is the local speed of sound of the axial excitations. For a cigar BEC, this 1D integral is $3\mu/7$. The difference with the previous formula is small: we replaced the "4" by a "3". This leads to a chemical potential of 2.1 kHz and a 1D parameter $a_s n_1 \sim 1$. Still this value is quite low to ensure validity of the Thomas-Fermi approximation. In this intermediate regime, we should use the Gaussian Ansatz to describe our cloud. We can compute the expected shift by evaluating the integral (169)

$$\Delta\nu = \frac{g}{Nh}\int \frac{1}{\pi\sigma^2}\frac{n_1^2(z)}{\pi\sigma^2}e^{-2r^2/\sigma^2}\,\mathrm{dr} = \frac{1}{Nh}\int g_1 n_1^2 \mathrm{d}z. \tag{172}$$

With this description, the 3D integral of gn^2 is the same as the 1D integral of $g_1 n_1^2$. I did not find an analytical expression for this integral. Still, a numerical integration is possible and is shown on Figure 50. The solid blue line of the right panel of Figure 50 represents the expected detuning from equation (172) as a function of the value $a_s n_1(0)$. Here we observe that for a 0.9 kHz shift (grey line), we expect $a_s n_1$=1.3. This result is in agreement with the other one found with the speed of sound method in section 4.B.

Summary We used three different methods to recover the atomic density: time-of-flight expansion, Bogoliubov excitation spectrum, and *in situ* spectroscopy. We showed that the parameter $a_s n_1$, which describes the regime of the gas, was close to 1. It indicates that the gas is neither described by the 1D mean field regime nor by the 3D cigar-shape regime. Within the Gaussian Ansatz formalism, we measured the 1D parameter to be $a_s n_1 = 1.3(1)$, indicating that the number of atoms[20] is roughly twenty thousand and the chemical potential is 2.6(2) kHz. The typical temperature is 30 nK and should be compared with $mc^2/k_B = 53(6)$ nK for a speed of sound of 10.5(6) mm/s.

[20]For a gas in a trap (30 Hz, 1 kHz) and a parameter $a_s n_1(0) = 1.3$, the parameter we introduced in the BEC description section parameter have the following value. The $a_s n_1$ averaged value is $a_s N/L = 0.8$, $\chi = 20$, and the peak atomic density is typically $3 \cdot 10^{13}$ at/cm^3. The BEC length is 180 µm while the correlation length is larger than 1 mm which means we do have a BEC and not a quasi-BEC. The healing length is 1.1 µm and the BEC width typically 2.5 µm. The gas is indeed far from the Lieb-Liniger regime as $\gamma = 3 \cdot 10^{-5}$

Chapter IV

The microchannel plate to probe momentum correlations

The main advantage of using metastable helium lies in the ability to detect individual atoms. We therefore dedicate this chapter to the description of our detector, the MicroChannel Plate (MCP) and the delay lines. In the first section, we explain how the detector works (section 1.A) and allows to reconstruct the position and the arrival time of single atoms (section 1.B). We describe in particular the details of the reconstruction program. In the second section, we detail the installation of a shield that protects the MCP, which was heated by the vertical laser. The last section models the MCP as N parallel on-off detectors. We also emphasize the limits of the detector: the maximum number of particles that can be detected in section 3.B and the saturation issues in section 3.C.

What we knew, what is new ? The installation of the shield to protect the MCP was done in the early stage of my work in the laboratory. Its side effect on the detectivity led us to work on and change the reconstruction program that are described here.

1. MCP detection principle

This section introduces the MCP operation: a metastable helium atom colliding a surface takes off an electron which is accelerated by a strong electric field. Collisions in the channel trigger an electronic cascade. The signal then propagates into two perpendiculars delay lines placed below the MCP and is digitized. The atom position and impact time on the detector can then be reconstructed.

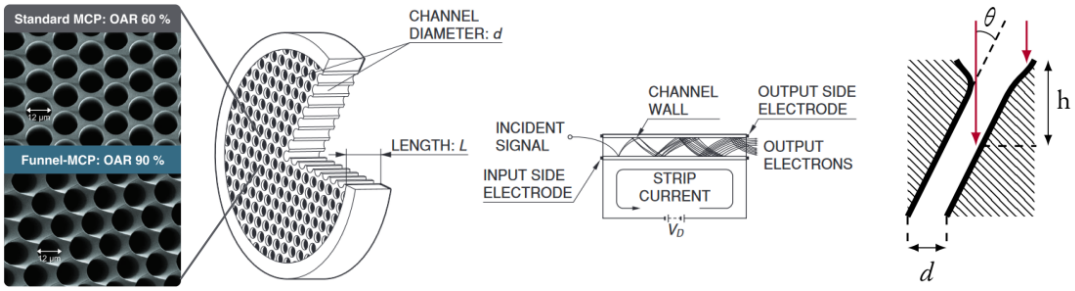

Figure 51: Left: Scheme of a MCP and pictures of the two types of MCP send by Hamamatsu. The new generation of *funnel type* MCPs has a greater open-air ratio which increases the probability for the electron to trigger an electronic cascade. This type of MCP was installed on our experiment by Marolleau (2022). Middle: principle of the electronic cascade triggered by an incoming atom : the teared out electron is accelerated by an electric field of 1.3 kV/mm and is expected to takes off an other electron when colliding in the channel. Repeating this process, a single electron is converted into an electronic cascade. Right: the tilt θ of the channel forces an incoming atom to collide on the surface and set also the time precision. Indeed the time uncertainty depends on the channel size and tilt as well as on the atom velocity v as $\Delta t = d/v \tan\theta$. ©Hamamatsu Photonics and Marolleau (2022).

1.A From a metastable atom to an electronic signal

A metastable helium atom generating an electronic cascade

When a He* atom hits the inconel[1] surface of the MCP, the probability it takes off an electron is expected to be around 50-70 % (Vassen et al., 2012). The teared out electron must then enter the channel and triggers an electronic cascade, as it is accelerated by a strong electric field of 1.3 kV/mm.

In order to increase the probability for the electron to *stay* in the channel and be accelerated, the open-air ratio, surface covered by channels over the total surface of the MCP, was increased from 50% to 90%, as illustrated in Figure 51. When an atom enters a channel, as the latter is tilted, it can take off an electron at the beginning of the channel or after a maximal distance $h = d/\tan\theta$ where $\theta = 20$ is the tilt angle of the channel and $d = 12$ µm is the diameter of the channel. As the MCP is located 45 cm below the science chamber, the helium velocity when they enter a channel is roughly 3 m/s hence the MCP geometry gives a lower bound for the time resolution of 5 µs.

Signal propagation in the delay lines

Above the MCP are installed two perpendicular delay line : a signal triggered by the electronic cascade will then propagates along the two delay lines, on both direction. The line being coiled, the velocity at which the pulse propagates in the transverse direction is not the speed of light, but the speed of light divided by the loop number. The number of loops is 100 in our case, which gives an effective velocity of 1 mm/ns. The transverse velocity along each axis are slightly different as it is 1.02 mm/ns along x and 1.13 mm/ns along Y. This value depends on the manufactured delay lines. Once the signal exited the delay line, it is amplified with a

[1] Inconel is a nickel-chromium-based superalloy "often utilized in extreme environments where components are subjected to high temperature, pressure or mechanical loads" (Wikipedia).

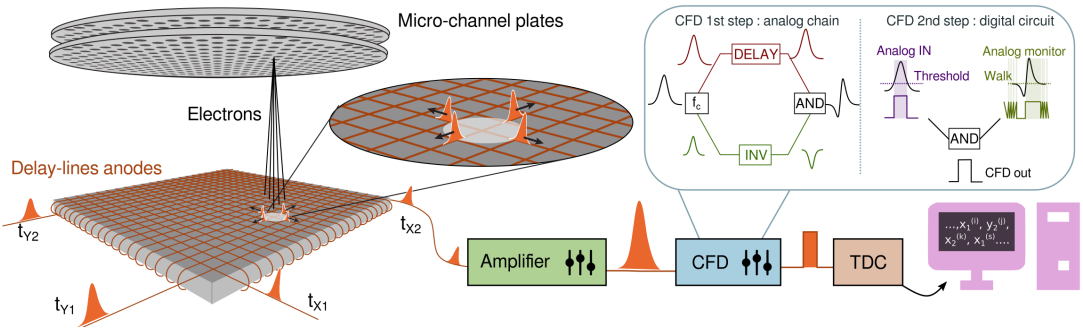

Figure 52: Propagation and amplification of the electronic cascade into a time quadruplet. The signal generated by the electronic cascade propagates without dispersion through the delay line. The later being coiled, the transverse velocity of the pulse is not the speed of light but 1 mm/ns. The signal of each channel is then amplified and digitized by the CFD and TDC (see text for description). The computer collects then a list of arrival time on each channel X_1, X_2, Y_1 and Y_2. ©Left figure courtesy of David Clément (2019).

gain of 80 and digitized by the constant fraction discriminator (CFD) and the time-to-digital discriminator (TDC), as illustrated in Figure 52.

The Constant Fraction Discriminator

The role of the CFD is to produce an analog gate signal whose leading edge does not depend on the amplitude of the incoming pulse.

The CFD analog chain: constructs the so-called *analog monitor signal*. To do so, it splits the signal in two, characterized by the fraction f_c, whose recommended value is 0.35. This value is the one set on our experiment. The first part of the signal is passed through a 2 ns delay line, which should be compared with the typical width of a pulse, a few ns[2]. The second signal is inverted. The *analog monitor* signal is then the sum of those two signals $A_{mon}(t) = f_c A_{in}(t) - A_{in}(t-\tau)$. This is represented by the first CFD inset of Figure 52.

The CFD digital circuit generates a digital pulse from the analog monitor signal and the input signal. The parameters to tune the properties of the CFD output are the *Threshold* and the *Walk* level. The analog gate generated signal is positive if the two following conditions are met:

1. the input signal A_{in} must be above the threshold value (set by the user),
2. the analog monitor signal $A_{mon}(t)$ is greater than the Walk level Z.

Those two conditions are represented in the right CFD inset of Figure 52.

[2] In the CFD Manual, RoentDek suggests the following to set the delay line value: "*If the pulse rise time RT is defined as the time from reaching 10% to 90% of the signal maximum, the delay shall be equal or smaller (50-80%) than this rise time RT, depending on the CFD fraction ratio f. For small CFD fractions (<0.5), a thumb rule for an appropriate CFD delay D is D = RT (1-f).*" This value was set on 07/07/2022 in our experiment.

The time-to-digital discriminator

The analog gate signal generated by the CFD is then digitized by the TDC, based on a Field Programmable Gate Array (FPGA) chip developed by R. Sellem and D. Heurteau within the Paris-Saclay University. It can work up to a rate of 4.1 MHz per channel, with an elementary coding step of 120 ps and a resolution of 62(3) ps (Nogrette et al., 2015). I will not provide further details on how the TDC works and refer the interested reader to the previous reference or to Marolleau (2022) and Cayla (2018). We assume for the following that the TDC sends a list of digitized times per channel to the computer.

1.B Reconstruction of individual particles

We now move on to the description of the reconstruction algorithm that identifies atoms from the list of times sent by the TDC. The first step of the reconstruction algorithm is the so-called *demuxing operation*[3], which consists of sorting elements by time and by channel. The second step is to discriminate which times can match an atom and gather times by quadruplets. As I neither studied not study nor modify the first step of this program, the interested reader should refer to Marolleau (2022) for detailed explanations. Here, I will focus on the reconstruction part, assuming the program starts with four sorted lists of times X1, X2, Y1, and Y2, one for each channel.

Timing conditions that must satisfy a reconstructed atom

When an atom triggers an electronic fountain, one should obtain four times t_{X1}, t_{X2}, t_{Y1}, and t_{Y2}. Note that all these events should be *close enough*. In the terminology introduced by Schellekens (2007), the events should belong to the same *time-bulb*, which is visually represented in light green in Figure 53. In other words, the time difference between each time should be lower than the propagation time t_D along the entire MCP diameter D:

$$\forall i,j, \quad |t_{Xi} - t_{Xj}| < t_D \quad ; \quad |t_{Xi} - t_{Yj}| < t_D \quad ; \quad |t_{Yi} - t_{Yj}| < t_D \tag{173}$$

This will be useful not to try all quadruplets in the algorithm. The time difference between the X delay lines gives the position of the atom on the X axis and so for the Y axis. Indeed, the position of the detected atom depends only on the velocity of the propagation signal along each delay line :

$$X = \frac{c_{x,\perp}}{2}(t_{X1} - t_{X2}) \quad , \quad Y = \frac{c_{y,\perp}}{2}(t_{Y1} - t_{Y2}) \tag{174}$$

where $c_{x,\perp} = 1.02$ mm/ns is the velocity of the signal along the X axis and $c_y = 1.13$ mm/ns along the Y axis. Those values depend on each delay line but should be the same, with 10% construction tolerance.
The position of the detected atoms must be *on* the MCP and one must therefore have

$$X^2 + Y^2 \leq D^2/4. \tag{175}$$

The total length of the wires being constant, the time it takes for the signal to go through it should be constant too. The propagation time through the X delay line should be equal to the one along Y (up to a constant) and therefore the quantity S

$$S \equiv t_{X1} + t_{X2} - t_{Y1} - t_{Y2} \sim Cst \tag{176}$$

[3]This name refers to a demultiplexer (demux), which is a digital circuit that takes a single input signal and routes it to one of several output lines, based on a set of control signals (selectors).

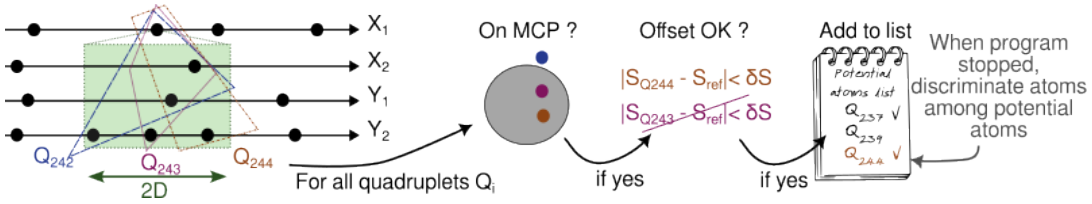

Figure 53: Scheme of the reconstruction algorithm. We loop over the X1 channel and test all quadruplets in the X1 time-bulb, represented in light green in the figure. In the example above, there are three candidates. Among those quadruplets, we select those who fulfill conditions (173), (175) and (177) to the *potential atoms* list. Here, Q_{243} and Q_{244} felt on the MCP but only the offset of Q_{244} was within the authorized range. Once we reconstructed all potential atoms, atoms are extracted from this list, but making sure that a single time is not involved in two different quadruplets.

should be conserved. In practice, the offset is not constant but depends on the location on the MCP. This was already the case with the previous MCP and electronics generation (Schellekens, 2007), and it was reported in other setups (O. Jagutzki et al., 2002). Each new detector must be calibrated to have a reference map of the local offset value $S^{ref}(X,Y)$. We will describe the calibration of the detector in the next section 2.B. Once calibrated, any atom candidate that will be reconstructed must satisfy the condition

$$|t_{X1} + t_{X2} - t_{Y1} - t_{Y2} - S^{ref}(X,Y)| < \epsilon_S \tag{177}$$

where ϵ_S is small compare to D. It is 6 time units, compared to the 700 time units diameter of the MCP.

Description of the reconstruction algorithm

From a technical perspective, the algorithm was developed in `C++`. Its execution time is typically a few hundred milliseconds, much shorter than an experimental cycle (10 seconds), allowing for real-time reconstruction. The first algorithm to account for the atoms' impact positions was implemented by Schellekens (2007) and improved by Perrin (2008). It was rewritten from scratch by Amodjee (2020) when the new electronics developed by Nogrette et al. (2015) were installed. Since summer 2022, the program has been monitored with Git and stored in a public GitLab repository.

In addition to the algorithm currently running on the experiment's computer, it is now possible to re-run the reconstruction algorithm with different parameters using the heliumtools re-reconstruction module[4].

The reconstruction algorithm pseudo-code is written in Program 54. We loop over one channel, here $X_1 = [a, ...]$, and select all events on the tree other channels in the time window $[a - D, a + D]$. For all quadruplet in this window event, we test conditions (175) and (177) i.e. if the atom candidate is on the MCP and if its offset is near the reference value $S^{ref}(X,Y)$. If yes, we add it to the list of *potential atoms*, which is not the definitive list of atoms. We then sort this potential atoms list by their offset difference value and loop over the elements of the list, the different *candidates*. We do not want a single time signal to reconstruct two different atoms. Therefore, we accept a candidate only if each time that define its location is

[4]This is possible if the raw data are saved. We do not save all data on a daily basis because of the memory usage. In 2023, we saved all data resulting in a 610 Go folder. We decided to save raw data only when needed.

not already in the atom list. Because the list was ordered by offset difference value, it means that we give the priority to small offset discrepancy.

```
D = 80 # diameter of the MCP, in TDC time unit
type X1, X2, Y1, Y2  = list #of ordered times
possible_atoms = [] # empty list
while X1.is_not_empty():
    a = X1.begin()
    # Suppress elements that will never be used since X1 is time
    ↪  ordered
    {X2, Y1, Y2}.suppress_all_events_before(a - D)
    selected_events = {[a], X2, Y1, Y2}.select_all_events_before(a+D)
    for each quadruplet Q = {a, b, c, d} in selected_events:
^^I    bool test1 = is_the_atom_on_MCP(Q)
^^I    bool test2 = is_offset_zero(Q)
        if test1 & test2 :
            possible_atoms.append({a, b, c, d})
    X1.pop(a)
# We sort the potential atom list by their offset value
# to iterate over the potential_atom list
possible_atoms = sort_by_absolute_offset_value(possible_atoms)
atoms = []
# Test all candidate: we do not want the same time
# to reconstruct 2 different atoms
for candidate in possible_atoms:
    is_true_atom = True
    for i in range(4):
        time_Xi = candidate[i]
        # check that each time of the atom is not
        # already in the atom list
        if candidate.is_in(atoms[:,i]):
            is_true_atom=False
    if is_true_atom:
        atoms.append(candidate)
```

Figure 54: Pseudo-code of the reconstruction

Summary This section went through the detection process of single atoms: the latter provokes an electronic cascade that generates four impulsions, propagating through delay lines. The arrival time of each signal is then digitalized by a TDC and saved onto a computer. *A posteriori* (but in real time compare to the experiment cycle that is 10s), an algorithm sorts out the digital times to reconstruct the position and impact time of individual particles.

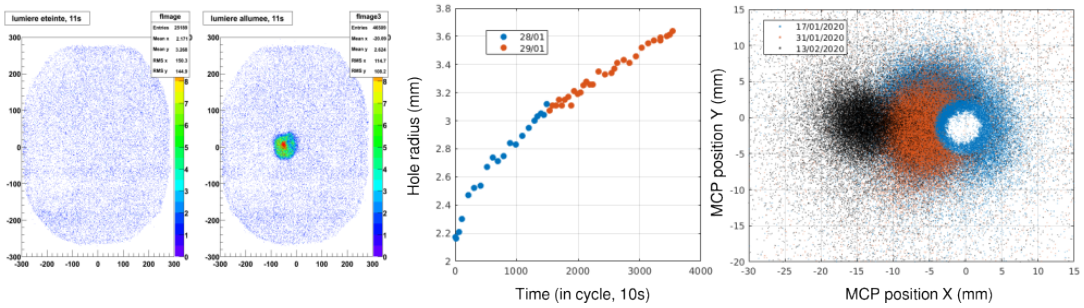

Figure 55: Left: Dark signal of the detector reported by Jaskula (2010). The MCP map is acquired during 11 s and signal is due to the "*ambient light reaching the detector through the upper viewports*". On the right subplot, the dipole trap was turned on for several seconds to heat the plate before it is switched off for the acquisition. We observe a clear effect of the laser on a 3 cm region. Note that with the Hamamatsu model, the dark current is much lower and can be explained by residual ions in the vacuum chamber. Middle: evolution of the hole radius of the MCP on the 28th of January, 2020. Time is in cycle unit, typically 10 seconds. The dipole trap is off for the first 6 seconds and then ramped from 0 to 1.8 W in 500 ms, kept for 600 ms at maximum power and damped to 0.5 W in 4 seconds. Right: Position of BEC after it was kicked by the Raman transfer. Blue is the original position of the BEC, orange is the one after the first Raman beam was tilted and the dark one is the one after both Raman beam were tilted with respect to the Y axis. Because of optical access, it is not possible to increase this angle.

2. Protection and analysis of our MCP

2.A Protection of the detector

The MCP under fire: genesis of the problem

Our BEC geometry is cigar-shaped in the vertical direction and this trap is created using a tightly focused vertical laser and a shallow horizontal beam. After RF evaporation, the magnetically trapped cloud is transferred to the dipole trap through the single vertical beam. This vertical geometry is such that the laser beam hits and heats the detector, on a scale of 1 cm^2. When installed in 2009, the team made sure that the 1 W dipole trap heating effect on the MCP was not a problem (Jaskula, 2010), even thought they observed an effect on the dark current as shown in Figure 55. Upon changing the dipole trap laser source, the increased power of 4 W did not damage the detector. The latter was burnt in 2019 when exposed to 4W for the total duration of the experimental cycle[5], rendering it unable to detect atoms any longer in this 1 cm^2 region. The new MCP model installed in 2019 developed by Hamamatsu, was expected to have a better quantum efficiency (Marolleau, 2022). It turns out that its resistance to heat was also lower hence it was also burnt in January 2020 with a 3.5 W beam ramping to 0.5 W in 4 seconds.

[5]The ODT beam was kept on during the MOT and magnetic trap steps in order to keep hot AOMs so that the laser power at the moment the trap is loaded was nice.

The team in hot water: choice of the shield solution

The possibilities to overcome this issue were the following.

1. Change the geometry to have a cigar shaped BEC in the horizontal direction.
2. Perform the evaporation in the horizontal axis.
3. Use two *vertical* beams going through the two windows at 7 degrees.
4. Use a single beam at 7 degrees and incline all optical lattices (optical dipole trap, 1064 lattice beams, Bragg diffraction beams).
5. Add a shield on the MCP to protect it and modify the Raman transition to deflect atoms so that they do not hit this protection.

We are primarily focused on one-dimensional physics along the elongated direction. The first option implies that both the BEC and the pairs reach the MCP simultaneously. However, in the existing setup, we frequently observe MCP saturation. This occurs when the particle flux is excessively high (Nogrette et al., 2015) which is typically the case when a BEC reaches the detector, causing the electronics to lag and potentially compromising the arrival time on each channel[6]. The second option was tested and a cloud was successfully loaded but the density and oscillations frequencies were not high enough to obtain a BEC (Amodjee (2020), Marolleau (2022)). Among the third and fourth option, the fourth is better as the third one mix the horizontal and vertical confinement. In the context of DCE modulation, modulating the trap width for the DCE project would be more difficult with this setup. The rationale behind choosing the fifth option is not entirely clear to me. At that time, the *shield* solution was anticipated to be relatively straightforward as the Raman beams were already set to deflect the atomic beam. The idea to place this shield on a mechanical shutter (NASA, 2003) was rapidly put aside because of the complexity of adding such a mechanical piece under vacuum. Note that is exists also MCPs with a hole , typically used in particle physics to let a high flux going through the detector. This option is not available with an 8 cm diameter MCP. It was therefore decided to install a non-removable shield. In retrospect, I am now convinced that the fourth option would have been a better choice[7], but I do not remember it was an option at that time.

In the literature, another experiment needed the MCP not to be placed just under the trap. Van Der Beek et al. (2020) installed a vertical lattice to measure gravity while measuring the interference pattern with an MCP. They moved the MCP beside and deflected the atomic beam with a magnetic coil. This is not a problem when measuring a flux of particles. This magnetic solution is however not possible for us. The free fall of m=1 atoms is affected by residual magnetic field of the vacuum chamber. Furthermore, we want a good precision on the impact position of particles and need a really high stability and I do not expect a magnetic gradient to be really precise.

[6]Note however that I am not sure if the saturation would still apply if the BEC is horizontally elongated. An *in-trap* cigar-shape BEC turns into a pancake after time of flight. This means that the detection duration of the cloud would be much longer: some tens of ms to be compared to less than 1 ms in this work. For a twenty thousands atoms BEC, this would mean that the flux would be of the order of

[7]We manufactured mechanical piece and ordered the material to process to this tilt of the experimental setup. Such modification is however quite important and would need at least one month of work (if everything goes well, which is quite rare). We decided to wait for nice experimental result before starting such modification.

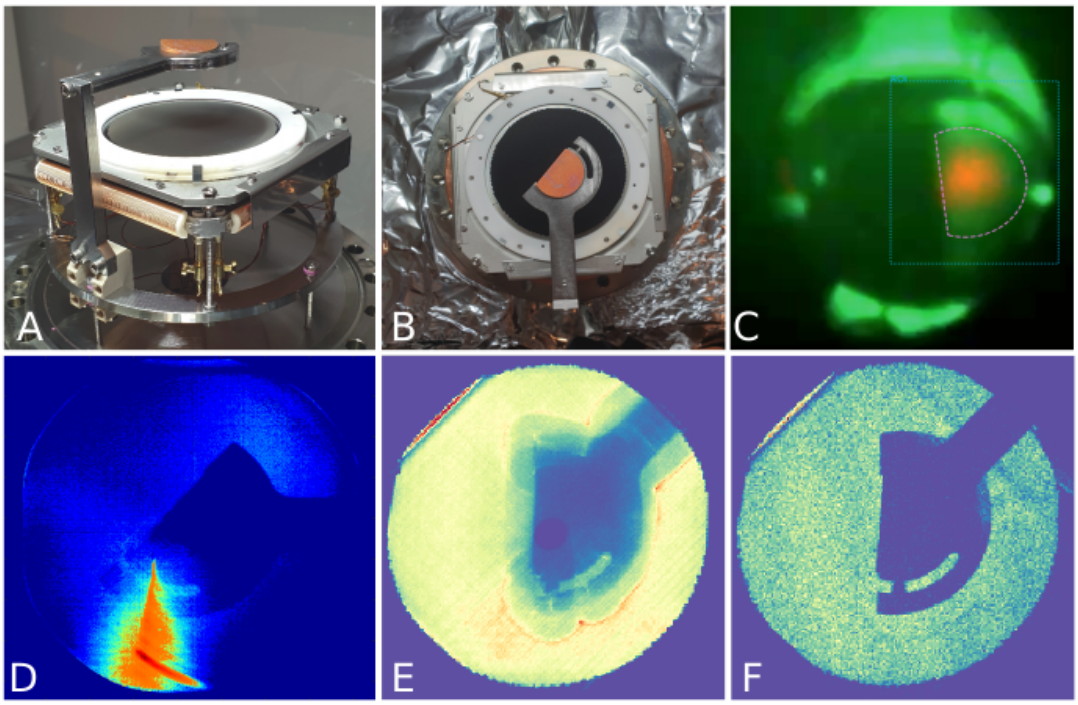

Figure 56: Pictures of the *pastille* that was installed on the detector to prevent the laser burning the MCP. A & B) Picture of the pastille during its installation on the MCP. The white piece is made of ceramic in order to isolate the pastille from the -2kV ring. C) Photography of the pastille taken from the top of the vacuum chamber, through an infrared viewfinder. The dipole trap laser, colored in red, is switched on a few ms at low power and is superposed to the picture of the MCP, lit by a flashlight. The pink dashed curve represents the copper part of the *pastille* that reflects more than 90% of the laser power. D) Gain map of the old Burle MCP on the testing bench shined with UV photons, before we installed id on the experiment. The shield effect did not seem to have side effect. E) Gain map of unpolarized helium atoms. The green dashed circle represent the region where the BEC and the pairs are detected. One can see that the *pastille* seems to have no effect in this region. F) Gain map of the pastille when only non-magnetic atoms hit the detector : they do not cover in a uniform way the pastille because they are released from a few µK cloud. Installation of the pastille was done in December 21 and January 22.

Lending an ear to the detector: shield installation

The first version of this *shield* or *pastille* was made of a stainless steel arm holding a 1550 nm treated mirror that was cut. When installed under vacuum, the coating came off and we decided to replace the mirror by a simple diffusive copper piece. The copper piece diameter is therefore 2.54 mm, cut at 5 mm from the center. It is tilted with respect to the vertical axis by 7 degrees, so that the beam is not reflected towards the atoms. Its resistance to temperature was tested in September 2021, on a dedicated bench: illuminating it continuously with a 1 W laser, the temperature stabilized around 60 °C after a few hours under 10^{-7} mbar. The shield was exposed with UV photons and revealed no side effect, even with the laser turned on as represented by the image D of Figure 56.

In October, the shield was installed in the vacuum chamber, and we soon noticed its impact on the gain map. Nearby atoms were disrupted, particularly around the corner, causing the

formation of *ears* structure, named also *les zoreilles* in French, as illustrated in image E of Figure 56. The arm shield being attached to the -2.6 kV anode, we thought that this effect was due to the voltage difference between the shield and the MCP front, whose voltage is near 0 V. We decided, therefore, to ground it, isolating the shield from the -2.6 kV metallic ring. This can be seen in the image A of Figure 56 where the metallic arm is attached with a peek ceramic piece. This had no effect on the ears. The ears effect was *in fine* magnetic : the image F of Figure 56 represents a $m = 0$ cloud sufficiently hot to cover the entire surface of the MCP. The *ears* seem no longer present. It turns out that one can still see a small effect on the atomic density.

2.B Offset and resolution map of the detector

Procedure

As introduced in the previous section, the quantity $S = t_{X1} + t_{X2} - t_{Y1} - t_{Y2}$, called the offset, should be conserved. This quantity should be even zero if the propagation time were equal, the CFD of each time channel exactly the same and the propagation perfect in the line. In practice, it is not equal to zero but also depends on the location on the detector. To realize this *offset map* or *gradient map*, we expose the MCP to a really low flux of atoms in order not to saturate the detector[8] so that the atom number is decreased by a factor ten. We must also change the reconstruction algorithm. In this case, we do not take the reference offset map. We impose however more strict conditions to ensure that the quadruplet matches the signal of an atom: we require to reconstruct an atom that the quadruplet should be the unique candidate in its time-bulb.
We will use the following convention.

- The unit of this section is the time unit (t.u.) of the TDC (120 ps). It should be compared with the *time diameter of the MCP*, the time it takes for an electronic signal to propagates through the delay line. This is approximately 80 ns and depends on the delay line. The ratio of the two gives 666. It is half the number of *pixels* due to the TDC digitalization. Note that this is much smaller than the number of channels of the MCP along one axis.
- As the TDC returns integers, in order not to lose precision, the X *time position* is defined as $t_{X1} - t_{X2}$: we do not divide per two as in equation (174). The same remark applies for Y.
- We neither divide by the propagation time as in (174). The discrepancy between the two delay lines explains why the shape of the MCP in Figure 57 is not round.

In order to have many statistics per pixel, the results shown below are the outcome of a few tens of hours experiment.

[8] This is done by turning off the transverse molasses and decreasing the MOT loading duration.

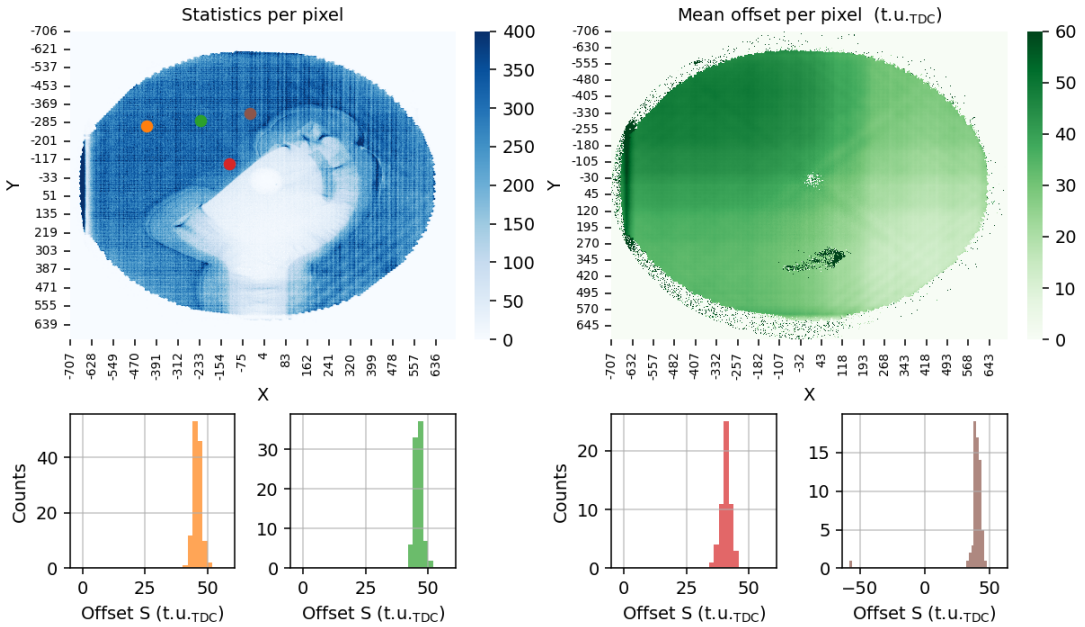

Figure 57: Top: gain and offset maps of the detector after the shield installation. The left map represents the number of shots used to compute the offset map. The right panel represents the mean of the offset distribution per pixel. Bottom: the offset distribution for four pixels of the detector. The pixel locations are represented with markers on the blue gain map. Data obtained in July 22 and analyzed with the heliumtools mcp_map module.

Results: the not so constant offset map

For each detected atom, we record its position and its offset. The number of atoms per pixel is shown on the left panel of Figure 57: it is typically a few hundreds. The map was acquired with unpolarized atoms hence we clearly see the ugly ears at the corner of the shield. For each pixel of the detector, we have an offset distribution $D_S(X,Y)$. Typical distributions for four pixels is shown in the bottom row of Figure 57. The location of the pixel is shown by colored dots on the blue map. We see that the distributions are not centered exactly at the same value: the first distribution is shifted compared to the third one. It reflects that the offset quantity is not a constant but depends on the location on the detector. Because of the definition of the offset, the offset value can only take pairs of integers. We observe that the width of the distribution is typically 2 or 3 bins, which means it is 2-4 time units.

From the distribution $D_s(X,Y)$ associated to each pixel, we can define a local mean value $S(X,Y)$ that is the mean of the offset distribution. The right panel of Figure 57 represents the 2D map of this mean: it is called the offset map. It is also referred to as *gradient* as we observe that the offset drifts along the MCP from 0 (right bottom corner) to 60 t.u. (top left): the offset is a local offset. This offset map is then used in the reconstruction program on a daily basis to compare a quadruplet candidate to the tabulated offset.

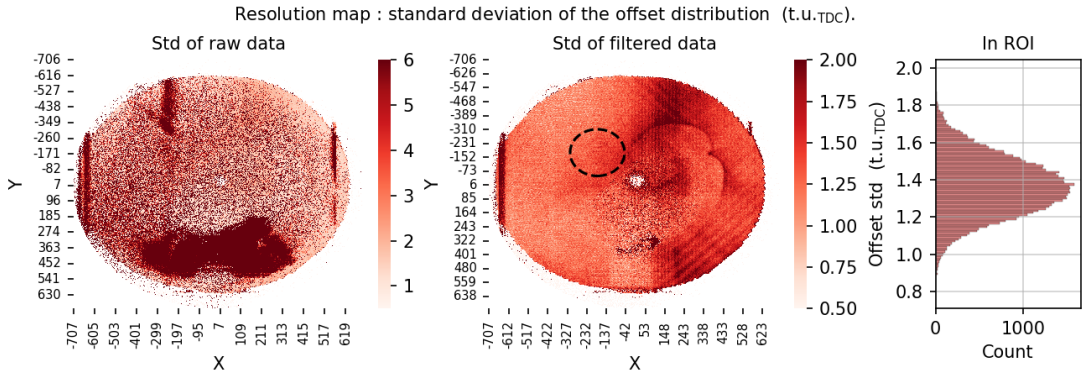

Figure 58: Resolution map of the detector. The left figure is just the standard deviation of the offset distribution for each pixel. The right subplot is the standard deviation of the *filtered* distribution. For each pixel for which we took out points that were outside the median ± 10 TDC time-steps. This filter removed 1.3% of the shots. Data obtained in July 22 and analyzed with the heliumtools mcp_map module.

Results: the resolution map

Figure 58 shows the standard deviation of the offset distribution for each pixel. The left panel is the standard deviation of the distribution for each point. The map seems to exhibit a high inhomogeneity: similar works carried out by Marolleau (2019) or Cayla (2018) did not reveal such inhomogeneities. Furthermore, we observe many "hot" pixels (darker color) revealing a really high standard deviation. When looking closely to the histograms of those hot pixels, we found anomalously high or low values. A closer look to the right marron histogram of Figure 57 reveals an offset value of -55 t.u., while the majority is around 45. It is those anomalous values that are responsible for the strong inhomogeneities of the map.

We are interested in the width of the distribution, hence we should get rid of this anomalous values. This is done by filtering the data that are not "near" the local mean offset $S(x, y)$:

$$D_s(X,Y) = \left\{ s \in D_S(X,Y) : \ |s - S(X,Y)| < 10 \right\} \tag{178}$$

The resulting map is shown on the top middle panel of Figure 58 in red. The variation of the resolution is much smoother and closer to the value reported by Marolleau (2019). However, we still observe an effect of the shield near acute angles. The area of interest is depicted with a black dashed circle: it is where the BEC arrives. On the top right is represented the distribution of the standard deviation of the pixels of the interest area. In this region, the offset standard deviation is $\sigma_{std} = 1.4(2)$ t.u. This value is in agreement with 1.1(2) t.u., the value measured by Marolleau (2022) on the same MCP, with the same electronics, but with UV photons and without the shield.

Discussion on the resolution of the detector

The spatial resolution of the detector was measured by Nogrette et al. (2015) using a grid and looking at the point spread function on the detector. They showed that the measured quantity was linked to the offset distribution width σ_{std}. Indeed, the later quantity gives a good estimate of how much we are sure that the atom did hit the detector at the position (X, Y) and not at the position $(X + \delta X, Y + \delta Y)$. Let's recall the process: the electronic cascade excites the delay line on which an electronic pulse propagates. The width of the pulse is a few ns from which we extract an "official time". When the pulse shape is "clean" and always the same, we can expect the TDC to be accurate in determining the center of the pulse[9]. Ultimately, the precision is fixed by the timing step of the TDC of 120 ps. We can therefore introduce σ_T, the uncertainty associated to the ability to discriminate the center of the pulse. Assuming the offset uncertainty is associated to the uncertainty σ_T for each channel[10] (X_1, X_2, Y_1, Y_2), we write the uncertainty on σ_S as

$$\sigma_S = \sqrt{\sigma_{X1}^2 + \sigma_{X2}^2 + \sigma_{Y1}^2 + \sigma_{Y2}^2} = 2\sigma_T. \tag{179}$$

The transverse resolution of the detector can then be deduced from the transverse velocity of each delay line (174) and the measured uncertainty associated to the offset

$$\sigma_x = \frac{c_{x,\perp}}{2\sqrt{2}}\sigma_S \qquad \sigma_y = \frac{c_{y,\perp}}{2\sqrt{2}}\sigma_S \tag{180}$$

Table IV.1 reports the RMS width of the offset distribution from the literature in which all authors use the same electronics. Depending on the reference, the MCP studied was from the brand Burle or the same as the one we use (from Hamamatsu). We observe that the standard deviation of the offset distribution on the new Hamamatsu MCPs is smaller by a factor of 5. This is at first surprising as the transverse resolution is mainly due to the electronics. A possible explanation for this improvement is that the new MCPs triggers a cleaner electronic pulse on the delay lines. This makes the TDC operation more efficient, and we approach the final limit of the transverse resolution, that is the time step of the TDC.

During the reconstruction process, the offset of quadruplet candidates is compared to the reference offset. The standard deviation reported in Table IV.1 provides us the typical value to which this difference should be compared. In the program, we allow typically a deviation of 5 time units. This also gives us the in-plane resolution of our detector. From (179), we see that the transverse resolution is 60 µm.

When the non-uniform offset is no longer stable over time: strange drift of the offset reference

Before going to the next section, I would like to emphasize a weird drift that was observed on the experiment. After the realization of the offset map, we realized that the mean offset exhibited a slow drift on the order of a month. This was never noticed before: the offset map was never used on a daily basis. This drift can be observed in Figure 59 where we plot the offset mean value of the detected atoms for various dates. This drift is significant with respect

[9] We can draw a parallel with a Gaussian fit here: when the experimental signal is clean enough, one can extract the center of a Gaussian with a precision much higher than the width of the Gaussian. However, when the experimental signal is dirty and the shape changes at each repetition, the precision will be much lower.

[10] In their work, they changed the incoming particle flux and the acquisition time, namely the TDC. Those two parameters have an effect, but it is much smaller than the noise associated to the detection time of each channel.

Table IV.1: Comparison of the value measured in the literature for the transverse resolution of the detector. Note that the values from Cayla (2018) are not stricly reported in the text of his thesis. The value reported here was extracted from a colored resolution map. The factor of 2 that differs with the two other reference can be linked to the definition of resolution/offset that I misunderstood. In the other work, the quantity that I refer to as σ_{std} is clearly the RMS width.

Reference	MCP type	Incoming flux	Offset std $\bar{\sigma}_{std}$ (t.u.)	Offset std $\bar{\sigma}_{std}$ (µm)
Nogrette et al. (2015)	Burle	UV	7.7(4)	920(50)
Cayla (2018)	Burle	UV	3.3(5)	400(60)
Marolleau (2022)	Burle	UV	6(1)	720(120)
Marolleau (2022)	Hamamatsu	UV	1.1(2)	130(20)
This work	Hamamatsu	Atoms	1.4(2)	170(20)

to the tolerance of the offset deviation, which is typically 5 t.u. We found no explanation to this observation. After July 2023, the TDC threshold were changed making impossible the comparison with the data represented here. Note however that a CFD was changer due to a failure a few months after and might be the responsible for this drift. During the year 2024, we did not witness such drift.

Summary This section reported the installation of a shield to protect the MCP. Such device strongly affects the gain map, especially atoms with a magnetic moment. We also reported the measurement of the quantity called the *offset* to calibrate the detector. We then discussed the transverse resolution of the detector.

3. Physical description and limits of the detector

3.A Model of the MCP

In quantum optics, theory of single photo-detection is due to Glauber (1963b) in a seminal paper called "The Quantum Theory of Optical Coherence". In his work, he shows that single-photon detector measure the normal ordered fields hence are quite adapted to measure (normal ordered) correlation functions. We reproduce part of this work in Figure 60: the notation $E^{(-)}$ correspond to our (atomic) creation operator $\hat{a}^\dagger$ and $E^{(+)}$ matches the annihilation operator $\hat{a}$ while $|i\rangle$ refers to the initial (atomic) field. All the machinery developed within the quantum optics community can be applied to our detection scheme. In particular, theory of photo-electron counting, further developed by Glauber (1963a) and Kelley and Kleiner (1964), can be applied to our measure.

It should also be emphasized that single particle detection is not a Gaussian operation (Sasaki and Suzuki, 2006). A particle-number-resolving detector projects the measured mode i of a (Gaussian or not Gaussian) state on a non-Gaussian n-particle Fock state $|n\rangle_i$ (Lvovsky et al., 2020). The non-Gaussian operation of our detector could be studied using the tools developed by Hloušek et al. (2021) as performed by Grygar et al. (2022) with photons. This

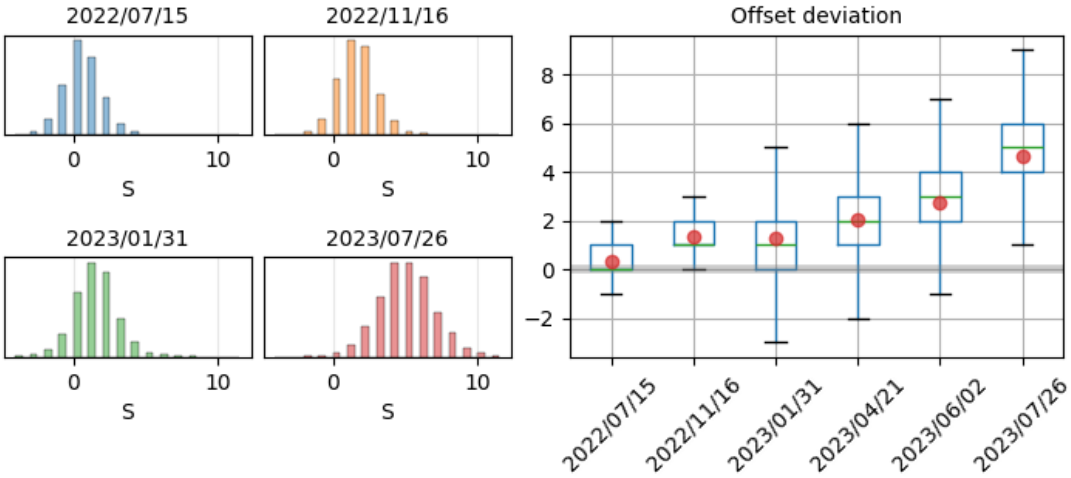

Figure 59: Offset drift between 2022 and 2023. For each date, we gather atoms detected on the region of interest on which is detected the BEC. We then computed the distribution of the offset deviation : the offset minus the reference offset. The left panel represent the distribution of four different distribution of offset distribution at different times. Each subplot represent a month since the realization of the offset map in July 2022: the first, in blue, is centered at 0 as it was done at the moment of the offset map. The second one, orange, was acquired a few month after and already presented a significant drift. The two other plots represent the offset distribution after 6 and 12 months. Right plot: box-plot of distributions over time. The green bar represents the median, the blue box the 1st and 3rd quartiles, and the black ends are calculated using 1.5 times the inter-quartile range (the distance between the 1st and 3rd quartile). We have added the mean in red.

would however require a better imaging system to infer the properties of the BEC.

3.B Maximum number of particle per mode

In Figure 60, we represented the MCP as an assembly of $N \sim 10^7$ independent detectors as if each micro-channel could work in parallel. However, all micro-channels are connected to the same electronics which prohibits the detection of "simultaneous" events. Here, we aim to describe how many particles per mode one can detect. We first need to describe the size of the input state: the atomic wave-function we aim to measure is localized on a size which is roughly given by the BEC size. We naively model the collective excitation by a Gaussian wave-function $\psi_0 \propto e^{-z^2/2\sigma_0^2+ikz}$ where $\hbar k$ is the momentum of the quasi-particle and σ_0 is the typical width of the wave-function. Left panel of Figure 61 shows that the typical width of our Gaussian wave-function can be related to the BEC length. Due to Heisenberg relation, the initial width of this wave-packet in momentum is $\tilde{\sigma}_0 = 1/\sigma_0$. When the trap is switched off, the wave-packet expands and the typical size of the wave-packet is given by (Le Bellac, 2007)

$$\Delta x = \frac{1}{\sqrt{2}}\sqrt{\frac{1}{\tilde{\sigma}_0^2} + \frac{\hbar^2\tilde{\sigma}_0^2 t^2}{m^2}} = \frac{1}{\sqrt{2}}\sqrt{\sigma_0^2 + \frac{\hbar^2 t^2}{m^2\sigma_0^2}} \sim \frac{\hbar t}{\sqrt{2}m\sigma_0}. \tag{181}$$

On the right panel of Figure 61, we show the typical size of the wave-function when it reaches the detector as a function of the initial BEC length[11]. Typically, we observe that after

[11] First note that the size of the wave-function is not the size of the $k = 0$ BEC, whose size is broadened by

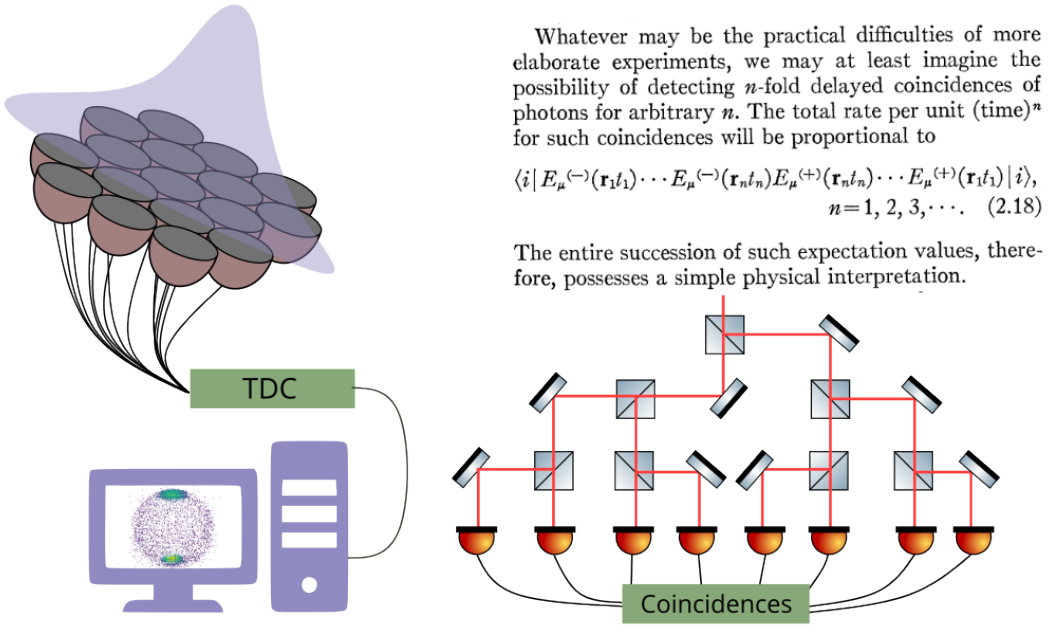

Figure 60: Left: model of the detector as N independent single particle detectors. The atomic wave-function is delocalized over all the detectors but only one "clicks" when an atom is detected. Right top: reproduction of Glauber (1963b) and his "Gedankenexperiment" experiment to measure the n^{th} order correlation function. Right bottom is an optical analog to measure the n=8th order equal time correlation function. For photons, the wave-function must be *broadened* using beam-splitters and many single photon detectors (SPDs). One could also extend the photon path at each beam splitter to detect it with the same SPD to lower the cost of the setup (Krishnaswamy et al., 2024). For an atomic momentum microscope the wave-function expansion during the time of flight is such that the wave-packets expands "for free".

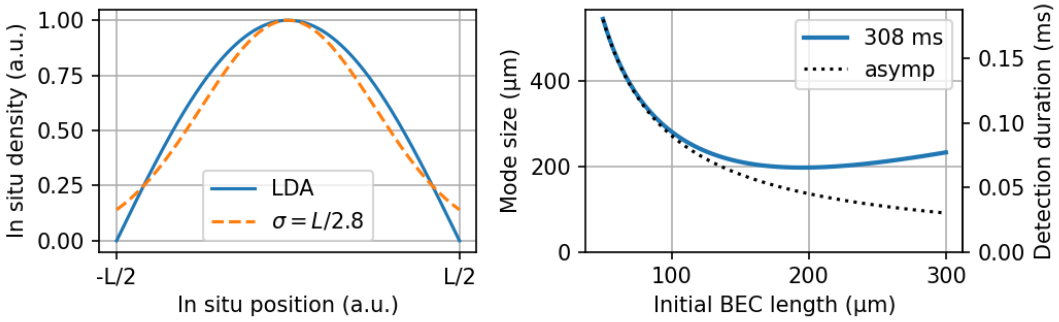

Figure 61: Left: In situ density of the cloud. The blue solid curve represents the density profile of a BEC in the local density approximation, which is almost a Thomas-Fermi profile. The orange dashed curve represents a Gaussian whose width is $\sigma/\sqrt{2}$. The collective excitation is delocalized over the BEC at $t = 0$. Right: typical width of a single mode given by equation (181) as a function of the initial BEC size. Note the prefactor is not expected to be correct because of our too simple model.

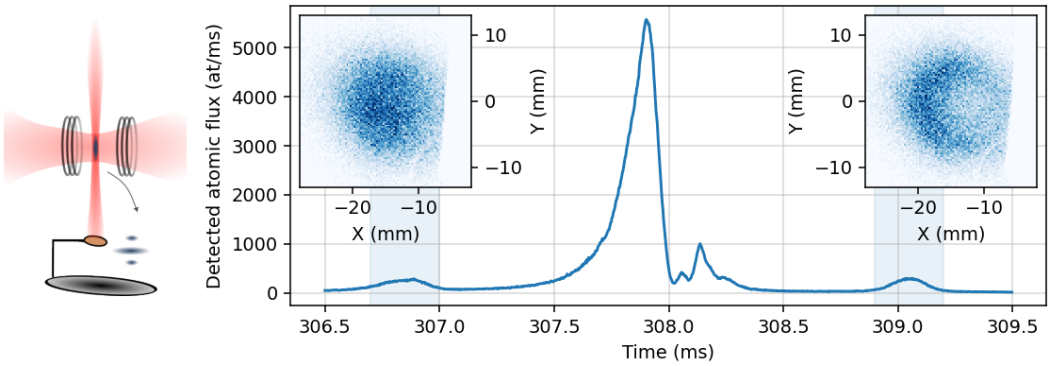

Figure 62: Left: the experimental setup. Right: detected atomic flux as a function of time. The BEC is the central peak that arrives at 308 ms. We can see that when the atomic flux is too high (higher than a few MHz), the electronics saturates. It causes the density to drop at 308 ms. The two insets represent the transverse profile of the side bands, that hit the MCP at 306.8 ms and 309.1 ms (blue shaded regions). A hole is visible on the second peak transverse density profile: it is due to the saturation of individual micro-channels.

a 308 ms time-of-flight, the size of a mode is some hundred of microns. When they reach the detector, atom move typically at 3 m/s. This means that a single mode of the atomic wave-function is measured in 100 µs. The current electronic we use can "reconstruct three-dimensional coordinates of particles at rates up to 3.2 MHz" (Nogrette et al., 2015). This provides us that the atom number should be much lower than 300 atoms per mode. Within the optical analog drawn in Figure 60, our setup is therefore equivalent to 300 single particle detectors. The number of particle of the state we measure must be lower than this number of single particle detector: Sperling et al. (2012b) showed that we should be able to detect a mode with (just) a few particles[12]. Note however that for a thermal state with mean population $\bar{n}$, the variance is given by $\bar{n} + \bar{n}^2$. It means that we cannot fully resolve the full counting statistics of a state with a mean number of particles higher than 10.

3.C Saturation

As we saw in the last chapter (see Section 4.A), there are typically a few tens of thousands of atoms in a BEC. When released from the trap, atom-atom interactions cause the BEC to expand and its aspect ratio to invert. The initial cigar-shape BEC turns into a pancake. After a 308 ms time-of-flight, the "pancake thickness" is typically a few hundreds of microns. It means that some 10^4 atoms are detected within $\sim$ 0.3 ms. This flux is too high to count precisely the number of atoms, and it saturates the electronics. The saturation is clearly illustrated in Figure 62, at 308 ms: when the atomic flux exceeds the TDC maximal flux (a few MHz), the signal drops to zero. This saturation does not affect the useful signal *i.e.* the correlated pairs that arrive before and after the BEC, highlighted with the blue shaded area.

Another type of saturation however affects the signal we aim to measure. Once a metastable helium atom triggered an electronic fountain, it takes a few ms for the channel to

interactions. Second, because of our (too) simple model, the mode size I refer to should be taken with caution as the pre-factor are note correct. Still it provides a good estimate of the observed mode size as we shall see later.

[12] In their papers, authors show that "the number of on-off detectors N must exceed the photon number by a few orders of magnitude in order to sufficiently discriminate different Fock states". In an extension of their work, Sperling et al. (2012a) show that the measured counting statistics converges to the real statistics as $1/N$.

charge back and be able to re-detect another atom. The positive velocity side bands reach the MCP only 1 ms after the BEC (around 309 ms). The two insets in Figure 62 show the transverse density of the two sidebands. We observe a hole at the middle of the transverse profile of the second peak: this is a result of the micro-channel saturation due to the BEC. Central to the following of this work is our ability to deflect (only) the BEC to prevent this saturation.

3.D Efficiency, tomography and conclusion

So far I did not mention the efficiency of the detector. It was estimated by Ténart (2021) to be 53(2)% on a different experimental setup. This value has a simple explanation: when a metastable atom tears off an electron, there is a 1/2 probability that the electron enters the channel (Vassen et al., 2012). On our experiment, our less performant imaging system did not allow such precise measurement. In the end of this manuscript, we use a self-consistent method to find a 25(15)% efficiency and the relative number squeezing observed by Leprince (2024) provides a lower bound of 15% on the quantum efficiency. Recently, Allemand et al. (2024) performed the tomography of the detector, showing that it is indeed well described by a binomial law, validating our toy model of Figure 60.

Due to the channel tilt (and not the coding step[13]), the time at which an atom tears out an electron varies by ± 5 µs, see Figure 51. For a 3 m/s atom velocity, the longitudinal resolution is therefore ± 15 µm. On the transverse plane, the measurement in Table IV.1 leads to a resolution of ± 60 µm. In terms of *in-trap* velocity, this gives a resolution of 0.05 and 0.2 mm/s, in agreement with Hercé (2023).

Summary In this chapter, we introduced the MCP and the delay lines, that allow us to reconstruct the 3D momentum distribution of the state. Even though the shield that protects the detector influences the detection and covers partially the MCP, it does not affect its resolution. The measured resolution (0.05 and 0.2 mm/s) is smaller than the mode size (1 mm/s and 10 mm/s) which allow us to resolve each mode, for atom number smaller than a few dozens.

[13] Note that this totally disagrees with the "astonishing" resolution of 2 ns reported by Hodgman et al. (2017) which allow them to "Solve the Quantum Many-Body Problem via Correlations Measured with a Momentum Microscope". Still, I hope our smaller resolution will not prevent us from Solving the Quantum Origin of the Early Universe...

Chapter V

Controlling the quasi-particle creation

This chapter focuses on the pair creation process and its dynamics. In the first section, we observe the breathing mode of the BEC (1.A), then implement the protocol proposed in section 2.C of Chapter 1 to drive oscillations at an arbitrary frequency ω_d. In subsection 1.C, we measure the wave-vector of the detected quasi-particles as a function of frequency which allow us to recover the Bogoliubov dispersion relation. The next section focuses on the exponential pair creation process. We observe a strong oscillation of the atom number that we explain in subsection 2.C. Such oscillation is due to the non-adiabaticity of the mapping from the phonon basis to the atom basis that was introduced in the chapter 1, section 3.C. Subsection 2.D focuses on the measurement of the growth rate. We observe a deviation from the theoretical growth rate, which we interpret as the decay rate. Although these measurements are preliminary, they align with the decay rate recently derived by Micheli and Robertson (2022) for a quasi-BEC. Finally, in subsection 2.E, we present the saturation of the growth process, and in subsection 2.F, we report on an unexpected shift in the phonon wavevector.

What we knew, what is new ? The experiments reported in this chapter were conducted as part of this PhD work and represent original research.

1. Measuring the Bogoliubov dispersion relation

We start this section 1.A by observing the BEC breathing mode. We then apply the protocol of the first chapter to better control the oscillation of the BEC.

1.A Observation of the breathing mode of the BEC

Controlling the transverse oscillation of the BEC is central to this work. As an initial validation, we reproduce the experiment reported by Chevy et al. (2002) to observe the breathing mode of the BEC. We achieve this by modulating the trap's laser power for 8 cycles, near the expected resonance around 2.05 kHz. Subsequently, we hold the BEC for an additional duration, varying from 1 to 4 ms, and detect the cloud on the MCP after a 308 ms time-of-flight. Figure 63 displays four snapshots of the transverse density. Notably, the cloud width along the anti-diagonal in the bottom left image is smaller than in the bottom right one. The right panel shows the standard deviation of the BEC width along the diagonal (green triangles) and

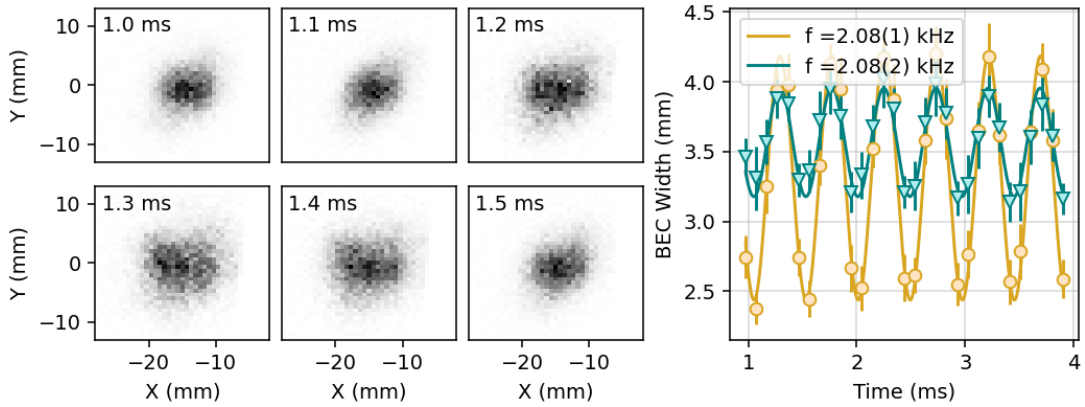

Figure 63: Breathing mode of the BEC: The laser power is modulated over 8 periods with a relative amplitude of 8% at 2.05 kHz, close to the trap's resonant frequency. After excitation, the BEC is held in the trap for a duration τ. Left: Snapshots of the cloud taken at 1.0, 1.1, 1.2, and 1.3 ms. In the bottom-left image (1.1 ms), the cloud appears thinner than in the bottom-right image (1.3 ms). Right: width of the BEC as a function of time. The first four data points correspond to the images shown on the left. The different symbols represent different directions: the yellow circles correspond to the anti-diagonal (thinnest direction at 1.1 ms), while the green triangles represent the diagonal (widest direction).

the anti-diagonal (yellow circles) as a function of time. The error bars represent the deviations from a few experiment repetitions. The breathing mode frequency is measured at 2.08(1) kHz, which corresponds to twice the trap frequency. Depending on the configuration of the dipole trap and the period at which the experiment is carried, the breathing mode frequency in the following sections will range between 2 and 2.1 kHz.

For a transversely symmetric trap, one would expect the transverse density profile to be symmetric as well. However, we observe that the BEC oscillations are larger along the anti-diagonal than along the diagonal. This discrepancy can be seen in the left snapshots, but it is more clearly visible in the right plot, where the oscillation amplitude differs by a factor of 2 between the two axes. There are two possible explanations for this discrepancy:

- Does the horizontal trapping laser break the transverse symmetry? The transverse trapping due to the x-aligned horizontal laser differs in the x and y directions. However, its contribution to the transverse potential is negligible compared to the vertical laser beam. It changes the y-frequency by only 0.1% relative to the x-frequency. Furthermore, the preferred axis for the BEC oscillation is at 45 degrees with respect to this symmetry.
- Are there optical aberrations in the vertical laser causing this discrepancy? Optical aberrations in the vertical laser could modify the trap symmetry. However, if this were the case, we would expect to find another frequency at which the other axis of the BEC enters a breathing mode. We did not find such a frequency.

As a conclusion, we clearly observe the breathing mode of the BEC even though we noticed an unknown symmetry breaking of the collective oscillation. In the following part, we focus on the axis that exhibits the highest oscillation.

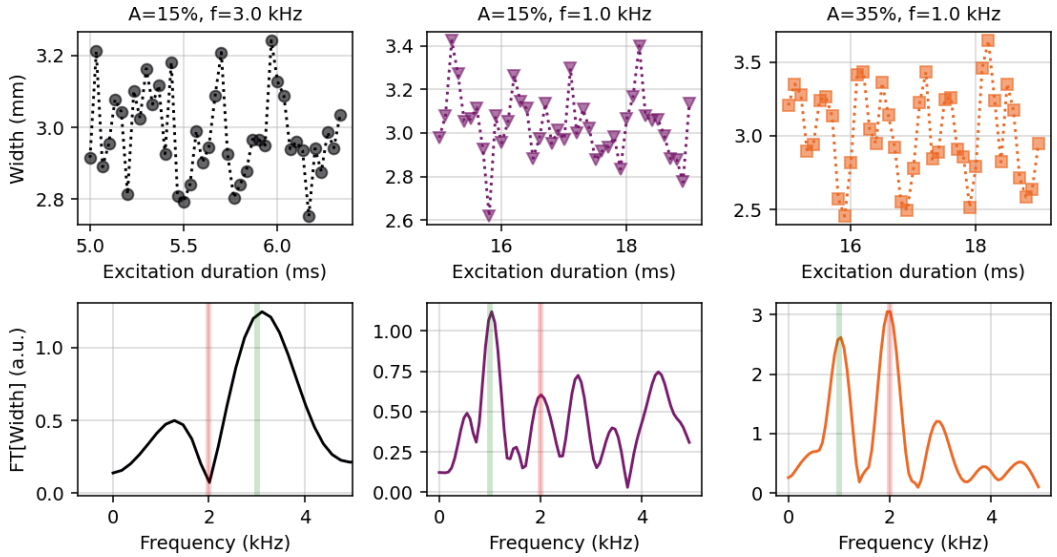

Figure 64: Width of the BEC as a function of time in the trap while the laser power is modulated at 3 kHz (left) and 1 kHz (middle and right). On the two first panels, the amplitude of the excitation is 15% of the laser power while it is 35% on the third one. Second row: Fourier transform of the first row. ®Data obtained on the 23rd of July 2024.

1.B Forcing the BEC oscillation

In the second section of the first chapter, we showed that we can force the BEC oscillation at any frequency, by turning on slowly the modulation of the trap. In the theoretical proposal, we used a low amplitude of modulation, which resulted in a variation of the BEC width of a few percents. Experimentally, such small oscillation is indiscernible from the shot-to-shot noise: the modulation amplitude must be higher.

Protocol: We modulate the transverse frequency of a BEC in a (30 Hz, 1.05 kHz) dipole trap. The trap is modulated with a frequency different from the breathing mode frequency of 2.1 kHz. The modulation of the trap is turned on as proposed in the first chapter, Sec. 2.C in equation (38), with a hyperbolic tangent function and a characteristic time $\tau = 3$ ms. The amplitude of the modulation is some dozen of percents of the final power of the dipole trap *i.e.* it is sufficiently large to induce visible oscillation of the BEC width.

Result: The first row of Figure 64 represents the width of the BEC as a function of the time in the trap. The excitation frequency is 3 kHz (first panel) and 1 kHz (second one) and the amplitude of the modulation is 15% of the final laser power. On the last panel, the frequency is 1 kHz, as in the middle one but the amplitude is 35%. The second row displays the Fourier transform, of the first row, computed with zero padding and apodization. The driving frequency is highlighted by a vertical shaded green line while the breathing frequency resonance is shown in red.

Discussion: The "oscillations" of the first row of Figure 64 are less obvious than the one displayed in Figure 63, they are quite noisy. The amplitude of the signal ranges from 2.8 to 3.2 mm while it ranged from 2.2 to 4.2 mm in Figure 63. Here, we need to look at the Fourier transform of the signal to have information about its spectrum, as depicted in the second row. In the first and second panels, we observe a peak that is slightly above the noise, at the driving frequency highlighted with the green vertical bar (3 kHz on the left and 1 kHz in the middle).

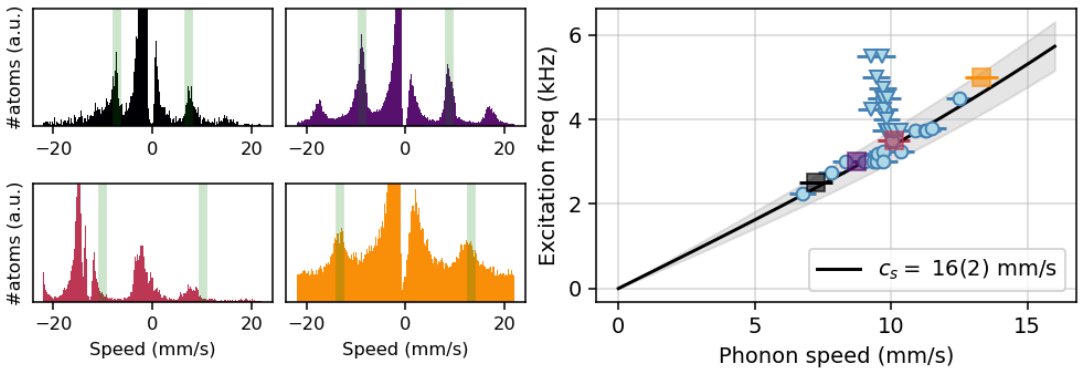

Figure 65: Excitation spectrum of the BEC. The intensity of the laser is modulated at different frequencies, amplitude and duration. Left: raw data that shows the momentum distribution of the gas for four different modulation frequencies. The position of the observed phonon peaks are identified (green shaded vertical bars). Right: the excitation frequency as a function of the phonon peak velocity. The color of the square points matches the color of the left histograms. The other blue points lie either on the Bogoliubov dispersion relation curve (circles) or on a narrow peak around 9.5 mm/s (triangles). ®Data obtained on May 23.

On the last panel, the amplitude of the modulation was increased to 35% of the laser power. In this case, the Fourier component at the driving frequency clearly detaches from the noise, but the breathing mode is also excited: the BEC oscillates at two frequencies. As a conclusion, we see that it is not easy to force the oscillation of the BEC, or at least to measure that it is the case, because of the shot-to-shot fluctuations. Also, we see that it is hard not to excite the breathing mode when increasing the amplitude of the modulation.

1.C Exciting Bogoliubov modes to measure the dispersion relation

If the BEC perfectly oscillates at ω_d, so does the sound speed $c_s^2 = c_{s,0}^2(1 + A\sin(\omega_d t))$. To directly relate sine variation of the BEC width to sine variation of the sound speed, we assumed here the amplitude of the modulation was small enough. This is not necessary the case, and it will lead to the presence of different frequencies in the spectrum of c_s. Still, if we assume the sound speed oscillates at ω_d, it excites two Bogoliubov modes at $\pm k$ such that $E(k) = \hbar\omega_d/2$. Here, $E(k) = \sqrt{\epsilon_k^2 + 2mc_s^2\epsilon_k}$ is the energy of the Bogoliubov mode and $\epsilon_k = \hbar^2k^2/2m$. By tuning the oscillation frequency ω_d, it is therefore possible to probe the Bogoliubov dispersion relation.

Protocol: The experiment is carried out in a single vertical dipole trap (7 Hz, 1.5 kHz), and the intensity of the laser is modulated at different frequencies. In this configuration, the breathing mode frequency is 3 kHz. The experiment is repeated for various amplitudes and durations of the modulation in order to observe pairs. The number of oscillations ranges from 10 near resonance to 50 away from resonance; the amplitude from 10% to 80%. For each configuration, the momentum of the phonon peaks, if they are visible, is identified.

Results: The left panels of Figure 65 represent raw data for four different excitation frequencies. They display the histogram of detected atoms as a function of their reconstructed speed. The central peak corresponds to the BEC, and the two sidebands are the phonon peaks, highlighted with green vertical bars. The right panel of the figure shows the modulation frequency a function of the fitted phonon speed. The color of the four squares matches the color of the plots on the left panel. The solid black curve represents the Bogoliubov dispersion re-

lation for a sound speed of 16(2) mm/s. The other points are represented in blue triangle and circles.

Interpretation: The experimental points of the dispersion relation can be split into two groups: one lies on the Bogoliubov curve (blue circles), and the other one is a narrow peak around 10 mm/s, regardless of the excitation frequency (blue triangles). The first group allows us to recover the Bogoliubov dispersion relation as explained above. The second one is a consequence of parametric resonance. Indeed, in the third section of the first chapter, we saw that the number of created phonons with momentum k is governed by the dimensionless parameter R_ω (Busch, 2014).

$$R_\omega \sim \frac{4}{A_\omega} \frac{|2E(k) - \hbar\omega|}{\hbar\omega} \tag{182}$$

where A_ω is the relative amplitude of the Fourier component at frequency ω of c_s^2. Here, $E(k)$ is defined as $\sqrt{\epsilon_k^2 + 2mc_s^2\epsilon_k}$ *i.e.* the mode Bogoliubov energy before the modulation is turned on. When R_ω is smaller than 1, the phonon creation process is exponential. In subsection 1.B, we saw that even though the BEC width is forced at frequency ω_d, the BEC tends to oscillate at $2\omega_{\perp,0}$. We have therefore a competition between phonons with momentum $k_{\perp,0}$ so that $E(k_{\perp,0}) = \hbar\omega_{\perp,0}$ and phonons with momentum k_d such that $E(k_d) = \hbar\omega_d/2$. The most visible phonon peak will be the one for which the resonance parameter is the smallest.

The y-axis of Figure 65 shows the modulation frequency ω_d. In some cases, we succeed in exciting the driven Bogoliubov mode k_d (round markers). However, in other cases (triangles), the resonance parameter at $2\omega_{\perp,0}$ exceeds R_{ω_d}, and we observe phonons whose momentum $k_{\perp,0}$ is such that $E(k_{\perp,0}) = \hbar\omega_{\perp,0}$.

Summary In this section, we observe the breathing mode of the BEC. We also show that it is possible to force the BEC to breath at a defined frequency despite the resonance mode. We force the BEC oscillation and succeed to observe the Bogoliubov dispersion relation, despite the resonance due to the breathing mode.

2. Exponential creation of phonons

2.A Exponential creation of phonons

Within the resonant window, the number of created phonons is expected to be exponential. To observe this exponential creation of phonons, we excite the 2.1 kHz breathing mode of the BEC for 4 periods, with a laser amplitude of 20%. The cloud is then kept in the trap for an additional duration, ranging from 2 to 6. The amplitude of the breathing is shown on the first panel of Figure 66.

The number of phonons as a function of time is shown on the middle panel of Figure 66. On the right panel is shown the histogram of the atomic density on grey scale as a function of the atom speed (y-axis) and the time N_{osc}. For each slice the x-axis (each time), the color scale shows the longitudinal density of the atomic signal. The horizontal black spot in the middle is due to the BEC, whose signal saturates the color scale chosen to depict the phonon peaks. The asymmetry of the BEC, with a higher density on the positive velocity side, is due to incorrect settings of the Bragg deflector, whose frequency was misconfigured. This histogram helps to visualize the width of the phonon peak, quite visible on the right of the graph. In particular, we see that width of the peak is of the order of 1-2 mm/s, near the size of one mode. We now

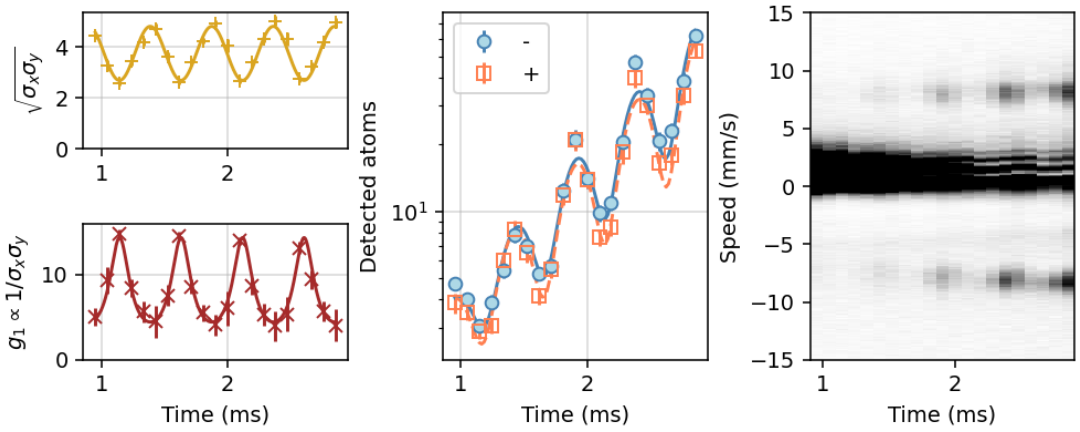

Figure 66: Left: oscillation of the BEC radius (top) and the effective 1D coupling constant (bottom). The solid line is a sine fit with a 30% (top) and 50% (bottom) amplitude and gives the breathing mode frequency of 2.08 kHz. Middle: Number of phonons created as a function of time in the positive velocity peak (orange squares) and negative peak (blue circles). The y-axis is in log scale. Error bars represent the standard deviation over the square root of the repetition number: the error on the measured population (see the appendix 4.C). Right: 2D-histogram of the atom-density as a function of time. The box size chosen for the middle plot is 0.8 mm/s centered on ±8.3 mm/s. The color-scale saturates the high density BEC and its asymmetry is due to the Bragg deflector whose velocity selection was badly set and to the saturation of the detector. ®Dataset taken on the 26th of July 24.

focus on the exponential growth of the phonon population. Following Micheli and Robertson (2022), we fit the experimental data with the following function:

$$n_k(t) = \left(n_k^{(in)} + (2n_k^{(in)} + 1)\sinh\left[\frac{G_k}{2}(t - t_0)\right]^2 \right) \times \left[1 + \alpha_k \cos(2\pi f t + \phi)\right]. \tag{183}$$

In the following, we will discuss the expected and measured value of those fit parameters.

2.B Initial thermal seed and initial time of the squeezing

The initial phonon population $n_k^{(in)}$ and the initial time t_0 play somehow the role of the offset and the amplitude in the exponential growth of phonons. The parameter $n_k^{(in)}$ in Eq. (183) is the thermal population of phonons before the modulation: it is the thermal seed of the two-mode squeezed state. We measure a 44 nK temperature which means that we expect an initial thermal population of $n^{(in)} = 0.5$. Note however that this population is the number of atoms for a single mode. Here, we use an integration volume of 1 mm/s along z, and 60 mm/s along x and y. We find an initial thermal population of 3(1) and 2(2) atoms per mode for the negative and positive peak, which is higher than the expected one. The fit results assume a 0.5 quantum efficiency of the detector.

The second parameter t_0 is the initial time of the squeezing. If the BEC was instantaneously excited at $N_{osc} = 0$, it should be null. However, the excitation process last 4 periods hence we can expect that t_0 ranges from 0 to -4, in units of the breathing mode frequency $2\omega_\perp$. Here, we find that $t_0 = 0.4 \pm 0.3\, T_{osc}$ and $t_0 = 0.1 \pm 0.6\, T_{osc}$. This result is consistent with our expectations.

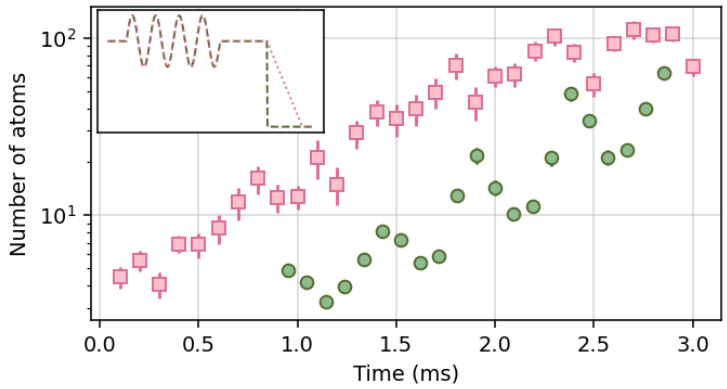

Figure 67: Number of atoms as a function of time when the trap is suddenly switch off (green circle and dashed curve) or ramped down in 1.5 ms (pink square and dotted curve). The inset shows the time profile of the trapping laser power. ®Data taken on the 09/09/24.

2.C Oscillation of the occupation number

The last term in (183) takes into account the oscillations of the measured population at twice the frequency of the trap. Here, we observe a quite large amplitude of the occupation number (around 50%), which is not expected in the phonon population. This oscillation is due to the non-perfect mapping of the phonon field to the atomic field, that we discussed in the first chapter, section 3.C If we write the phonon population in the *in situ* atom basis, we have[1]

$$n_k^{(at)}(t) = n_k^{(ph)} \times \frac{\hbar^2k^2/2m + mc_s^2}{\hbar\omega_k}\left[1 - \frac{mc_s^2}{\hbar^2k^2/2m + mc_s^2}\cos(2\omega_k t + \phi)\right]. \tag{184}$$

Numerical evaluation of the cosine pre-factor gives 0.7. The amplitude of the oscillation in Figure 66 are only 0.50(3) and 0.55(5). The difference between those two values is due to the expansion of the trap: the interactions are not abruptly switched off. The mapping between the phonon and the atom basis is neither adiabatic nor instantaneous. As a result the oscillation amplitude we observe are weaker. If it is not possible to switch faster the oscillations, we can open adiabatically the trap in order to better map the phonon basis to the atomic basis. To do so, we open the trap by ramping down the transverse confinement in 1.5 ms. The laser trap power is shown in the inset Figure 67: see the pink dotted curve compared to the green dashed one when the trap is suddenly switched off. On the main plot of Figure 67, we show the number of atoms with this adiabatic opening (pink squares) and with the sudden opening (green circles). We clearly see that the oscillation is less visible and almost suppressed, as expected.

[1] To obtain this equation, we express the atomic field population in the phonon basis, as in equation (56). We then use the phonon operator evolution during parametric amplification in equation (50). We then assume $\alpha_k \sim \beta_k$ (see their definition in Eq. (51)): at late time, their modulus squared is $\sinh^2(G_k t)$. We also assume the initial thermal population for the k and $-k$ modes to be equal. Finally, we assume that $\int \omega_k \mathrm{d}t \sim \omega_k t$ which is the term that appears in the cosine. Consider that (u_k, v_k) are the Bogoliubov coefficient that map the phonon basis to the atomic one, see eq (44). Within the bracket of (184), the constant term come from $|u_k|^2 + |v_k|^2$ while the oscillation is due to $u_k v_k^\star$. In particular, it means that such oscillation does not appear in the phonon basis.

2.D Growth rate of the phonon occupation

Theoretical growth rate

The third parameter of equation (183) is the growth rate G_k. In absence of damping, Busch et al. (2014) predict the growth rate to be

$$G_k^{th} = \frac{\omega_k}{2} \frac{a}{1 + k^2\xi^2/4} \tag{185}$$

where a is the amplitude of the oscillation of the effective 1D coupling constant $g_1 \propto 1/\sigma_x\sigma_y$, with σ_i the radius of the BEC along i. The bottom left panel of Figure 66 represents the variation of the 1D coupling constant.

At first, to extract this value, I fitted with a sine function. However, the amplitude of the modulation seemed underestimated. To better estimate it, we fit the product $\sigma_x\sigma_y(t)$. We then compute the Fourier transform $\tilde{g}_1(\omega) = FT(1/\sigma_x\sigma_y)$. We ectract then a as the ratio of the amplitude at the breathing frequency over the amplitude of the peak at zero frequency $\tilde{g}_1(2\omega_\perp)/\tilde{g}_1(0)$. Equation (185) also involves the product of $k\xi$. To access this value, we use the speed of the two phonon peak to recover the BEC properties, as explained in chapter 3, section 4.B. In the end of this section, we however report on a shift of this peak. But the dependance of the theoretical growth rate on the $1/1 + k^2\xi^2/4$ is weak and the difference due to the shift is smaller than the uncertainty associated to a extracted from $\tilde{g}_{1D}$.

We expect a growth rate of 1.7(1) ms^{-1}. From the fit of formula (183), we find a measured growth rate of 1.39(4) ms^{-1} for the negative peak and 1.32(4) ms^{-1} for the positive one[2]. We observe a quite large discrepancy between the theoretical value and the experimental one.

Measurement of the growth rate in different conditions

This experiment was repeated varying the amplitude of the modulation, hence the gain of the process. Left panel of Figure 68 reports the fitted growth rate as a function of the theoretical growth rate. The solid grey line is a $y = x$ line as a guide to the eye. The closer the experimental points to this line, the better the agreement between the experimental gain and (185). The blue circles and orange square represent the growth rate of the negative and positive peaks. The uncertainty along the y direction is a combination of the uncertainty of the fit and the result of the fit for various integration volumes. All points lie below the theoretical curve, and the higher the growth rate, the higher the difference. On the right panel of Figure 68 is shown the difference between the theoretical and the measured growth rate. Either the theoretical growth rate is overestimated, or one should take into account the decay of the phonons.

The latter "slowing of the exponential growth" of phonons in a quasi-BEC via Beliaev-Landau damping[3] was actually predicted by Micheli and Robertson (2022). In their work, the authors provide an analytical formula and write the *corrected* growth rate as

$$G'_k = G_k^{th} - \Gamma_k \tag{186}$$

where the phonon decay rate is

$$\Gamma_k = \frac{c_s}{\xi} \frac{k_B T}{mc_s^2} \frac{1}{n_1\xi} \left(f_+(k\xi) + f_-(k\xi)\right) \tag{187}$$

[2]When varying the size of the integration volume, we do not observe the fitted rate to change more than within the uncertainty bar. The uncertainty reported here takes into account both the uncertainty of the fit and the dispersion (when there is one) associated to the fit result for each integration volume.

[3]We introduced Landau and Beliaev damping in the first chapter, section 2.A.

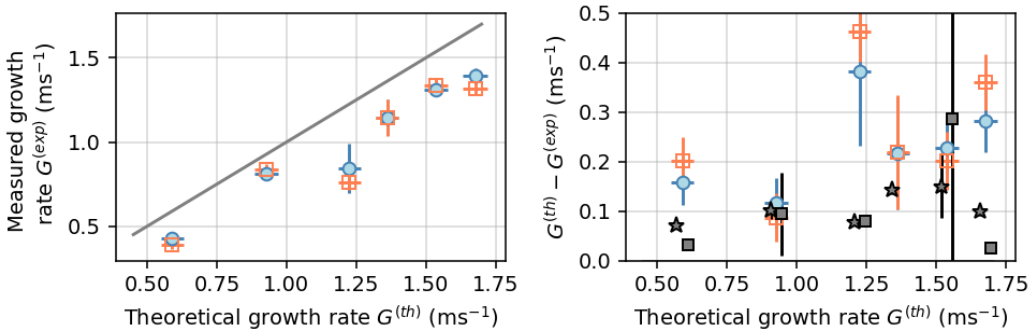

Figure 68: Left: Growth rate of the phonon number as a function of the theoretical growth rate (185). The solid grey line is a $y = x$ line as a guide to the eye. The blue circles and orange squares represent the measured growth rate for the $-k$ and $+k$ peak. Horizontal error bars are associated to the uncertainty on the oscillation of the effective 1D coupling constant. Right: Difference between the theoretical growth rate and the measured one. The grey stars show the decay rate (187). ®Datasets taken in July & September 2024.

and

$$f_{\pm}(k\xi) = \frac{1}{2}\frac{k^2\xi^2}{(\omega_k/c_s k)^2}\frac{(\omega_k/c_s k \pm 1/2)^2}{v_k^{gr}/c_s \mp 1}. \tag{188}$$

Here $\omega_k = \omega_\perp$ is the Bogoliubov energy of the quasi-excitation and $v_k^{gr} = \mathrm{d}\omega_k/\mathrm{d}k$ is the group velocity of the quasi-excitation at momentum k. In addition to the gas 1D parameters ξ, c_s, numerical evaluation of Eq. (187) requires the temperature. To measure the temperature, we fit the tails of the momentum distribution. To have enough statistics, we concatenate data with different excitation time. For two datasets, the "temperature" depends strongly on the maximal excitation time used to measure the temperature. Indeed, as the system is far for equilibrium, measuring the temperature can be misleading. The error-bars on the decay rate measurement is mainly due to this uncertainty on the measure of the temperature.

We reported the value of the decay rate (187) on the right panel of Figure 68 as black stars. The different values for each point are due to different experimental conditions, in both the density of the BEC and the temperature (datasets were taken in different weeks and our experiment lacks reproducibility). Here we do not observe a good agreement between (187) and the measured decay rate.

First, the decay rate (187) was derived for quasi-BEC while we have a BEC. Even though preliminary work and numerical simulations by Micheli and Robertson (2024) showed however that (187) could be extended to elongated BECs, further checks are needed. Second, we never took into account the harmonic trap hence the fact that the BEC is not homogeneous along z.

Our BEC is not a 1D gas : as introduced in the first chapter, Landau decay of Bogoliubov excitations in 3D gases were also studied by Pitaevskii and Stringari (1997) as

$$\Gamma_k = \frac{27\pi}{17}\omega_k \times \frac{2\pi^2(k_b T)^4}{45\hbar^3 c_s^5 mn} \tag{189}$$

where n is the density. We reported this decay rate as black square on Figure 68. Because of the fourth power dependance with the temperature, the error-bars are much bigger for two points. We do not observe a better agreement with experimental points. Note that it was also derived for homogeneous condensate.

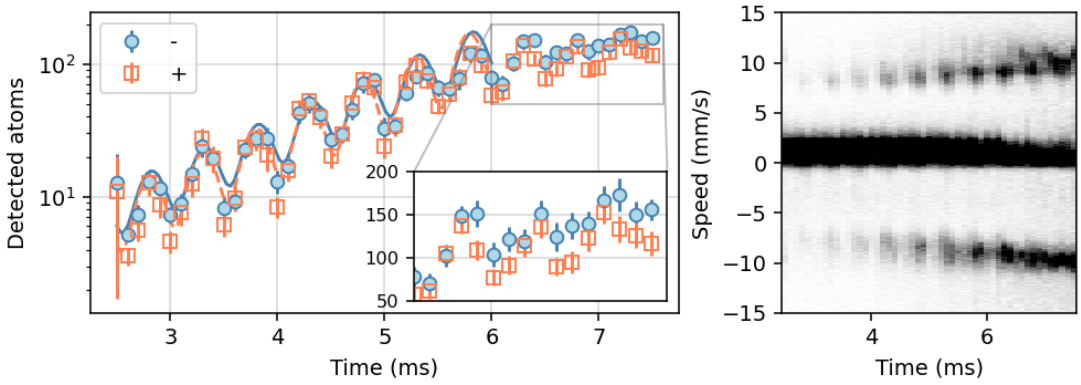

Figure 69: Left: number of detected atoms as a function of time in a integration volume of 3 mm/s. Right: 2D histogram plot of the atomic density as a function of time. ®Dataset taken on the 04/09/24.

To conclude this part, as predicted by Micheli and Robertson (2022) we observed the slowing down of the exponential growth. However, the decay rate that we measure is not capture by the theoretical prediction. These results are however really preliminary and will lead to further investigations, both experimentally and theoretically.

2.E Saturation of the phonon growth

In Figure 69, we show the evolution of the phonon population over a wider range than previously observed. We take an integration size of 2 mm/s, a bit larger than the 1.5 mm/s mode size. Of course, the larger the integration volume, the larger the detected maximal population. The right panel represents the 2D histogram of the momentum density as a function of time.

Pylak and Zin (2018) studied numerically (classical field simulations) the growth process. In their work, they show that for a temperature of 30 nK, the phonon occupation population is expected to saturate at a few hundred. Their theoretical expectation is coherent with our observation. In a different study, Robertson et al. (2017b) showed that non-linear effects can no longer be neglected when the phonon occupancy reaches the value $n_1/10\delta k$. Here, δk is the momentum resonance width and n_1 is the 1D density. In our configuration, this corresponds again to a few hundreds of particles.

Within a linear stability analysis, de Valcarcel (2002) also studied the growth dynamics of a mode. From his work, we obtain the expected saturation of the population which was also derived by Liebster et al. (2023)

$$N_{max} = N_0 \frac{\sqrt{G_k^2 - \Gamma_k^2}}{mc_s^2/\hbar} \frac{E_k}{5\epsilon_k + 3mc_s^2} \tag{190}$$

where $\epsilon_k = \hbar^2 k_{ph}^2/2m$ is the phonon kinetic energy and $E_k^2 = \epsilon_k^2 + 2mc_s^2\epsilon_k$ its energy. Here G_k refers to the theoretical gain and Γ_k the decay rate that we discussed above. We measure $G_k = 0.92(4)$ ms^{-1} using Eq. (185) and extract $\Gamma_k = 0.12(4)$ using the exponential growth fit, shown as a solid line in Figure 69. Here again, the higher uncertainty comes from the BEC atom number. We define the BEC properties using the phonon speeds which is in between 8 mm/s (short time) and 10 mm/s (long time). We estimate the maximal population to 420(50). In Figure 69, we observe the atom number saturates around 150 (integration volume of 1.5

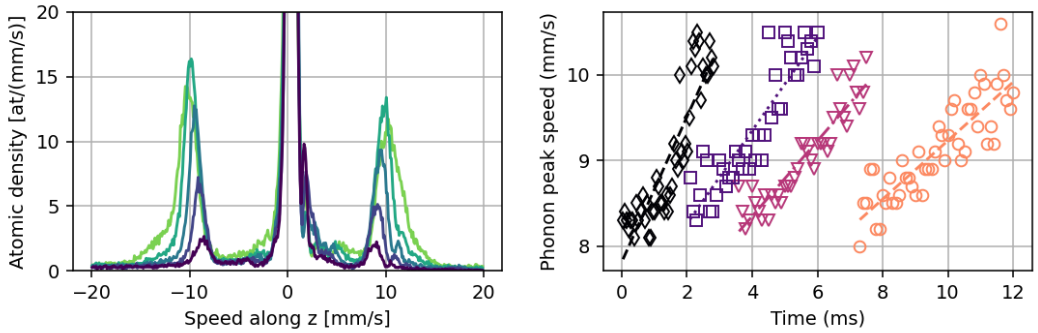

Figure 70: Left: atomic density at different times, from 2 ms (darkest color) to 6 ms (lightest color). Right: Position of the peak density as a function of time. Each color/symbol corresponds to different growth rate of Figure 68. ®Data taken on the 25/04/24 (left) and September 2024 (right).

mm/s) and 200 (for a 2 mm/s integration volume). The difference between the two can be explained by the efficiency of our detector, which ranges between 20% and 50%.

Conclusion: Different theoretical works expect a saturation of the phonon production once the population reaches a few hundred quasi-particles. Here, we also observe such saturation; however, a quantitative study seems complicated. First, the atom number approaches the saturation limit of our detector, and second, our high uncertainty on the detection efficiency clearly limits our knowledge.

2.F Shift of the density peaks

On the 2D histograms of Figure 66 and Figure 69, one can see that the two phonon peaks seem to move apart. This subsection reports on such phenomena. On the left panel of Figure 70, we show the momentum distribution at different times, ranging from 2 ms (dark green) to 6 ms (light green). We note that the width of the peaks increases with time and an asymmetry in their broadening. Furthermore, the peaks maximum shift away from the BEC: the momentum of the density maximum is smaller at short time (dark color) than at long time (light green).

Faraday waves in quantum gases were studied in other groups. The first work conducted by Engels et al. (2007) studied the wave vector dependance with the excitation frequency, but did not report on a shift in time of the wave vector. This study triggered many theoretical works, especially by Nicolin et al. (2007) and Nicolin (2011). In their work, the authors performed 3D Gross-Pitaevskii simulation of the system, focusing on the resonant wave vector k_{res}. However, neither do they report on a shift in time of k_{res}. They also provide raw images of their numerical simulation at different time: based on these data, no drift is observed.

In his PhD thesis, Groot (2015) reports on such drift of k_{res}. In addition, he reports on the "revival" of the Faraday wave: the spatial modulation appears then disappears before reappearing again. Such revival was further studied by Nguyen et al. (2019) who showed it was related to the axial breathing mode of the BEC (lowest quadrupolar mode), whose frequency is between $\sqrt{5/2}\omega_z$ (3D cigar-shape) and $\sqrt{3}\omega_z$ (1D Thomas-Fermi) (Stringari, 1996). However, the authors do not report on a shift in time. Similar experiment was carried by Hernández-Rajkov et al. (2021) with a molecular Fermi superfluid. In their work, they provide the time evolution of the density Fourier spectrum. Clearly, even though the saturation of the colormap of their figure does not allow a precise measurement, k_{res} does not seem to shift in time.

Faraday-like patterns were also studied on a 2D setup by Liebster et al. (2023). In their work, the authors provide the Fourier transform of the density for different times: we observe on their setup a shift of k_{res}[4].

In the work of Groot (2015), the author relates the shift of k_{res} to the axial breathing mode of the BEC. In the left panel of Figure 70, we plot the speed of the resonant phonon as a function of time. Each color and marker shows a different modulation strength hence growth rate. If the shift is related to the trap frequency, the displacement should not depend on the growth rate. On the data reported, the trap frequency is constant, and we observe a different shift dynamics. Here, the speed of the peak displacement seems to depend on the modulation strength. This pushes for a complementary explanation to this harmonic trapping effect. Furthermore, this shift is also observed on the experiment conducted by Liebster et al. (2023) in which the authors have a homogeneous BEC.

To conclude this section, the shift of these phonon peaks remains un-explained. To further investigate this, it would be interesting to witness the revival of the Faraday pattern reported by Nguyen et al. (2019).

Summary In this section, we observe the exponential growth of the phonon occupation number, on almost two decades. We show that the growth dynamics is in agreement with theoretical predictions. The measured growth rate, presented in section 2.D, is smaller than the theoretical growth rate due to phonon interaction, as predicted by Micheli and Robertson (2022). We also observe the saturation of the growth dynamic. Here again, our result is in agreement with theoretical predictions even though our setup is not well suited to measure such a high atom number. In the last section 2.F, we report on the shift of the phonon peaks whose origin remains unknown.

[4]This shift can be observed on the inset of their figure 2.b), but I was noticed by one of the authors, Elinor Kath. They also do not (yet) have an explanation for this shift.

Chapter VI

Observation of quasi-particles entanglement

This chapter presents the main result of this work: the observation of non-separability of the $(k, -k)$ quasi-particle modes. We start this section with an analysis of the density of the dataset that we use throughout this chapter. We then review the key aspects necessary to measure the correlation signal: the deflection of the BEC, its stability and its influence on the correlation signal, as well as the adiabatic opening of the trap to better map the phonon basis onto the atomic one.

The second and third sections of this chapter use two different methods to measure the local and cross-correlation signals. The first method computes what we call integrated momentum correlations, by constructing a 3D histogram of atomic pairs between two large regions. In this approach, we lose information about the specific momentum of the modes that contribute to the correlation signal. The next section, however, retains the mode position, allowing for the measurement of a well-defined momentum mode. Both methods yield similar results.

In the last section, we further study the statistics of each mode to verify they can be modeled by a thermal Gaussian state. This is important to use the criterion derived in the second chapter. We then measure the population and the 4-body correlation function. We conclude on the observation of entanglement. We also discuss on the value of the relative number squeezing and reconstruct the state taking into account the quantum efficiency of the detector that we estimate around 25(10)%. Finally, we report on the measurement of the correlations *via* the Cauchy-Schwarz ratio and relative number squeezing for various excitation durations.

What we knew, what is new ? The experiments reported in this chapter were conducted as part of this PhD work and represent original research.

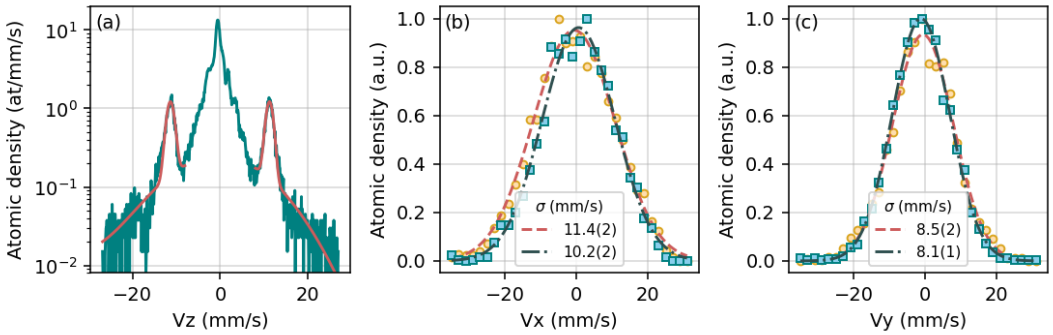

Figure 71: Density profile of the pairs along v_z, v_x and v_y on each panel. On panel (a), the solid red line fits the pairs and the temperature as described in chapter 3, section 4.B. On panels (b) and (c), the fit is Gaussian for which the standard deviation σ is given in the legend. Yellow circles and blue squares refer respectively to the negative and positive velocity peaks.

1. Experimental method

1.A Density analysis

On the dataset we analyse throughout this chapter, we modulate the transverse trap frequency by 20% during 4 oscillations at twice the trap frequency (2 kHz). We then wait for an additional delay of 3 periods (1.5 ms) before we ramp down the power of the trap in 1 ms. The density profile of the detected atoms is shown in Figure 71. In panel (a), we show the density profile along v_z, in log scale. The red solid line is a fit that includes the excited quasi particles and the tails of the distribution. The fit function was discussed in chapter 3, section 4.B. From this fit, we extract a temperature of 49(1) nK. The Gaussian fits of the two peaks yields a standard deviation of 0.85 and 0.80 mm/s. From their position around ± 11 mm/s, we estimate the mean atom number of the BEC to 10 000. In particular, it means the ratio $k_B T/mc_s^2$ is 1.4. In panels (b) and (c) of Figure 71, we show the transverse density profile along the v_x and v_y axis. Yellow circles and blue squares shows respectively the negative and positive velocity peak profiles. The red dashed line and blue dashed-dotted line respectively are Gaussian fit yielding to a standard deviation of 10-11 mm/s along v_x and 8 mm/s along v_y.

1.B Bragg deflection to prevent saturation

As discussed in section 3.C of the fourth chapter, the BEC saturates the detector which prevents the detection of the second phonon peak. A solution to get rid of this saturation is to deflect the BEC using a sharp and velocity selective Bragg pulse, introduced in the third chapter (see Sec. 3.D). Once the trap is turned off, we deflect the BEC after a delay of 1 ms, by applying a 2 ms *sinc* shape mirror pulse, characterized by a 1.88 kHz Rabi frequency. Figure 72 shows the reconstructed atomic flux recorded by the MCP: the thin and high peak at 312 ms corresponds to the BEC while the peaks at 307 ms is the un-deflected part. More than 95% of the BEC atoms have been kicked out from the region of interest. In Figure 71, the central peak shows the remaining un-deflected atoms. We do not observe any saturation effect on the secondary phonon peak, similar to the one presented in Figure 62.

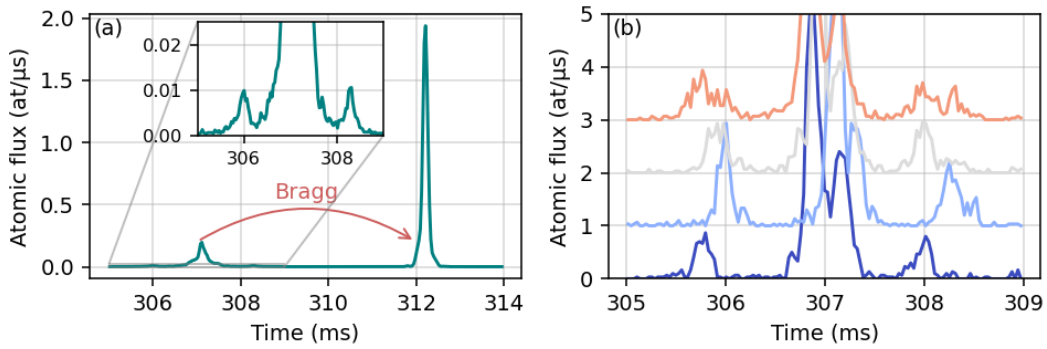

Figure 72: (a) The Bragg pulse deflects the BEC that arrives at 312 ms instead of 307 ms. (b) Four single shot density profiles of an unstable acquisition, lifted vertically by 1 at/µs for clarity. When the initial speed of the BEC fluctuates, it shifts the arrival time of the two pairs and destroys the measurement of the $(k, -k)$ correlation. ®October 2024 & June 2022.

1.C Stability of the BEC

We also aim to measure $(k, -k)$ correlations: it means that we need to precisely reconstruct the speed of each atom with an uncertainty much smaller than a mode size (typically 1 mm/s, or less, this depends on the configuration). Figure 72(b) shows four different shots with a high number of pairs. We see that at each shot, the position of the pairs shifts. This is due to shot-to-shots fluctuations of the entire cloud. They can be measured using the arrival time of the BEC. Is the "breathtaking" stability of 10 µs claimed in section 2.C enough to observe $(k, -k)$ correlations?

The BEC arrival time is measured using a dedicated low-pass oscilloscope which records the MCP signal before the time-to-digital converter. It allows partially getting rid of the electronic saturation (the 5 MHz TDC saturation), but not the MCP channels saturation. Panels (a) and (d) of Figure 73 show the BEC signal for four consecutive shots and two different datasets. In the upper panel, the BEC stability is 50 µs while it is 10 µs for the lower panel.

In the following, we study the correlation map *i.e.* the $g^{(2)}(v_1, v_2)$ function where

$$g^{(2)}(v_1, v_2) = \frac{\#\text{of indep. pairs at } v_1 \text{and } v_2}{(\#\text{of atoms at } v_1) \times (\#\text{of atoms at } v_2)}. \tag{191}$$

We therefore need to define an integration size for which we consider that the speed of an atom is v_1. This integration volume is a 3D volume that we call *voxel* (we might sometime also call it *box*). For the map presented below, this voxel size is 0.3 mm/s along v_z and 80 mm/s along the transverse direction v_x, v_y. Panels (b) and (e) of Figure 73 respectively show this $g^{(2)}(k_1, k_2)$ map for two different datasets. White color indicates absence of correlation; the bluer, the stronger the correlation. Panel (f) was annotated with the different correlated regions: $g^{(2)}_{++}$ and $g^{(2)}_{--}$ refer to the local correlations of the positive and negative peaks; $g^{(2)}_{+-}$ to the cross-correlation. The map is symmetric by construction about the diagonal.

On the diagonal lies the local correlation $k_1 = k_2$ and on the anti-diagonal, the cross-correlation $k_1 = -k_2$. Theoretically, we expect a thin line on the edges of the diagonal, as $g^{(2)}_{k,k} = 2$ for thermal bosons (Jeltes et al., 2007). In the center, we however expect that $g^{(2)}_{k,k} = 1$, due to the Poissonian statistics of the BEC mode (Schellekens et al., 2005). We also expect a bluer region in the top left and bottom right corners, in which lies the cross-correlation, annotated by $g^{(2)}_{+-}$ on Figure 73(f).

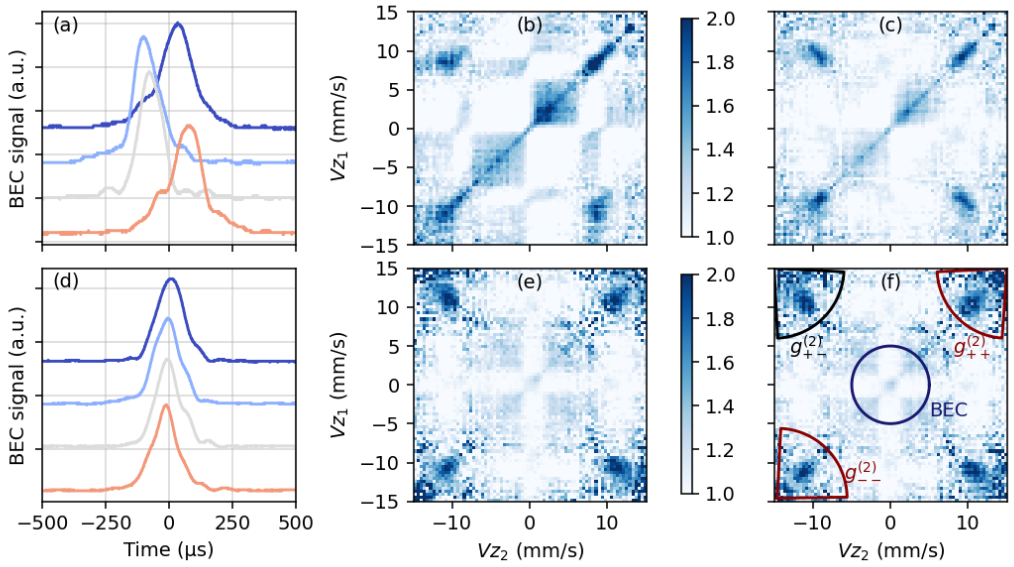

Figure 73: Influence of the BEC stability on the correlation map for a 50 µs stability (top panels) and a 10 µs stability (lower panels). (a-d) Signal of the BEC recorded with an oscilloscope plugged on the MCP for four successive shots. The zero corresponds here to 312 ms, which is the time at which the Bragg deflected BEC hits the MCP. (b-f) Map of the second order correlation function $g^{(2)}$. On panel (c) and (f), each atom speed has been rescaled using the BEC arrival time. ®September & October 2024.

We observe that the map (b), for which the stability is 50 µs, is slightly scrambled compare to (e) (10 µs stability). We observe the appearance of patterns. To further analyze this phenomenon, we develop a numerical model inspired by Bonneau (2011) in the appendix, section 1.B. The idea of this model is to simulate the state that we detect, to add fluctuations and look at how the fluctuations influence the correlations. The instability can be expressed in terms of *in trap* BEC initial speed fluctuations: 50 and 10 µs represent 0.5 and 0.1 mm/s. They should be compared to the mode size, which is typically 1 mm/s. When the instability is not negligible with respect to the mode size, the correlation signal is artificially increased. This is visible in the top right corner of panel(b) of Figure 73. In fact the effect of the instability is more present in the region where the atomic density changes abruptly with k, typically at the edge of the phonon peaks. In the appendix, we show that the Cauchy-Schwarz ratio is less sensitive to the influence of the instability: the reason is that it involves both the local and cross correlation.

For the data we focus on, the stability is 10 µs. Nevertheless, to further improve the reconstructed velocity distribution, we rescale the speed of each shot using the arrival time of the BEC.

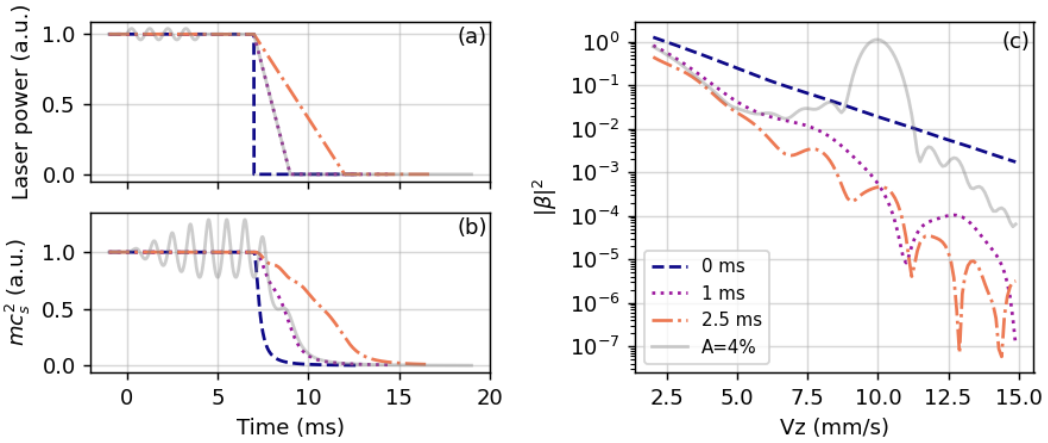

Figure 74: Time profile of the laser power (a) and the sound speed mc_s^2 (b). The right plot shows β, who's square gives the number of quantua produced from vacuum due to the non-adiabatic opening of the trap. In the limit where the interactions are instantaneously switched off, it matches the quantum depletion. Each curve corresponds to a different ramp of 0 ms (dashed), 1 ms (dotted) and 2.5 ms (dashed dotted) without excitation. The solid grey curves corresponds to an excitation of 4% for 4 periods and a ramp of 1 ms.

1.D Adiabatic opening of the trap

As we saw in section 3.C of the first chapter, we want to measure the quasi-particle state. As we measure atoms, it is important to map the quasi-particle basis onto the atom one: we need to adiabatically switch off interactions. In the last chapter, section 2.C, we saw that the natural expansion of the BEC is not adiabatic enough to well map the phonon basis onto the atom basis. To slow down the density decrease, the transverse trapping laser power is ramped down while keeping the vertical confinement. The laser ramp is shown in Figure 74(a) while panel (b) shows the theoretical sound speed, proportional to the inverse of the square of the BEC transverse size. The longer the ramp (dashed dotted orange), the slower the switch-off duration. The right plot shows $|\beta_k|^2$[1] as a function k. It corresponds to the number of pairs of the quantum depletion. When the interactions are slowly turned off, the number of quasi-particles created from vacuum is largely decreased.

Due to remnant magnetic fields in the experiment vacuum chamber, we cannot turn off the trap in a too long time. For the data presented here, the ramp duration is 1 ms. On Figure 74(c), we see that the 1 ms curve (dotted) at 10 mm/s is close to the 2.5 ms curve (dashed dotted) and more than one order of magnitude below the sudden shutdown (dashed). The grey curve shows the number of atoms after a typical modulation. We conclude that for such ramp, we are close measuring the phonon basis.

Experimentally, comparing different durations of this ramp is not straightforward. When we ramp down the transverse laser power, the BEC keeps breathing for a longer duration than if we instantaneously shut down the trap. This means that we still produce quasi-particles hence we cannot really compare in density two durations of this laser power ramp. We need to compare the effect on the correlation signal for which an entire day of acquisition is often needed. This 1 ms choice could therefore be improved in the future.

[1] We defined $|\beta|^2$ in equation (51), section 3.C of the first chapter.

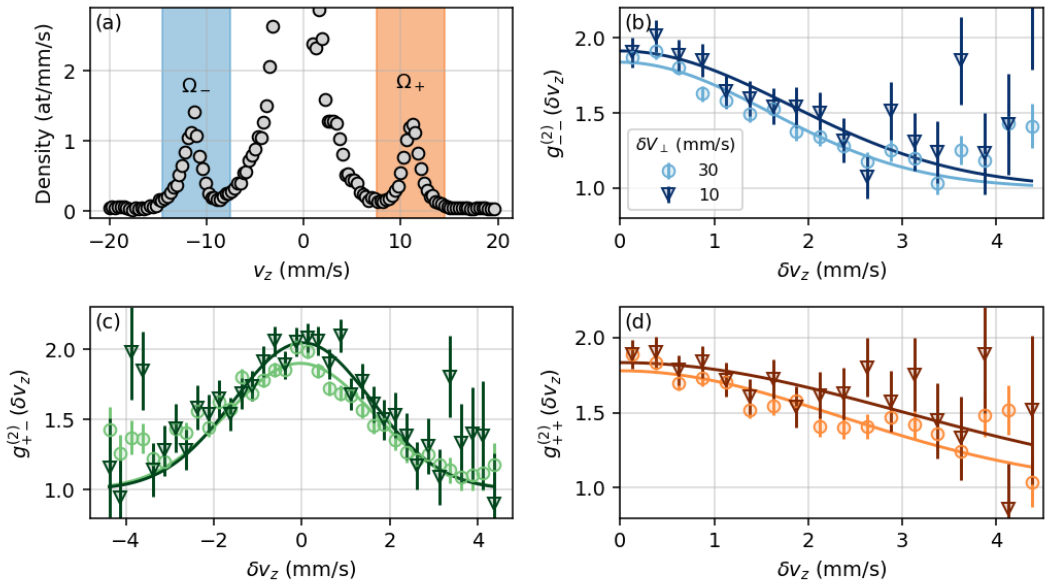

Figure 75: (a) Atomic density as a function of v_z. We define two regions Ω_- (in blue) and Ω_+ (in red) around the peaks in which we compute respectively local (Panels b and d) and cross correlations (Panel c). The transverse integration is set to 30 mm/s (light circles) and 10 mm/s (dark circles). ®Dataset taken on October 2024.

2. Probing correlations via momentum-integrated correlations

We now turn to the analysis of the correlation and start with the momentum-integrated correlation method.

2.A Method

Panel (a) of Figure 75 shows the density profile of the pairs. We select two opposite volumes $\Omega_\pm$ of size 7 mm/s along z, around each peak at ±11 mm/s. We compute local correlations in each of these volumes and compute the cross correlation between them. The volume along the z-axis is highlighted by the shaded blue and orange area in Figure 75(a). To compute the correlation function, we realize the 3D histogram of the velocity difference (local correlation) and sum (cross correlation). To normalize this quantity, we compute the same 3D histogram meshing different cycles. We describe the code in section 4.B of the appendix (see also Schellekens (2007) and Ténart (2021)). The bin size is set to 0.25 mm/s along v_z and 3 mm/s along v_x and v_y. These values are smaller than the correlation length along each direction to fully resolve it. In each volume $\Omega_\pm$, we compute the local correlation function

$$g^{(2)}_{ii}(\boldsymbol{\delta k}) = \frac{\int_{\Omega_i} \langle \hat{a}^\dagger_{\boldsymbol{k}} \hat{a}^\dagger_{\boldsymbol{k}+\boldsymbol{\delta k}} \hat{a}_{\boldsymbol{k}} \hat{a}_{\boldsymbol{k}+\boldsymbol{\delta k}} \rangle \, \mathrm{d}\boldsymbol{k}}{\int_{\Omega_i} n_{\boldsymbol{k}} n_{\boldsymbol{k}+\boldsymbol{\delta k}} \mathrm{d}\boldsymbol{k}} \tag{192}$$

which is a 3D function. For a thermal state, we expect $g^{(2)}_{ii}(0) = 2$ and the correlation to decay over a scale given by the inverse size of the source (Gomes et al., 2006; Butera et al., 2021). This in analogous to the Hanbury-Brown and Twiss experiment (Brown and Twiss,

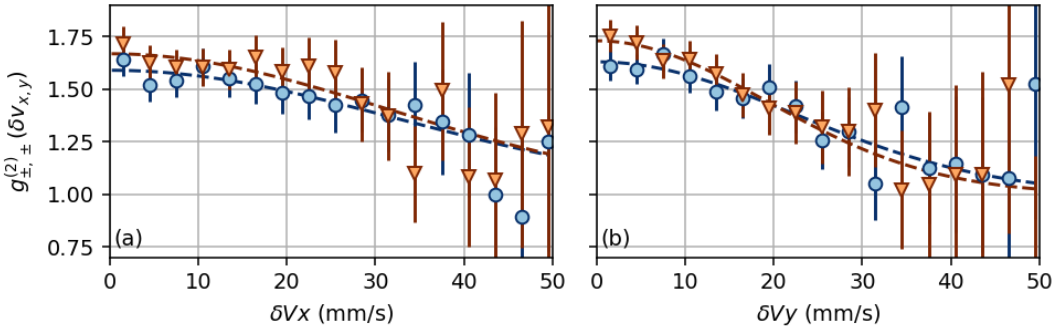

Figure 76: Local correlation function of beam Ω_- (blue circles) and Ω_+ (orange triangles). Lines are Gaussian fits with standard deviation $\sigma_x = 30(5)$ mm/s and $\sigma_y = 21(2)$ mm/s.

1956), in which the light intensity correlation function between two separated telescopes, gives access to the size of the thermal source (a star in their case). On panels (b) and (d) of Figure 75, we show the variation of $g^{(2)}_{ii}(\boldsymbol{\delta k})$ as a function of δv_z. In this case, we integrated over the transverse direction, hence we show

$$g^{(2)}_{ij}(\delta k_z) = \iint_{-\Delta k_\perp}^{\Delta k_\perp} g^{(2)}_{ij}(\boldsymbol{\delta k}) \frac{\mathrm{d}\delta k_x \mathrm{d}\delta k_y}{(2\Delta k_\perp)^2} \tag{193}$$

which depends on the transverse integration volume $\Delta k_\perp$. In panels (b, c, d) of Figure 75, the transverse integration is 30 mm/s (light circles) and 10 mm/s (dark triangles). The amplitude of the correlation increases as $\Delta k_\perp$ decreases but so does the noise.

In Figure 76, we show the transverse local correlation function $g^{(2)}_{\pm\pm}(\delta k_x)$ (panel a) and $g^{(2)}_{\pm\pm}(\delta k_y)$ (panel b). Lines are Gaussian fits yielding a correlation length of 30(5) mm/s along x and 21 mm/s along y. We observe that the length of the transverse correlation is similar to the transverse size of the cloud in Figure 71. It means that there is mainly a single mode along the transverse direction. The population of the excited transverse levels is really low.

We define also the cross-correlation function[2]

$$g^{(2)}_{+-}(\boldsymbol{\delta k}) = \frac{\int_{\Omega_-} \langle \hat{a}^\dagger_{-\boldsymbol{k}+\boldsymbol{\delta k}} \hat{a}^\dagger_{\boldsymbol{k}+\boldsymbol{\delta k}} \hat{a}_{-\boldsymbol{k}+\boldsymbol{\delta k}} \hat{a}_{\boldsymbol{k}+\boldsymbol{\delta k}} \rangle \, \mathrm{d}\boldsymbol{k}}{\int_{\Omega_i} n_{-\boldsymbol{k}+\boldsymbol{\delta k}} n_{\boldsymbol{k}+\boldsymbol{\delta k}} \mathrm{d}\boldsymbol{k}} \tag{194}$$

and show $g^{(2)}_{+-}(\delta v_z)$ in panel (c) of Figure 75. Here also, the transverse integration is 30 mm/s for the light grey circles and 10 mm/s for the black triangles.

[2] In fact, it does not change much if we replace the "+" sign of the cross correlation function by a "−" sign along v_x and v_y. The signal goes even higher when choosing a − sign, which is what we do here.

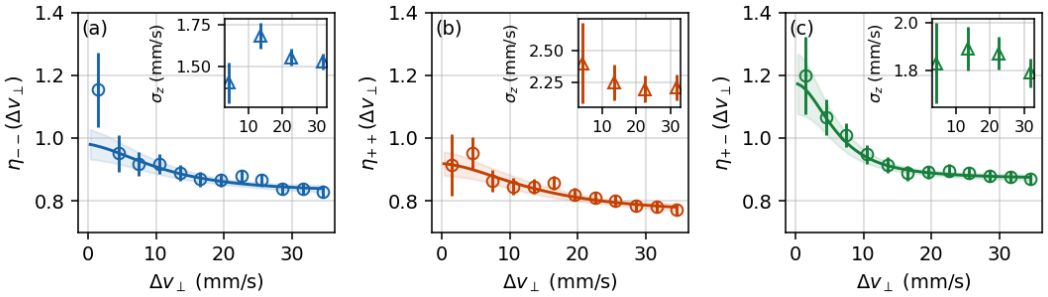

Figure 77: Amplitude of the local (a-b) and cross (c) second order correlation function. Solid line is a fit using (198). Insets show the fitted width σ_z in (196) for 1 out of 3 points. We do not observe significant change wen we decrease the transverse size.

2.B Measurement of the peak correlation value

Following Ténart (2021), we model the second order correlation function by a Gaussian

$$g_{ij}^{(2)}(\boldsymbol{\delta k}) = 1 + \eta_{ij} \prod_{\alpha=x,y,z} \exp\left(\frac{-\delta k_\alpha^2}{2\sigma_\alpha^2}\right) \tag{195}$$

where η_{ij} is the peak value of the correlation function and σ_α is the correlation length along the direction α. After a transverse integration $\Delta k_\perp$, this means that the amplitude of the correlation is

$$g_{ij}^{(2)}(\delta k_z) = 1 + \eta_{ij}(\Delta k_\perp)\exp\left(\frac{-\delta k_z^2}{2\sigma_z^2}\right) \tag{196}$$

where the amplitude of the 1D integrated correlation is

$$\eta_{ij}(\Delta k_\perp) = \frac{\pi\sigma_\perp^2}{2\Delta k_\perp^2}\mathrm{erf}\left(\frac{\Delta k_\perp}{\sqrt{2}\sigma_\perp}\right)^2. \tag{197}$$

We therefore fit the integrated correlation function with a Gaussian function. Typical fits are shown as solid lines in panels (b-d) of Figure 75. We report in Figure 77 the amplitude of the local correlation $\eta_{\pm\pm}$ in panels (a-b) and the cross correlation η_{+-} in panel (c) as a function of the transverse integration $\Delta v_\perp$. In the insets, we show that the width of the correlation σ_z does not vary much.

According to Eq. (197), we expect the amplitude of the correlation to vanish when the transverse integration radius is much larger than the transverse correlation radius. Here, we observe that the amplitude reaches a non-zero plateau value. This is due to the fact that the gas is almost 1D and the signal is not washed out by other transverse modes, which are not populated. We therefore adjust experimental data with the following function

$$\eta_{ij}(\Delta k_\perp) = A\frac{\pi\sigma_\perp^2}{2\Delta k_\perp^2}\mathrm{erf}\left(\frac{\Delta k_\perp}{\sqrt{2}\sigma_\perp}\right)^2 + B \tag{198}$$

where A, B and $\sigma_\perp$ are free parameters. The value of $A + B$ gives access to the amplitude of the correlation signal and the value of $\sigma_\perp$ to the transverse correlation width. The solid line in Figure 77 shows the fit result and the shaded area the associated fit uncertainty.

Concerning the transverse correlation width, we find $\sigma_\perp$ =8(10) mm/s and 11(15) mm/s. The uncertainties are quite large but these values are consistent with the transverse radius of

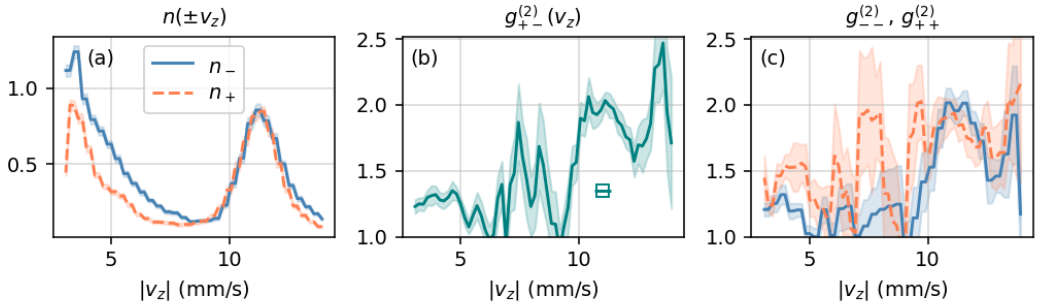

Figure 78: Number of atoms (a), cross correlation (200) (b) and local correlation functions (199) (c) as a function of the momentum. Voxel size is 0.7mm/s along v_z and 80 mm/s along v_x and v_y. ®Same dataset as Figure 75.

the pairs (10(1) mm/s along v_x and v_y). This is also coherent with the correlation radius along v_x which is 12(1) mm/s and v_y 11(1) mm/s measured in a different dataset, as discussed in section 1.C of the appendix.

The peak value of the correlation is given by the value of A and B, which yields $g^{(2)}_{--}(0) = 1.98(5)$ and $g^{(2)}_{++}(0) = 1.93(4)$ for the local correlation functions and $g^{(2)}_{+-}(0) = 2.2(1)$ for the cross correlation.

Summary This section introduces momentum-integrated correlation. By constructing a 3D histogram of atomic velocity differences, we obtain a 3D function that depends on the three momentum components v_x, v_y, and v_z. We model the correlation with a Gaussian function, which allows us to extract the peak value of the correlation signal. We find $g^{(2)}_{--}(0) = 1.98(5)$ and $g^{(2)}_{++}(0) = 1.93(4)$ for the local correlation. For the cross correlation, we find $g^{(2)}_{+-}(0) = 2.2(1)$.

3. Probing correlations via momentum-resolved correlations

3.A Momentum-resolved correlations

In the previous section, we integrated over a large volume $\Omega_\pm$ and lost information about the position of the modes. Here, we take another point of view: we compute the second order correlation functions between opposite modes, defined in voxels. The local correlation function is defined by

$$g^{(2)}_{ii} = \frac{\langle (\hat{a}^\dagger_i)^2 \hat{a}^2_i \rangle}{\langle \hat{a}^\dagger_i \hat{a}_i \rangle^2} = \frac{\#\text{ of pairs}}{(\#\text{ of atoms})^2} \tag{199}$$

and the cross-correlation by

$$g^{(2)}_{ij} = \frac{\langle \hat{a}^\dagger_i \hat{a}^\dagger_j \hat{a}_i \hat{a}_j \rangle}{\langle \hat{a}^\dagger_i \hat{a}_i \rangle \langle \hat{a}^\dagger_j \hat{a}_j \rangle} = \frac{\#\text{ of pairs between i \& j}}{(\#\text{ in i})(\#\text{ in j})}. \tag{200}$$

Here, i and j refer to the mode position whose size is given by the voxel size. In Figure 78(a), we plot the number of detected atoms in voxels of size $(80^2 \times 0.7)$ mm^3/s^3 as a function of the momentum. The size of the box along z is shown in panel (b) with the horizontal bar and

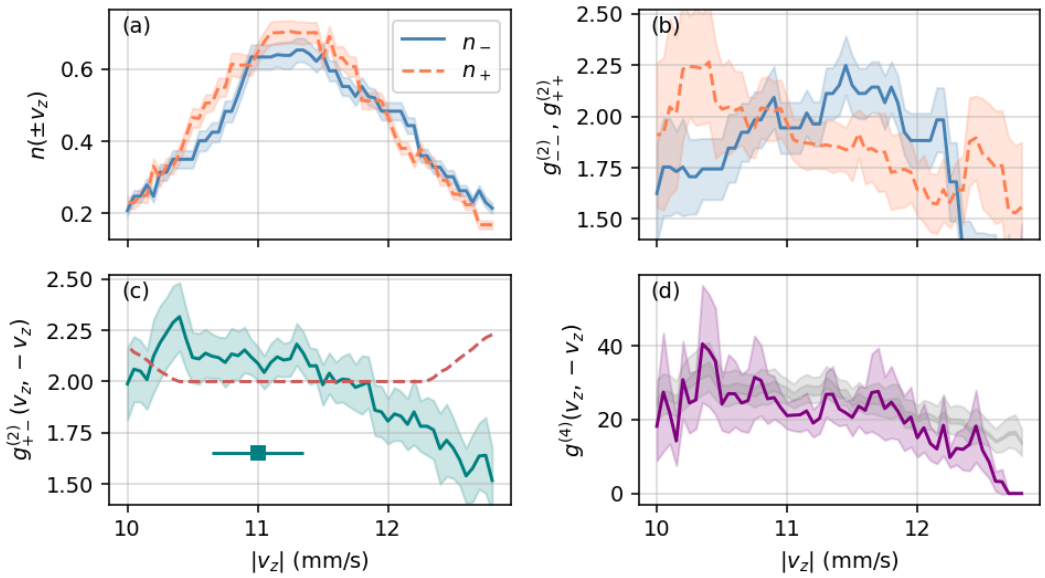

Figure 79: (a) Number of atoms, (b) local correlation (199), (c) cross correlation (200) and (d) fourth order correlation functions (201) as a function of the momentum. The dashed red line in (c) is the non separability threshold from Eq. (142) assuming a 0.5 quantum efficiency and the population in panel (a). ®Same dataset as Figure 75.

the square marker. Here, we show a solid curve for clarity reasons. However, it is made of experimental points separated by 0.35 mm/s which means that there is a sliding average. The blue solid curve shows the negative peak and the orange dashed one the positive peak. The speed ranges from 3 mm/s to 14 mm/s and the density is peaked around 11 mm/s.

On panel (c) of Figure 78, we show the local correlation function (199) as a function of v_z. The solid blue curve shows $g^{(2)}_{-v_z,-v_z}$ and the orange dashed curve $g^{(2)}_{v_z,v_z}$.

- In the [2,5] mm/s range, we have a mixture between thermal atoms and condensed atoms. In this range, we expect the second order correlation function to be between 1 (coherent BEC) and 2 (thermal depletion), as studied by Hercé et al. (2023). This matches our observations.
- In the [5, 15] mm/s range, we expect to observe bosonic bunching, leading to a value of $g^{(2)}_{k,k} = 2$. This is what we observe in the [10,13] mm/s region, where the Bogoliubov pairs are excited, but the correlation does not reach this value for lower speed. This is because the correlation value is only achieved when the voxel size approaches zero. Here, the voxel size exceeds the mode size, so we do not expect to accurately measure the true correlation value. In fact, this "momentum-resolved" correlation method does not allow precise measurement of the value of the correlation when the population is too low. The fact that it gives a value close to 2 in the region [10,13] is due to the fact that a single Bogoliubov mode dominates the signal, and its high population suppresses the contribution from other modes.

In panel (b) we show the cross-correlation function (200) for which we observe a clear correlated signal at the peak density, around 11 mm/s.

In Figure 79, we zoom onto the correlated peaks. The voxel transverse size is decreased to 30 mm/s to better capture the value of the correlation, while keeping a reasonable signal-to-noise ratio. On the z axis, the voxel size is kept at 0.7 mm/s, while the position of the voxel

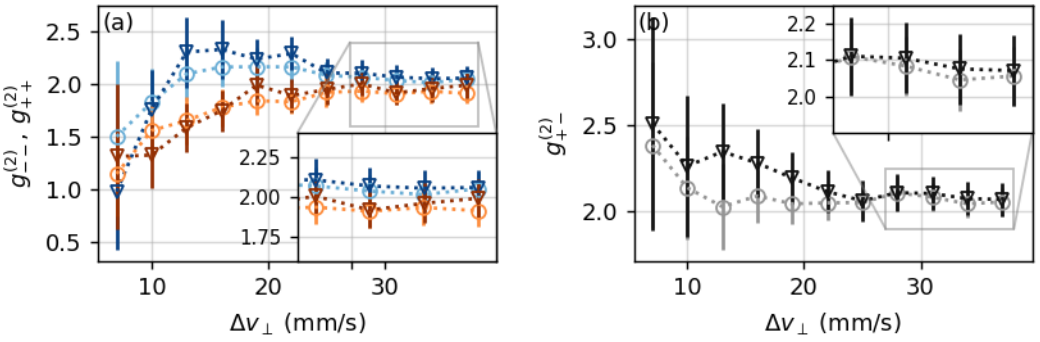

Figure 80: Local (a) and cross (b) correlation functions as a function of the voxel size along v_z. Each hue and marker refer to the voxel transverse size that ranges from 60 to 20 mm/s (see legend). In panel (a), blue and orange color refer respectively to the negative and positive velocities. The position of the two modes are ±11 mm/s. ®Same dataset as Figure 75.

is changed by 0.1 mm/s per point. Each point of the curve is not independent: we perform a sliding average. The marker in panel (c) shows the size of the voxel compared to the x-axis range. In each plot, the line shows the mean value and the shaded area the standard deviation of the distribution computed with bootstrap methods. The fact that the line is not so smooth reflects also the uncertainty. As the raw data for each point is not independent, we compute the mean value and the standard deviation over different bootstrap realizations.

Panel (a) shows the atom number in a single voxel of the negative (solid blue) and positive (dashed orange) peaks. Panel (b) shows the *single voxel* second order local correlation function (199). We observe that, within the large uncertainty bars, the value is compatible with 2. Panel (c) shows the *single voxel* second order correlation function. The dashed red line shows the non-separability threshold, see eq. (142) of chapter 2, section 4.B. This non-separability thresholds depends on the population shown in panel (a) and on the detector's 50% quantum efficiency. We observe here that the correlation signal goes (almost) significantly above this threshold value[3]. In the last panel (d) of Figure 79, we show in solid purple line the fourth order correlation function

$$g^{(4)}_{ij} = \frac{\langle (\hat{a}^\dagger_i)^2 (\hat{a}^\dagger_j)^2 \hat{a}^2_i \hat{a}^2_j \rangle}{n_i^2 n_j^2}. \tag{201}$$

The purple shaded area shows the standard deviation of $g^{(4)}$ while the grey shaded area is its theoretical algebraic bounds, based on the value of $g^{(2)}$

$$4\left(g^{(2)}_{12} - 1\right)^2 \leq g^{(4)}_{12} - 16 g^{(2)}_{12} + 12 \leq 6\left(g^{(2)}_{12} - 1\right)^2. \tag{202}$$

that we discussed in the second chapter, section 4.E. Note however that the grey shaded area takes into account the uncertainty of the second order correlation function : the width of the curve is larger by a factor 4 compared to the theoretical interval $2(g^{(2)}_{12} - 1)^2$. We observe here that the fourth-order correlation function remains relatively close to this bound.

As we said, the value of the correlation is reached in the limit where the voxel size goes to zero. In Figure 80, we keep the voxel position at 11 mm/s and progressively decrease

[3] Note however that this reasoning cannot really stand if we keep decreasing the voxel size to measure the value of $g^{(2)}$: in the limit of vanishing size, the population goes also to zero. The correlation value obtained in this limit should be compared to the threshold value for the state's population, *i.e.*, the population within the voxel size.

the transverse voxel volume. Along v_z we take a voxel length of 1.3 mm/s (equal to the coherence length in momentum, shown in light color circles) and 0.9 mm/s (smaller). We show the second order correlation function as a function of the voxel radius along $v_{x,y}$. On panel (a), we show the local correlation function of the positive peak (orange colors) and the negative peak (blue colors). The correlation signal remains compatible with 2, although uncertainties are fairly large. When the transverse volume becomes too small (smaller than 10 mm/s here), we observe that the local correlation seems to decrease. This is due to a lack of signal which is more dramatic for the auto-correlation than for the cross correlation. Indeed, the auto-correlation measures the number of pairs within the same voxel.

On panel (b) we show the cross correlation function, which lies above 2, but not significantly. When we decrease the transverse volume size, the correlation seems to increase but, here again, not significantly. To better capture the value of the correlation signal in the limit of vanishing voxel size, we will therefore integrate over v_z in the next paragraph.

Before moving to the next paragraph, note that even though the second order correlation function is not significantly above 2, the Cauchy-Schwarz ratio $C_{\mathcal{S}}$ is significantly larger than 1. For example, for a transverse integration radius of 30 mm/s, we have $C_{\mathcal{S}}$ =1.056(25) and mean populations of 0.98(4) and 1.05(4).

3.B Integrating the momentum-resolved correlation

We show in Figure 81 the second order correlation function map $g^{(2)}(v_{z1}, v_{z2})$. Panel (a) shows the entire symmetric map with a voxel volume of (0.4×80^2) mm^3/s^3. Panel (b-d) show a zoom on respectively the cross correlation, the negative peak auto-correlation and the positive peak auto-correlation. Note that there is no sliding average here. On these maps, the voxel length was reduced to 0.3 mm/s, much smaller than the mode size. To better capture the correlation we integrate over ± 10 to ± 11.5 mm/s: this interval is highlighted in color on each map.

Method 1

Protocol: we compute the number of pairs in a voxel of size $\boldsymbol{\Delta v} = \Delta v_z \times \Delta v_x \times \Delta v_y$. We set the value of Δv_z, which is a compromise between our mode size (1.3 mm/s) and our stability (0.1 mm/s). It allows to fully resolve the correlation peak without washing out the cross-correlation signal, which is sensitive to shot-to-shot fluctuations. We then define $\Omega_\pm = [\pm 10, \pm 11.5]$ mm/s, which is the region in which we will perform the integration. We therefore define the 1D local correlation function

$$g^{(2)}_{\pm\pm}(\delta v_z) = \sum_{\substack{v_{z1}-v_{z2}=\delta v_z \\ (v_{z1}+v_{z2})/2 \in \Omega_\pm}} \langle : n_{v_{z1}} n_{v_{z2}} : \rangle \Big/ \sum_{\substack{v_{z1}-v_{z2}=\delta v_z \\ (v_{z1}+v_{z2})/2 \in \Omega_\pm}} \langle n_{v_{z1}} \rangle \langle n_{v_{z2}} \rangle \tag{203}$$

where $n_{v_{z\alpha}}$ is the number of atoms in a voxel of size $\boldsymbol{\Delta v}$ at position $v_{z\alpha}$. The average $\langle \cdot \rangle$ means average over experimental realizations and the two normal ordering dots ":" refer to the fact that $\langle : n_{v_{z1}} n_{v_{z2}} : \rangle$ counts the number of pairs between the two voxels. In other words, it counts the number of coincidence counts between the two voxels. Geometrically, the integration process consists in integrating along the diagonal of Figure 81. Symmetrically, we define the 1D cross-correlation function

$$g^{(2)}_{+-}(\delta v_z) = \sum_{\substack{v_{z1}+v_{z2}=\delta v_z \\ (v_{z1}-v_{z2})/2 \in \Omega_+}} \langle n_{v_{z1}} n_{v_{z2}} \rangle \Big/ \sum_{\substack{v_{z1}+v_{z2}=\delta v_z \\ (v_{z1}-v_{z2})/2 \in \Omega_+}} \langle n_{v_{z1}} \rangle \langle n_{v_{z2}} \rangle \,. \tag{204}$$

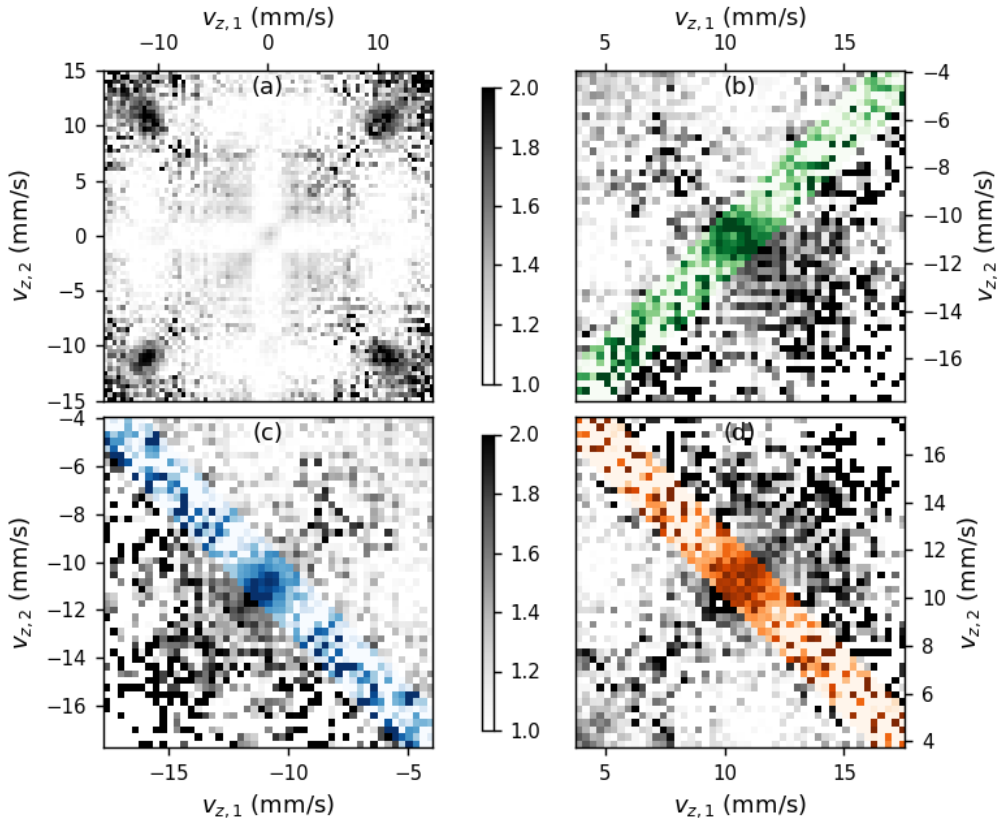

Figure 81: 2D map of the second order correlation function $g^{(2)}(v_{z1}, v_{z2})$. Panel (a) shows the entire map, which is symmetric over the diagonal. Panel (b-d) shows respectively a zoom on the cross correlation function (bottom right corner of panel (a)), the negative peak auto-correlation (bottom left of (a)) and the positive peak auto-correlation (top right corner of (a)). Voxel size of 0.4 mm/s for (a) and 0.3 mm/s for (b-d). ®Same dataset as Figure 75.

where the normal ordering is no longer needed as the two voxels never coincide.

We show in Figure 82 these 1D correlation functions. Panel (a) shows the positive peak, panel (b) the negative one and panel (c) the cross correlation. To shorten notations, we did

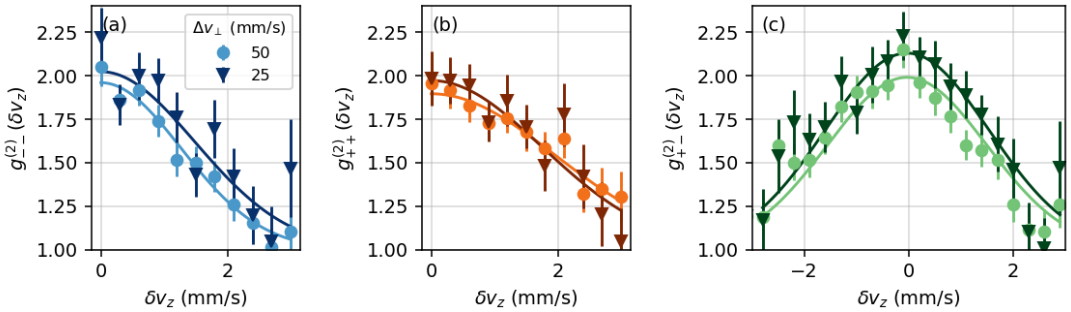

Figure 82: 1D local correlation function $g^{(2)}_{++}$ (panel a) and $g^{(2)}_{--}$ (panel b) defined in Eq. (203). Panel (c) shows the cross correlation function $g^{(2)}_{+-}$ defined in Eq. (204). ®Same dataset and voxel size as Figure 81.

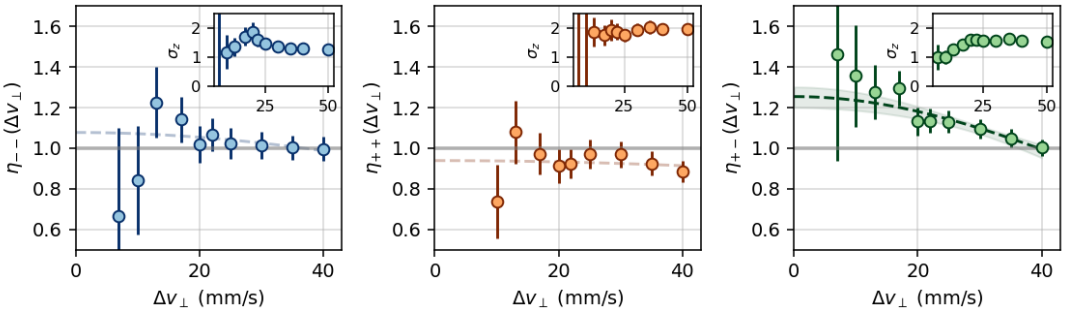

Figure 83: Amplitude of the second order correlation function defined in (205) as a function of the transverse size of the voxel. The insets show the width σ_z in mm/s. The 1D second order correlation function were defined in Eqs. (203) and (204). Dashed line are a fit using (206). ®Same dataset as Figure 82.

not write explicitly the dependence of $g^{(2)}_{\pm,\pm}$ on the voxel size $\boldsymbol{\Delta v}$. The size Δv_z influences the number of points *i.e.* our ability to resolve the correlation width and $\Delta v_{x,y} = \Delta v_\perp$ is the transverse integration volume. We do not change Δv_z but we will decrease the transverse integration volume to extract the value of the correlation in the limit where the voxel size vanishes. In Figure 82, the transverse integration volume is 50 mm/s (light circles) and 25 mm/s (dark triangles). As previously, we fit the correlation with a Gaussian function

$$g^{(2)}(\delta v_z) = 1 + \eta_{\Delta v_\perp} \exp\left(-\delta v_z^2 / 2\sigma_z^2\right) \tag{205}$$

where $\eta_{\Delta v_\perp}$ is the amplitude of the Gaussian function that depends on the transverse integration volume.

In Figure 83, we show the value of $\eta_{\Delta v_\perp}$ as a function of the transverse integration. A value of $\eta_{\Delta v_\perp}$ of 1 means that the peak value of the local correlation is 2. The insets report the value of the width of the Gaussian, σ_z, defined in Eq. (205). The fitted width depends slightly on the transverse integration. The extracted amplitude of the local correlations (panels a and b) are in remarkable agreement with the expected value of 1 for a thermal state ($g^{(2)}_{\pm\pm} = 2$). On panel (c), we show the extracted amplitude of the cross-correlation which goes significantly above 1. The dashed line is an ansatz from inspired from section 2.B

$$\eta_{ij}(\Delta k_\perp) = A \frac{2\pi\sigma_\perp^2}{\Delta k_\perp^2} \mathrm{erf}\left(\frac{\Delta k_\perp}{2\sqrt{2}\sigma_\perp}\right)^2. \tag{206}$$

We find a transverse radius $\sigma_\perp$ of 23(1) mm/s, which is a factor 2 higher than in the previous section. It leads to a peak value of $g^{(2)}_{+-} = 2.25(5)$.

For the negative and positive peaks of the local correlations, this ansatz led to a value of 2.07(6) and 1.94(5) respectively. However, the fitted values of $\sigma_\perp$ deviate even more from the correlation length, reaching 39(1) and 70(1) mm/s. Fit are shown with shaded dashed lines in Figure 83.

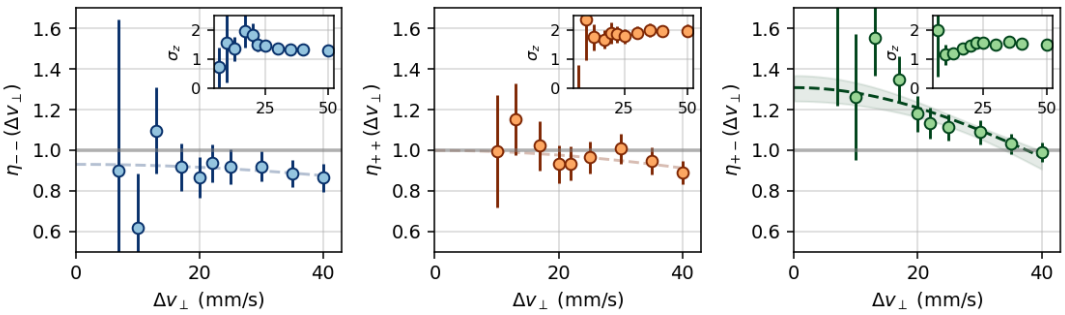

Figure 84: Amplitude of the second order correlation function defined in (205) as a function of the transverse size of the voxel. The insets shows the width σ_z in mm/s. The 1D second order correlation function were defined in Eqs. (203) and (204). ®Same dataset as Figure 82.

Method 2

In the previous method, we integrated over the numerator and normalized the correlation by the integral of the density product, see Eqs. (203) and (204). It is also possible to directly integrate over the normalized second order correlation function

$$g^{(2)}_{\pm\pm}(\delta v_z) = \sum_{\substack{v_{z1}\pm v_{z2}=\delta v_z \\ (v_{z1}\mp v_{z2})/2\in\Omega_\pm}} g^{(2)}_{\pm\pm}(v_{z1}, v_{z2}). \tag{207}$$

As before, we fit the with a Gaussian function and extract the width and the amplitude $\eta_\pm$ of the Gaussian. Results are shown in Figure 84. We also fit the data using Eq. (206) which leads to a peak value of $g^{(2)}_{--} = 1.93(8)$, $g^{(2)}_{++} = 2.00(6)$ and $g^{(2)}_{+-} = 2.30(7)$.

Summary In this section, we measure the local and cross correlations of the two phonon peaks. We measure the local correlation and cross correlation using two techniques and show they are in remarkable agreement with 2. The average of the two measurements gives $g^{(2)}_{--} = 2.00(8)$ for the negative peak and $g^{(2)}_{++} = 1.97(6)$ for the positive peak. For the cross correlation, we find a value of $g^{(2)}_{+-} = 2.27(7)$, which significantly exceeds 2. These measurements are in agreement with the ones measured in the previous section 2.B, using the momentum-integrated correlation method. We also report on a violation of the integrated Cauchy-Schwarz inequality, which is a signature of particle entanglement (Wasak et al., 2014).

4. Conclusion on entanglement

Our goal in this section is to draw conclusions about entanglement. To extract as much information as possible about the state, we analyze various observables. We have already measured the second-order correlation functions; now we examine the 4-body correlation function and relative number squeezing. Additionally, we aim to confirm that the state is thermal so that we can apply the criterion derived in Chapter 2.

In the previous sections, we measured the value of the local correlation function and showed that it is compatible with 2. In the discussion in Chapter 2, section 4.G, we emphasized that the derived criterion is valid only if the state is not displaced and $\langle \hat{a}_k^2 \rangle = 0$. To further confirm this, we examine the single-mode statistics. In the first part of subsection 4.A, we

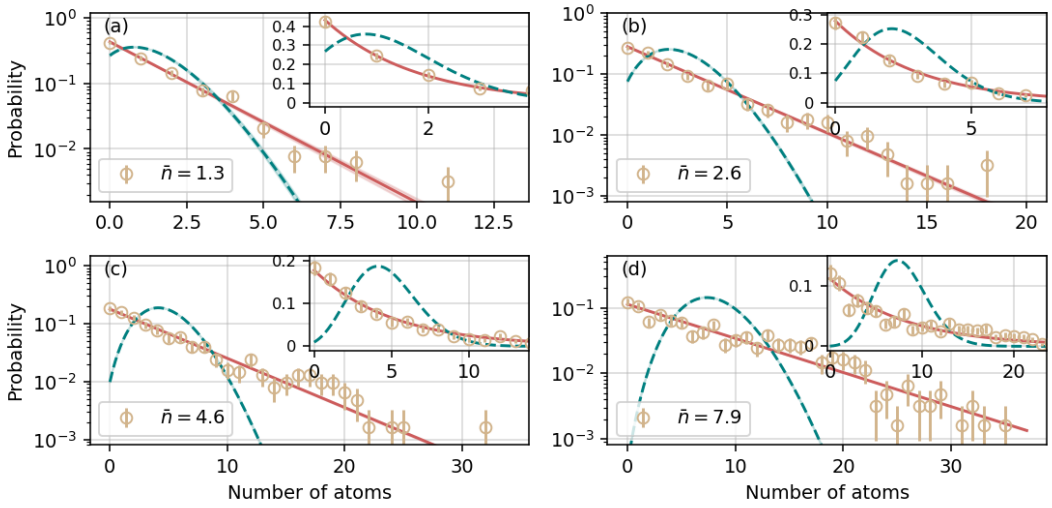

Figure 85: Full counting statistics of the sidebands. We plot the probability distribution function of the atom number. The yellow circles show the experimental statistics. The solid red line and dashed blue line show the thermal and Poissonian distributions, calculated based on the measured mean atom number with no free parameter. The inset shows the same data without log scale. ®Same dataset as Figure 70 in chapter 5, section 2.F, 500 shots per panel, voxel size of 0.6 and 80 mm/s.

show a good agreement with thermal statistics by using additional datasets to vary the mean population of the state. We then compare the experimental distribution's proximity to that of a slightly displaced state, and we compute the N-body local correlation function to highlight the dependence on thermal statistics.

In subsection 4.B, we measure the population of the state using the mode size given by the width of the correlation functions. We can compare $g^{(2)}$ to the smaller bound that assesses entanglement, as discussed in the second chapter, section 4.B. We finally measure the 4-body correlation function and discuss how its value influence the non-separability of the state. In subsection 4.D, we discuss the influence of the non-unit quantum efficiency of the detector. In this section, we also measure the normalized variance and compare it to the expected value.

Finally, we conclude in subsection 4.F on the presence of entanglement. We also report measurements of the Cauchy-Schwarz ratio across various excitation durations. Initially, entanglement is detected, but at later times, it is no longer observable.

4.A Full counting statistics of a single mode

Fock probability distribution

We begin by demonstrating our ability to fully resolve the statistical properties of an individual mode. Here, we analyze a different dataset in which the excitation duration was varied. Figure 85 reports such probability distribution for four different mean populations. Our goal is to emphasize that, whatever the population, the single mode statistic is always well-described by a thermal statistics.

The statistical properties of thermal and coherent states are fully determined by their mean

number of particles[4]: they are shown respectively with solid red and dashed blue lines[5]. Each panel shows the probability distribution for a different excitation duration, hence a different mean atom number. Regardless of the population, the probability distribution remarkably agrees with a thermal distribution over three orders of magnitude. The limitation is in fact the number of experimental repetitions.

Comparing the Fock probability distribution with a coherent state

Importantly, the criterion derived in the second chapter only applies for non-displaced Gaussian states. To better quantify this, we parametrize the state by a fraction f_{th}, keeping its mean population constant and writing the mean of the state and its covariance matrix as

$$\boldsymbol{\mu} = 2\sqrt{\bar{n}(1-f_{th})}\begin{pmatrix}\cos\theta\\ \sin\theta\end{pmatrix} \quad , \qquad \boldsymbol{\sigma} = (2\bar{n}f_{th}+1)\mathbb{I}_2. \tag{208}$$

Here the Fock distribution is not sensitive to the angle θ of the displacement. The mean number of particles in the state is fixed, and we only change the relative fraction of coherent versus thermal atoms f_{th}. When $f_{th} = 0$, the state is coherent, and when $f_{th} = 1$, the state is thermal. To quantify the difference between the probability distribution of $\hat{\rho}_{f_{th}}$ and $\hat{\rho}_{exp}$, we evaluate the quadratic distance between the two distributions, normalized by the experimental uncertainties. Note that the fraction f_{th} is insensitive to the detection efficiency[6] η, as it only affects the mean population $\bar{n}_{det} = \eta\bar{n}$ and not f_{th}. This ensures that the analysis directly probes the state's relative displacement.

Panel (a) of Figure 86 shows the distance between the two distributions as a function of the thermal fraction f_{th}. The positive mode is represented in orange and the negative mode in blue. For the triangles, the longitudinal size of the voxel is larger than the mode size (2.7 mm/s). For the square and round markers, the voxel size is 0.7 mm/s, which is smaller than a mode size.

We observe the maximum distance consistently occurs at $f_{th} = 0$. It means that the probability distribution is never well described by a fully coherent state, which was already clear from Figure 85. However, we observe that the minimum for each curve occurs at different thermal fraction f_{th}^{min}. Notably, for larger voxel sizes, the distribution is neither thermal nor Poissonian and $f_{th}^{min} \sim 0.5$. For such a voxel size, we might in fact counting several (thermal) modes. As a result, the overall distribution departs from a simple thermal form, instead following a multimode thermal distribution (Goodman, 2015). When the mean population per mode $\bar{n}$ is the same, the probability distribution is known and is a function of $\bar{n}$ and the number of modes m. When $m = 1$, one recovers the thermal distribution, but the probability distribution tends to a Poissonian distribution as $m \to \infty$ (which directly relates to the central limit theorem). This was experimentally studied by Perrier et al. (2019), using a multimode source of two-mode squeezed states. This multimode effect is likely what we observe for these triangles as the voxel size is larger than the mode size. When the transverse voxel size decreases to a size similar to that of the mode, or smaller (circles and squares), the minima of the curves shift towards $f_{th} = 1$. In this case, we probe the statistics of a single mode.

[4] A fully coherent state follows a Poissonian distribution $P_{coh}(n) = \bar{n}^n e^{-\bar{n}}/n!$ and a thermal state a geometric law $P_{th}(n) = \bar{n}^n/(1+\bar{n})^{n+1}$. When the state is neither fully coherent nor fully thermal, an additional parameter is required to fully characterize the state. This was for example shown in Figure 34 where we plotted different probability distributions, changing the fraction of coherence of the state, the mean number of particles being fixed.

[5] These analytical probability distributions are plotted as continuous lines, although they are inherently discrete.

[6] See equation (88), a pure loss channel transforms $\boldsymbol{\mu}_{det} = \sqrt{\eta}\boldsymbol{\mu}$ and $\boldsymbol{\sigma}_{det} = \eta\boldsymbol{\sigma} + (1-\eta)\mathbb{I}_2$.

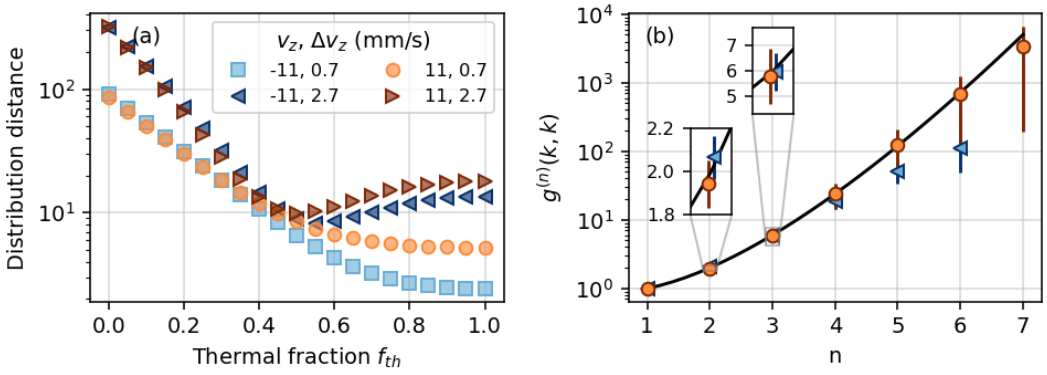

Figure 86: Left: distribution distance between the observed probability distribution and the thermal fraction of the mean population f_{th} defined in (208). The distribution distance is defined as $\sum_i |P_i^{(f_{th})} - P_i^{(exp)}|^2/\Delta^2 P_i^{exp}$ where P_i refers to the probability distribution of the experimental and the displaced/thermal state define by f_{th}. $\Delta^2 P_i$ refers to the Poissonian error on the experimental measurement. The color and shape of the markers refer to different position and voxel size (see legend). Right: the n^{th} order correlation function as a function of n, computed in a voxel of size Δv_z=0.7 and $\Delta v_{x,y}$=30 mm/s for the negative (blue triangle) and positive peak (red circles). The two markers have been slightly displaced on the x-axis for readability. ®Same dataset as last section.

N-body local correlation function

However, in section 4.G of the second chapter, especially Figure 34, we showed that the probability distribution of a slightly displaced state is not really far from a thermal state. To further verify the absence of coherence, we show in panel (b) of Figure 86 the n^{th} order normalized correlation function $g^{(n)}$ up to the seventh order. As it can be seen in (209), the influence of a non-zero $\langle \hat{a}_k^2 \rangle$ is more and more visible as n increases. The solid line represents $n!$, which is the expected value for a thermal state. Blue triangles and red circles respectively show the correlation value for the negative and positive peaks. For the negative peak, a significant discrepancy is observed for $n > 4$. On the other hand, for the positive peak, we observe a remarkable (and surprising) agreement. Indeed, we calculate the correlation function in a single voxel with a 0.7 mean population. To determine $g^{(4)}$, we analyze coincidence counts that involve at least 4 atoms simultaneously. For a thermal distribution and 1400 realization, the expected number of cycles with at least 4 detected atoms is 40. It decreases to 7 cycles for $g^{(6)}$ and only 3 cycles for $g^{(7)}$.

To assess entanglement, the criterion derived in the second chapter's section 4.B requires that the un-displaced Gaussian state also to satisfy $\langle \hat{a}_k^2 \rangle = 0$. Using Wick expansion and introducing[7] $\alpha_k := \langle \hat{a}_k^2 \rangle / \langle \hat{a}_k^\dagger \hat{a}_k \rangle$, one can show that

$$g^{(2)}_{k,k} = 2 + |\alpha|^2, \qquad g^{(3)}_{k,k} = 6 + 9|\alpha|^2, \qquad g^{(4)}_{k,k} = 24 + 72|\alpha|^2 + 9|\alpha|^4. \tag{209}$$

Based on the error bars[8] in Figure 86(b), the measurement of $g^{(2)}$ is consistent with 2.0 with an uncertainty of 0.1. We also have $g^{(3)} = 6(1)$ and for the positive peak, $g^{(4)}_{kk} = 25(9)$. Using

[7] We use here a different notation than in the second chapter's 4.A equation (134) as α is now normalized to the mean population.

[8] Error bars were evaluated with the bootstrap method.

these uncertainties, we estimate that $|\alpha|^2 < 0.1$ using $g^{(2)}_{k,k}$. We also have $|\alpha|^2 < 1/9$ using $g^{(3)}_{k,k}$ and $|\alpha|^2 < 9/72$ using $g^{(4)}_{k,k}$. Here, all these measurements agree that $|\alpha|^2 < 0.1$. In the previous sections, we measured the local correlation with two methods, finding its value consistent with 2.00 with an uncertainty of 0.05. Thus, we reasonably assume $\langle \hat{a}_k^2 \rangle = 0$ in the following analysis.

4.B Towards entanglement : measurement of the population

Our previous measurements showed that the k and $-k$ modes of the state are well described by a thermal state. We can therefore use the theoretical work of the second chapter. We measured a second order cross correlation function of 2.2(1) in section 2.B and 2.27(7) in section 3.B. The mean value is therefore 2.24(7). Assuming the state is Gaussian, we showed that the state is thermal; hence we can use Wick expansion to write

$$g^{(2)}_{k,-k} = 1 + (|\langle \hat{a}_k \hat{a}_{-k} \rangle|^2 + |\langle \hat{a}_k \hat{a}^\dagger_{-k} \rangle|^2)/n_1 n_2. \tag{210}$$

First, if we assume that $\langle \hat{a}_k \hat{a}^\dagger_{-k} \rangle = 0$, it means that the state is entangled as it implies $|\langle \hat{a}_k \hat{a}_{-k} \rangle|^2 > n_1 n_2$ which is an entanglement witness[9] (Hillery and Zubairy, 2006). If we do not assume $\langle \hat{a}_k \hat{a}_{-k} \rangle = 0$, we showed in the second chapter, section 4.B that the bound on $g^{(2)}$ to certify entanglement shifts, depending on the state population.

From the correlation length that we measured in the previous sections 2.B and 3.B, we define the voxel length to 1.5 mm/s to evaluate the population. Along v_x and v_y, we set the size of the box using the correlation length evaluated in section 2.A: 30 mm/s along v_x and 21 mm/s along v_y. The size of the transverse box is therefore $\sim 3\sigma_{x,y}$ where $\sigma_{x,y}$ is the fitted standard deviation of the sidebands (see section 1.A). This leads to a mean population of 0.93(4) and 0.95(4) detected atoms. For this choice of boxes, we observe a violation of the Cauchy-Schwarz inequality $C_S = 1.04(2)$ and relative number squeezing $\xi^2 = 0.92(4)$. The value of the local correlation function computed in a single voxel is compatible with 2 as $g^{(2)}_{--} = 1.94(9)$ and $g^{(2)}_{++} = 1.98(12)$.

We show in Figure 87 the probability distribution of each mode. The probability distribution is in excellent agreement with a thermal distribution (solid red line), which further confirms the thermal statistics of each mode.

Using the entanglement witness derived in the second chapter, section 4.B and the measured population (which is greater than $1/\sqrt{2}$) we observed $g^{(2)}_{k,k} > 2$ which means that, assuming the state is Gaussian, it is entangled. We would like now to quantify this entanglement using the logarithmic negativity. The author of the second chapter claimed that the measurement of the two- and four-body correlation functions allow to quantify the entanglement of the Gaussian state. We now proceed to such measurement.

[9] This was discussed in section 2.D of the second chapter.

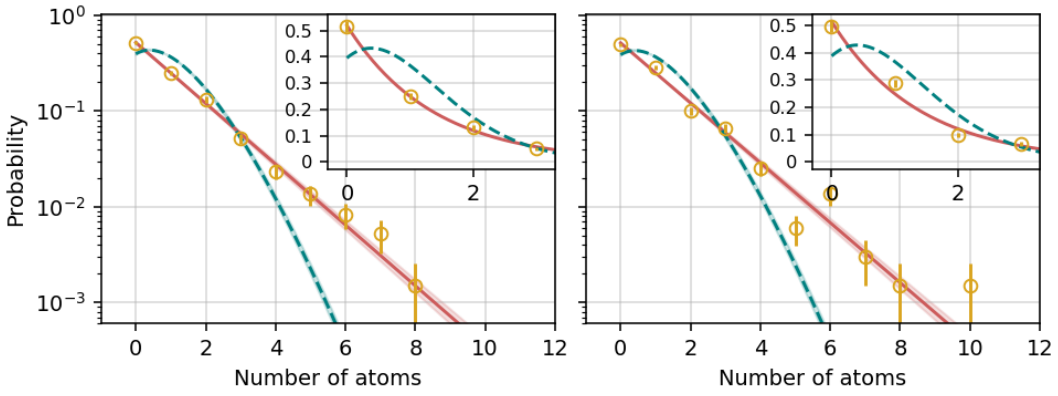

Figure 87: Full counting statistics of the dataset we analyze throughout this chapter, in a voxel of length 1.5 mm/s. The transverse size is $4\sigma_x$, where σ_x is the Gaussian standard deviation defined in section 1.A. The mean number of detected atoms is 0.93(4) and 0.95(4) and the normalized variance between the modes is 0.92(4), the Cauchy-Schwarz ratio 1.04(2). ®Same dataset as last section.

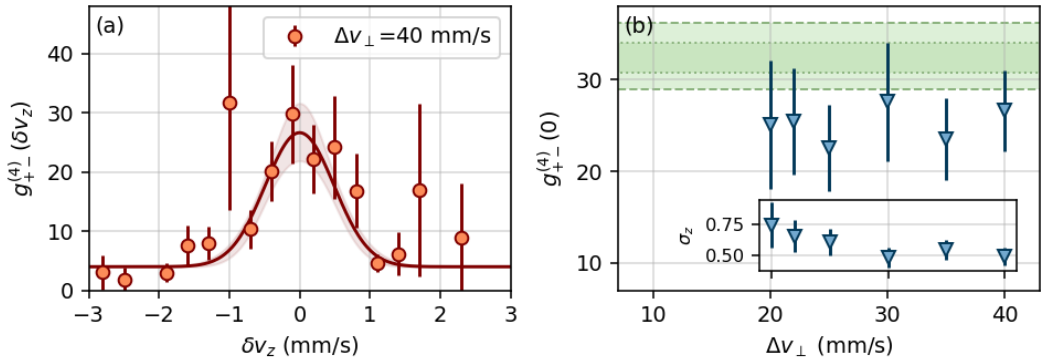

Figure 88: (a) Fourth order correlation function defined in (212), as a function of δv_z. A Gaussian fit yields a peak value of $g^{(4)}_{k,-k} = 26(4)$. (b) Extracted peak value of $g^{(4)}(0)$ as a function of the transverse integration. Here, we cannot decrease more the transverse integration to keep enough signal. The inset shows the fitted width of $g^{(4)}(\delta v_z)$, in mm/s. ®Same dataset as last section.

4.C Quantifying entanglement via the 4-body correlation function

Measurement of $g^{(4)}$

We now report on the measurement of the four-body correlation function, formally defined as

$$g^{(4)}_{k,-k} = \frac{\langle : \hat{a}^{\dagger 2}_k \hat{a}^{\dagger 2}_{-k} \hat{a}^2_k \hat{a}^2_{-k} : \rangle}{\langle \hat{a}^\dagger_k \hat{a}_k \rangle^2 \langle \hat{a}^\dagger_{-k} \hat{a}_{-k} \rangle^2} \tag{211}$$

The procedure to measure it is the same as the one described in section 3.B. On panel (a)

of Figure 88, we show

$$g^{(4)}_{+-}(\delta v_z) = \sum_{\substack{v_{z1}+v_{z2}=\delta v_z \\ (v_{z1}-v_{z2})/2 \in \Omega_+}} g^{(4)}_{+-}(v_{z1}, v_{z2}). \tag{212}$$

where Ω_+ has been defined in Figure 81(b). From a Gaussian fit[10], shown as a solid line in Figure 88(a), we extract the peak value of $g^{(4)}(\delta v_z = 0) = 26(4)$ for this 40 mm/s transverse integration volume. In Figure 88(b), we plot the fitted value of $g^{(4)}_{+-}(0)$ as a function of the transverse integration volume. For a thermal Gaussian state, the 4-body correlation function is bounded, and we have

$$4\left(g^{(2)}_{k,-k} - 1\right)^2 \leq g^{(4)}_{k,-k} - 16 g^{(2)}_{k,-k} + 12 \leq 6\left(g^{(2)}_{k,-k} - 1\right)^2. \tag{213}$$

This means the value of $g^{(4)}_{k,-k}$ is centered on a narrow interval of width $2(g^{(2)}_{k,-k} - 1)^2$. Given the measured value $g^{(2)}_{k,-k} = 2.24(7)$, the fourth-order correlation function is predicted to fall within $[29.99, 33.07]$. Taking into account the 0.07 uncertainty in the measurement of $g^{(2)}_{k,-k}$, this interval becomes $[28.20, 35.26]$. These intervals are reported in the shaded green area of Figure 88(b), between dashed and dotted curves.

First, we observe that the points lie near the minimal allowed value. Second, the uncertainty on the measurement of $g^{(4)}_{k,-k}$ is larger than the interval in which we need to determine its value, which makes impossible a reliable measurement. Here, the value of $g^{(4)}_{k,-k}$ is more compatible with its minimal value.

Influence of $g^{(4)}_{k,-k}$ on the degree of entanglement

The measurement of $g^{(4)}_{k,-k}$ allows to discriminate the relative value between $|\langle \hat{a}_k \hat{a}_{-k} \rangle|$ and $|\langle \hat{a}_k \hat{a}^\dagger_{-k} \rangle|$. We reintroduce the notations of the second chapter, section 4.A and define

$$c_k := \langle \hat{a}_k \hat{a}_{-k} \rangle, \qquad d_k := \langle \hat{a}_k \hat{a}^\dagger_{-k} \rangle. \tag{214}$$

When $g^{(4)}$ is close to its minimal value in Eq. (213), it means that either $|c_k| \ll |d_k|$, or $|d_k| \ll |c_k|$. The fact that the second order correlation function is above 2 and that the population is high makes impossible the second scenario: such state would not respect the *bona fide* condition. We have therefore $|c_k| > |d_k|$. When $g^{(4)}_{k,-k}$ is close to its highest value, it means that $|d_k| \sim |c_k|$. In the second chapter, we also defined θ in Eq. (157) which is a normalized quantity taking into account the value of $g^{(2)}_{k,-k}$ and $g^{(4)}_{k,-k}$, that varies monotonically with $g^{(4)}_{k,-k}$. We show in Figure 89 the value of the logarithmic negativity as a function of θ. The solid purple line uses $g^{(2)}_{k,-k} = 2.24$ and the dotted curves its lower and higher uncertainty. The line stops at $\theta \sim 0.3$ due to the *bona fide* condition: for such high value of $g^{(2)}_{k,-k}$ and the measured population, it is not possible for the value of $|d_k|$ to be too high. The position of this region depends on the value of $g^{(2)}_{k,-k}$: the dotted curve for which $g^{(2)} = 2.17$ has a critical value for θ of ~ 0.4 while it is 0.25 for $g^{(2)}_{k,-k} = 2.31$. Our measurement of $g^{(4)}_{+-}$ is more compatible with $\theta = 0$. It is therefore more likely that the logarithmic negativity of the state is 0.4(1). We see however from this figure that a non-zero value of d_k cannot *de-entangle* our state. In fact, it can only increase entanglement as seen here.

[10] For the fourth order correlation function, the offset is 4.

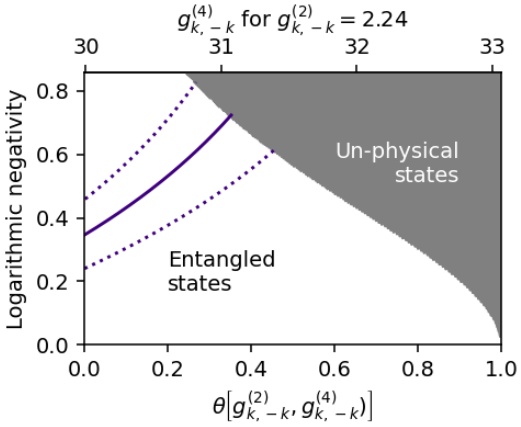

Figure 89: Logarithmic negativity of the state for which $g^{(2)} = 2.24(7)$ as a function of θ. θ increases with the value of $g^{(4)}_{k,-k}$.

The measurement of $g^{(4)}_{k,-k}$ indicates that it is more likely that $\theta = 0$ hence that $d_k = \langle \hat{a}_k \hat{a}^\dagger_{-k} \rangle = 0$. In the next section, we take into account the efficiency of the detector to reconstruct the state before the detector.

4.D Influence of the non-unit efficiency

We now assume that $\langle \hat{a}_k \hat{a}^\dagger_{-k} \rangle = 0$, which is a reasonable assumption given our measurement of $g^{(4)}_{k,-k}$. Additionally, we assume the detected mean populations are identical and equal to 0.94. We now study the influence of the non-unit detection efficiency.

Parametrization of the state

Based on our simplifications, the state is simply parametrized by two numbers : c_k and n_k. In the following, to lighten notations, I assume that c_k is real and positive (it involves otherwise the modulus of c_k). The second order correlation function that we measured is not affected by losses and provides us the value of $c_k^{(det)}$ through the value of $n_k^{(det)} = 0.94$:

$$c_k = n_k \sqrt{g^{(2)} - 1} \tag{215}$$

Effect of losses can be modelled by mixing each mode with the vacuum on a beam-splitter with efficiency η. As seen in the second chapter, section 1.D it changes the covariance matrix $\boldsymbol{\sigma} \longrightarrow \eta\boldsymbol{\sigma} + (1-\eta)\mathbb{I}_2$. With our parametrization, effect of losses is even simpler:

$$n_k = n_k^{(det)}/\eta \quad , \qquad c_k = c_k^{(det)}/\eta. \tag{216}$$

The state we describe is a two-mode squeezed thermal state. Physically, it is better to describe it with two other numbers: the squeezing parameter r_k and the initial (thermal) mode occupancy $n^{(in)}_{k,th}$. The covariance matrix of this state was also discussed in chapter 2, section 1.E. Nonetheless, we can access the value of $n^{(in)}_{k,th}$ and r_k through the value of c_k and n_k:

$$\tanh(2r_k) = \frac{2c_k}{2n_k+1} \quad , \qquad 2n^{(in)}_{k,th} + 1 = \frac{2n_k+1}{\cosh(2r_k)}. \tag{217}$$

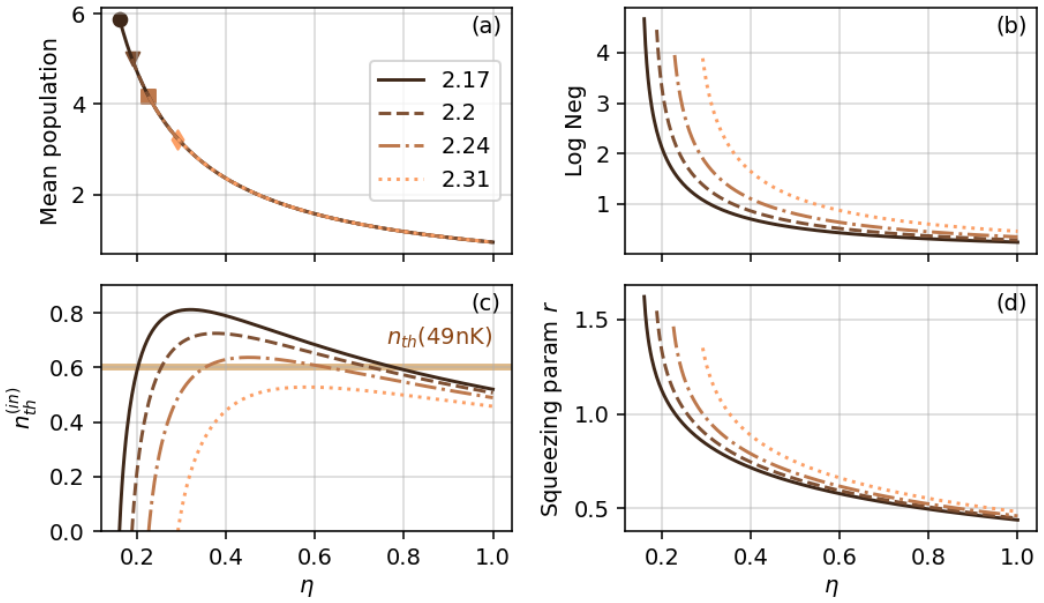

Figure 90: (a) Mean population of the state taking into account the detection efficiency η of the detector. (b) Logarithmic negativity defined in Eq. (218), (c) initial thermal population and (d) squeezing parameter defined in Eq. (217). The color and style of each curve match a different value of the second order correlation function, given in panel (a).

and the value of the logarithmic negativity is given by

$$E_{\mathcal{N}} = -\log_2\left[(2n_{k,th}^{(in)}+1)e^{-2r_k}\right]. \tag{218}$$

In Figure 90, we plot some state properties as a function of the quantum efficiency of the detector η, which range between 20 and 50%. Each curve represents a different value of the second order correlation function, taken in the uncertainty range of $g^{(2)} = 2.24(7)$.

Panel (a) shows the state mean population: the smaller the efficiency, the larger the mean occupation of the reconstructed state. The markers show the position where each curve stops for the corresponding value of $g^{(2)}$: the highest the value of $g^{(2)}$, the smallest the value η_{min} for which our parametrization is physical. Indeed, for a given value of $g^{(2)}$, the Gaussian state with the highest mean population that has this value of $g^{(2)}$ is the two-mode squeezed vacuum state. For this state, we have $g^{(2)} = 2 + 1/\bar{n}$. The minimal value of the efficiency is therefore $\eta_{min} = (g^{(2)}_{k,-k} - 2)n_k^{(det)}$. Hence, the larger $g^{(2)}_{k,-k}$, the larger the minimal efficiency. With $g^{(2)} = 2.24$, we see that the quantum efficiency is at least 23%, and if we consider the lower uncertainty, it is at least 17%.

Panels (b) and (d) of Figure 90 show respectively the logarithmic negativity and the squeezing parameter r_k. We observe that they monotonically increase with $1/\eta$. Here again, the smaller the quantum efficiency, the larger the *real* state and the larger its correlations.

Even more interesting is the initial thermal population of the state, shown in panel (c). From the temperature of 49 nK, measured in section 1.A, we expect the initial thermal population to be 0.6. This means that we can find an estimate of the quantum efficiency using the measured value of the correlation function and the population. The orange dotted curve for which $g^{(2)}_{k,-k} = 2.31$ does not intersect this value: it is likely that the second order correlation function is smaller than this value. The other curves however intersect this $n_{k,th}^{(in)} = 0.6$ value:

Table VI.1: Degree of entanglement and detection efficiency depending on the value of the second order correlation function assuming a 0.6 initial thermal population. η refers to the quantum efficiency of the MCP, r_k to the squeezing parameter, $E_{\mathcal{N}}$ to the logarithmic negativity, $\xi^2_{k,-k,\eta}$ to the relative number squeezing that should be observe given η.

$g^{(2)}_{k,-k}$	η	r_k	$E_{\mathcal{N}}$	n_k	$\xi^2_{k,-k,\eta}$
2.17	0.2	1.1	2.1	4.7	0.84
2.2	0.25	1.0	1.8	3.5	0.81
2.24	0.36	0.85	1.3	2.6	0.77

the $g^{(2)}_{k,-k} = 2.24$ curve for $\eta = 0.36$ and the $g^{(2)}_{k,-k} = 2.2$ and 2.17 respectively for $\eta = 0.25$ and 0.2.

Once known the quantum efficiency, we can recover the logarithmic negativity of the state which is given in Table VI.1.

Surprisingly, we observe in table Table VI.1 that the degree of entanglement of the reconstructed state increases when the detected second order correlation function increases. This is in fact not so surprising if one thinks that $g^{(2)}_{k,-k}$ is unaffected by losses. The smaller $g^{(2)}_{k,-k}$ is, the larger the mean population of the state (at fixed value of the initial population), hence the larger the squeezing strength.

The value of n_k and c_k also fixes the expected value of the relative number squeezing $\xi^2_{k,-k,\eta} = \mathrm{Var}(n_{-k} - n_k)/(n_{-k} + n_k)$. Last column of Table VI.1 shows the theoretical value of the detected normalized variance $\xi^2_{k,-k,\eta}$

$$\xi^2_{k,-k,\eta} = 1 - \eta + \eta\xi^2_{k,-k}. \tag{219}$$

It was shown by Jaskula et al. (2010) that the value of the normalized variance is more accurate when the integration volume is large (which is the opposite of the correlation signal). If we increase the voxel size to 3 mm/s along v_z and 80 mm/s along $v_{x,y}$, we measure a normalized variance of 0.83(1). According to Table VI.1, this value is compatible with a second order correlation function of 2.24(7) as it corresponds to $g^{(2)}_{k,-k} = 2.18$. Nonetheless, doing so, we are also counting thermal modes that contributes to increase the measured normalized variance.

4.E Two-mode Fock probability distribution

Still assuming $d_k = 0$, the value of $g^{(2)}_{+-}$ and the population completely characterize the state. In particular, we can compute the expected two-mode probability distribution and compare it to experimental data. Figure 91 compares the measured state (left) and the expected one (right) given the measured populations and a correlation value of $g^{(2)} = 2.2$ (I choose 2.2 due to the last measurement of the variance). We observe a good agreement between the two distributions. From the quantum efficiency of the detector, we can even model the Fock probability distribution of the state. It is a two-mode squeezed thermal state with $r_k \sim 1$ and $n^{(in)}_{th} = 0.6$. It corresponds to the probability distribution that we would measure with a 100% quantum efficiency. We show this probability on the bottom panel of Figure 91. On this probability distribution, we clearly show the pronounced diagonal which is a characteristic of a two-mode squeezed state. For a two-mode squeezed vacuum state, this two-mode probability distribution lies only on the diagonal. When there is a thermal seed, the diagonal is broadened.

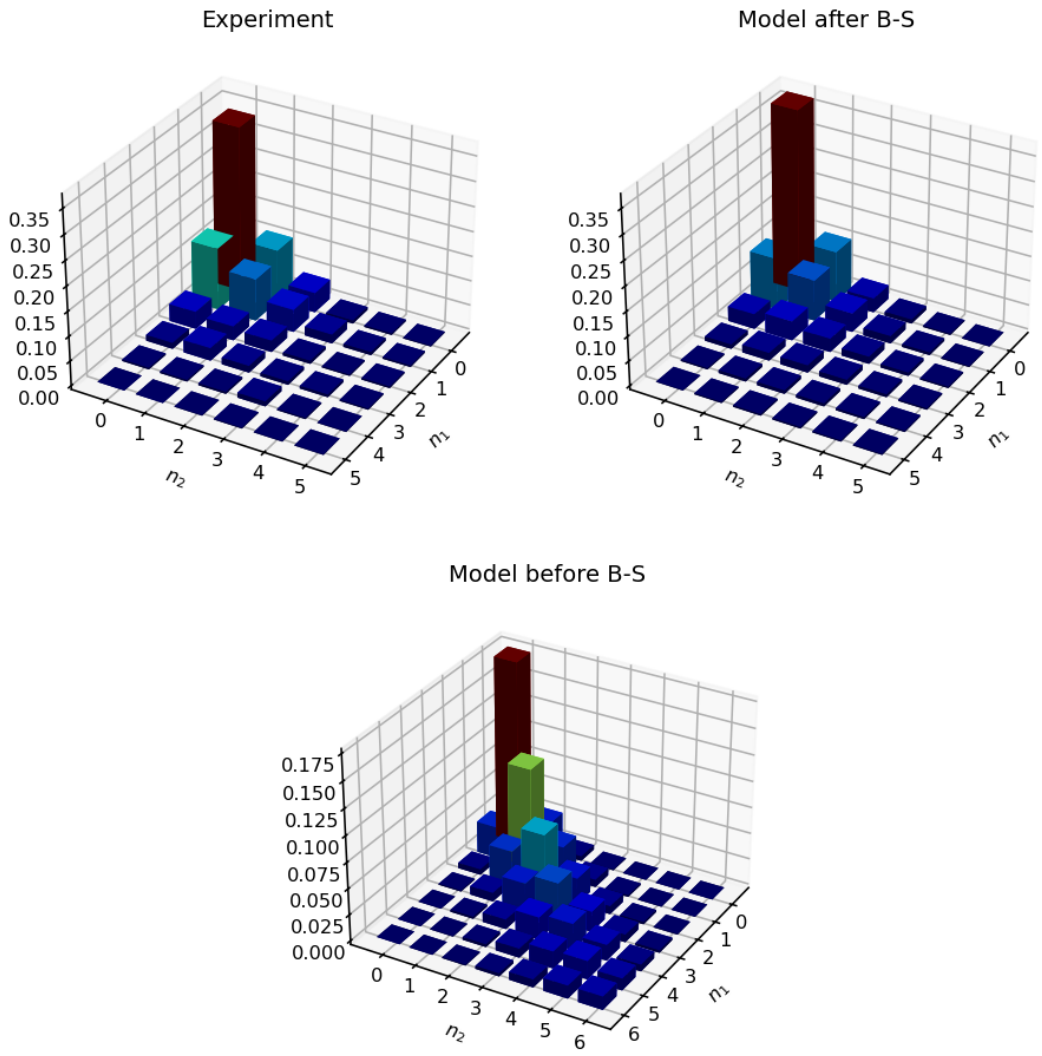

Figure 91: Two-mode probability distribution as a function of the number of particles in mode 1 n_1 and mode 2 n_2. Left panel shows experimental data; Right panel shows the state model by a Gaussian TMSth state for which $g^{(2)} = 2.2$ and a detected population of 0.92. Bottom panel shows the 2D distribution of the same state before detection (before the beam-splitter that models the losses). ©Theoretical distributions obtained using the Walrus library (Gupt et al., 2019).

4.F Conclusion

In this final section, we investigated deeper the single mode statistics to further check that it behaves like a thermal state. Such verification is important to use Wick theorem and use the theoretical work of chapter 2. In the second section we measured the population of the state. From the measured population and the value of the second order correlation function, we assess that the state is entangled. This is the major result of this PhD thesis.

In the next section, we measured the fourth order correlation function. This measurement is compatible with a value $g^{(2)} = 2.24(7)$, even though the error-bars are quite large. This measurement is also slightly more compatible with the lower value of the $g^{(2)}$ uncertainty *i.e.* 2.17. Finally, the 4-body correlation function is compatible with the fact that $\langle \hat{a}_k \rangle = 0$,

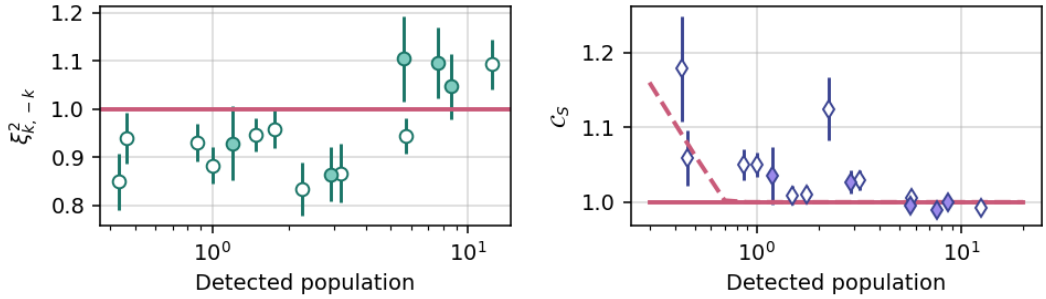

Figure 92: Evolution of the normalized variance (right) and the Cauchy-Schwarz ratio (right) as a function of the detected population. The red horizontal line on the right subplot indicates the limit for relative number squeezing. On the right plot, the red lines show the bound on the threshold value for the Cauchy-Schwarz ratio derived in chapter 2. The dashed line does not take into account the quantum efficiency and the solid line account for a 25% quantum efficiency. ©Data taken in April 2024.

which is expected from theory. In the last section, we further checked the consistency of our reasoning and, knowing the initial thermal population, we showed that our state is well-modeled by a two-mode squeezed thermal state with parameter $r_k = 1.0$ and initial thermal population 0.6, detected with a 0.25 quantum efficiency. We also measured a normalized variance of 0.83(1). All measurements agree that

1. the state is entangled,

2. the state that we detect has a logarithmic negativity of 0.4(1),

3. if we take into account a 25(10)% quantum efficiency, the squeezing parameter of the reconstructed state is 1.0(7). The corresponding logarithmic negativity is 1.8(9).

A future direction for this experiment is to monitor entanglement throughout the parametric creation process, *i.e.*, by varying the excitation duration. Currently, we have not quantified entanglement through logarithmic negativity for each dataset as we have done in this chapter. However, we assessed the degree of violation of the classical Cauchy-Schwarz inequality ($\mathcal{C}_S > 1$) and the relative number squeezing. These results are presented in Figure 92 as a function of the detected population.

Assuming the state is Gaussian and thermal, the measurement of the Cauchy-Schwarz ratio and the population allow witnessing entanglement. Above the red line in Figure 92, the state is entangled due to the lower bound on $g^{(2)}$ that we adapted for $\mathcal{C}_S$. The state is also *particle entangled* without any hypothesis, as shown by Wasak et al. (2014).

These data were collected across various experimental configurations over different weeks. In Figure 93, we rescaled the different excitation processes to align them on a common x-axis representing time. We used the dataset with filled markers in Figure 93 as a reference. In this particular experiment, we excited the gas with a modulation amplitude of 8% for 8 periods at the 2 kHz breathing mode. After the excitation, we then let an additional delay ranging from 4 to 12 periods (2 to 6 ms), during which the BEC continued breathing and excited pairs of quasi-particles. The time axis in Figure 93 thus refers to this additional delay. To align other experimental points, we calculated the theoretical growth rate based on the properties of

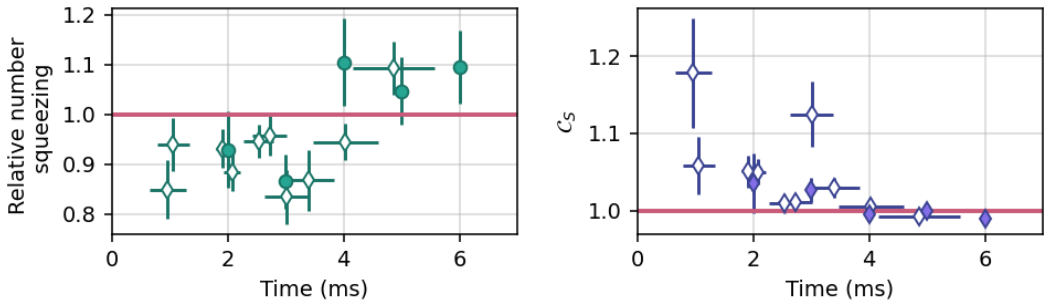

Figure 93: Evolution of the normalized variance (right) and Cauchy-Schwarz ratio (right) as a function of the excitation time. The filled markers has been taken on the same day and serve as a reference to define the excitation duration. ©Data taken in April 2024..

each excitation process (amplitude, number of excitations, and additional delay) along with the specific BEC properties of each dataset.

At short time, the state is entangled (or at least particle entangled). At later time, entanglement is lost, or we fail to detect it.

Summary In this chapter, we report on the observation of entangled quasi-particles. We show that the N-body correlation function of the single mode is well-described by a Gaussian thermal state up to the 7^{th} order. We measure the mode mean population to be 0.93(4) and 0.95(4). It means that the measurement of the cross-correlation functions $g^{(2)}_{k,-k} = 2.2(1)$ and 2.27(7) in the previous sections 2.B and 3.B. From the $g^{(2)}$ entanglement witness derived in the second chapter, we can already conclude on the non-separability of the state. The measured value of the 4-body correlation function 26(4) is compatible with the measured value of $g^{(2)}_{k,-k}$. Futhermore, even though the uncertainty of this measurement is large, the value we obtain is more compatible with $\langle \hat{a}_k \hat{a}^\dagger_{-k} \rangle = 0$. We therefore estimate the logarithmic negativity of the detected state to be 0.35(15). Modeling our state with a two-mode squeezed thermal state, we take into account the quantum efficiency of our detector, and with a sef-consistent reasoning that uses the initial thermal occupation, we estimate the quantum efficiency of the detector to 25(10)%. This value is consistent with the minimal relative number squeezing reported by Leprince (2024) on a multi-mode two-mode squeezed vacuum state. This self-consistent reasoning yields a squeezing parameter of 1.0(7) and a logarithmic negativity of 1.8(9) for the bi-partite quasi-particle state. Finally, we report on the observation of the violation of the Cauchy-Schwarz inequality and relative number squeezing as a function of the excitation duration. The quantumness of the state is lost after 4 ms.

Conclusion

This thesis reports on the observation of the production and entanglement of quasi-particles pairs in a time-modulated Bose-Einstein condensate (BEC). To summarize the content of the manuscript without repeating the introduction, we take here the historical perspective of this PhD.

1. Conclusion

The first year of my PhD was dedicated to experimental work focused on repairing the He* BEC apparatus. After a year of modifications, we obtained our first BEC in a crossed dipole trap in March 2022. Just a few weeks later, we produced our first pairs of atomic (entangled?) particles using a blue-detuned lattice, a technique well-established within the team (Bonneau et al., 2013). Although this did not constitute new scientific results, it marked a team milestone: for the first time in four years, we successfully produced pairs over a long acquisition time. However, the extended period of machine downtime, along with numerous technological upgrades (including changes to the detection process), interrupted the transmission of knowledge between PhD students. This meant that we could not directly benefit from prior expertise in data analysis and existing efficient code. Following the good practices introduced by Python enthusiasts Alexandre and Quentin, we developed *heliumtools*, a collaborative Python module that is object-oriented, efficient, and user-friendly.

The first experiment resembling the Dynamical Casimir Effect (DCE) was conducted in June 2022, and I presented these first experimental results at the *Optique Nice* conference. At that time, the stability of the BEC arrival time was not yet sufficient to observe clear opposite-momentum correlations. Our progress in both data analysis and the fast cooling of He* to degeneracy were stopped in the end of 2022. We encountered new technical issues among which a vacuum leak that took five months to fully resolve. As "les emmerdes, ça vole toujours en escadrille", the dipole trap laser failed soon after (though this was quickly fixed). Once these issues were resolved, we focused on the Bragg interferometer and shaping the pulses, exploring a variety of configurations, which are detailed in the manuscript of Charlie Leprince (2024). A publication has been submitted to present these results (Leprince et al., 2024). In May 2023, we gathered two weeks of DCE data. Although the correlation signal did not reach the expected value, this period marked the successful measurement of the Bogoliubov dispersion relation. These results were presented at the *Analog Gravity* summer school and conference that I attended in Benasque, Spain.

After this conference, we shifted our focus and began a series of Hong-Ou-Mandel atomic interferometry experiments in the summer of 2023, varying the input state properties of the interferometer and adjusting the pulse shapes for the mirror and beam-splitter. This successful series led to our first Bell inequality test in October 2023. Unfortunately, this attempt did not yield the expected oscillations in the Bell parameter. Returning briefly to the DCE project, we

observed relative number squeezing in November 2023. However, the position and size of the pinholes that filter out unwanted modes needed to be well-adjusted in order to observe this sub-shot-noise signal. Following a relatively minor series of breakdowns and upgrades in the winter of 2024, we dedicated a full month to DCE-like experiments in the spring of 2024. We observed a reproducible and clear violation of the classical Cauchy-Schwarz inequality and relative number squeezing which led us to start to write an article.

We therefore ask ourselves: can relative number squeezing and/or violation of the classical Cauchy-Schwarz inequality enable us to draw conclusions about entanglement? This question, along with the preparation of this manuscript, led me to explore these correlation witnesses in greater detail, as well as the distinction between particle entanglement and mode entanglement. Violation of the classical Cauchy-Schwarz inequality has been shown to serve as a *particle* entanglement witness, while in this work, we focus on uncovering *mode* entanglement.

Turning to mode entanglement, I focused on the hypothesis $\langle \hat{a}_k \hat{a}^\dagger_{-k} \rangle = 0$. One possible way to test this assumption is by implementing an atomic interferometer that mixes the k and $-k$ modes. The output of the interferometer oscillates with an amplitude given by the modulus of this coherence term. However, this approach would require adjusting the Bragg beams angle, which is not straightforward due to optical access constraints. Furthermore, the team's primary objective remains the realization of a (second) Bell test, for which the beams angle must remain unchanged. While drafting the "entanglement" chapter of this manuscript, I delved into Gaussian state formalism - first introduced to me during the 2023 Benasque summer school. This study led first to the derivation of the $g^{(2)}$ bound to assess entanglement, and then to the $g^{(2)}/g^{(4)}$ criterion, which are now at the core of the second chapter of this work. A publication is in preparation on this result.

In the data we collected, the violation of the Cauchy-Schwarz inequality was permitted by a decrease of the local correlation function, rather than an increase above 2 of the cross-correlation function. After completing the initial chapters of this manuscript, I returned to the experiment. We began by investigating the growth process, which highlighted a strong alignment with theoretical predictions. Furthermore, the pronounced oscillation in atom number during exponential growth indicated that mapping the phonon basis to the atom basis relying only on the natural transverse expansion was insufficient. Consequently, we implemented the adiabatic opening of the trap, which, combined with meticulous experimental preparation to ensure stability, allowed us to reveal mode entanglement in October 2024. A publication is in preparation on these results.

2. Outlooks

Our proof for non-separability lies on the assumption that the state is Gaussian. If this is not the case, Wick theorem does not apply, and we are unable to relate correlation functions to mode entanglement. Some critics might argue that the Gaussian assumption is too strong, as non-locality with massive particles entangled in external degrees of freedom has yet to be demonstrated. A natural outlook of this work is therefore to wonder if this pair creation process could lead to an experimental violation of Bell inequalities.

Such experiment *à la Aspect* requires the use of 2×2 modes *i.e.* a product of two-mode squeezed state $|\psi_{k,-k}\rangle \otimes |\psi_{k',-k'}\rangle$. With photons, this experiment was realized by Rarity and Tapster (1990). With atoms, such violation was not yet evidenced even though two experiments gave preliminary promising results (Dussarrat et al., 2017; Thomas et al., 2022). In order to use the source we described in this manuscript for such experiment, we need to improve two important elements.

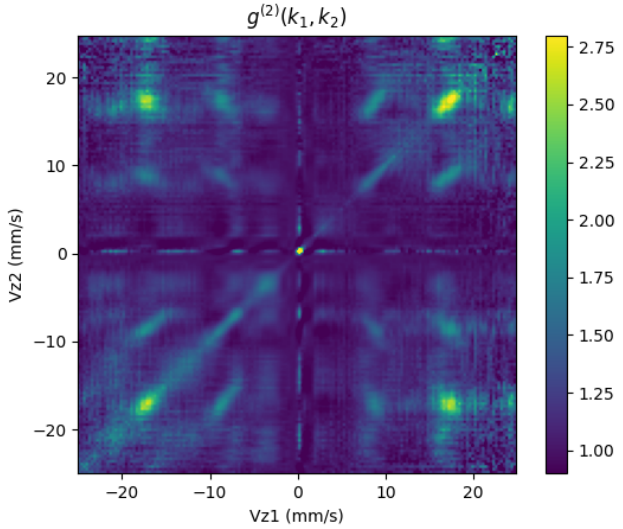

Figure 94: $g^{(2)}$ correlation map after long time and strong excitation process.

- The interferometer described in the previous references requires a product of two-mode squeezed states. With our pair creation process, this could be *in principle* possible by modulating the trap power with two frequencies ω_1 and ω_2. This would result in the parametric excitation of two modes $(k_1, -k_1)$ and $(k_2, -k_2)$ such that $\omega(k_1) = \omega_1/2$ and $\omega(k_2) = \omega_2/2$. However, given the difficulties reported in chapter 5 to excite a well-controlled Bogoliubov mode, this option seems unreasonable.
- The Bell inequality derived with this specific Mach-Zenhder interferometer involves 4-modes but only two-particles. It means that the probability to have 4 particles in the interferometer must be really low: the mean population of the two-mode squeezed states must be lower than 0.14 atoms per mode. In this work, the initial thermal population is 0.6 *i.e.* even before squeezing, the state population is too large. The momenta of the two-mode squeezed states must therefore be much larger than ξ^{-1} so that the initial thermal seed is negligible.

One possibility to overcome these problems is to take advantage of the already installed blue-detuned lattice to parametrically excite Bogoliubov modes (Krämer et al., 2005; Lellouch et al., 2017).

Future work will also investigate deviations from Bogoliubov-de Gennes theory. Specifically, when driving the system further out of equilibrium, we observe correlations between Bogoliubov modes. A typical example is shown in Figure 94. In the density profile, a strong peak appears at $k = \pm 9$ mm/s and a smaller one around $2k = \pm 18$ mm/s. Such secondary resonance is expected in periodically driven systems at frequency ω_d, where Floquet analysis reveals a series of resonances $n\omega_d/2$ for $n \in \mathbb{R}$. Microscopically, assuming a linear dispersion relation, this excitation process is explained by the annihilation of two excitations with momentum k and the creation of excitations with momentum $2k$. The presence of such excitations has already been reported in the literature (Nguyen et al., 2019; Hernández-Rajkov et al., 2021); however, it would be valuable to track the growth of correlations between different modes. Such correlations naturally raise the question of whether the state is multimode entangled and how to reveal it.

Appendix

This appendix contains experimental details of the experiment. The first section contains additional information related to the core of the manuscript. The second one reports on the change of our sequencer and is intended to be a guide for future PhD students. The next section contains technical information that had no interest to figure in the main text but should not be lost. Finally, the last section focuses on the correlation codes.

1. General appendix

1.A Detecting particle entanglement of spin-1/2 systems

During this thesis, we asked our-self many questions about how to detect entanglement. Many entanglement criteria were derived to detect spin squeezing. Among them, Tóth et al. (2007) derived a class of entanglement witnesses among which one involves commuting observables that are accessible with our detector. Hyllus et al. (2012) derived later a recipe to generalize these spin squeezing criteria that are defined with system with fluctuating number of particles. I am now a bit skeptical on the applicability of this criterion to our state, but I think that this work (even though I did not participate much in it) should not be lost as it could be useful. Note that a similar approach was used by Krešić et al. (2023) to detect entanglement, but authors do not provide their derivation.

Extension of a practical entanglement witness for fluctuating number of particles

When one deals with a two mode system, one can describe the properties of the quantum state as a fictitious spin-1/2 defining

$$\hat{J}_z = \frac{1}{2}(\hat{a}^\dagger\hat{a} - \hat{b}^\dagger\hat{b}), \qquad \hat{J}_x = \frac{1}{2}(\hat{a}^\dagger\hat{b} + \hat{b}^\dagger\hat{a}), \qquad \hat{J}_y = \frac{1}{2i}(\hat{a}^\dagger\hat{b} - \hat{b}^\dagger\hat{a}) \tag{220}$$

where $\hat{a}$ and $\hat{b}$ are the annihilation operator of each mode. This was for example used by Estève et al. (2008) to describe the two-mode properties ot a double-well BEC. This is convenient because many entanglement criteria have been derived for spins system. Furthermore, many of them involve variance and/or mean of the $\hat{J}_i'$ operators, rendering there experimental calculation quite easy. Still, in order to measure the expectation value or its square of $\hat{J}_{x,y}$, one needs to mix the two modes and therefore in our case an interferometer. However, the sum of the square of the x and y angular momentum has a quite simple expression:

$$\hat{J}_x^2 + \hat{J}_y^2 - \frac{\hat{N}}{2} = \hat{a}^\dagger\hat{a}\hat{b}^\dagger\hat{b} = \hat{n}_a\hat{n}_b. \tag{221}$$

This means in particular that this quantity can be measure with a particle detector. Among the (many) criteria in the literature, it turns out that one does involve this sum.

Theorem - An Optimal Spin Squeezing Inequality
Considering an ensemble of N qubit states, the violation of the following inequality implies entanglement (Tóth et al., 2007)

$$\langle \hat{J}_i^2 \rangle + \langle \hat{J}_j^2 \rangle - \frac{N}{2} \leq (N-1)(\Delta \hat{J}_k)^2 \tag{222}$$

where i, j, k can take any permutation of x, y, z.

The left hand-side on (222) is nothing but the right hand-side of (221). Here however, the number of atoms N is fixed. This criterion is of particular interest for a single-particle detector as

$$\hat{J}_x^2 + \hat{J}_y^2 - \frac{\hat{N}}{2} = \hat{a}^\dagger \hat{a} \hat{b}^\dagger \hat{b} = \hat{n}_a \hat{n}_b, \tag{223}$$

i.e. the criterion is accessible experimentally. However, the latter witness is defined for a fixed number of particles. It was also shown by Hyllus et al. (2012) how spin-squeezing parameters can be extended to systems with a fluctuating number of particles. This was derived recently by Boiron (2024).

Theorem - Tóth-Boiron entanglement witness
Consider a system of $N = n_a + n_b$ bosons in two modes a and b. Defining the quantity

$$\mathcal{W}_B := \mathrm{Var}(\sqrt{\hat{n}_a + \hat{n}_b - 1}\frac{\hat{n}_a - \hat{n}_b}{2})/\langle \hat{n}_a \hat{n}_b \rangle \tag{224}$$

if a state violate the inequality $\mathcal{W}_B \geq 1$, it is particle entangled.

Proof. We use the superselection rule and write the density operator as

$$\hat{\rho} = \sum_n Q_n \hat{\rho}_n, \qquad \sum_n Q_n = 1, \qquad 0 \leq Q_n \leq 1 \tag{225}$$

We define the operator $\hat{A} = \hat{P}\sqrt{\hat{N}-1}\hat{J}_z\hat{P}$ where $\hat{P} = 1 - |00\rangle\langle 00|$ is a projector so that the square root in the definition of $\hat{A}$ is always defined. We have therefore

$$\langle \hat{A} \rangle = \sum_n Q_n \langle \hat{A} \rangle_n = \sum_{n \geq 1} Q_n \sqrt{n-1}\, \langle \hat{J}_z \rangle_n \tag{226}$$

with $\langle \hat{O} \rangle_n = \mathrm{Tr}(\hat{\rho}_n \hat{O})$. The Cauchy-Schwarz inequality leads to

$$\langle \hat{A} \rangle^2 = \left(\sum_n Q_n \langle \hat{A} \rangle_n \right)^2 \leq \sum_n Q_n \langle \hat{A} \rangle_n^2 \tag{227}$$

and therefore

$$\mathrm{Var}(\hat{A}) = \sum_n Q_n \langle \hat{A}^2 \rangle_n - \left(\sum_n Q_n \langle \hat{A} \rangle_n \right)^2 \geq \sum_n Q_n \left(\langle \hat{A}^2 \rangle_n - \langle \hat{A} \rangle_n^2 \right). \tag{228}$$

Given that at fixed n, the value of $\mathrm{Var}(\hat{A}) = (n-1)\mathrm{Var}(\hat{J}_z)$, we have that

$$\mathrm{Var}(\hat{A}) \geq \sum_{n>0} Q_n (n-1) \mathrm{Var}(\hat{J}_z) \tag{229}$$

We now apply the entanglement criterion from equation (222) for each n with x and y on the left-hand side and z on the right-hand side. This implies that for any separable states, the following inequality must hold

$$\mathrm{Var}(\sqrt{\hat{n}_a+\hat{n}_b-1}\frac{\hat{n}_a-\hat{n}_b}{2}) \geq \sum_n Q_n \langle \hat{J}_x^2+\hat{J}_y^2-\frac{\hat{n}}{2}\rangle_n \tag{230}$$

which is equivalent to

$$\mathrm{Var}(\sqrt{\hat{n}_a+\hat{n}_b-1}\frac{\hat{n}_a-\hat{n}_b}{2}) \geq \sum_n Q_n \langle \hat{n}_a\hat{n}_b\rangle_n = \langle \hat{n}_a\hat{n}_b\rangle\,. \tag{231}$$

□

Obviously, a Fock state violates this inequality as it violates the Cauchy-Schwarz inequality. If we apply stricto-sensu the criterion to a two-mode squeezed state with mean population ν, one has Boiron (2024)

$$\mathcal{W}_B = (1-\eta)\frac{2\nu}{1+2\nu} < 1. \tag{232}$$

As the variance, this criterion is sensitive to the efficiency η of the detector. However, is always smaller than one hence this criterion seems robust to a pure loss channel on a two-mode squeezed vacuum state.

Discussion

The main question is now: *can we apply this criterion to our system ?*

In the derivation of the witness, we used the superselection rule: this means we assumed that a superposition of different number states is not possible. In some sense, I think one must however be careful: this rule must be applied to the entire space of the system. Here, we applied the superselection rule on the system $A \cup B$: this is correct if $A \cup B = \Omega$ where Ω represents all the states accessible to the system. This is the case for example if A and B are the (only) two levels of a spin or if A and B are the two wells of trap (Estève et al., 2008). Suppose now the entire Hilbert state is a 3 level system for each particle, labeled A, B and C. This could be for example a spin 1 system or our system if one consider the BEC, the k and the $-k$ mode. Applying the superselection rule to the subsystem $A \cup B$ means that there are no particles that are on a coherent superposition of $A \cup B$ and C. This is in contradiction with how we theoretically describe our state as it is a two-mode squeezed state. I would therefore say that we cannot apply this criterion to our state.

Numerical tests

For the rest of this section, we will check numerically if $\mathcal{W}_B$ could be a (mode) entanglement witness for Gaussian states. Sadly, I did not succeed in expressing generally $\mathcal{W}_B$ as a function of the covariance matrix, rendering it impossible to demonstrate if it can be an entanglement witness. It can however be computed using the projection of the density matrix on the Fock basis, the joint probability distribution that we introduced in the first section of the second chapter. We adopt here the same procedure that we have done in section 3.D of the second chapter.

In Figure 95, we represented the variations of $\mathcal{W}_B$ for various states. The squeezing parameter is kept constant but the initial thermal population is changed. On the x axis is the initial population of mode 1, and the different colors represent the initial population in mode

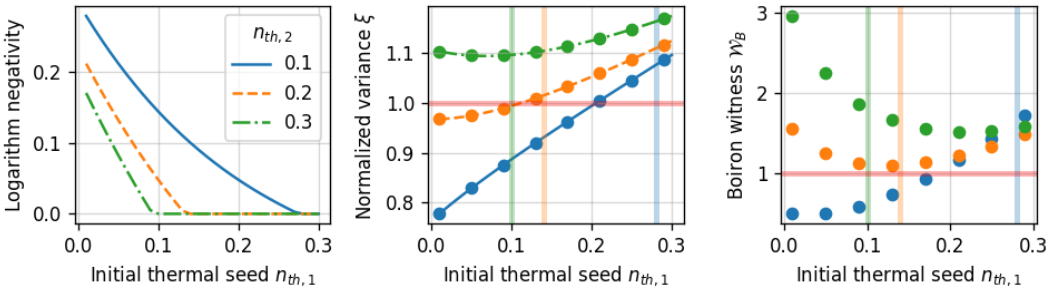

Figure 95: Comparison of possible entanglement witnesses. The left panel represents the logarithm negativity as a reference, the middle panel the normalized variance, and the right panel $\mathcal{W}_B$. The squeezing parameter is $r = 0.14$, chosen so that the particle number is not too high for computational reasons. On the x axis of each curve lies the initial thermal population of mode 1, and curve colors represent the initial population in mode 2. The state is entangled at first (low initial thermal population in mode 1) and then becomes separable when the initial thermal population is too high. The middle panel represents the normalized variance, which might witness entanglement when below 1. The light vertical bars split the x axis between entangled (left) and separable (right) states with the same colors. For some of the states represented here, the joint probability distribution was extracted, making it possible to compute both the normalized variance and $\mathcal{W}_B$. The normalized variance value extracted from the joint distribution is represented through the round markers. As they all lie on the curves, we conclude that the distribution was extracted with a sufficiently good cutoff. On the right panel is represented the quantity $\mathcal{W}_B$ from equation (224). When the initial population of mode 2 is low, $\mathcal{W}_B$ detects entanglement: the blue dots lie below the red line. However, it ceases to detect entanglement before the normalized variance stops. For example, when mode 2 has an initial thermal population of 0.2, it fails to witness entanglement at all, while the normalized variance is still below 1. On the other hand, we see that it never witnesses a separable state as entangled in this particular example. ©Distributions obtained using the Walrus library (Gupt et al., 2019).

2. The left panel represents the logarithm negativity, an entanglement criterion, the middle panel the normalized variance (a possible entanglement witness), and on the right panel the quantity $\mathcal{W}_B$. On the middle and right panels, the vertical lines represent the limits beyond which the state is not entangled (gPPT), with the color corresponding to each curve chosen in agreement with the legend.
When the population in mode 2 is low, $\mathcal{W}_B$ and the variance witness entanglement (they are below 1) over a reasonable range, with the variance being a little bit more precise as it goes above one after $\mathcal{W}_B$. When the initial population of mode 2 is a bit higher, $\mathcal{W}_B$ never witnesses entanglement, while the normalized variance does but over a small range. When the initial population in mode 2 is too high, both criteria fail to witness entanglement. This is expected because the two final populations are too different, causing the variance to fail to witness entanglement as seen in Figure 28.

In Figure 96, we fix the mean number of particles in the Gaussian state to 0.2 on the left and 2.2 on the right (taken equal for both modes). We change the strengths of the correlation between the two modes, namely the values of $|\langle \hat{a}_1 \hat{a}_2 \rangle|$ and $|\langle \hat{a}_1 \hat{a}_2^\dagger \rangle|$ in the covariance matrix. These values are bounded: the grey region on the plot corresponds to an unphysical region where the Schrödinger-Robertson inequality (105) is not satisfied. Here again, the PPT

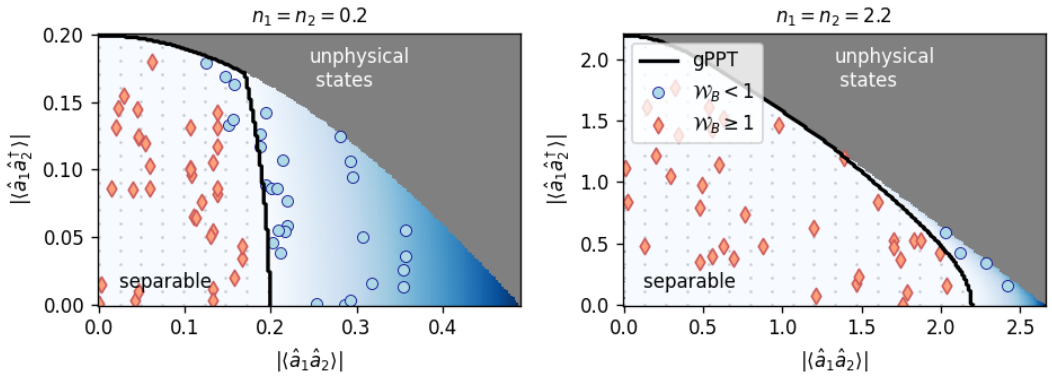

Figure 96: Failure of the $\mathcal{W}_B$ witness candidate $\mathcal{W}_B$ to reliably witness mode entanglement. For these plots, the population was kept constant ($n = 0.2$ on the left and $n = 2.2$ on the right) while the correlation between the modes was changed, namely $|\langle \hat{a}_1 \hat{a}_2 \rangle|$ on the x axis and $|\langle \hat{a}_1 \hat{a}_2^\dagger \rangle|$ on the y axis. Depending on the value of these operators, the state can be separable (on the left of the solid black curve, which is the PPT criterion) or entangled (on the right). The colorscale shows the logarithm negativity. The reds and blue dots represent the states where $\mathcal{W}_B > 1$ (orange) and $\mathcal{W}_B < 1$ (purple), respectively. On the left plot, we observe blues dots in the separable region. This means this witness detec entanglement for a separable state. This potential entanglement witness must be rejected. ©$\mathcal{W}_B$ was computed using the Walrus library (Gupt et al., 2019).

criterion splits the space in two: separable states lie on the left (states for which the correlation $|\langle \hat{a}_1 \hat{a}_2 \rangle|$ is weak), and entangled states lie on the right of the map. The color scale represents the logarithm negativity. The markers represent the quantity $\mathcal{W}_B$, which claims entanglement for blue dots and does not witness it for orange diamonds. On the left subplot, some blue circles witness entanglement while the state is not. This means that $\mathcal{W}_B$ *cannot be considered as an entanglement witness when the coherence is not null*.

1.B Impact on the correlations of the BEC arrival time fluctuations

In section 1.C of the sixth chapter, we explained that fluctuations of the cloud speed can destroy the measurement of the cross-correlations and enhance the value of the local one. Here, we numerically investigate the influence of a random average velocity on the atom distribution. Our method is close to the method of Bonneau (2011) but a bit more sophisticated as we add the bosonic bunching (thermal statistics).

Method

- **BEC**: We randomly sample the number of atoms per shot, n_i^{bec}, from a Poisson distribution. For each shot, we sample the momentum of each atom from a beta distribution (2,2) that looks like a Thomas-Fermi profile. The radius is fixed to 4 mm/s. The BEC corresponds to the central lobe in Figure 97.
- **Thermal atoms**: We sample thermal atoms in a similar manner. We model our gas with N independent thermal modes, each with a width of $\sigma_{mode} = 0.5$ mm/s. The number of thermal atoms is determined by Bose-Einstein statistics with a quadratic dispersion relation (non interacting gas or phonons). Once the number of thermal atoms per mode

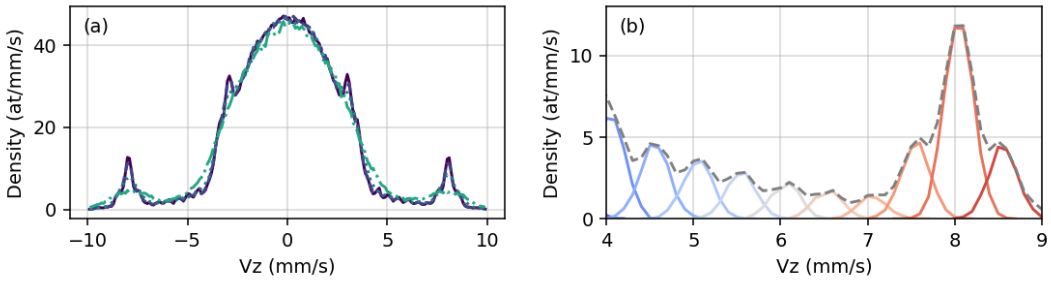

Figure 97: Density profile of our model. The central peak is the BEC, the wings a thermal distribution and the side-band two thermal distributions. On the right panel, the distribution of each individual mode is shown in color and the dashed grey line show the total distribution.

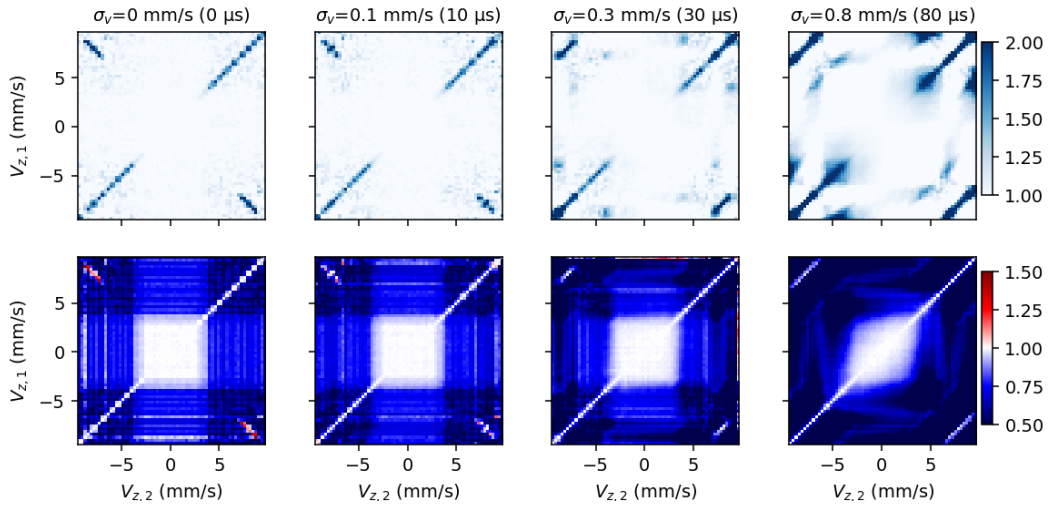

Figure 98: Two-dimensional plot of the second order correlation function $g^{(2)}(v_1, v_2)$ (top) and the Cauchy-Schwarz ratio $C_{\mathcal{S}}$.

per cycle is known, the momentum of each atom is drawn from a Gaussian distribution with a width of $\sigma_{mode}/3$. On the density profile of Figure 97, the slight secondary peak along the BEC tails is due to the fact that thermal atoms are sample for velocities greater than 3 mm/s.

- **Pairs**: We replace 3 modes of thermal atom by pairs with momenta around 8 mm/s. Note that this means that we assume we have a two mode squeezed state and not a two-mode squeezed thermal state. The reason is that it simplifies the model and I do not expect it to change much the result. The number of atoms is sampled from a thermal distribution and each peak is sampled from a Gaussian distribution of width $\sigma_{mode}/3$.

We then randomly sample the atom table with a 0.5 probability to account for the efficiency of the detector. Panel (b) of Figure 97 shows the momentum distribution of different modes, represented by various colors. The total distribution is plotted as a grey dashed line. Once the atom table is complete, we randomly shift the velocity distribution of each cycle to take into account the instability. The shift is drawn from a Gaussian distribution with a width σ_v. Once the atom table is complete, we compute correlations using the same algorithm as for "real" data.

Results

The simulated 2D correlation maps are shown in Figure 98. The first line shows the 2D map of the second order correlation function and the second the Cauchy-Schwarz ratio

$$C_S = \frac{g^{(2)}(v_1, v_2)}{\sqrt{g^{(2)}(v_1, v_1) g^{(2)}(v_2, v_2)}}. \tag{233}$$

Each column corresponds to a different instability σ_v, ranging from 0 mm/s (perfect) to 0.8 mm/s (awful). The local correlation function (boson bunching) lies on the diagonal while anomalous correlation lie on the anti-diagonal. We focus on the first $g^{(2)}$ map. At the center, the local correlation function is equal to 1 as the statistics of the mode is poissonian. On the edge of the distribution, the statistics is thermal and the local correlation goes to 2. We observe normal correlation on a wider range than cross-correlations: it is due to the fact that only 3 modes [7.7, 8, 8.5] mm/s are correlated while the other are just thermal uncorrelated atoms. On the second raw (Cauchy-Schwarz ratio), red color indicates "quantumness".

For the second column, which is the best stability we have achieved, the correlation are already affected. We still violate the Cauchy-Schwarz inequality (there is some red in the upper left corner) but the violation is weak. When the instability increases (third panel), we completely loose this violation and therefore the ability to assess entanglement. Here, the instability (0.3 mm/s) approaches the width of a mode, around 0.5 mm/s. We see that the instability must be (much) smaller than the width of a single mode. On the last panel, we show the 2D map for a large instability of 0.8 mm/s (80 µs). Such instability completely distort the correlation map. In fact, the instability artificially create correlations where the variation of the atom number is important. Such spurious correlations are dramatic to use the criterion derived in the second chapter as it requires the state to be thermal and un-squeezed: $g^{(2)}_{k,k} = 2$. Here, we see that the instability can increase the measured value of the local correlation.

To further investigate this, we focus on the sideband region (around 8 mm/s) and on the diagonal (local correlation) and anti-diagonal (cross correlations). Each column corresponds to a different instability. On the first raw of Figure 99, we show the local correlation function. The red square corresponds to the expected value and each color refers to a different size of the analyzed voxel. In the stable case, we see that the smaller the analysis box, the closer to 2 $g^{(2)}_{k,k}$. This is because the modes overlap and as we probe the statistics in a finite-sized box, we become sensitive to the nearby mode. When instability increases, we see that the local correlation is enhanced: the smaller the box, the highest the "spurious" correlation. A deeper analysis revealed that this artificial increase of the local correlation is stronger when the density changes with v_z, which is typically the case as we have a narrow peak.

The second row shows the second-order correlation function. The red squares represent the expected value for a two-mode squeezed state $2 + 1/\bar{n}$. Surprisingly, we observe a quite larger discrepancy between the expected value and the numerical point, even for the "stable" sample. This is particularly true for the peak at 7.5 mm/s, less populated than the 8 mm/s one (1.3 and 5 mean atoms), and for the smallest voxel. We see here that the integration volume should not be too large and should roughly match the size of the mode. When the instability increases to 0.1 mm/s, the second-order correlation function hardly exceeds 2, which prohibits the detection of entanglement. On the opposite, when the instability increases, $g^{(2)}_{k,-k}$ goes above 2 due to spurious correlations. The last row of this plot shows the Cauchy-Schwarz inequality ratio. In this case, the theoretical points match the numerical ones when the integration volume matches the size of the mode (orange, 0.5 mm/s). When the instability increases to 0.1 mm/s, we again observe that we fail to detect entanglement. However, for higher instability, the

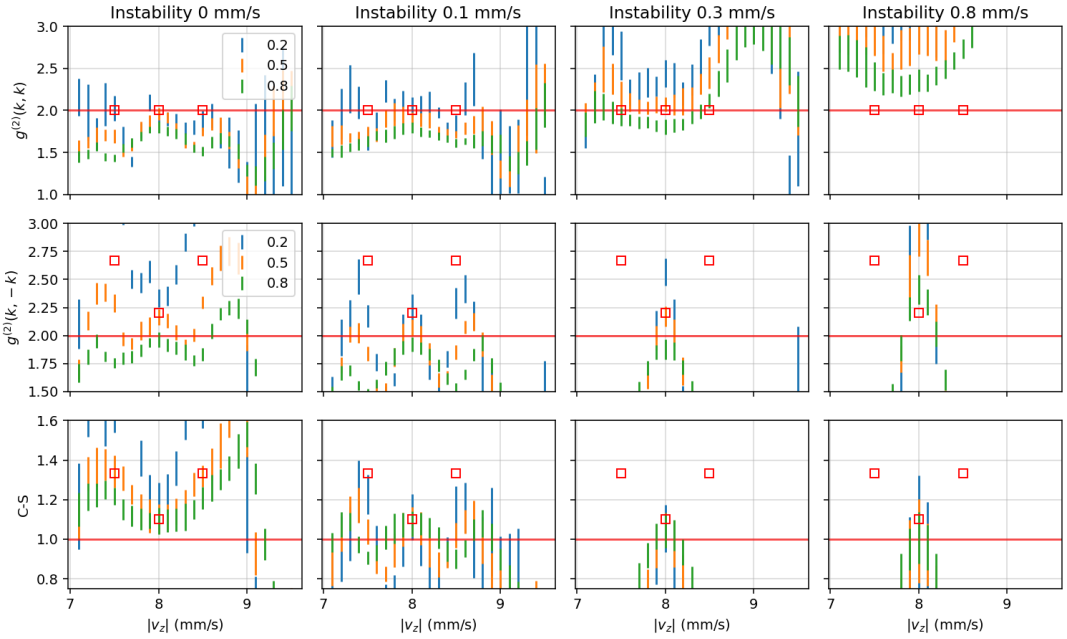

Figure 99: Two-dimensional plot of the second order correlation function $g^{(2)}(v_1, v_2)$ (top) and the Cauchy-Schwarz ratio $C_{\mathcal{S}}$.

Cauchy-Schwarz inequality is not violated due to spurious correlations. It seems more robust to those instabilities.

1.C Local correlation function

In this subsection, I report on the measurement of the local correlation on a different dataset that the one presented in the sixth chapter, section 2.A. Particularly, the temperature is lightly larger hence the contribution of thermal modes that were not squeezed is more important. The chemical potential of the gas was also higher which increases the population in the transverse level of the trap, allowing to measure the correlation length in this direction (in the dataset presented in the main text, the correlation function in the transverse direction was almost flat). We select a volume Ω_B of atoms, near the positive peak at 10 mm/s. This is represented by the shaded area in Figure 100(c). Subplots (a-b) of Figure 100 shows the density of this v_z cut. A Gaussian fit (solid red curve) yields a width of $\sigma_{x,y} = 11$ mm/s.

On the second row, we show the local normalized second order correlation function integrated over the volume Ω_B. The latter is defined as

$$g^{(2)}_{CL}(\boldsymbol{\delta k}) = \frac{\int_{\Omega_B} \langle \hat{a}^\dagger_{\boldsymbol{k}} \hat{a}^\dagger_{\boldsymbol{k}+\boldsymbol{\delta k}} \hat{a}_{\boldsymbol{k}} \hat{a}_{\boldsymbol{k}+\boldsymbol{\delta k}} \rangle \, \mathrm{d}\boldsymbol{k}}{\int_{\Omega_B} n_{\boldsymbol{k}} n_{\boldsymbol{k}+\boldsymbol{\delta k}} \mathrm{d}\boldsymbol{k}}, \tag{234}$$

where the index CL stands for colinear. The $g^{(2)}_{CL}(\boldsymbol{\delta k})$ function has 3 variables δv_x, δv_y and δv_z. Each panel (d-f) of Figure 100 shows $g^{(2)}_{CL}$ along one direction: v_x on the left, v_y in the middle and v_z on the right. The color and style of each curve correspond to different integration volume along the two other axis. For example, on panel (f) is plotted $g^{(2)}_{CL}$ as a function of δv_z for $\delta v_{x,y} = 0 \pm 15$ mm/s (circles), 10 mm/s (triangles) or 5 mm/s (squares).

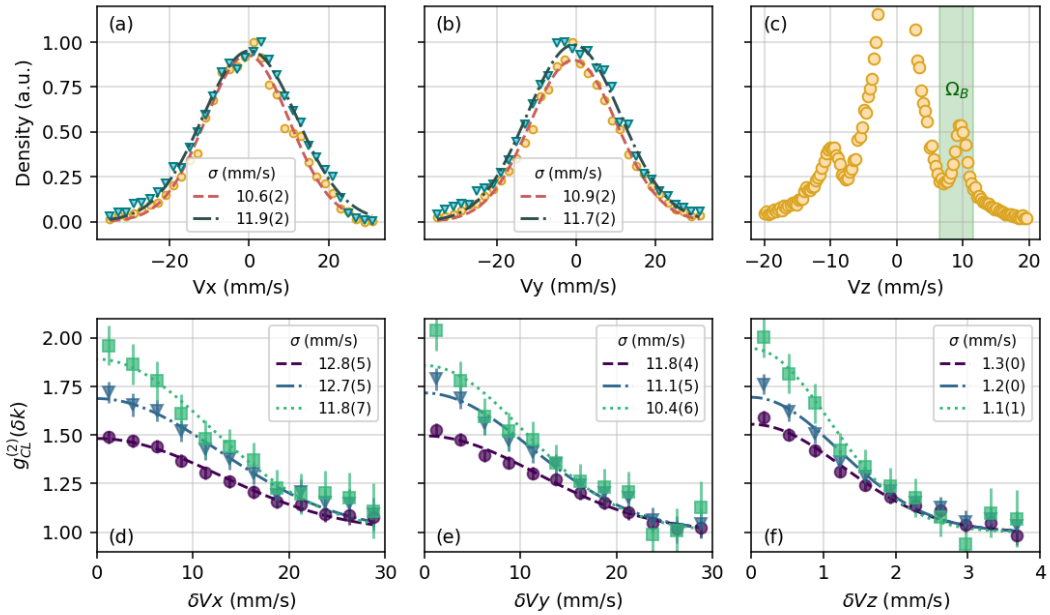

Figure 100: First row: Density along v_x and v_y of the region Ω_B, shaded in green on subplot (c). Second row: normalized second order correlation function along each axis. Each color/symbol corresponds to a different integration volume along the others axis. The integration volume along the v_z is (2, 1, 0.5) mm/s and it is (15,10,5) mm/s along $v_{x,y}$ for the symbols (round, triangle, square). ®Dataset taken on September 2024.

In Figure 100, we adjusted the correlation functions with a Gaussian[11] fit whose width give 11-12 mm/s along the x and y axis. Applying *stricto sensu* the result of Gomes et al. (2006) which relates the source sice s to the correlation length (in momentum) by $s = 1/\sqrt{2}\sigma_k$, we obtain $s = 1$ µm. This value is really close to the harmonic oscillator length $\sqrt{\hbar/m\omega_\perp} = 1.4$ µm.

In the longitudinal direction, we find a correlation length of 1.1(1) mm/s. If we express this *in trap* speed in terms of distance after a 308 ms time-of-flight, this implies that the correlation length is approximately 300 µm. Using Figure 61 of the fourth chapter section 3.B, this indicates that the initial wave-function size is of the order of 100 µm, in agreement with the BEC size we expect (150-200 µm). We also observe here that the second order correlation value reaches 2 when $\delta v_z \to 0$, which confirms that our measurement is consistent with a thermal state.

[11] The width σ refers to the Gaussian RMS width $e^{-x^2/2\sigma^2}$.

2. QControl3, our python based experiment program

Before spring 2021, the experiment was controlled with a homemade hardware, interfaced with Matlab but the materials was suspected to be failing hence it was decided to replace it. The choice was made to use the Adwin Pro 2 hardware with a python wrapper QControl3 developed by the MPQ researchers Christoph Gohle, Sebastian Blatt and Christian Groβ. This python wrapper was imported by Marc Cheneau in the group who uses it on the LCF Strontium experiment.

Note that this section does not intend to explain how QControl and the sequencer are interfaced and communicate : this can be found in Raven (2022). This note is rather meant to introduce QControl3 through an installation guide and a user-guide for the next PhD students on the experiment (or other experiments).

The first section explains why we chose to use the Adwin and QControl and gives a really short introduction of the sequencer features and its hardware configuration. The second part is intended to be a tutorial on how to write a very simple script with QControl, introducing important concepts : this can be of interest if one wants to install QControl3 on its experiment. The third one focuses on the *remote drivers* that allows one to code additional devices (arbitrary function generators for example, cameras etc..) and explains how to code a really simple (and useless for the one presented) remote driver. Finally, the fourth part describes how we coded our sequence and the choices we made for the scripts.

2.A From Adwin to QControl3

Change motivation : Adwin & QControl

The choice to use the ADwin-Pro II system was made on the 1st February, 2021 in a meeting during which we decided to stop to persist on trying to run the experiment on its current configuration. On the "to-change" list, in addition to the sequencer, were also the cooling laser, the magnetic trap coils, the transverse molasses, the current power supply as well as possibly the MOT beams. In the LCF Quantum Gases group, all teams except the Quantum Dynamics use the National Instrument material together with Cicero[12] developed by Keshet and Ketterle (2013). The advantage of the Adwin material was its availability : Marc had one additional sequencer in spare and proposed us to test it. Considering the other changes were also expansive, we decided to stay with this material and to save money for other investments[13].
Of course, the hardware material does not impose to work with the QControl software: to my knowledge, the Sodium experiment at the Laboratoire de Physique des Lasers uses also the Adwin-Pro II material but together with a Matlab wrapper developed by Aurélien Perrin. The Adwin material is also used in Wien[14] together with the Labscript program developed by Starkey et al. (2013). In a quantum optics experiment, the Adwin-Pro II material was also used to perform *real-time quantum feedback to prepares and stabilize photon number states*

[12]The year 2021 A.C. The Quantum Gases NI users group is entirely occupied by the Cicero Words Generator. Well not entirely! One small team of Rubidium still holds out against the Cicero dictator and is ruled by Spartacus. See the CiceroIsa Project for more information.

[13]I would like to thank a lot Marc for the sequencer. I think that our team did not paid the sequencer back, and as good accounts make good friends, I guess we should... But OK, this is permanent researcher business. Nevertheless, in general, I think this illustrates the atmosphere of cooperation among the six research teams within the group, which I have been able to benefit from throughout my thesis. The credit for this good atmosphere goes to all the permanent researcher staff, whom I thank for it.

[14]The Adwin labScript driver developed within the Leonard Lab can be found here and was implemented by Schabbauer (2023).

Table VI.2: Adwin cards available wit QControl and their authorized address range. Lecture : to run QControl with Adwin material, one must use at least 1 and less than 4 digital cards and set their address number between 1 to 4. It is possible to use also a RTD8 card

Card name	Number range	Address value range
DIO-32	1-4	1-4
AOUT8/16	0-6	5-10
MIO4	0-1	14
RTD8	0-1	15

by Sayrin et al. (2011). It was distributed more recently as a python package NQontrol by Darsow-Fromm et al. (2020)
Nevertheless, working with QControl3 seemed the best option as the LCF strontium team was working with this wrapper and we could benefit from Marc experience. With hindsight, the criticism I would address to QControl3 would be the non-free online access to the code[15] making the collaboration to this project not trivial. The documentation is not yet complete even though I will try to make a contribution based on this note.

Adwin Pro-II features

We use the ADwin-Pro II system with a processor module T12 that "provides high performance using 1 GHz clock rate, 1 GB memory, and a 64-bit FPU (double precision) for float calculations" according to the Adwin documentation. Beside this "heart" module, we currently have two other types of cards that perform analog and digital signals. Analog outputs modules, *Pro II AOut-8/16*, have 8 channels with 16 bit resolution, a voltage range of ±10 V and a settling time of 3 s. Digital output modules *DIO-32* composed of 32 TTL channels with edge output of 100 MHz with time stamp. Even thought the value of 100 MHz seems to allow a minimum pulse duration of 10 ns, the minimum value allowed by QControl3 is 5 µs.

Adwin Pro-II hardware configuration

The following section resume the Adwin Pro-II material configuration that is needed to use it with QControl3 on a Linux based computer. First, the Adwin driver must be installed - the 5th driver and not the most recent one - following the documentation. Once the connection with the sequencer is established, a fixed (local) IP address should be set to the device and then saved into a driver property file, using the `adconfig add` command.

```
$ adconfig config 00:22:71:03:08:F8 IP 192.168.1.4  MASK
↪  255.255.255.00
$ adconfig add 0x001 TYPE net IP 192.168.1.4
```

One must then *declare* the number and the address of each card using the ADPro software, only available on a Windows. Note that the minimal configuration for QControl3 to work is with one DIO-32 card. To choose the number and the address of each card, one should respect the Table VI.2 conventions. Note also that one could use ADpro to control the outputs of the cards to check the hardware output signals.

[15] Even though the code is shared under the GNU GPL3 free software license, one needs to request access each year to the maintained repository on the MPQ Gitlab server which does not help the collaboration.

2.B Introduction to QControl3

In this section, I will walk you through getting start with QControl3. The first subsection provides a guide on installing the various QControl packages on your computer, while the second introduces the declaration of different channels that will be used in scripts. The third subsection covers the client and the various commands associated with it, while the fourth outlines the structure of a simple script. In this part, we will focus on a single Timing Controller, meaning that only the sequencer channels will be accessible. Programming and using other Timing Controllers will be discussed in a dedicated section.

Figure 101 summarizes the basic functionalities of QControl. The strength of the code lies in enabling multiple clocks to evolve in parallel once the *starting signal* is given by the main clock. This can be particularly useful for using the same device twice during a sequence or for providing feedback within the same sequence. Any clock with independent timing is referred to as a *Timing Controller*, and only one of them is the absolute master of time – in our case, it will, of course, be the sequencer. Each Timing Controller is a node in the *Timing System* and can have various devices under it: the so-called *Timing Devices*. For example, a current generator will be a Timing Device and a child of a Timing Controller, that can control several other devices. Below the Timing Device node, it will be necessary to create temporal channels so that the user can send instructions to the device (e.g., "current 2 A; output on"). Note that the words *timing* in front of each word is not only here to show off but to emphasize the fact that any action on a timing channels is done at a given time. For example, the instruction "output on" sent to the current generator will be sent at a given time of the sequence. The relationships between Timing Controller, Timing Device, and Timing Channel will be discussed in the following section. Here we will simply explain how to add a Timing Controller to our Timing System and then create user channels from existing timing channels.

Installation

The QControl3 programs can be downloaded from the MPQ gitlab server or from the fork branch on our (public) gitlab server. Note that QControl was developed on Linux-based computers, but it seems that it was extended for Windows. In the following, I will assume that one works with Linux. Depending on the devices used in your experiment, a various number of packages can be needed, but we will focus here on the minimal configuration in order to run the simplest sequence possible. The first step is to create a virtual environment so that QControl3 is not installed on your python's system distribution. In the following, any installation will be done within the qc3 virtual environment, even if it is not specified. There are four essential packages needed to use QControl3.

- `qunits` is used by all other packages and hence **must be installed first, after having install `cython`**. It ables the use of physical quantities in script, which is quite convenient.
- `qcontrol3_base` is the core of the program : it contains the timing server which communicates with all the remote devices, the Adwin sequencer being one of them.
- `qcontrol3_driver_timing_adwin` is the driver that ables the QControl3 program to dialogs with the Adwin sequencer.
- `qcontrol3_driver_timing_softwareremote` is the driver that ables QControl3 to dialog with other remote devices than the Adwin Pro-II sequencer. It is not strictly speaking necessary to run a first sequence but it is a low level driver that will be rapidly needed, to control cameras or waveform generators for example.

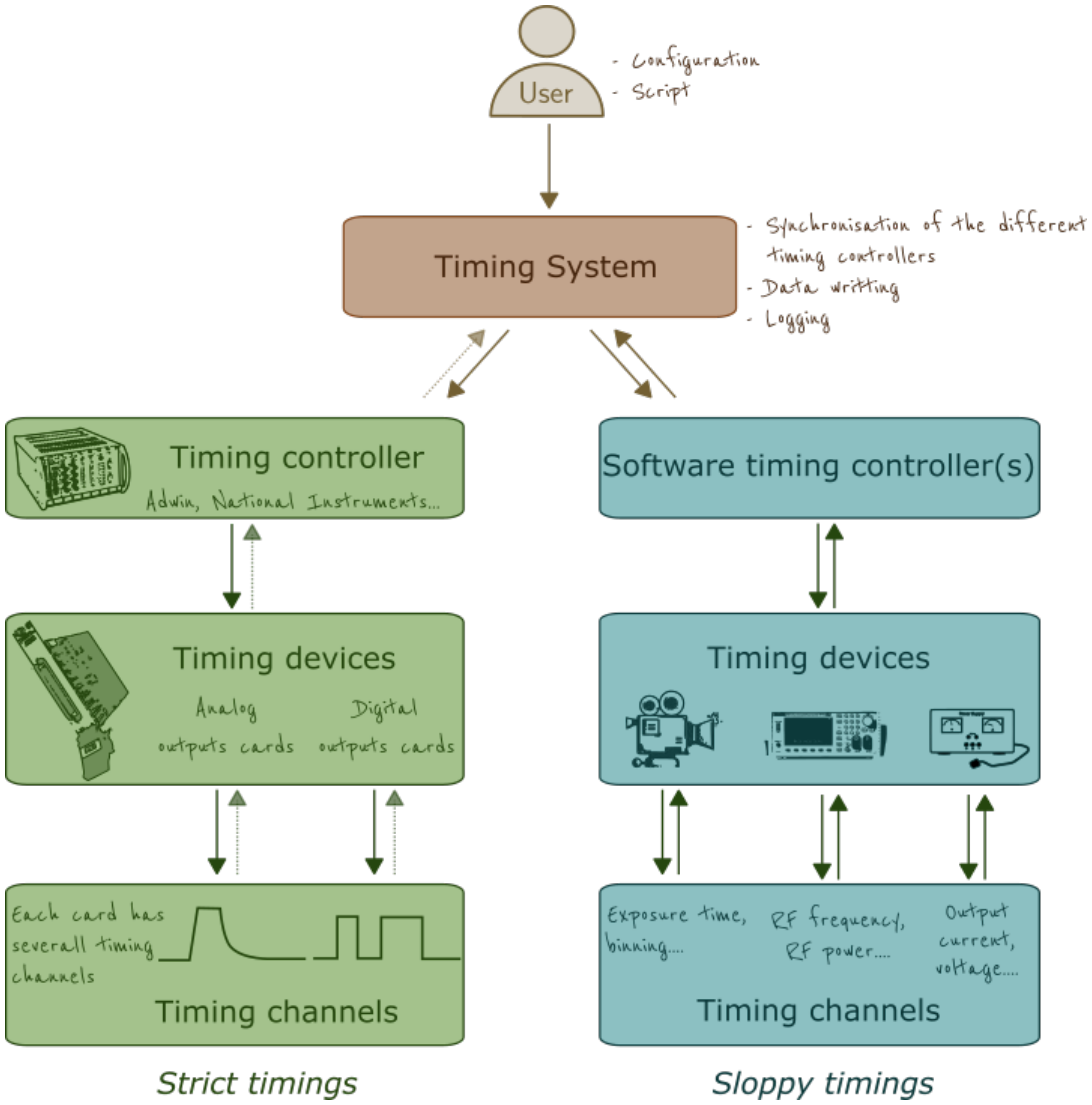

Figure 101: QControl3 timing system. The user script is compiled and a sequence of events is passed to the Timing system composed of Timing Controller and Software Controller. The clock of each controller will evolve independently : Timing Controller time is set by the sequencer clock while Software Controller time will be set by the computer on which the remote runs. The sequencer timing is "strict" since it controls digital and analogue output up to the nanosecond scale while Software Controllers have more sloppy timings - typically some ten of ms. Programming devices during a run and not before able the use of the same device at two different time in the experiment in different configurations. For example, we use the same current generator to perform compensation magnetic fields during the optical molasses and for the magnetic compensation to maintain a bias during the optical dipole trap. An other example of the use of this soft timing is the trigger of the evaporative RF ramp that is trigger with a "Output On" command sent with a remote server at soft time. Double arrows between blocks mean that timing channels can also send back measured values to their timing controller : it is the case for example for a camera which returns the image, or an oscilloscope that returns the measured voltage. In principle, it is possible to register analog signal with inputs cards of the Adwin material but this was not yet implemented. ©Inspired from M. Cheneau seminar.

After installing those packages[16], one should be able to run a first simple sequence. To dialog between the client (you) and the different server, QControl3 use Pyro communication. Therefore, one must start by launching the `name-server` in a terminal, within your virtual environment[17]. In a new terminal, the `event-server` can be launch and will create several directories in your home directory:

- `.qc3` stores the configuration file `qc3conf.json`. It is initialized with default values and can be customized following the documentation of the QControl3 base repository.
- `qc3data` stores the data after each experiment run.
- `qc3log` stores log messages.
- `/qc3scripts` will contain your script, subscripts and hardware configuration[18].

```
+ - qc3scripts
       + - config
       |  + - channels.py
       |  + - hardware.py
       - myscript.pys
```

Figure 102: Typical content of the qc3scripts directory.

Summing up, we have now initiated both the name server and event server, essential prerequisites for launching the main server.

Declaration of the hardware and user channels

So far, properties of the hardware processor did not matter but this must now be configured in the `qc3scripts` folder, which `config` folder will be read when launching the main server. The server will first import the `hardware_setup` function from the `hardware.py` file. The argument that is passed to this function *tsys* is the timing system. This is the "*the root instance of the hardware tree on which one should add your timing controllers.*" In QControl language, a timing controller is a complex object with timing channels, that often dialog with an external device. In the example we provide in Program 103, we add to the timing system the Adwin Timing Controller. Note that in the declaration of the Adwin Timing Controller, one must specified the device number and the number of different cards used. The device number must match the one set previously using the adPro software in subsection Adwin Pro-II hardware configuration.

Timing controllers like the Adwin Timing Controller contains several timing channels but one must now create so-called *user_channels* so that the user is able to interact with them.

[16] To install a package, one should clone it from the git repository, change to directory and install it as a developper :`python setup.py develop`. This means that rather than copying the package's files into the site-packages directory (as it would with a regular installation), it creates a symbolic link or .pth file that points to the project's source code directory. This enables you to modify the source code and the changes will take effect without the need for reinstallation (*i.e.* running again the setup file installing again). Note also that I recommand to use the `python setup.py develop` command rather than the `pip install -e .`. Indeed, depending on which command we used to install the package, the `qcontrol3-create-package` that we use after in the tutorial did not worked. See the Laboratory Journal on the 06/10/23 for more informations.

[17] The code to launch the name server (or the event-server) is `(qc3-env) $ name-server` where, the `(qc3-env)` keyword highlights that one must works within your favourite environment but will be dropped after.

[18] Note that you could have an error if you do not have yet entered your hardware configuration. If so, continue to next subsection and run again the `event-server`.

```
from qcontrol3.driver.timing.adwin import AdwinTimingController

def hardware_setup(tsys):
    """Define the hardware setup.
    Parameters
    - - - - - - - - - -
    tsys : TimingSystem
        The root instance of the hardware tree. Add your timing
↪   controllers to it.
    """
    adw = AdwinTimingController(
        "ADWIN0",
        processor=12,
        number_dio32=1,
        number_aout8_16=1,
        device_number=1,
        is_dummy=False,
    )
    tsys.add_child(adw)
    tsys.set_master_by_name("ADWIN0") # set the master timing
    ↪  controller for the system.
```

Figure 103: Minimal example for the file `hardware.py`. Tests can be perform disconnected from the real sequencer by setting the adwin system dummy.

This is done in the `channels.py` file. In the Program 104, we create two user channels : one is digital while the other is an analog channel.

```
import os
from qcontrol3.tools.units import u

orgdir = os.getcwd() # change the directory for easy usage of subdirs
os.chdir(os.path.dirname(__file__))
def channel_setup(tsys):
    tch = tsys.get_node("ADWIN0.DIO0.DO01")
    tch.create_user_channel("DIGITAL_01",
       "Description of my digital output 01",
       default_value=False)
    tch = tsys.get_node("ADWIN0.AOUT0.AO4")
    tch.create_user_channel("ANALOG_04",
       "Description of my fivth analog output",
       default_value=0*u.V)
os.chdir(orgdir) # change the directory back
```

Figure 104: Creation of two user channels from timing system nodes. Note that one can display the timing system tree `tsys.tree` to check available timing channels.

Once the hardware is declared, *User Channel* must be created in a `channels.py` file: this will able the client to access and modify the values of timing channels. *User Channels* are created using the `create_user_channel` method which take as argument a name[19], a description and a default value. The later will be set at the beginning of each cycle. Once a *User Channel* has been created, its value can be changed with the `qcontrol3-client` and it is accessible in any file with the `.pys` extension.

Once those file are completed, the last configuration step is to launch the server running the `qcontrol3-server` command. If an error occurs at this stage, it probably means that there is an error in the hardware and/or channel declaration.

Communicating with the qcontrol3-client

Any command that a user want to send to the server must passes through the client called `qcontrol3-client`. I will not list all the client functionalities but restrict myself to some of them. The `set_channel_value` function ables to change a value of a timing channel: it must be followed by the name of the user channel associated to this timing channel and by its value. The type of the value depends on the type of the channel: it is a boolean for digital outputs and a string with a voltage unit for analog outputs. For example, with the configuration and the user channels declared inProgram 103 and Program 104 one could send the following commands to the server:

```
$ qcontrol3 -client set_channel_value DO0_01 True
$ qcontrol3 -client set_channel_value AOUT0_4 "6 V"
```

The `reset_defaults` command resets all timing channels to their default value that was set when instancing the associated user channel.

To run a script, one must first create a file whose extension is “pys” in the qc3script repository. This ables the script to access global variables like `iter_step`, `iter_value` as we shall see after. To run a script, the user must first declare which file should be upload, then upload it and finally run it :

```
$ qcontrol3 -client set_pys_file my -script -name.pys
$ qcontrol3 -client upload_task
$ qcontrol3 -client run_single
```

It exists three different running modes :

- `run_single` : the task runs only once and the system stops when the task is over,
- `run_looped` : the task is run while the user stops the execution with the `qcontrol3-client stop` command.
- `run_iteration` : the task is run but the script is executed several times. A list, called `iter_list` is browsed as the iteration progress. Two name reserved variables `iter_step`, ranging from 0 to the size of the list uninclosed and `iter_value`, which takes a value of the `iter_list` at each iteration represent the progress of the iteration. The idea behind it is to enable the scan of a parameter in the script.

Before going into greater details on how to write a script, let’s mention that the `upload_and_run_single script.pys` command ables to declare, upload and run a script file. This commands exist also for iteration and looped modes.

[19] The name of the channel must be composed of caps, number and “_”. Note that it is in the qc3 documentation that “the convention is that this is all upper case with a number at the end if appropriate. This number indexes several channels of the same kind and starts with 0.”

Running a first script

A script inherits from the Script class and must be save with the ".pys" extension so that it has access to global variables such as `iter_list`, user channels defined in `channels.py` file or other global variables in QControl. In a script, the basic syntax to add an event on a timing channel is `add(t, val)` where `t` is the time at which the channel must take the value `val`[20]. An example of a minimal script file is given in Program 105.

```
from qcontrol3.server.script import Script
from qcontrol3.tools.units import u

iter_list = [1, 2, 3, 4]
class MyScript(Script):
   def __init__(self):
        super().__init__()

    def main(self):
        time = 10.0 * u.ms  # absolute deadtime for Adwin sequencer
        DIGITAL_01.add(time, True)
        DIGITAL_01.add(time + (1 + iter_step) * 10 * u.ms, False)
        time += 220 * u.ms
        ANALOG_04.add(time, 2 * u.V)
timing_script = MyScript()
```

Figure 105: Basic script in which we change the value of a digital user channel to True and False at various time and the value of an analog channel to 2 V a bit later. Note that the user channel name used in this script is the one declared in the Program 104. Because this script has the .pys extension, it has access to user channels and iter_list related properties (see text). QControl3 will then call the `main` method of the timing script.

However, the idea is not to use directly user channels in the main script but to wrap them into more complex object, tht should inherits from the `ScriptObjects` class. Regarding this, (DigitalObjects) and analog outputs (AnalogObjects) are already defined in `qcontrol3_base`, with methods that conveys more their purpose than the `add` method. For our current example, one could define objects in a different file (here devices.pys) that should be imported in the main script.

In this case, the `main` function of the script could read

Summary In summary, in this section, we learned how to declare user channels from already defined timing channels and how to modify their values using the server (live) or in a script (at specific times). In the next section, we will explore creating timing channels and their associated timing devices.

[20]The type of the value depends on the timing type : it is a boolean for a `TimingChannelBool`, like Digital outputs of the sequencer. To understand deeper the different type of TimingChannel and user channel, I would recommend to create from scratch a *remote device* following the subsection - a *Timing Device* composed of several type of Timing Channels in qc3 terminology.

```
from qcontrol3.server.script import ScriptObject
from qcontrol3.scripts.base.digital import DigitalObject, Shutter
from qcontrol3.scripts.base.analog import AnalogObject

class ScriptDevices(ScriptObject):
    def __init__(self) -> None:
        super().__init__()
    self.molasses_shutter = Shutter(DIGITAL_01)
    self.mot_aom = AnalogObject(ANALOG_04)
```

Figure 106: This file wraps user channels into more compex objects that will be used by the final user.

```
from qcontrol3.server.script import Script
from qcontrol3.tools.units import u
from config.devices import ScriptDevices

iter_list = [1, 2, 3, 4]
class MyScript(Script):
   def __init__(self):
        super().__init__()
        self.devices = ScriptDevices()

    def main(self):
        time = 10.0 * u.ms  # absolute deadtime for Adwin sequencer
        self.devices.molasse_shutter.add_pulse(time, duration = (1 +
        ↪  iter_step) * 10 * u.ms)
        time += 220 * u.ms
        self.mot_aom.ramp_to(time, 2 * u.V, duration = 100 * u.ms)
timing_script = MyScript()
```

Figure 107: A script that is a bit more evaluate than the previous one. Devices are imported from an other file with a more *user-friendly* name and with other methods than the `add` one. For example, the mot_aom use the ramp_to method and one could imagine objects with other methods (exponential ramps for example).

2.C Remote server and drivers

Often, in a cold atom experiment, one needs to use several other instruments, for example waveform generators or cameras. In QControl, commands are sent at various time during a task, offering the possibility to use one instrument in two different configurations during a run or to assign a value at an instrument after having perform a measurement within the same task.

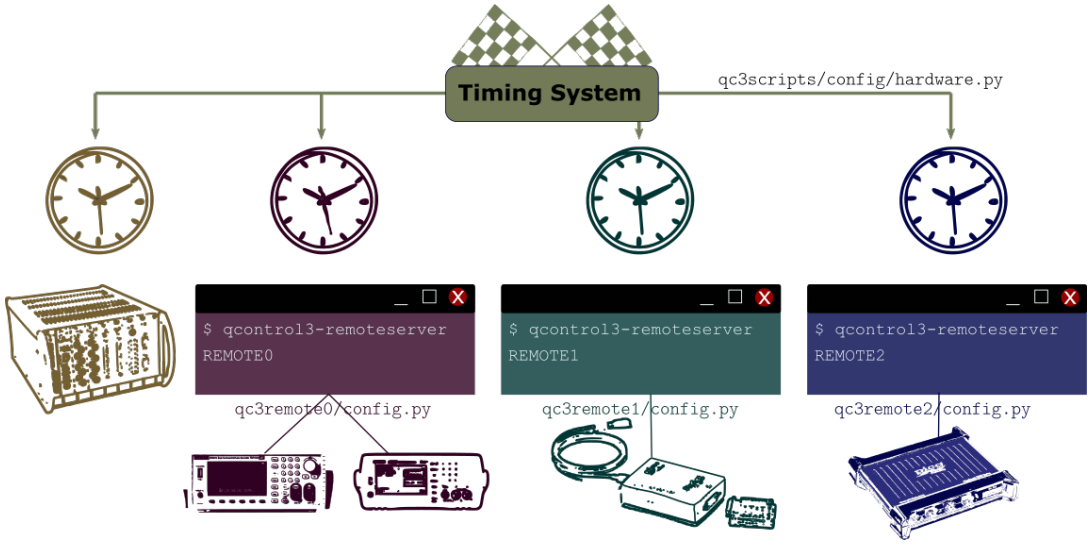

Figure 108: This scheme is a specific zoom of Figure 101 on the different Timing Controllers. Before launching the client, the user must start all remote server that host the remote timing controllers. When a run is about to start, the timing system provides timing controllers its list of events and then launch the *official start signal*. Until the end of the run, each remote timing uses its own clock as time reference, based on the starting signal. On this scheme, this is underlined by each remote timing controller represented as shells of the computer. The sequencer clock is of course internal and set as the *master timing controller* in the `qc3cripts/config/hardware.py` file. The link between timing device as waveform generators or oscilloscopes are defined in each remote configuration file. Note also that the name of each remote (`REMOTE1` for example) and their location (the folder that contains the `config.py` file) must be declared in the qcontrol configuration file (in `~/.qc3` on linux).

The remote server

As shown in Figure 101, timing devices are controlled by the software controller. The command

```
$ qcontrol3 -remoteserver REMOTE0
```

starts the remote server which can be seen as the actual remote controller. Launching this command for the first time should create a `qc3remotecontroller0` in your home path. Remote devices of your experiment should be declared in the `config.py` file of this folder[21]. Note that the hardware properties of your instrument must be filled in this file : for example, instrument that use the VISA standard communication protocol can be controlled with an existing VISA driver class. Since this remote class can be used for several instruments, it is in the `config.py` file that the user fills hardware informations such as the IP address, its name and other properties (timeout, encoding...). Even though various drivers already exist, it is often needed to create a new remote device. In the following, we will see how to create a simple driver from scratch.

[21] Note that several remote controllers can be launched. To do so, one just have to create a new directory with a `config.py` file and declare the path to this directory and the name of this remote in `~/.qc3/qc3conf.json`.

Creating a remote driver

In this section, we will create a device that will query a database to print in the terminal the meteo in a city (provided by the user) at a precised time. To do so, we need a string timing channel so that the user can set the city and a boolean channel such that when set to `True`, the device prompt the meteo to the database and print it.

In QControl, remote drivers consist of a python package that should respect the QControl3 package tree. To ensure that, we will use the dedicated command

```
$ qcontrol3 -create -package
```

in which you will have to fill the type of package you want to create, its name and description. This creates a new directory on your computer that contains the relevant file tree as well as a git repository. A `setup.py` file is also created to install it in your python environment[22]. Since we want to create a meteo driver, we will create in the following *misc* package named `meteo_driver.py`.

The Figure 109 tries to summarize the links between the two software devices that compose a diver defined in Program 110. The upper part of the later sets up the client part of the driver : the `MeteoDevice` class defined in the driver is a Software Device composed of two String type and Boolean type timing channels whose names are respectively `LOCATION` and `TRIGGER`. Nothing is implemented in this part since they are just used to assign the value set by the user to the remote device. Indeed, one can see that timing channels that are children of the `MeteoDevice` inherit from `SoftwareTimingChannel` class and not from `TimingChannel`.

The second part of the code defines the remote part and the `RemoteMeteoDevice` class. This class has also two timing channels as children whose name are also `SCRIPT_ADDRESS` and `TRIGGER`. Classes that define those children inherit from the `TimingChannel` class. Whenever one channel value of the (client) software device is changed, the value of the associated remote timing channel is modified too through the "`set_value_raw`" method. Note that this correspondence is only possible if the names of each channel are identical. In the example, both the children of the `MeteoDevice` and the `RemoteMeteoDevice` have the same name - `METEO_NAME.TRIGGER` for example. When a channel is modified, the `io_update` method of its parent is also called, which can be view as callback. Note also that a software device can retrieve the value of its children channels through its "`children`" dictionary attribute. In our driver, we therefore use the `io_update` method : given that the default value of the trigger channel is False, whenever its value is set to True, the driver get the meteo from the location.

Once your file driver is ready, the driver must be declared as a timing device on both remote and client parts. The remote part must be set up in the `config` file of the remote controller repository[23] while the client part should be set up in the `hardware` file of the configuration script folder.

We first declare the remote part of the device, in this case in the config file of the remote0 directory. Since we want to provide the meteo from to different website, we create two drivers whose name and url addresses are different. Note that the name define here define the name of the timing channel, for example here, one of the timing channel name is `REMOTE0.METEO_CIEL.TRIGGER`.

[22] It is recommended to install this package as a developer (`python meteo_driver/setup.py develop`). Doing so, the installation process will create symbolic links that point to your driver software so that any modification in your driver does not need a new installation in your environment.

[23] The default repository is `~/qc3remotecontroller0/` with default name being `REMOTE0`

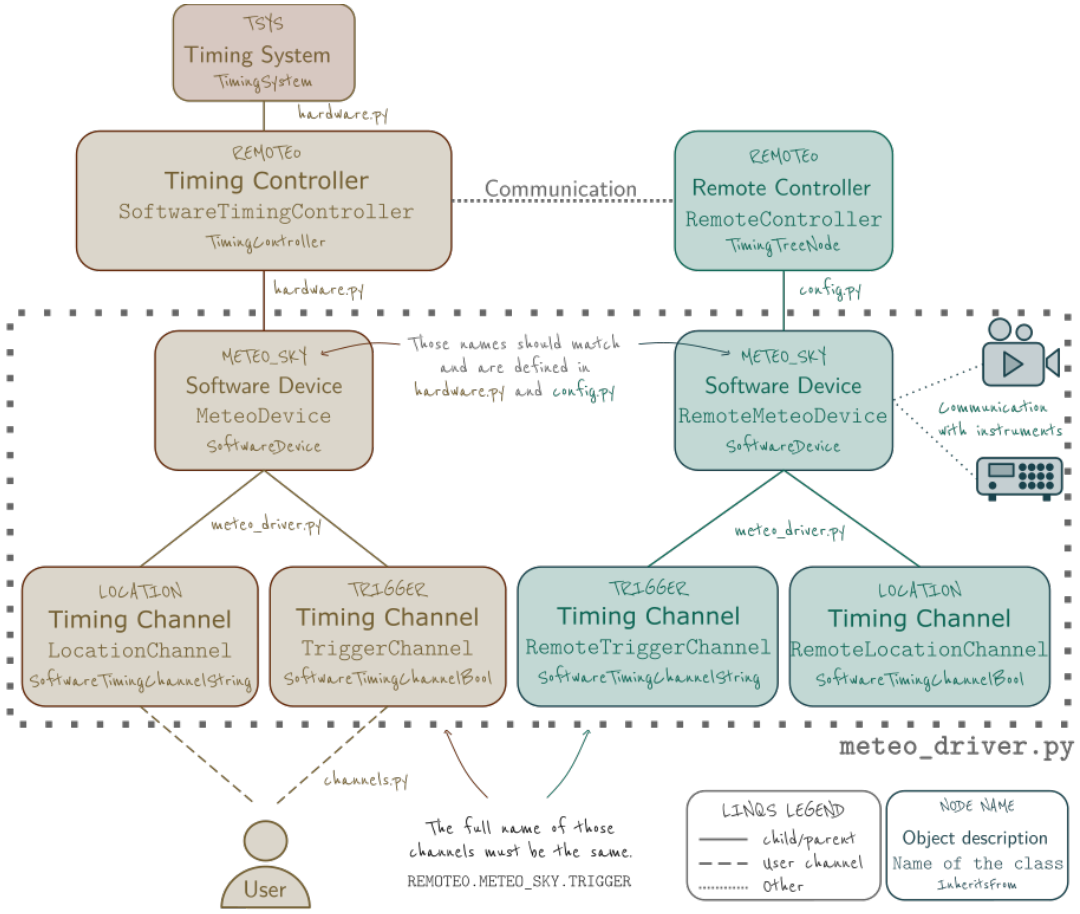

Figure 109: This scheme is a zoom from Figure 101 on the specific driver `meteo_driver.py`. Relation between objects are represented by lines : solid for child/parent relation, dashes for user channels and dotted for others. Next to each line is given the file in which the relation must be set. Each frame contains the description of the object with its name of the associated node, the object description in QControl3 language, the name of the class and the class the object inherits from (see legend). The driver is composed of two software devices one being the remote part (green) and one the client part (brown). In the driver file are defined the two times two timing channels that compose the driver : two are children of the remote part of the driver and the two other are channels of the client part. The user creates user channels associated to those timing channels : changing a channel value - on the client side - sends an update on the remote side through the communication channel between the Remote Software Controller and the Remote Controller. This is made possible if the two names coincide.

Now that that devices are created, we need to start the remote controller before starting the client[24]. Once this hardware part is done, we need to do the same on the client side. This is done in the `hardware_setup` function of the `qc3scripts/config/hardware.py` file. In our case, we just need to :

- instantiate the timing controller corresponding to remote0 and add it as a child of the timing system,
- instantiate all software drivers with the same name defined in the remote configuration

[24] to launch the remote0 server, one must run `$ qcontrol3-remoteserver REMOTEO`

```
This code is not available on PDF.
```

Figure 110: The meteo_device example. This code creates the links between the mete_devices and its timing channels. The brown part of Figure 109 is the local part of the driver with which the user will communicate. The green part of the driver is in the second part of the code : the remote part. See text for more description.

```
#file : config.py
from qcontrol3.driver.misc.meteo_driver import RemoteMeteoDevice
def hardware_setup(remote_controller):
    # 1. instantiate device
    dev1 = RemoteMeteoDevice(name = "METEO_CIEL",
                             description= "query meteo to meteo
                             ↪ -ciel.com",
                             url_adress = "www.meteo
                             ↪ -ciel.com/database")
    # 2. add it to the remote_controller
    remote_controller.add_child(dev1)

    dev2 = RemoteMeteoDevice(name = "METEO_FRANCE",
                             description= "query meteo to meteo
                             ↪ -france.fr",
                             url_adress = "www.meteo -france.fr/public
                             ↪ -db")
    remote_controller.add_child(dev2)
```

Figure 111: Declaration of the remote part of the script driver in config.py of the remote0 controller.

file and add them as the child of the timing controller

```
from qcontrol3.driver.misc.meteo_driver import MeteoDevice
            (....)
def hardware_setup(tsys):
            (....)
    rem0 = RemoteSoftwareTimingController("REMOTE0")
    tsys.add_child(rem0)
    dev = MeteoDevice("METEO_CIEL")
    rem0.add_child(dev)
    dev = MeteoDevice("METEO_FRANCE")
    rem0.add_child(dev)
```

Figure 112: Completion of `harware_setup` function of Program 103. Declaration of the devices should align with the declaration done in the remote configuration file, i.e. names must match.

Now that this is done, one can create user channels associated to those timing channels in the `channels.py` file. The full name of a timing channel consists of all the nodes that compose it, extending from the trunk to the leaves and separated by dots. For example, to create a user channel associated to the trigger timing channel of the device that query the meteo from meteo-france.fr, one must use the following syntax, in `channels.py`:

```
tch = tsys.get_node("REMOTEO.METEO_FRANCE.TRIGGER")
tch.create_user_channel("METEO_FRANCE_TRIG", "", default_value =
↪  False)
```

Even though it is recommended to create user-friendly devices name, we can now use our device to get the meteo just by adding to our script Program 105 the following lines.

```
time = 300 * u.ms
METEO_FRANCE_LOC.add(time, "Brest")
METEO_FRANCE_TRIG.add(time + 30 * u.ms, True)
METEO_FRANCE_TRIG.add(time + 80 * u.ms, False)
```

If you look into the remote0 shell, you will see that during the cycle, and at the *exact* moment (up to a few milliseconds), the temperature is printed. Well done !

Note that our device do not save the meteo inside the hdf5 file in our case. If this is needed, for a camera driver for example, the driver can inherit from the WriterDevice class. This class inherits from the SoftwareDevice class but has already two timing channels defined of type boolean (`TRIG`) and string (`HDF_PATH`). When the first one is set to *True*, the driver called the `initialize_capture` method and when set to False it ends the capture by calling the `end_capture` method, and saves the acquired data into the HDF5 file, whose path is given by the string channel, after calling the `process_data` method.

Summary In summary, in this section, we learned how to create a driver from scratch. Once the code is set up, the driver must be installed in your environment and declared both in the remote part (`config.py`) and the server part (`hardware.py`). Once device is instantiated and added as a grand-child of the timing system, it is possible to create user-channels associated to those channels (`channels.py`). User channels can then be wrapped into more complex object or just used with the *add* method in the script.

2.D Our current configuration

I will now give a brief overview of how we structure our code and way of coding sequences. We discovered QControl3 and started to understand its logic while we had other experimental issues, so we had to balance proper coding and quick - and dirty - implementation in order to progress on the experiment. As we had no clear tutorial, it took time to clearly understand the logic behind QControl and, as Python beginners, we had tried our best to do it as clean as possible. Writing this thesis appendix made me realized however that our way to code sequences was in fact quite proper and logical. Last but not least, I think that what belongs to Caesar must be returned to Caesar : even though it is not clearly valued in his PhD thesis, Quentin Marolleau (2022) made a major contribution to our script structure during summer 2021. His work pioneered the current code structure.

For future developers, note the code has (slightly) diverged in two (reversible) aspects from the *official* QControl3 version.

1. Experimental parameters are not hardcoded in the scripts but are stored in a parameter file that is read during each script execution, i.e., for each run. This choice is motivated in the first following subsection. The consequence is that the `iter_values` are dictionaries which raises an type error when the program tries to save it in the HDF archive.

2. We do not save data with the HDF format as motivated in the see the second subsection and we must therefore assign a custom identifier per shot, as explained in the third subsection. The consequence of this choice is that we changed a few lines in the `qcontrol3_base` code in order to store the experimental configuration. More details are given below.

Defining a parameter value and scanning a parameter

All values used in our code are not hard-coded but defined in a so-called sequence_parameters dictionary. This dictionary is loaded from a json file of the same name. This format was chosen for its nice readability properties - even thought we do not read it any more. At the first iteration of the script, this file content is saved in a hidden file (`.sequence_parameters.json`) so that the user cannot modify any parameter during a sequence. The content of the file is then loaded into a dictionary, and interpreted in terms of dimensioned quantities[25].

The **iter_list** is supposed to be the list containing the scanned parameter values. As we understood QControl logic, if a user wants to scan the MOT AOM frequency, he would hard-write the frequency defined in the script by the `iter_value` so that this value is updated at each run. In our case, every parameter being encoded in the parameters dictionary, we need to update this dictionary at each run. An element of the iter_list is therefore a dictionary whose entries are keys of the parameters dictionary, for example, `{"MOT | AOM | freq" : 80 * u.MHz}`. Since the iter_list elements were not thought to be dictionaries therefore it produce an error when QControl tries to save the iter_value into the HDF5 file. Some remarks about the iter_list definition :

- it can contain several entries to perform double scans,
- it is a global value of `pys` files so it is define when the script is uploaded and not at each run. In practice, this means that we define the iter_list at the first execution, *e.g.* when iter_step is -1[26].

Saving data

The data repository has the following form `day / SEQ / STEP` where `SEQ` is the sequence number, an integer starting each day at and `STEP` is the shot iteration number. Even thought QControl3 gives the possibility to save all data associated to a run into a single HDF5 file, we finally decided to abandon this way of saving data. First reason is that opening an HDF5 file to get a few information or just an image is quite long compare to a simple file : one has to open *all* data and not only the one you are interested in. Loading data to briefly analyze a sequence was a pain when the number of runs was above 100[27]. An other reason is that variables and

[25] For example, the dictionary entry string `"3 V"` will be changed to `3 * u.V`, a qunits quantity.

[26] When the `pys` file is uploaded, it is parsed and exectuted a first time with iter_step value `-1`. The file is then executed at each run with iter_step increasing value ranging from 0 to the length of the iter_list minus one.

[27] This problem is also because of the software we used needed to open all file at once, which is not optimized.

scripts are not easily accessible in HDF5 file which is not convenient when one needs only to check an old sequence. Because of this choice, we always run iterations, and never loop nor single runs, because we need the iter_step to increase at each cycle so that we know at which iteration in the sequence we are.

QControl allows the user the option to save or not save its data. In addition to the HDF file containing the data, QControl also generates an HDF5 archive with the experimental configuration. A graphical user interface (GUI) called sequence_viewer was developed in Munich to load this file and display the content of each channel in the sequence. To avoid reprogramming this entirely, we made some modifications to `qcontrol3-base` to save only this experimental configuration file. It is worth noting that updating the Python version or the qcontrol3-base from the MPQ may necessitate an update to this modification.

The HeliumScript class and spirit of the code

Any script we use in the lab inherits from the HeliumScript class, which contains methods and attributes common to any script. This class sets the sequence number, the cycle number, the sequence directory, loads the `sequence_parameters` and update it if one scans a parameter. When the user starts a sequence, the following steps are performed by the HeliumScript class.

- it sets the default path to look for camera picture and configuration files,
- it sets the cycle id, defined as the absolute time of the current cycle in seconds, relatively to the epoch time for QControl3 (the first qcontrol-Helium-MOT time 1619049600: April, 22nd of 2021 for humans),
- it sets the day directory, defined the sequence number and its associated directory depending on the last folders in the day directory. If the last folder was 014, this means that the sequence is 14 if the iteration step is greater than 1 or it means that one starts a new sequence hence it creates the folder 015 and set the sequence number to 15. Not that this fragile way of saving data implies that one should not modify the day folder on the server when the experiment is running.
- it loads the sequence parameters file from the hidden sequence parameters file. If the iteration step is 0, it copies the `sequence_parameters.json` file into the hidden file so that parameters of a sequence cannot be changed while running.
- it updates the parameters dictionary with respect to the iteration value of the `iter_list`.
- it instantiates script devices i.e. it gives nice name to user_channels.
- it instantiates subscripts class like Raman or cMOT for example. Note that as shown in Figure 113, subscripts are instantiated with the sequence parameters and they also instantiates script devices (as they inherits from the ScriptObject class)

Note that the helium script also defines methods to save data that should be called at the end of any script to save the content of the script folder.

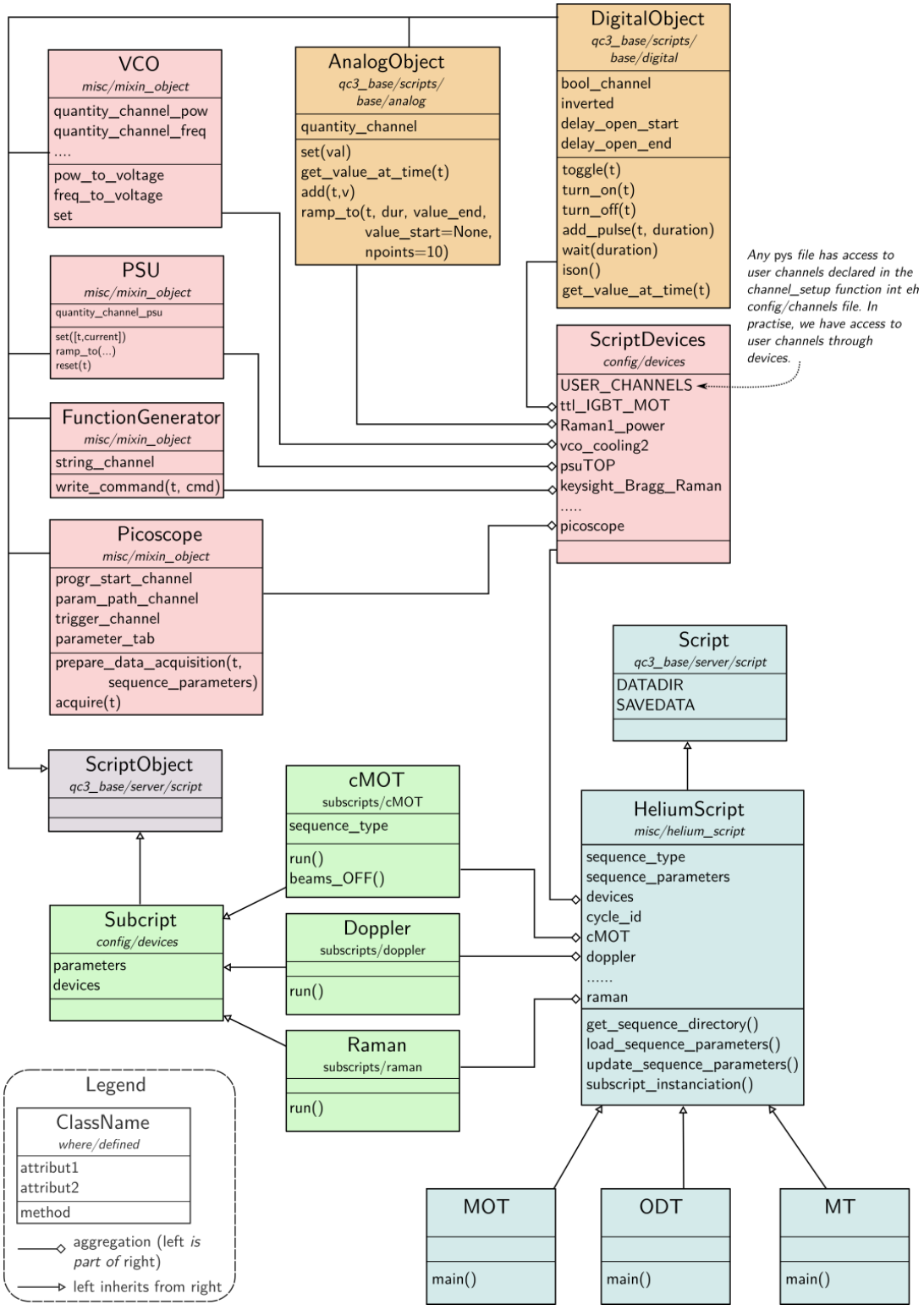

Figure 113: UML diagram of our scripts. Inheritance is represented by an arrow toward the mother class and aggregation with a diamond near the aggregate. Any script (MOT, MT, ODT) must have a `main` method to be run that contain the list of event of the sequence and inherits from the HeliumScript class, our base mother class. When instantiated, the HeliumScript gathers the sequence parameters from a configuration file and interprets its entries as qunits quantities. It then instantiate all device (red) from the experiment : channels of the sequencer as well as string channels to dialog with different instruments. A device can be a simple `DigitalObject` (a switch for example) or a more complex object composed of several other channels (a VCO for example is composed of two `AnalogObject` and one `DigitalObject`). The class instantiates also each subscripts, passing it the parameter dictionary and the devices instantiated. The various method defined in each subscript are then called by the daughter class.

Remotes currently implemented

As with any other cold atom experiment, we use many other devices that are programmed and triggered during a sequence. Each device requires a specific driver:

- **SCPI**: Many manufactured devices use the SCPI convention to send commands. Such devices were already programmed. This is how we program the Rigol DG4202 (for radio-frequency evaporation and the 1064 nm pair lattice power ramp), the Anapico (radio-frequency generator for the Raman 2 beam and the 1064 nm lattice), the Keysight 33522B waveform generator (sinc shaping for the Bragg pulses), and the Agilent devices.
- **Socket-type devices**: Some other devices do not work with SCPI commands but with a less evolved protocol scheme called socket. This is the case with the R&S HMP4040 power supply (magnetic bias during the molasses and the dipole trap), and the TTI TGF4242 waveform generator (RF frequency sweep for the Bragg pulses).
- **Camera Xenics**: We have never been able to remotely control the camera. Since we do not change its properties much (exposure time and so on), we program it on a daily basis to save the picture in a folder when the camera is triggered. The driver then accesses this folder and uploads the latest image found to the sequence repository (or the HDF file when it was used).
- **The MCP driver** simply writes in a file where the TDC driver should save the data (it saves the 'cycle_prefix'). Indeed, the TDC acquisition window is set by a digital trigger. The recorded data are then sent to a Windows computer for Windows driver reasons, on which the reconstruction program runs continuously. Each time the program receives data from the TDC, it reads a file in which the cycle prefix is written.
- **Picoscope drivers**: PicoTech develops PC oscilloscopes that can be remotely controlled. In order to save experimental signals, we have developed three drivers:
  - *The Picoscope3000* driver, for a four-channel oscilloscope, is used to monitor and fit the Bragg interferometric sequence. We use it to access the absolute phase of our interferometer.
  - *The Picoscope2000* driver, for the two-channel device, is used to save and fit the arrival time of the BEC on the MCP and to recenter data.
  - *The Picolog* driver registers data with a lower time-base to enhance the possible drifts of beam power (cooling lasers especially, for example the MOT).

The scan controller

On a daily basis, we use a Figure 114 called `scan-controller`. The idea of this GUI was to be as the more agnostic possible meaning the code can be effortless run without it[28]. When running an experiment, we want to run a sequence providing all experiment parameters, which variable should be changed at each cycle (scanned in our language) and which value to save for the analysis[29]. Hence, the ScanController just saves three files :

- `sequence_parameters.json` : contains the value of the experiment parameters,
- `.scan_parameters.json` : contains a dictionnary with the parameters that should be scanned : it contains the *key* of the parameter (its unique identifier), its minimum and maximum values as well as the number of values to scan. This file is then red

[28] At first, we used to define within the code the parameters valueas well as the scanned parameters so in order to have a smooth implementation, this code was thought to be compatible with the way we used to work.

[29] All parameter values are saved at each run, but since only a small fraction of them are of particular interest for the immediate analysis, we store them in a dedicated file.

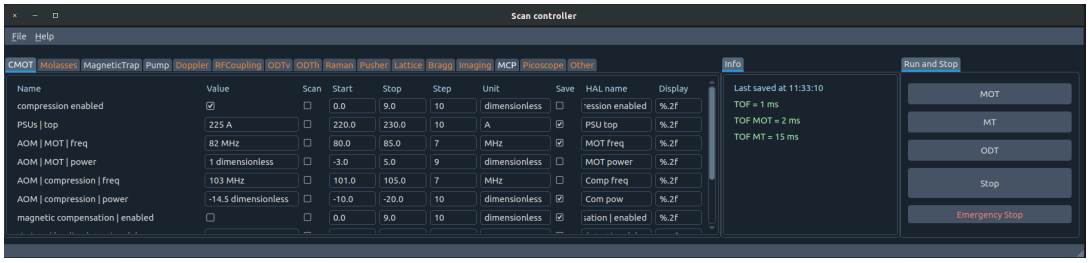

Figure 114: The GUI used to monitor the experiment. The user define here the parameter used and if the parameter should be saved in a specific file for immediate analysis. Scanning a parameter is made possible by clicking the *Scan* button. Subsequence are separated in different tabs, who's color change depending if the subsequence is run or not. For developers, the code tried to respect the "MVC" (Model-View-Controller) design pattern.

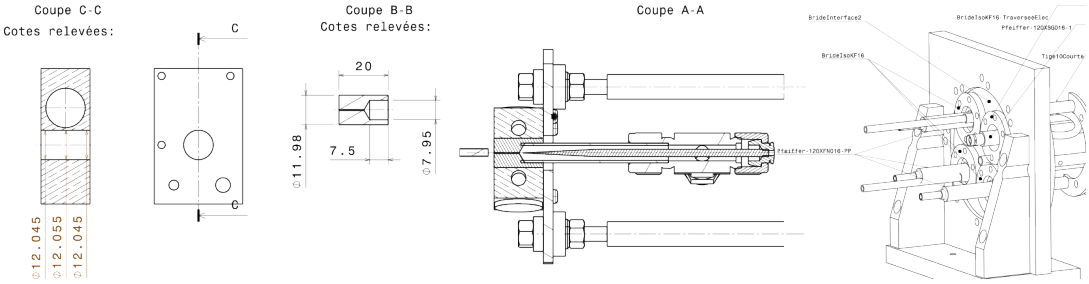

Figure 115: The boron nitride diameter should not exceed 12 mm in order to put it in the copper piece : its diameter should be 11.97(1) mm. The width of the small hole is 500 µm while the other one should match the diameter of the glass tube (slightly above 8 mm). ©Plans by Jean-René Ruillier.

and interpreted by the `scan_from_controller` and function from qc3scripts. In order to perform more complex scans (i.e. changing twice parameter at the same time), it is possible to redefine within the code the `iter_list` instead of calling the `scan_from_controller` function.

- `.hal_dictionary.json` : contains a list of the parameters that are registred at the end of the run. Note that the unit complited in the scan controller must match the true unit of the parameter or it will raise an error when QC3 tries to executes the file.

3. Technical details about the experiment

3.A The source of metastable helium

Due to a crack in the weld between the flange and the pipes that carry liquid nitrogen to the source, we had to dismantle the source and take it to a welder in December 2022. While reassembling the source onto the flange, I broke the glass. Consequently, it was necessary to machine a new boron nitride piece (which breaks when the glass is removed) and a new glass piece. We took this opportunity to re-measure the copper piece - see Figure 115.

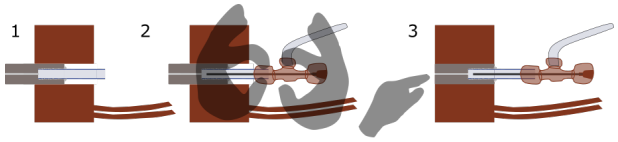

Figure 116: Replacement protocol. See text for description.

Replacement protocol

We needed several attempts before successfully installing a stable source - see the January, 2023 and February 2024 laboratory journal for more information. The challenge in installing the source lies in threading the Swagelok connector onto one side of the glass while avoiding inducing torsional force on the glass. On the other side, the glass is bonded to boron nitride, itself inserted into the copper block. In our initial attempt, we tried assembling the Swagelok connector and the glass before bonding the latter. The issue was that access to the glass once the assembly was complete was too constrained, and we couldn't achieve a secure joint to prevent helium leakage. Following two unsuccessful attempts[30], the fourth version of the source proved to be more stable. The procedure for its installation is as follows.

- The glass is pressed into the boron nitride, and adhesive is applied to the glass-nitride junction. The adhesive used is the glue Devcon home 5 minutes epoxy from *Thorlabs*[31].
- The boron nitride attached to the glass is then slightly inserted into the copper cube from the rear. To prevent the glue from breaking, the nitride-copper friction must be low and the better is not to insert entirely the Boron nitride. The Swagelock connector is then approached and screwed in. To do so, it can be practical to have at least three hands: one holds the glass between two fingers to prevent any rotation, while the other two tighten the Swagelok connector. The danger here is inducing rotation on the glass while screwing: as the nitride part is embedded in the copper part, the friction between these two pieces prevents the rotation of the nitride-glass block. It is the adhesive that may give way, which would also probably break the boron nitride piece.
- Once the Swagelok connector is screwed in, the entire boron nitride assembly is inserted into the copper by heating the later to make it expand. Congratulations, the source is now ready to be tested!

Once the source is installed, one has to *believe* - at least a bit - in it before it works properly.

[30]The second version of the source, installed from January 12 to 16, 2023, had a glass with a diameter that was slightly too large for the Swagelock connector. However, we managed to load a MOT even if the atom number was not optimal. After three days, the discharge no longer occurred. For the third source, the remaining dimensions of the nitride were a bit too large, and we couldn't achieve discharge on January 17 and 18.

[31]I tested the resistance of three different adhesives to liquid nitrogen. To do this, metal pieces were glued together and then immersed in liquid nitrogen for several hours. Once returned to room temperature, they were detached, and the strength of the bond was evaluated. Among the tested adhesives, 1. TorrSeal from Thorlabs, 2. the Devcon home 5 minutes epoxy also from Thorlabs, and 3. Loctite double bubble Transparent Adhesive, the second one appeared to be the most robust.

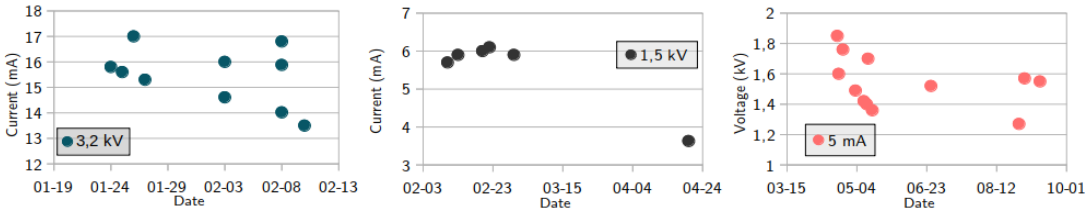

Figure 117: Evolution of the discharge properties of the 2023 vintage. We started working with the previous discharge parameters, with a large current/voltage before decreasing it to 5 mA and 1.5 kV. We worked with voltage control for 3 months before switching to current control on May. Note that if each point represents the discharge property of a single day, it was observed that these values can vary throughout the course of that day.

Vintage 2023 feedbacks

At first, the discharge was not stable and we observed the same flashes as reported in the main text (January, 20th). With the previous version of the source, we used to work with a voltage of roughly 2 kV and a current of 16 mA (discharge was controlled by the current value). With this new setup, such current needed a quite high voltage to obtain. Please note that the voltage mentioned hereafter does not refer to the voltage applied to the metallic needle. Indeed, between the power supply and the needle, there are 150 kΩ electrical ballasts.

- From the 20 to the 24 of January, we worked with voltage control discharge at 2.2 kV. Turning on the discharge, the current starts aroud 10 mA but decreases to a value between 1.5 and 3 mA.
- From the 24 of January to the 10 of February, we increased the voltage to 3.2 kV. Our goal was to recover the current value of the previous source - which was not a really good idea. We observed lightnings in the glass tube on a daily basis and a discharge in the helium tube on the 10th of February. This motivate us to decrease the voltage.
- From the 10th of February to the 20th of May, we worked still with voltage control of the discharge but with 1.5 kV in order to have more or less 5 mA. This was due to lightnings in the helium tube and the fact that we did not observed any atom number difference in the magneto-optical trap when varying the source current, as shown in Figure 118.
- On the 20th of May, the current of the discharged was around 2.8 mA for a voltage of 1.5 kV and stopped on its own twice. The voltage was increased to 1.85 kV in order to recover roughly 5.8 mA. From this day, the source discharge is under current control with 5 mA. One can see on the right graph of Figure 117 the variations of the voltage discharge.

Vintage 2024 feedbacks

After one year, the discharge stopped and we had to replace it. The source change took us roughly a month as we needed to open four times the source before having a stable situation. To make a long story short, here are the replacement we needed to do.

- We found that the plastic tube supplying helium was completely burnt at the connection with the Swagelok connector, requiring us to cut and reconnect it.
- We changed the skimmer that was heavily soiled, perhaps inhibiting current conduction. We replaced it with the original one (it was only changed once in the 30 y.o. life of the experiment)

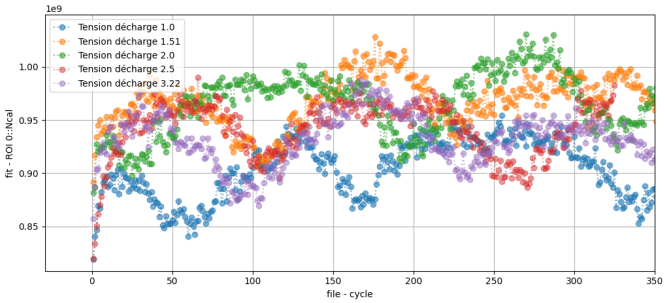

Figure 118: Number of atoms in the MOT as a function of time for different voltages. Each color matches a voltage of the source (in kV units). The current for each voltage from 1 kV to 3.2 kV are 3 mA, 5.7 mA, 8 mA, 10 mA and 13.6 mA. Oscillations are due to room temperature fluctuations - and bad MOT fiber injection and the the author does not guaranty the absolute number of atoms. See the Laboratory Journal of the 10/02/2023 for more information.

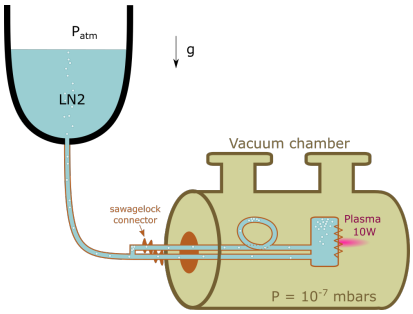

Figure 119: Possible scheme to bring LN2 to the experiment. A dewar of liquid nitrogen is placed above the experiment vacuum chamber and, thanks to gravity, pipes are full of liquid nitrogen. When the liquid vaporizes, it escapes from the top of the dewar which has a free surface with air. A possible issue with this scheme would be bubbles that might not be able to escape from the pipes because the slope is not constant. Note that it would be better to use a cold head in order to cool down as in Keller et al. (2014).

- We noticed that the plastic tube was positioned outside the three rods prevented the flange to complete its full course. We put it back inside.

3.B Liquid nitrogen cooling

3.C Water cooling of the experiment

The power dissipated by the magnetic trap is quite high: around 5 kW. Up to 400 A pass through diodes, IGBTs, and coils, which requires cooling them with chilled water. Our experiment room is connected to the cold water circuit managed by the “Infra” service of the Institut d’Optique. This circuit is common to all the laboratory’s experiment rooms and must remain closed. The laboratory rooms are in parallel: closing one valve does not prevent the other laboratories from being supplied. However, this means that one laboratory can short-circuit the others. I have not managed to get a clear answer on how the flow/pressure of the cold water circuit is managed.

Furthermore, we do not want to use the chilled water circuit to cool the magnetic trap coils. Indeed, the water may contain impurities that could clog the coils, whose inner diameter is .

Table VI.3: The first two measurements of the water flux were made with the open-loop water system. The pressure difference between the pump and the output of the coils was, therefore, the city water supply pressure plus the overpressure from the HVX pump. Since the installation of the chiller, the pressure difference is now only due to the HVX pump and is 8.5 bar, regardless of the water flux. To measure the flow-rate in each coil, the valves of the other are closed and the HVX pump is kept on. A flux meter allows to monitor the flux.

Date	Dipole (courbure)	Quadrupole (gradient)	Compensation	Total
Browaeys (1999)	4 l/min	2 l/min	4 l/min	n.c.
18/06/2020	2x1.9 l/min	2x1.2 l/min	2x1.9 l/min	10 l/min
09/02/2024	2x1.6 l/min	2x1.2 l/min	2x1.6 l/min	8 l/min
09/08/2024	2x1.4 l/min	2x0.9 l/min	2x1.4 l/min	7.5 l/min

Additionally, certain parts could cause redox reactions with other experiment rooms, which has already happened within the group[32] and caused a significant shutdown of the experiment. In December 2024, we installed a chiller to cool the magnetic trap coils. The chiller was bought from Eurodifroid, under reference ECH80AWI2RAC. Note that the chiller and its water level should be checked at least once a month. A 100 µm particle filter (RBM 126 filter 1" with 0.1 bar pressure drop at 2 m^3/h) was added to prevent blockages, for which the cartridge should be changed every 6 months. The water pump that circulates water in the magnetic coils is the HVX 15-bar pump, whose reference is given in Browaeys (1999). The water that flows in the magentic trap should be checked on a regular basis: Table VI.3 gives the waterflow that was measured when the trap was installed 30 years ago and the measurement performed in 2020. This measurement cannot be reproduced because the water-pressure is now lower[33]: it is only the 8.5 bar due to the HVX pump. The total water-flow of 8l/min should be checked regularly as it is now straight forward to look at it.

Our room is connected to the cold water circuit and is divided into two circuits: a "chiller" circuit and a "primary" circuit. It is represented on Figure 120. A pipe connects the chiller via 20 mm multiskin pipes installed in 2023. The other circuit is connected via plastic pipes of 16 mm installed in 2007, the year the building was created. This second pipe is connected to a manifold that allows the cooling of the various electrical devices in the experiment (Zeeman slower, diodes, pumps...).

The pipes that connect the chiller to the cold circuit are large because we fear that the flow might not be sufficient to cool the reservoir. A valve allows the regulation of the water flow coming from the institute's cold circuit. If this valve is fully open, the primary circuit is completely short-circuited. Its opening is a compromise between the cooling capacity of the chiller and the flow in the primary circuit. The flow in the primary circuit is measured using the water-meter installed on the Zeeman/IGBT/diode circuit. This flow-meter is routinely checked and should be around 3-4 L/min. A value below 2 L/min prevents to run the experiment with a stable BEC.

In September 2022, we encountered issues with the cooling of IGBTs and power supply diodes. To increase the water flow, we decided to connect the IGBTs in parallel. However,

[32] Note that the redox reaction that clogged the coils in Vincent Josse's experiment involved an aluminum part. In our experiment, all connections are copper (to my knowledge).

[33] The first two measurements of the water flux were made with the open-loop water system: the pressure at the input was the pressure of the water-city supply plus the pump while it is now only the pressure from the pump.

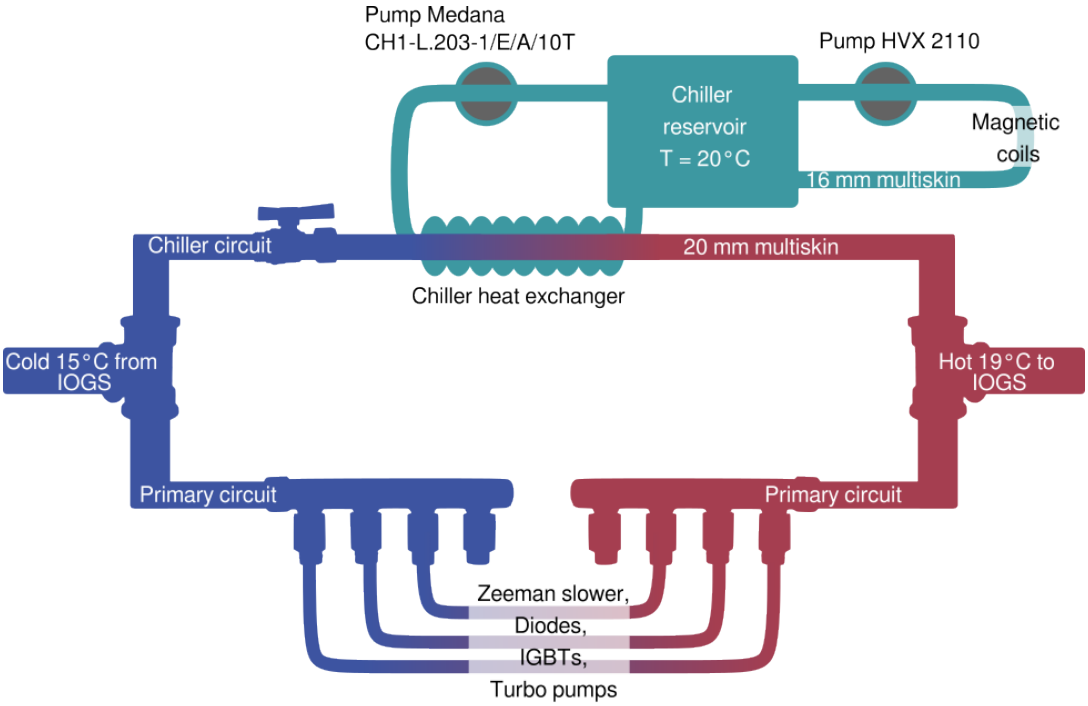

Figure 120: The chiller tank temperature is set by the user and should be above the temperature of the cold water circuit. To control the temperature of the tank, the machine acts on a servo valve that control the cold water circuit flux that passes through the heat exchanger. The water pump that circulates water in the magnetic coils is the HVX 15-bar pump, whose reference is given in Browaeys (1999). Note that the water drop due to the multiskin 16 mm pipes (10 m long) is estimated to be around 0.5 bar for a 10 L/min water flux and only 0.1-0.2 bar for the 20 mm model.

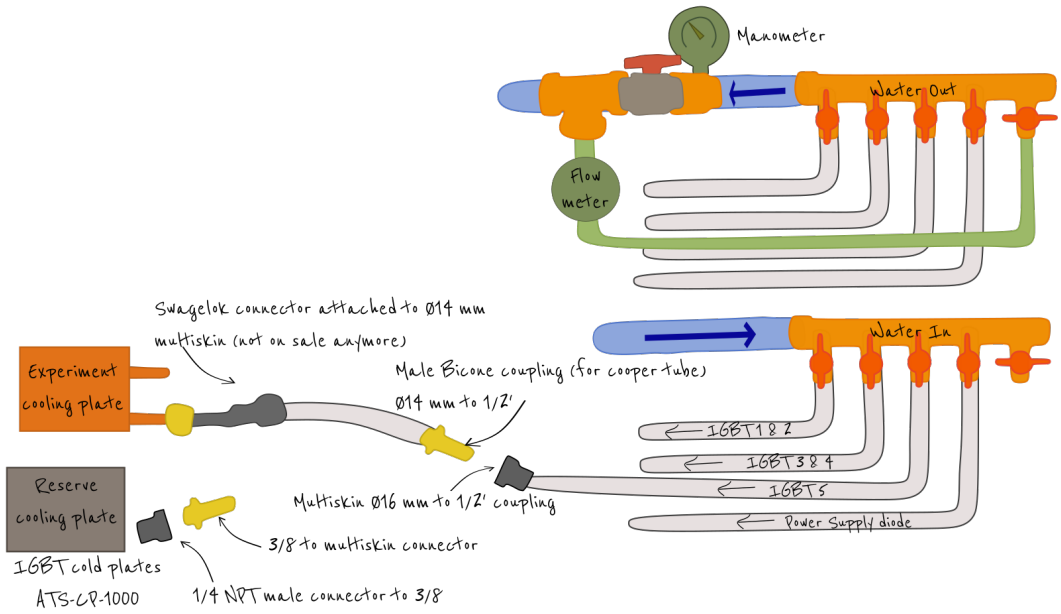

Figure 121: Watercooling apparatus. Note that we bought new cold plates for IGBTs that are available in the experiment room.

Table VI.4: IGBTs and diode water flux. One can see that the sum of individual water rate is clearly not equal to the water rate when all valves are open.

Date	Zeeman	IGBT 1&2	IGBT 3&4	IGBT 5	Diodes	Total (all open)
07/10/2022	2 l/min	2,6 l/min	2,5 l/min	2,4 l/min	2,2 l/min	4,6 l/min

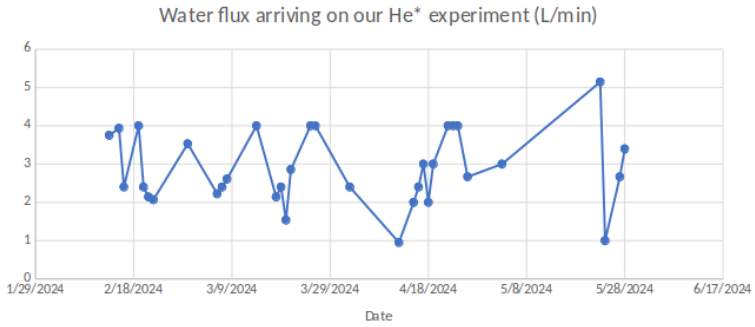

Figure 122: Evolution of the water-flow on the Zeeman/IGBTs/Diode branch of the cooling setup. A value below 2 means the experiment does not work well. Absence of measurement means that the water flux was not too low to carry an experiment.

the cooling pipes used in the experiment were Ø14 mm multiskin pipes, and this diameter is no longer a standard; we could not find any compatible connectors. Therefore, we modified our setup to use Ø16 mm multiskin pipes. Figure 121 provides information on the connectors used for this setup and Table VI.4 gives the water flows at different times. Sadly, this change of configuration did not improve enough the total water rate to avoid being distrub day to day. Nevertheless, it allows us at least to better monitor the water-flow rate.

3.D Optics

Dipole trap injection optics

The collimators that inject the laser beam from the "preparation" breadboard are 60FC-SMA-T-23-A-11-03 from Schäfter+Kirchhoff company, which means their focal length is 11 mm with 0.25 numerical aperture. We combine them to optical fibers supplied by NKT photonics that are connected to the High power SMA connector by Alpha Nov and cut at 5 degrees (this 5° cut angle is perpendicular to the polarization axis). Once connected, the polarization axis is indicated by the mark on the top of the fiber. On the collimator, the axis is perpendicular to the mark (faded edge on the part connected to the collimator's fiber): as explained by S+K, one should align the polarization axis with groove in the connector.

On Febrary 2023, when we changed the laser, we decided to install the S&K fiber collimators on mirror mounts. For this, we use Polaris mounts, which conveniently allows the collimator to be almost entirely inserted. To fit the collimator completely, I had to file down the small pins that hold the mirror (see Figure 123). The collimator is then secured with the top screw, just like a mirror. This way of holding the collimator is about a thousand times better than the previous method, where they were on solid supports. With this method, injection and fine adjustments are much easier and monthly adjustment too.

The following technique allows one to easily inject a fiber. It was suggested by Jan-Philipp

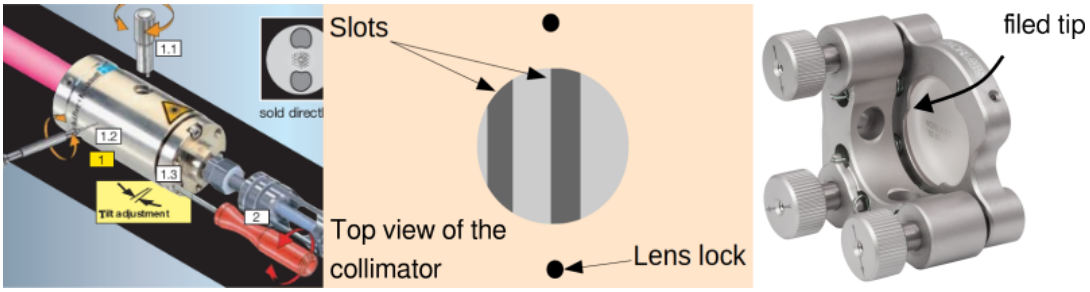

Figure 123: Sketch of the collimator. ©Left scheme from Schäfter+Kirchhoff and right picture from Thorlabs.

Bureik (2024).

- Install first a diaphragm in between the collimator and the last mirror to set up the vertical direction of the beam
- Without the fiber, make sure the beam goes through the collimator and observe a nice shape after the hole,
- With approx 100 mW of power, approach the fiber without plugging it totally. One should observe a bit of light at the output of the fiber.
- With small steps, kepp plugging gently the fiber in the collimator. You should never loose light at the output of the fiber. Adjust the injectoin by changing the rotation (polaris fiber coupling mount) and the translations screws (last mirror mount),
- Screw the fiber to the collimator, paying attention to the cut angle and optimize the output with the four screws.

Dipole trap waists: vertical beam

The vertical dipole trap was installed in 2010. Jaskula (2010) measured optically a waist of roughly 30 µm but then measured it to be 43 µm on the atoms (through parametric excitation). Bonneau (2011) reported also the value of 43(1.5) µm when measuring through parametric excitations. The difference between the optical measurement and atomic one is high but an explanation might be found. Indeed, when Perrier (2020) measured the waist of the horizontal beam optically, he realized that the camera was sensitive to the square of the intensity and not the intensity. In other words, it is a two photons process that excites the pixel. This means that the measured waist is too small by a factor $\sqrt{2}$ which would lead to $30\sqrt{2} \sim 42$ µm, in agreement with the waist measured on the atoms.
The optical setup was reinstalled by Perrier (2020) but without changing the vertical lens. He measured a value of 53 µm on the atoms (gravity compensation and parametric excitations) but expected also to measure a value closer to 40 µm[34]. Since that time, the dipole trap was realigned multiple time and the power meter used to calibrate the trap was not so reliable. Here we present the recent measurement of the waist by three means on the atoms (25/07/2024). The power of the dipole trap was calibrated with a new (and not burned) Thorlabs photodiode

[34] If the vertical trap is not purely vertical, it means that the effect of gravity is reduced by the cosinus of the angle. It means that for a fixed waist of the beam, a slightly tilted beam might compensate gravity where a purely vertical beam might not. This means that the apparent waist is smaller than the measured one. If the measured waist is larger, I would say that this was due to optical aberrations of the lens *i.e.* that the beam was not perfectly centered on the lens. Another uncertainty factor is due to the calibration of the power meter that was used to measure the power of the laser.

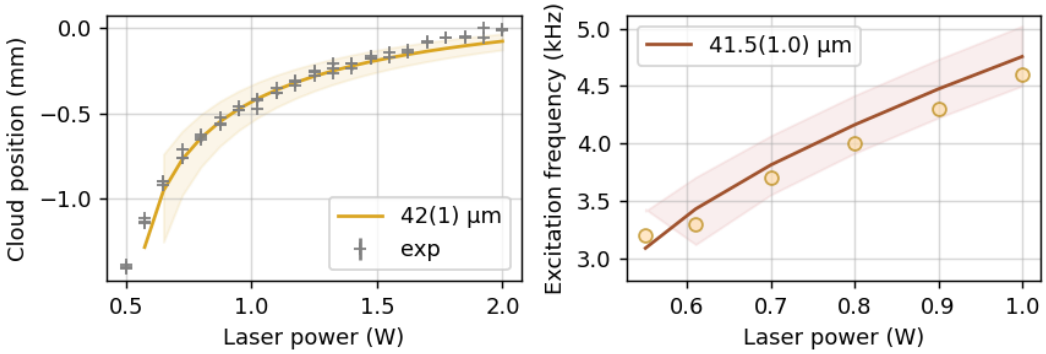

Figure 124: Measure of the waist by two different methods. Left: a snapshot of the cloud for various power gives access to the *in situ* position of the cloud. Data taken of February (25//2022). Right: excitation frequency of the breathing mode as a function of the laser power. Experimental points were extracted from various day, ranging from February 2022 to May 2024.

power sensor S132C that cannot measure more than 500 mW. Power above this value are extrapolated.

Measure by imaging the cloud's position and gravity: we load a dipole trap and decrease the power up to a final value. Because of gravity, when the power of the beam decrease, the minimum of the total potential is shifted down. Here, we decrease the power of the laser beam, let the cloud expand for 1 ms and take a snapshot (emission imaging). We then adjust the density profile of the cloud with a Gaussian function to obtain its position.
Results: On the left panel of Figure 124, the vertical position of the cloud is plotted as a function of the vertical beam power. The experimental points are fine-tuned by a waist of 42.5(3)µm which is in agreement with the expected waist.

Measure with parametric excitation: this method consists of modulating the intensity of the dipole trap at a given frequency. When the frequency of excitation is equal to twice the transverse frequency, the breathing mode is excited (Chevy et al., 2002). When the excitation amplitude is quite high: typically a fraction of the final power, the system is excited in a quite a "violent" way, heating occurs and the width of the detected cloud is increased (Lopes, 2014). We expect also to detect fewer atoms. However, we sometime detect more atoms at resonance: this is due to the fact that the width of the BEC increased. The atomic flux is therefore lower, which increases the *detected* atom number due to the saturation of the MCP. Note however that this breathing mode frequency is $2\omega_\perp$ only for a elongated trap: in the case of a spherical trap, its frequency is $\sqrt{5}\omega$ (Stringari, 1998).
Results: the excitation frequency is plotted as a function of the vertical power on the right panel of Figure 124. We adjust this curve with a theoretical waist of 41.5(1.0) µm. Note however that the experimental points that are reported here were extracted from different days (over a year and a half) and measured in different conditions (four different days). The power of the trap was not always really well calibrated due to a defective power-meter and a photodiode drift that was fixed recently.

Measure with gravity compensation: the single vertical dipole trap does not compensate gravity for all powers. At a threshold power, it will not be able to still trap atoms. The MCP detects a really low number of atoms and therefore allows identifying such power. Here we evaporate in the single vertical trap, for different power and look for the atomic signal on the

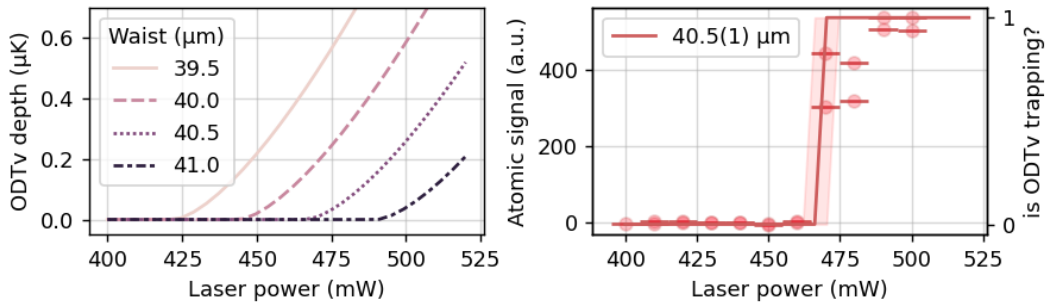

Figure 125: Left: horizontal dipole trap optical setup. The beam expander was installed on January 2024 and bought in 2017 from Acal BFI. Right: optical measurement of the waist of the horizontal dipole trap for a 1.5 magnification factor (top raw) and 2 (bottom row). The measurement was carried using a Gentec Beam profiler and are reported n triangle green (Y) or diamond yellow (X) for which the minimal measured waist is reported in the legend. The fit assumes a Gaussian beam: the important uncertainty associated to the fit reflects the fact that the waist longitudinal evolution is not proper. For a Gaussian beam with initial waist of 108 μm, we expect a 71 μm and 54 μm waist respectively for the 1.5 and 2 magnification factor. Data taken on the 05/02/2024.

MCP as a function of power. On the left panel of Figure 125 is shown the depth of the trap as a function of the laser power. Each curves shows the depth for different waist. The power at which the trap stops compensating gravity is the point where its depth null. The knowledge up to 10 mW of the threshold for which gravity is not compensated provides a measurement with a precision of 0.2 μm on the waist.
Results: the number of atoms as a function of the laser power is shown on the right panel of Figure 125. Each dots represents a single measurement. The red line shows if a dipole trap widh 40.5±0.1 μm still compensates gravity. Its value is 1 if yes, 0 if not. Its y-axis is represented on the right y-axis of the plot. Experimental points are separated by 10 mW, which gives the ability to determine the waist up to 0.2 μm. The horizontal errorbars are due to the calibration curve. The final uncertainty on this measurement is estimated to 0.2 μm.

Results We therefore measured with 3 different techniques the waist of the vertical laser beam. The gravity compensation one predicts a 40.5 μm with a precision of 0.2 μm. The 41(1) μm waist measured with parametric excitation should be taken with caution as it relies on dataset that were taken at quite different periods. Its value is in agreement with the waist measure with other techniques. However, the waist we measure by imaging the cloud *in situ* and evaluating its position due to gravity is not in agreement with the first techniques, even though this is not a $3-\sigma$ difference. A source of uncertainty not taken into account here is the calibration of the camera that was not really well done. Another explanation to this discrepancy is the presence of an unknown magnetic field gradient that could affect the trapping potential at really low power and changing the gravity gradient.

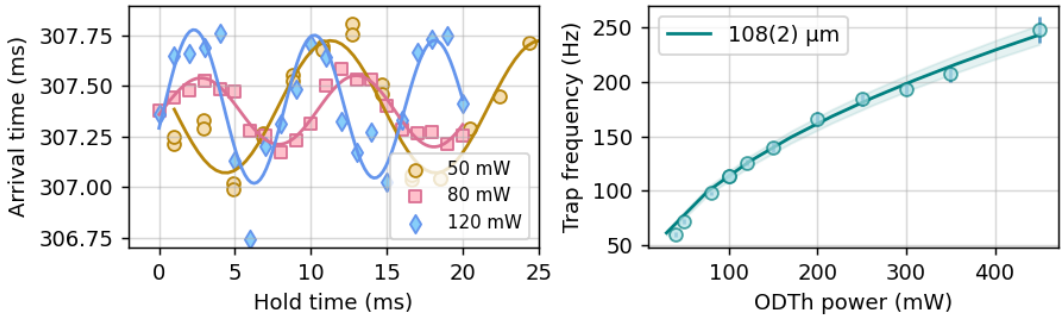

Figure 126: Measure of the waist of the horizontal beam. Left: after a quench, the BEC oscillates in the trap. Its arrival time exhibits the same oscillation frequency. Each symbols corresponds to a different laser trap. The line is a sine fit of the experimental data from which we extract the frequency of the trap, which is the same than the frequency of the atoms. Right: the trap frequency as a function of the laser power. The solid line is adjusted to the experimental data that gives a waist of 108(2) µm.

Dipole trap waists: horizontal beam

The waist of the horizontal beam was measured optically by two methods by Perrier (2020) who reported 107(3) µm and 110(4) µm. We report in this subsection that we measured 108(2)µm in agreement with his measures. The measurement was performed measuring the trap frequency for several powers: we then adjusted the theoretical curve with the waist as a free parameter. The trap frequency is measured by exciting the cloud in the first collective oscillation of the BEC (Stringari, 1996).

Protocol: we produce a BEC in the cross dipole trap (400 mW, 30 mW) respectively for the vertical and horizontal trap beams. At $t = 0$, we quench the horizontal beam power to a different power. We then hold the cloud in the trap for different durations. For each hold time, we record the arrival time of the cloud measuring the atomic flux on the MCP with an oscilloscope. Indeed, the horizontal laser beam is responsible for the vertical confinement. We observe the arrival time to oscillate as a function of the hold time in the trap as shown on the left panel of Figure 126. We fit the signal to get the frequency of the oscillation, which corresponds to the frequency of the trap. The measurement is repeated for different laser powers: Figure 126 shows the trap frequency as a function of the power of the laser.
Result: We adjust the waist of the trap to coincide the experimental data. This gives a value of 108(2) µm for the waist of the horizontal beam. This value is consistent with the value reported by Perrier (2020).

We also installed a beam expander on the experiment in January 24. The idea is to allow one to decrease the vertical confinement (the shallow axis) and therefore change the mode size to be less sensitive to center of mass fluctuations. In the right panel of Figure 127, we report the optical measurement of the waist of the horizontal beam. Measurement was performed using a Gentec beam profiler and the fit was double-check with a 2D home-made fit program.

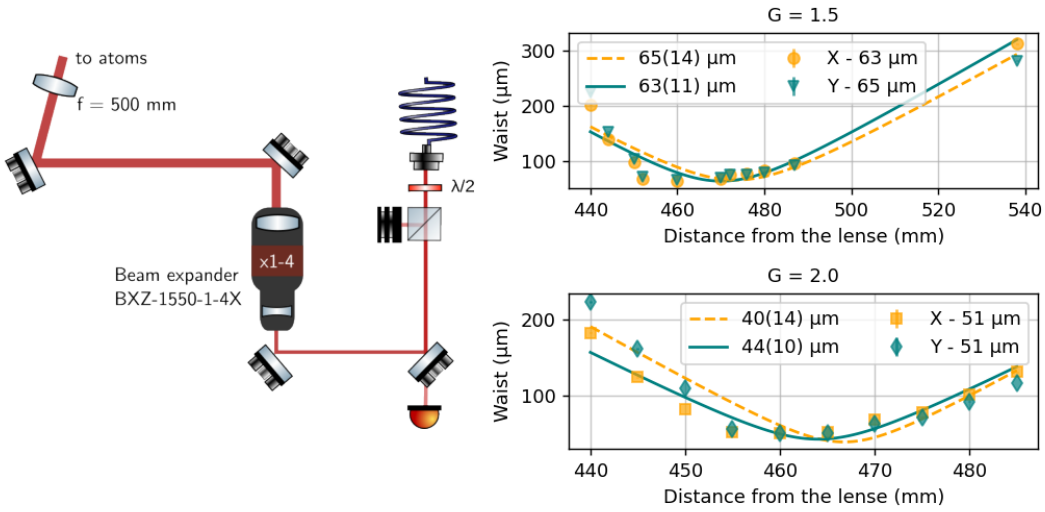

Figure 127: Left: horizontal dipole trap optical setup. The beam expander was installed on January 2024 and bought in 2017 from Acal BFI. Right: optical measurement of the waist of the horizontal dipole trap for a 1.5 magnification factor (top raw) and 2 (bottom row). The measurement was carried using a Gentec Beam profiler and are reported n triangle green (Y) or diamond yellow (X) for which the minimal measured waist is reported in the legend. The fit assumes a Gaussian beam: the important uncertainty associated to the fit reflects the fact that the waist longitudinal evolution is not proper. For a Gaussian beam with initial waist of 108 µm, we expect a 71 µm and 54 µm waist respectively for the 1.5 and 2 magnification factor. Data taken on the 05/02/2024.

Bragg alignement

The procedure to align the Bragg beams follows:

1. The Bragg beam should be visible with the infrared viewfinder : one beam should illuminate the bottom of Zeeman slower outpout bulge, the other the top.

2. The polarization are then turned by 45° from π to $\sigma^{-/+}$. The magnetically trapped cloud is shined typically for a few ms with a few mW. The number of atoms should drop as the beam allows the atoms to go from the trapped $m = 1$ state to the untrapped $m = 0$ state via spontaneous emission. This first alignment is performed separately for each beam and we work with the camera to assess the atom number in the cloud.

3. We now work with both beam with a π polarization and detect atoms with the MCP. We produce a BEC, release it and shine it with both laser. We then scan the duration of the Bragg pulse to observe a Rabi oscillation. The idea is to maximize the Rabi frequency as it is proportional to the product of the two beams intensity. An example is given in fig Figure 128, on the right where we plot the relative population between $|p = 0\rangle$ and $|p = \hbar k_b\rangle$ as the function of the duration of the pulse. Here, for each sequence represented by the color and style of the curve, we turn a screw. The alignment in sequence 45 (red dashed dotted) is better than in sequence 41 (solid blue).

4. Once the beam are centered on the atoms, one should check if the Bragg momentum is well aligned on the vertical axis with a Ramsey interferometer. To do so, we produce a

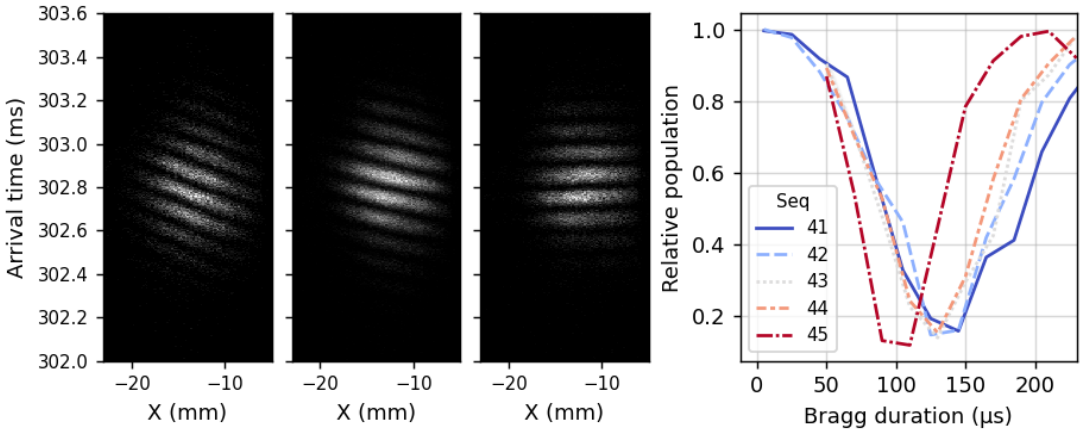

Figure 128: Left: Ramsey interference pattern when the beam is badly aligned (left) and better aligned (right, but yes, still not perfect). Right: Rabi oscillation for different sequences. At each sequence, a screw is turned to check if the Rabi frequency increases. Here we showed the begining of the Rabi oscillation but it is better to scan on the second arch as the difference between two frequencies is visible faster.

BEC. After 1 ms, we perform a first $\pi/2$ pulse and a second one, delayed by $\Delta t \sim 2.5$ ms. The two coherent cloud that were transferred by the first and then the second overlap and interfere due to gravity. The vertical interference period writes $2\pi/k_b g\tau$ (Leprince, 2024) and the fringes should be only along the vertical axis. If not, one of the mirror should be displaced macroscopically (a translation of the mirror mount and not a rotation with the screws) and the alignment procedure started back from step 1.

The left panel of Figure 128 represents three interference patterns. On the first picture, we clearly see that the fringes are tilted along X. One of the mirror was then unscrewed from its tie bar and moved by a few mm in the tilt angle direction. In the case where the fringes are tilted on the X direction, one of the mirror should be displaced along the horizontal. The two other pictures represent the interference pattern while iterating over the (boring) alignment procedure. Note that this method is really sensitive as the final relative angle were estimated to 0.08(3)° along X and 0.04(2)° along Y (Leprince, 2024).

4. Reconstruction and correlation codes

We developed our codes in a team project called heliumtools that can be installed as a python package. I will describe in the following how codes work and the choices that was made for computation speed.

4.A Correlations and data analysis

At the end of an experiment, we obtain a list of unique atoms at a given position in momentum space. When probing the normalized correlation function $g^{(2)}$ of two modes 1 and 2, the normalized variance $V_{1,2}$ and the Cauchy-Schwarz ratio $C_{1,2}$ are defined as

$$g^{(2)}_{1,2} = \frac{\langle : n_1 n_2 : \rangle}{\langle n_1 \rangle \langle n_2 \rangle}, \quad \xi_{1,2} = \frac{\mathrm{Var}(n_1 - n_2)}{\langle n_1 \rangle + \langle n_2 \rangle}, \quad C_{1,2} = \frac{g^{(2)}_{1,2}}{\sqrt{g^{(2)}_{1,1} \times g^{(2)}_{2,2}}}. \tag{235}$$

where the n refers to the mode population, the dots : to normal order and the variance of the population difference is $\mathrm{Var}(n_1 - n_2) = \langle (n_1 - n_2)^2 \rangle - \langle n_1 - n_2 \rangle^2$. Note that the brackets means *average value* hence it will be in the following be interpreted as *average over cycles*. When studying correlations, it is therefore possible to select two modes and compute the above quantity. However, in order to increase the signal to noise ratio, it can be better to average over modes in a selected region. In our experiment, we know *where* we create pairs, i.e. there position in momentum space is well defined, making possible to study the correlations between those two modes. However, it is possible to average over a wide range of modes in the system and then compute the integrated correlation function. In the following of this section, we will introduce both approaches, the first one being *momentum resolved correlations* as it keeps trace of the momentum of the considered modes, the second one being *momentum integrated correlations*. As we shall see, the first one ables to enhance Cauchy-Schwarz violation and/or sub-shot-noise variance, mode number statistics, while the second one allows a better estimation of the second order correlation, its height and width, and to reveal the Hanbury, Brown and Twiss effect (Jeltes et al. (2007)).

4.B Momentum integrated correlations

Presentation of the $G^{(2)}$ calculation After applying the 1064 nm optical lattice for less than a ms, we end up with two correlated beams (Bonneau et al. (2013)) A and B, composed of several modes in the longitudinal (z) and transverse direction (x and y). The idea of this method is to quantify the number of atomic pairs and the bosonic bunching : considering we have an atom located in $\vec{k}$ what is the probability to get an other atom near this atoms $(\vec{k} + \delta\vec{k})$ or opposite to this atom $(-\vec{k} + \delta\vec{k})$. To do so, we compute the 3D histogram of the momentum difference between. This gives access to the (non-normalized) second-order correlation function $G^{(2)}$. This function is however proportional to the density and does not captures efficiently what we study : bosonic bunching and anomalous correlations.

So far, we have only the non-normalized correlation function G hence one must normalized it with respect to density to obtain the normalized corelation function. To do so, we repeat Program 129 taking uncorrelated atoms, i.e. atoms from different cycles. Using the notations above, this means that `atom_j` should be taken from all other cycles than the cycle of `atom_i` (Schellekens, 2007; Ténart, 2021). Considering that we have N_{at} atoms per shot and N_{shot} shots, the complexity of the numerator calculation is $N_{at}^2 N_{shot}$ while the complexity of the denominator is $N_{at}^2 N_{shot}^2$. A way to decrease the complexity of the denominator is to normalize with only a fraction of the remaining shots or even to use only one other shot. I tried the later but the noise from the denominator was too important. Taking also a fraction of the cycles can be done but this does not change the complexity (even though it does decrease the calculation time which in practice is useful).

```
sx, sy, sz = 1,1,0.1 # definition of the resolution on each axis
G = initialize_voxel_map()
for cycle in all_cycles:
    for atom_i in cycle.get_atoms_list():
        for atom_j in cycle.get_atoms_list():
            if atom_j != atom_i:
                (dkx, dky, dkz) = atom_j.get_momentum() -/+
                ↪  atom_i.get_momentum()
                G[dkx/sx][dky/sy][dkz/dz] += 1
```

Figure 129: Pseudo-code of the construction of the three dimensional second order correlation function $G^{(2)}$. In this code, the voxel map G is a three-dimensional list. To populate the histogram, we iterate through all cycles, calculating the momentum difference between each pair of atoms. The requirement to ensure that both atoms are distinct reflects the normal ordering in the definition of the second-order correlation function. In other terms, this condition ensures that we do not correlate an atom with itself. The -/+ depends on the correlations one wants to probe : either local correlation (− for bosonic bunching) or cross-correlation (+ opposite momentum correlation). In this program, the parameters are the width of the voxel σ that should be narrow enough in order to visualize correlations *i.e.* they must be much smaller than the correlation length.

Implementation of the code I will turn now into a more detailed presentation of the code itself and the tools used. As Python is neither a compiled program like C or Fortran nor a pre-compiled program like Matlab, it is highly inefficient with `for` loops and one needs to find the best module that can carry the calculation. Let's reformulate what we are trying to compute : for a given cycle, we have a list of all atoms momentum in 3D $\{\vec{k}_i\}$ of size N_{at} and the list of all other atoms momentum $\{\vec{k}_j\}$ of size $N_{at}N_{shot}$. The first operation is to perform the cross product in order to get all $(\vec{k}_i, \vec{k}_j)$ couples and then to do the 3D histogram of the $\{\vec{k}_i - \vec{k}_j\}$ distribution. Typically, the number of atoms per shot is around 100 and the number of shots is a few thousands.

The cross product between the two lists $\{\vec{k}_{i,j}\}$ can be achieved with pandas merge, torch cartesian product or itertools methods while the 3D histogram can be achieved with numpy or torch histogramdd methods. Note that given the resolution of the MCP and the range of our data, we could work with 16 bits integers. Figure 130 represents the computation time needed to perform the cartesian product operation (left) or the 3D histogram (right) as a function of the number of cycles. One can see that the longest operation here is the cross product and I noted also that the instantaneous memory usage is much bigger that the resulting array. The better module to perform both operations is the torch module.[35]

[35]The quite poor performances of the numpy module led to the development of the fast-histogram module but that tackles only 1D and 2D histograms and the pytorch module by the CERN as explained here.

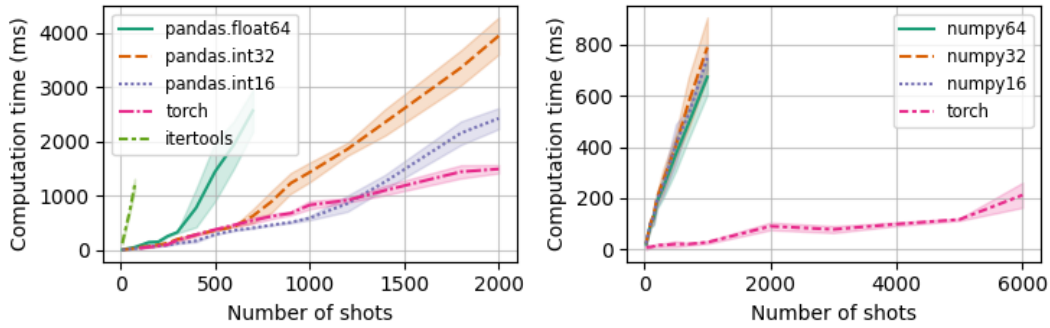

Figure 130: Comparison of the different modules performance with cartesian product (left) and 3D histogram (right) as a function of the number of shots N_{shots}. For a given module function, we compute the time it takes to perform the cartesian cross product of an array of size N_{at} and an array of size $N_{at} \times N_{shots}$. For the pandas module, this time strongly depends on the data type. For the 3D histogram calculation we represent the time it takes to perform the histogram with an initial array of size $N_{at}^2 \times N_{shots}$, returned by the cartesian product function. The computation time is performed 10 times for each curve and the shaded region represent the standard deviation over the 10 measurements. Here $N_{at} = 100$, using a - not anymore standard - 10 years old computer machine with 8Gb RAM.

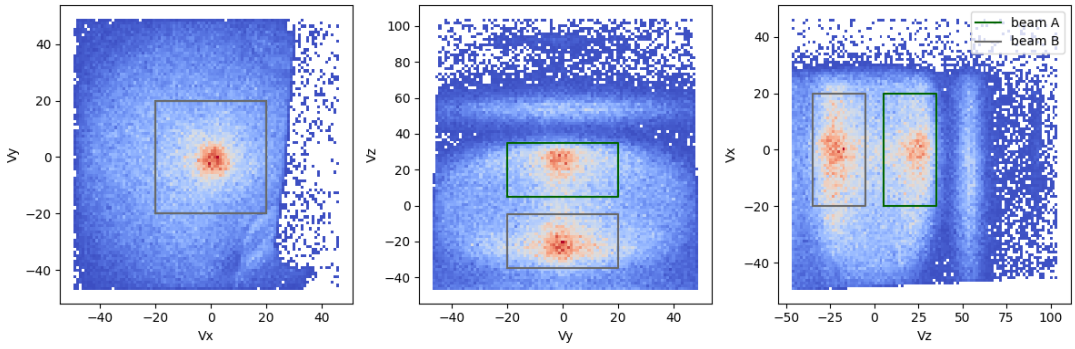

Figure 131: Two dimensional plots of the density of atoms. The two beams A and B are represented with the green and gray rectangles. Pairs produced with the 1083 nm laser in February 2024.

Practical description of the code Following the notation introduced by Lopes (2014) , we consider two beams A and B, represented by the green and brown rectangles region of interest in Figure 131. One must then defined the properties of the so-called *voxel map*, defined by the number of voxels in each axis and the voxel size. The later represent the ultimate precision that can be reach for a given axis. In order to emphasize the correlation amplitude, this length must be much smaller than the correlation length. Calling the `compute_correlations` method will define the `result` table that contains for each voxel $\delta\vec{v}$ the number of nearby pairs (`G2AA`, `G2BB` for each beam) and opposite pairs (`G2AB`). The quantity `result['G2AB'][0,0,0]` is therefore the number of opposite momentum pairs in the central voxel $\delta\vec{k} = 0$. When we represent the one-axis (say `z`) integrated correlation function, we define an integration volume along the two other directions (say `dx, dy`). The normalized correlation function is then simply given by `g2[z]=G2AB[-dx:dx, -dy:dy, z]/G2AB_denom[-dx:dx, -dy:dy, z]`.

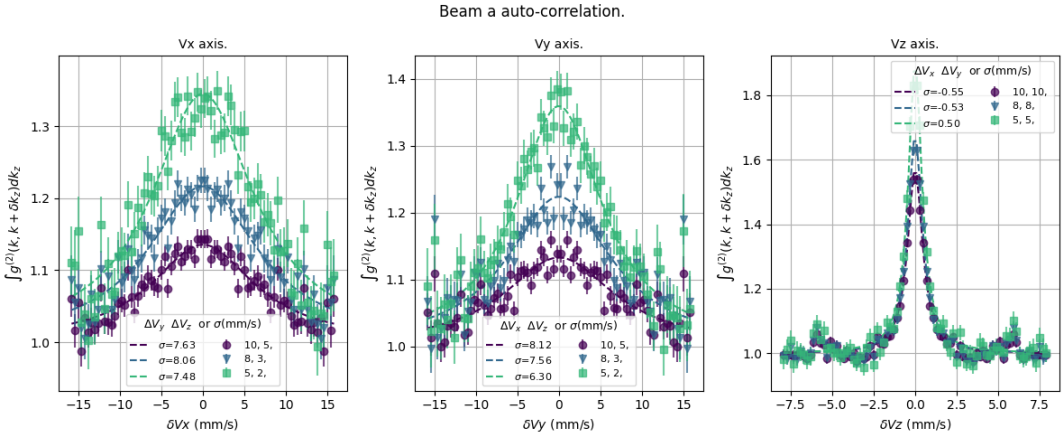

Figure 132: One dimensional integrated second order correlation function along x, y and z axis. For each curve (marker and color), the integration size along the two other dimensions is changed (see legend). One can see that the smaller the transverse integration is, the higher is the amplitude. If the Gaussian-fitted width of the correlation does not depend on the transverse integration, this would means that the correlation function is separable. On this dataset, it seems that this is the case (seems the case on this example). The fit function is lorentzian and error bars are obtained with bootstrapping. ®Data obtained in May 2022.

Bootstrapping The bootstrapping method enables estimation of the standard deviation of a sample using resampling with replacement. The idea is to resample with replacement and to recompute the quantity of interest with this new sample. One has then to recompute this quantity of interest $\{A_i\}$ N times and then study the probability distribution of the A_i. The width of the distribution gives the uncertainty deviation of the associated observable A. With this method, one can see that computing the denominator with a re-sampled sample is problematic as one might correlate an atom with itself, leading to 1. an obvious divergence of the denominator at $\delta\vec{k} = 0$ and 2. an HBT effect for the nearby atoms. For that reason, we do not evaluate the error on the denominator[36].

Momentum resolved correlation

At the end of an experiment, we obtain a list of three-dimensional speeds of an atom, and we must determine which mode(s) we want to examine—specifically, its size and position. We refer to such a region of momentum space as a *box* in the following. In the current version of the code, a box is represented as a dictionary that includes either its position and size or its boundaries along different directions[37].

[36]The denominator noise is really low with respect to the numerator. Indeed, the denominator calculation involves $N_{shots}^2 N_{at}^2$ terms while the numerator contains only $N_{shots} N_{at}^2$ terms.

[37]The format of a box matches the expected format of a Region of Interest (ROI) defined in the tools file of the package. It should be a dictionary whose keys are the axes of the ROI. The element can be either a list or a dictionary. A list will define the maximum and minimum boundaries of an ROI, while the dictionary can also define position and size.

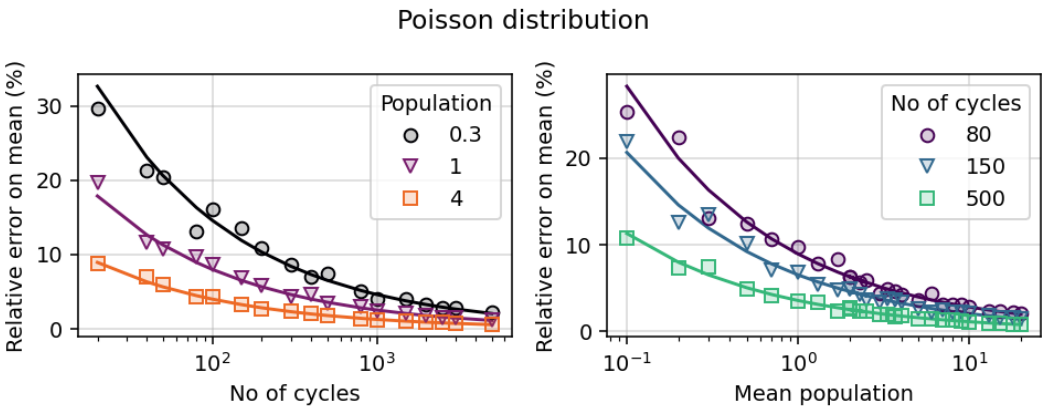

Figure 133: Relative error on the mean of a poisson distribution as a function of the number of cycles (left) and the population (right). The solid curves are given by equation (237) with no adjustable parameter.

4.C Errors on the particle number of a thermal and poisson distribution

The particle probability distribution of a thermal state follows the geometrical law

$$P_{th}(n) = \frac{\nu^n}{(1+\nu)^{n+1}} \tag{236}$$

where ν is the mean population. Especially, the mean associated to this distribution is $E_{th}(\nu) = \nu$ and the variance is $\mathrm{Var}_{th}(\nu) = \nu^2 + \nu$. This should be compared to the poissonian statistics with mean ν for which $P_{poi}(n) = \nu^n e^{-\nu}/n!$ hence $\mathrm{Var}_{poi}(\nu) = \nu$. For low populations ($\nu < 1$), the thermal and Poissonian distribution exhibits a similar variance as one can neglect ν^2 compared to ν. On the opposite, when the population is larger, the width of a thermal distribution is larger than the one of a Poissonian distribution. In particular, the standard deviation of the mean number of particle is equal to the mean. Such fluctuation of the particle number is a characteristic of thermal state, as we saw in the second chapter. When drawing randomly n samples from a thermal distribution, the standard deviation associated to the particle number is expected to be large. Does this mean that the uncertainty associated to the mean is large ?

Protocol: To answer this question, we randomly draw a sample with N_{cycle} elements from a thermal (respectively a poisson) distribution with a mean ν. We compute the absolute difference between the mean of the distribution $\bar{n}$ and the expected mean ν. We repeat this 100 times and compute the mean absolute error $\delta\bar{n} = \overline{|\bar{n} - \nu|}$. The relative error $\delta\bar{n}/\nu$ depends both on the theoretical population ν and the number of cycles N_{cycle}.

Results: The relative error $\delta\bar{n}/\nu$ is shown on Figure 133 for the Poissonian distribution and on Figure 134 for the thermal distribution. On the left panel is shown the relative error in percent as a function the number of cycles for three different populations (0.3, 1 and 4). On the right panel, it is shown as a function of the mean population. Note also that the dispersion of the relative error is of the order of the error: if one adds error bars on the graph, their size would be equal to the amplitude of the point.

We first consider the poisson distribution, shown on Figure 133, as a sanity check. On the left panel, we observe that the relative error $\delta\bar{n}/\nu$ scales with $\sqrt{N_{cycle}}$, and on the right panel, the relative mean error also scales with the square root of the population. The solid curves are

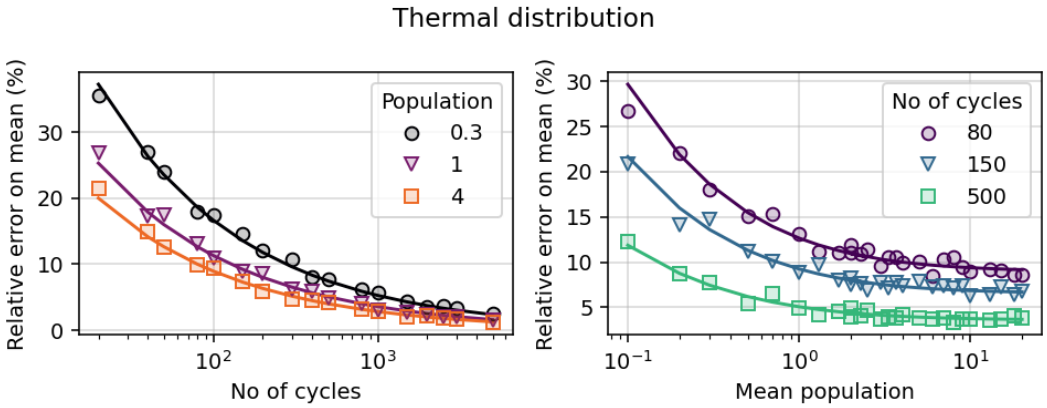

Figure 134: Relative error on the mean of a thermal distribution as a function of the number of cycles (left) and the population (right). The solid curve are given by equation (238) with no adjustable parameter.

given by the following formula, with a heuristic 0.8 prefactor and no adjustable parameter

$$\delta\bar{n}_{poi} = \frac{0.8\sqrt{\nu}}{\sqrt{N_{cycle}}}. \tag{237}$$

We now focus on Figure 134 and the thermal distribution. On the left panel, the relative error on the mean still scales with the square root of the number of shots $\sqrt{N_{cycle}}$. However, on the right graph on which the error is shown as a function of the mean population, we observe two slopes. For low population, the slope is similar to that of the Poissonian distribution. For higher populations however, the relative error is much higher than in the poisson case. This can be expected as the dispersion associated to the thermal distribution is ν while it is only $\sqrt{\nu}$ for the poisson distribution. As shown in Figure 134, data are well-adjusted by the following formula,

$$\delta\bar{n}_{th} = \frac{0.8\sqrt{\nu^2+\nu}}{\sqrt{N_{cycle}}} \tag{238}$$

i.e. the standard deviation divided by the square-root of the sample size, with an overall 0.8 factor.

Glossary

- **BdG** : Bogoliubov-de Gennes
- **BEC** : Bose-Einstein Condensate
- **CMB** : Cosmic Background Radiation
- **CFD** : Constant Fraction Discriminator
- **CSI** : Cauchy-Schwarz Inequality
- **DCE** : Dynamical Casimir Effect
- **DL** : Delay Lines
- **FPGA** : Field-Programmable Gate Array
- **GP** : Gross-Pitaevskii
- **gPPT** : Generalized Positive Partial Transpose, parfois noté (g)PPT
- **IGBT** : Insulated-Gate Bipolar Transistor
- **LN** : Logarithmic Negativity
- **MCP** : Micro-Channel Plate
- **MOT** : Magneto-Optical Trap
- **ODT** : Optical Dipole Trap
- **PPT** : Positive Partial Transpose
- **qBEC** : quasi Bose-Einstein Condensate
- **QFTCST** : Quantum Field Theory in Curved Space Time
- **RF** : Radio Frequency
- **SSR** : Superselection Rule
- **TDC** : Time-to-Digital Converter
- **TF** : Thomas-Fermi
- **TMS** : Two-Modes Squeezed State
- **TMSth** : Two-Modes Squeezed Thermal State
- **TOF** : Time-of flight
- **UV** : Ultraviolet

Bibliography

Adamek et al. (2013) - Adamek, J., Busch, X., and Parentani, R. Dissipative fields in de Sitter and black hole spacetimes: Quantum entanglement due to pair production and dissipation. *Physical Review D*, 87(12):124039, 6 2013. URL.

Adesso and Datta (2010) - Adesso, G. and Datta, A. Quantum versus Classical Correlations in Gaussian States. *Phys. Rev. Lett.*, 105(3):030501, 7 2010. URL.

Adesso et al. (2004) - Adesso, G., Serafini, A., and Illuminati, F. Extremal entanglement and mixedness in continuous variable systems. *Physical Review A*, 70(2):022318, 8 2004. URL.

Adesso et al. (2014) - Adesso, G., Ragy, S., and Lee, A. R. Continuous Variable Quantum Information: Gaussian States and Beyond. *Open Systems Information Dynamics*, 21(01n02):1440001, 6 2014. URL.

Agullo et al. (2022) - Agullo, I., Brady, A. J., and Kranas, D. Quantum Aspects of Stimulated Hawking Radiation in an Optical Analog White-Black Hole Pair. *Physical Review Letters*, 128(9):091301, 2 2022. URL.

Allemand et al. (2024) - Allemand, M., Jannin, R., Dupuy, G., Bureik, J.-P., Pezzè, L., Boiron, D., and Clément, D. Tomography of a Spatially Resolved Single-Atom Detector in the Presence of Shot-to-Shot Number Fluctuations. *PRX Quantum*, 5(4):040324, 11 2024. URL.

Amodjee (2020) - Amodjee, Z. Création et caractérisation de paires d'atomes corrélées: vers des tests de la mécanique quantique. Université Paris-Saclay. 2020. URL.

Anderson et al. (1995) - Anderson, M. H., Ensher, J. R., Matthews, M. R., Wieman, C. E., and Cornell, E. A. Observation of Bose-Einstein condensation in a dilute atomic vapor. *science*, 269(5221): 198–201, 1995.

Andrews et al. (1997) - Andrews, M. R., Kurn, D. M., Miesner, H.-J., Durfee, D. S., Townsend, C. G., Inouye, S., and Ketterle, W. Propagation of Sound in a Bose-Einstein Condensate. *Physical Review Letters*, 79(4):553–556, 7 1997. URL.

Arvind et al. (1995) - Arvind, Dutta, B., Mukunda, N., and Simon, R. The real symplectic groups in quantum mechanics and optics. *Pramana*, 45(6):471–497, 12 1995. URL.

Aspect et al. (1981) - Aspect, A., Grangier, P., and Roger, G. Experimental Tests of Realistic Local Theories via Bell's Theorem. *Physical Review Letters*, 47(7):460–463, 8 1981. URL.

Aspect et al. (1982a) - Aspect, A., Dalibard, J., and Roger, G. Experimental Test of Bell's Inequalities Using Time- Varying Analyzers. *Physical Review Letters*, 49(25):1804–1807, 12 1982a. URL.

Aspect et al. (1982b) - Aspect, A., Grangier, P., and Roger, G. Experimental Realization of Einstein-Podolsky-Rosen-Bohm *Gedankenexperiment* : A New Violation of Bell's Inequalities. *Physical Review Letters*, 49(2):91–94, 7 1982b. URL.

Barbosa et al. (2011) - Barbosa, F. A. S., De Faria, A. J., Coelho, A. S., Cassemiro, K. N., Villar, A. S., Nussenzveig, P., and Martinelli, M. Disentanglement in bipartite continuous-variable systems. *Physical Review A*, 84(5):052330, 11 2011. URL.

Bardeen et al. (1957) - Bardeen, J., Cooper, L. N., and Schrieffer, J. R. Theory of Superconductivity. *Physical Review*, 108(5):1175–1204, 12 1957. URL.

Bardou et al. (1992) - Bardou, F., Emile, O., Courty, J.-M., Westbrook, C. I., and Aspect, A. Magneto-Optical Trapping of Metastable Helium: Collisions in the Presence of Resonant Light. *Europhysics Letters (EPL)*, 20(8):681–686, 12 1992. URL.

Barroso et al. (2022) - Barroso, V. S., Geelmuyden, A., Fifer, Z., Erne, S., Avgoustidis, A., Hill, R. J. A., and Weinfurtner, S. Primary thermalisation mechanism of Early Universe observed from Faraday-wave scattering on liquid-liquid interfaces. 7 2022. URL.

Béguin et al. (2022) - Béguin, A., Rodzinka, T., Vigué, J., Allard, B., and Gauguet, A. Characterization of an atom interferometer in the quasi-Bragg regime. *Phys. Rev. A*, 105(3):033302, 3 2022. URL.

Belgiorno et al. (2010) - Belgiorno, F., Cacciatori, S. L., Clerici, M., Gorini, V., Ortenzi, G., Rizzi, L., Rubino, E., Sala, V. G., and Faccio, D. Hawking Radiation from Ultrashort Laser Pulse Filaments. *Phys. Rev. Lett.*, 105(20):203901, 11 2010. URL.

Beliaev (1958) - Beliaev. Energy spectrum of a non-ideal Bose gas. *Sov. Phys.-JEPT*, 7(2):299, 8 1958.

Bell (1964) - Bell, J. S. On the Einstein Podolsky Rosen paradox. *Physics Physique Fizika*, 1(3): 195–200, 11 1964. URL.

Benatti et al. (2020) - Benatti, F., Floreanini, R., Franchini, F., and Marzolino, U. Entanglement in indistinguishable particle systems. *Physics Reports*, 878:1–27, 9 2020. URL.

Berkowitz and Garner (1970) - Berkowitz, S. and Garner, F. J. The Calculation of Multidimensional Hermite Polynomials and Gram-Charlier Coefficients. *Mathematics of Computation*, 24(111):537–545, 1970. URL.

Berman and Bian (1997) - Berman, P. R. and Bian, B. Pump-probe spectroscopy approach to Bragg scattering. *Phys. Rev. A*, 55(6):4382–4385, 6 1997. URL.

Bogoliubov (1947) - Bogoliubov, N. On the theory of superfluidity. *Journal of Physics*, XI(1):23, 1947. URL.

Boiron (2024) - Boiron, D. A separability criterion for bipartite state with undefined number of particles, Private communication. 4 2024.

Bonneau (2011) - Bonneau, M. "Mélange à quatre ondes atomique dans un réseau optique". Université Paris Sud - Paris XI. 2011.

Bonneau et al. (2013) - Bonneau, M., Ruaudel, J., Lopes, R., Jaskula, J.-C., Aspect, A., Boiron, D., and Westbrook, C. I. Tunable source of correlated atom beams. *Physical Review A*, 87(6):061603, 6 2013. URL.

Brady (2023) - Brady, A. J. Gaussian Bosonic Systems and Semi-classical Black Holes. *Analog Gravity in 2023, Benasque summer school*, 2023.

Brady et al. (2022) - Brady, A. J., Agullo, I., and Kranas, D. Symplectic circuits, entanglement, and stimulated Hawking radiation in analog gravity. *Physical Review D*, 106(10):105021, 11 2022. URL.

Brandão et al. (2022) - Brandão, I., Tandeitnik, D., and Guerreiro, T. Qugit: A numerical toolbox for Gaussian quantum states. *Computer Physics Communications*, 280:108471, 2022. URL.

Brask (2022) - Brask, J. B. Gaussian states and operations – a quick reference. 3 2022. URL.

Braunstein and van Loock (2005) - Braunstein, S. L. and Loock, P. Quantum information with continuous variables. *Reviews of Modern Physics*, 77(2):513–577, 6 2005. URL.

Brennecke et al. (2008) - Brennecke, F., Ritter, S., Donner, T., and , T. E. Cavity Optomechanics with a Bose-Einstein Condensate. *Science*, 322(5899):235–238, 2008. URL.

Browaeys (1999) - Browaeys, A. Piegeage magnetique d'un gaz d'helium metastable : vers la condensation de Bose-Einstein. Université Paris Sud - Paris XI. 1999.

Browaeys et al. (2000) - Browaeys, A., Poupard, J., Robert, A., Nowak, S., Rooijakkers, W., Arimondo, E., Marcassa, L., Boiron, D., Westbrook, C., and Aspect, A. Two body loss rate in a magneto-optical trap of metastable He. *The European Physical Journal D - Atomic, Molecular and Optical Physics*, 8(2):199–203, 1 2000. URL.

Browaeys et al. (2001) - Browaeys, A., Robert, A., Sirjean, O., Poupard, J., Nowak, S., Boiron, D., Westbrook, C. I., and Aspect, A. Thermalization of magnetically trapped metastable helium. *Phys. Rev. A*, 64(3):034703, 8 2001. URL.

Brown and Twiss (1956) - Brown, R. H. and Twiss, R. Q. Correlation between Photons in two Coherent Beams of Light. *Nature*, 177(4497):27–29, 1 1956. URL.

Bücker et al. (2011) - Bücker, R., Grond, J., Manz, S., Berrada, T., Betz, T., Koller, C., Hohenester, U., Schumm, T., Perrin, A., and Schmiedmayer, J. Twin-atom beams. *Nature Physics*, 7(8):608–611, 8 2011. URL.

Bureik (2024) - Bureik, J.-P. Number Statistics and Momentum Correlations in Interacting Bose Gases. Université Paris-Saclay. 2024.

Busch (2014) - Busch, X. Dispersive and dissipative effects in quantum field theory in curved spacetime to model condensed matter systems. Université Paris Sud - Paris XI. 11 2014. URL.

Busch et al. (2014) - Busch, X., Parentani, R., and Robertson, S. Quantum entanglement due to a modulated dynamical Casimir effect. *Physical Review A*, 89(6):063606, 6 2014. URL.

Butera et al. (2021) - Butera, S., Clément, D., and Carusotto, I. Position- and momentum-space two-body correlations in a weakly interacting trapped condensate. *Physical Review A*, 103(1):013302, 1 2021. URL.

Campbell et al. (2006) - Campbell, G. K., Mun, J., Boyd, M., Streed, E. W., Ketterle, W., and Pritchard, D. E. Parametric Amplification of Scattered Atom Pairs. *Physical Review Letters*, 96(2):020406, 1 2006. URL.

Campo and Parentani (2005) - Campo, D. and Parentani, R. Inflationary spectra and partially decohered distributions. *Physical Review D*, 72(4):045015, 8 2005. URL.

Campo and Parentani (2006) - Campo, D. and Parentani, R. Inflationary spectra and violations of Bell inequalities. *Physical Review D*, 74(2):025001, 7 2006. URL.

Case (2008) - Case, W. B. Wigner functions and Weyl transforms for pedestrians. *American Journal of Physics*, 76(10):937–946, 10 2008. URL.

Castin (2001) - Castin, Y. *Bose-Einstein Condensates in Atomic Gases: Simple Theoretical Results*, volume 72, pages 1–136. Springer Berlin Heidelberg, Berlin, Heidelberg, 2001. ISBN 978-3-540-41047-8. doi: 10.1007/3-540-45338-5_1. URL.

Castin (2011) - Castin, Y. Mécanique quantique : seconde quantification et résolvante., Cours de M2 Concepts fondamentaux de la physique. 2011. URL.

Castin and Dum (1996) - Castin, Y. and Dum, R. Bose-Einstein Condensates in Time Dependent Traps. *Physical Review Letters*, 77(27):5, 1996.

Caves et al. (1991) - Caves, C. M., Zhu, C., Milburn, G. J., and Schleich, W. Photon statistics of two-mode squeezed states and interference in four-dimensional phase space. *Phys. Rev. A*, 43(7): 3854–3861, 4 1991. URL.

Cayla (2018) - Cayla, H. Measuring the momentum distribution of a lattice gas at the single-atom level. Université Paris-Saclay. 2018.

Cerf et al. (2007) - Cerf, N. J., Leuchs, G., and Polzik, E. S. *Quantum Information with Continuous Variables of Atoms and Light*. Imperial College Press, 2007. doi: 10.1142/p489. URL.

Chang et al. (2014) - Chang, R., Hoendervanger, A. L., Bouton, Q., Fang, Y., Klafka, T., Audo, K., Aspect, A., Westbrook, C. I., and Clément, D. Three-dimensional laser cooling at the Doppler limit. *Physical Review A*, 90(6):063407, 12 2014. URL.

Chen et al. (2021) - Chen, C.-A., Khlebnikov, S., and Hung, C.-L. Observation of Quasiparticle Pair Production and Quantum Entanglement in Atomic Quantum Gases Quenched to an Attractive Interaction. *Physical Review Letters*, 127(6):060404, 8 2021. URL.

Cheneau et al. (2012) - Cheneau, M., Barmettler, P., Poletti, D., Endres, M., Schauß, P., Fukuhara, T., Gross, C., Bloch, I., Kollath, C., and Kuhr, S. Light-cone-like spreading of correlations in a quantum many-body system. *Nature*, 481(7382):484–487, 1 2012. URL.

Chevy et al. (2002) - Chevy, F., Bretin, V., Rosenbusch, P., Madison, K. W., and Dalibard, J. The transverse breathing mode of an elongated Bose-Einstein condensate. *Physical Review Letters*, 88 (25):250402, 6 2002. URL.

Clark et al. (2017) - Clark, L. W., Gaj, A., Feng, L., and Chin, C. Collective emission of matter-wave jets from driven Bose–Einstein condensates. *Nature*, 551(7680):356–359, 11 2017. URL.

Clauser (1974) - Clauser, J. F. Experimental distinction between the quantum and classical field-theoretic predictions for the photoelectric effect. *Physical Review D*, 9(4):853–860, 2 1974. URL.

Clauser et al. (1969) - Clauser, J. F., Horne, M. A., Shimony, A., and Holt, R. A. Proposed Experiment to Test Local Hidden-Variable Theories. *Physical Review Letters*, 23(15):880–884, 10 1969. URL.

Clément (2019) - Clément, D. Momentum-space atom correlations in strongly interacting Bose gases. Université Paris Saclay. 10 2019. URL.

Clément (2022) - Clément, D. Experimental schemes to certify entanglement associated with pair creation, Private communication. 2022.

Človečko et al. (2019) - Človečko, M., Gažo, E., Kupka, M., and Skyba, P. Magnonic Analog of Black-and White-Hole Horizons in Superfluid He 3-B. *Phys. Rev. Lett.*, 123(16):161302, 10 2019. URL.

Cominotti et al. (2022) - Cominotti, R., Berti, A., Farolfi, A., Zenesini, A., Lamporesi, G., Carusotto, I., Recati, A., and Ferrari, G. Observation of Massless and Massive Collective Excitations with Faraday Patterns in a Two-Component Superfluid. *Physical Review Letters*, 128(21):210401, 5 2022. URL.

Compagno et al. (2018) - Compagno, G., Castellini, A., and Lo Franco, R. Dealing with indistinguishable particles and their entanglement. *Philosophical Transactions of the Royal Society A: Mathematical, Physical and Engineering Sciences*, 376(2123):20170317, 7 2018. URL.

Cooper et al. (2013) - Cooper, M., Wright, L. J., Söller, C., and Smith, B. J. Experimental generation of multi-photon Fock states. *Optics Express*, 21(5):5309–5317, 3 2013. URL.

Corman et al. (2014) - Corman, L., Chomaz, L., Bienaimé, T., Desbuquois, R., Weitenberg, C., Nascimbène, S., Dalibard, J., and Beugnon, J. Quench-Induced Supercurrents in an Annular Bose Gas. *Physical Review Letters*, 113(13):135302, 9 2014. URL.

Dalibard (2015) - Dalibard, J. Une brève histoire des atomes froids. *Cours du College de France*, 143, 2015. URL.

Dalibard (2022) - Dalibard, J. Les interactions dans les gaz d'atomes froids (II) : du problème à deux corps la limite macroscopique. *Cours du Collège de France*, 2022. URL.

Dalibard (2024) - Dalibard, J. Interactions magnétiques entre atomes froids : gouttelettes quantiques et états supersolides. *Cours du Collège de France*, 2024. URL.

Dall et al. (2013) - Dall, R. G., Manning, A. G., Hodgman, S. S., RuGway, W., Kheruntsyan, K. V., and Truscott, A. G. Ideal n-body correlations with massive particles. *Nature Physics*, 9(6):341–344, 6 2013. URL.

Dalton et al. (2017) - Dalton, B. J., Goold, J., Garraway, B. M., and Reid, M. D. Quantum entanglement for systems of identical bosons: I. General features. *Physica Scripta*, 92(2):023004, 2 2017. URL.

Darsow-Fromm et al. (2020) - Darsow-Fromm, C., Dekant, L., Grebien, S., Schröder, M., Schnabel, R., and Steinlechner, S. Nqontrol: An open-source platform for digital control-loops in quantum-optical experiments. *Review of Scientific Instruments*, 91(3):035114, 3 2020. URL.

Davis et al. (1995) - Davis, K. B., Mewes, M.-O., Andrews, M. R., Druten, N. J., Durfee, D. S., Kurn, D., and Ketterle, W. Bose-Einstein condensation in a gas of sodium atoms. *Physical review letters*, 75(22):3969, 1995.

De Nova et al. (2014) - De Nova, J. R. M., Sols, F., and Zapata, I. Violation of Cauchy-Schwarz inequalities by spontaneous Hawking radiation in resonant boson structures. *Physical Review A*, 89 (4):043808, 4 2014. URL.

de Valcarcel (2002) - Valcarcel, G. J. Faraday patterns in Bose-Einstein condensates. Amplitude equation for rolls in the parametrically driven, damped Gross-Pitaevskii equation, arXiv. 4 2002. URL.

Dodonov (2010) - Dodonov, V. V. Current status of the Dynamical Casimir Effect. *Physica Scripta*, 82(3):038105, 9 2010. URL.

Dodonov et al. (1994a) - Dodonov, V. V., Man'ko, O. V., and Man'ko, V. I. Photon distribution for one-mode mixed light with a generic Gaussian Wigner function. *Phys. Rev. A*, 49(4):2993–3001, 4 1994a. URL.

Dodonov et al. (1994b) - Dodonov, V. V., Man'ko, O. V., and Man'ko, V. I. Multidimensional Hermite polynomials and photon distribution for polymode mixed light. *Physical Review A*, 50(1):813–817, 7 1994b. URL.

Dowling and Milburn (2003) - Dowling, J. P. and Milburn, G. J. Quantum technology: the second quantum revolution. *Philosophical Transactions of the Royal Society of London. Series A: Mathematical, Physical and Engineering Sciences*, 361(1809):1655–1674, 8 2003. URL.

Duan et al. (2000) - Duan, L.-M., Giedke, G., Cirac, J. I., and Zoller, P. Inseparability Criterion for Continuous Variable Systems. *Physical Review Letters*, 84(12):4, 2000.

Dunjko et al. (2001) - Dunjko, V., Lorent, V., and Olshanii, M. Bosons in Cigar-Shaped Traps: Thomas-Fermi Regime, Tonks-Girardeau Regime, and In Between. *Physical Review Letters*, 86(24):5413–5416, 6 2001. URL.

Dussarrat et al. (2017) - Dussarrat, P., Perrier, M., Imanaliev, A., Lopes, R., Aspect, A., Cheneau, M., Boiron, D., and Westbrook, C. I. Two-Particle Four-Mode Interferometer for Atoms. *Physical Review Letters*, 119(17):173202, 10 2017. URL.

Eckel et al. (2018) - Eckel, S., Kumar, A., Jacobson, T., Spielman, I. B., and Campbell, G. K. A rapidly expanding Bose-Einstein condensate: an expanding universe in the lab. *Physical Review X*, 8(2): 021021, 4 2018. URL.

Edwards and Fauve (1994) - Edwards, W. S. and Fauve, S. Patterns and quasi-patterns in the Faraday experiment. *Journal of Fluid Mechanics*, 278:123–148, 11 1994. URL.

Engels et al. (2007) - Engels, P., Atherton, C., and Hoefer, M. A. Observation of Faraday Waves in a Bose-Einstein Condensate. *Physical Review Letters*, 98(9):095301, 2 2007. URL.

Estève et al. (2008) - Estève, J., Gross, C., Weller, A., Giovanazzi, S., and Oberthaler, M. K. Squeezing and entanglement in a Bose–Einstein condensate. *Nature*, 455(7217):1216–1219, 10 2008. URL.

Fadel et al. (2018) - Fadel, M., Zibold, T., Décamps, B., and , P. T. Spatial entanglement patterns and Einstein-Podolsky-Rosen steering in Bose-Einstein condensates. *Science*, 360(6387):409–413, 2018. URL.

Fedichev et al. (1998) - Fedichev, P. O., Shlyapnikov, G. V., and Walraven, J. T. M. Damping of Low-Energy Excitations of a Trapped Bose-Einstein Condensate at Finite Temperatures. *Physical Review Letters*, 80(11):2269–2272, 3 1998. URL.

Finazzi and Carusotto (2014) - Finazzi, S. and Carusotto, I. Entangled phonons in atomic Bose-Einstein condensates. *Physical Review A*, 90(3):033607, 9 2014. URL.

Finke et al. (2016) - Finke, A., Jain, P., and Weinfurtner, S. On the observation of nonclassical excitations in Bose–Einstein condensates. *New Journal of Physics*, 18(11):113017, 11 2016. URL.

Fliesser et al. (1997) - Fliesser, M., Csordás, A., Szépfalusy, P., and Graham, R. Hydrodynamic excitations of Bose condensates in anisotropic traps. *Physical Review A*, 56(4):R2533–R2536, 10 1997. URL.

Fuchs et al. (2003) - Fuchs, J. N., Leyronas, X., and Combescot, R. Hydrodynamic modes of a one-dimensional trapped Bose gas. *Physical Review A*, 68(4):043610, 10 2003. URL.

Gassot et al. (1999) - Gassot, H., Durante, M., Thiebault, A., and Vernay, E. Etude des contraintes thermiques a basse temperature d'une structure en niobium avec un revetement de cuivre realise par projection thermique. https://hal.in2p3.fr/in2p3-00007650. 1999. URL.

Gaunt et al. (2013) - Gaunt, A. L., Schmidutz, T. F., Gotlibovych, I., Smith, R. P., and Hadzibabic, Z. Bose-Einstein Condensation of Atoms in a Uniform Potential. *Physical Review Letters*, 110(20): 200406, 5 2013. URL.

Geen and Freeman (1991) - Geen, H. and Freeman, R. Band-selective radiofrequency pulses. *Journal of Magnetic Resonance (1969)*, 93(1):93–141, 1991. URL.

Gerbier (2004) - Gerbier, F. Quasi-1d Bose-Einstein condensates in the dimensional crossover regime. *Europhysics Letters (EPL)*, 66(6):771–777, 6 2004. URL.

Gerbier et al. (2006) - Gerbier, F., Fölling, S., Widera, A., Mandel, O., and Bloch, I. Probing Number Squeezing of Ultracold Atoms across the Superfluid-Mott Insulator Transition. *Phys. Rev. Lett.*, 96 (9):090401, 3 2006. URL.

Gessner et al. (2017) - Gessner, M., Pezzè, L., and Smerzi, A. Entanglement and squeezing in continuous-variable systems. *Quantum*, 1:17, 7 2017. URL.

Gisin (1991) - Gisin, N. Bell's inequality holds for all non-product states. *Physics Letters A*, 154(5-6): 201–202, 4 1991. URL.

Gisin and Peres (1992) - Gisin, N. and Peres, A. Maximal violation of Bell's inequality for arbitrarily large spin. *Physics Letters A*, 162(1):15–17, 1 1992. URL.

Glauber (1963a) - Glauber, R. J. Coherent and Incoherent States of the Radiation Field. *Physical Review*, 131(6):2766–2788, 9 1963a. URL.

Glauber (1963b) - Glauber, R. J. The Quantum Theory of Optical Coherence. *Physical Review*, 130 (6):2529–2539, 6 1963b. URL.

Gomes et al. (2006) - Gomes, J. V., Perrin, A., Schellekens, M., Boiron, D., Westbrook, C. I., and Belsley, M. Theory for a Hanbury Brown Twiss experiment with a ballistically expanding cloud of cold atoms. *Physical Review A*, 74(5):053607, 11 2006. URL.

Goodman (2015) - Goodman, J. W. *Statistical optics*. John Wiley Sons, 2015. URL.

Gregory (2023) - Gregory, R. *Primordial Black Holes and Higgs Vacuum Decay*, volume 1022, pages 289–311. Springer Nature Switzerland, Cham, 2023. ISBN 978-3-031-42095-5 978-3-031-42096-2. doi: 10.1007/978-3-031-42096-2_12. URL.

Grishchuk and Sidorov (1990) - Grishchuk, L. P. and Sidorov, Y. V. Squeezed quantum states of relic gravitons and primordial density fluctuations. *Phys. Rev. D*, 42(10):3413–3421, 11 1990. URL.

Groot (2015) - Groot, A. Excitations in hydrodynamic ultra-cold Bose gases. Utrecht University. 2015.

Gross et al. (2010) - Gross, C., Zibold, T., Nicklas, E., Estève, J., and Oberthaler, M. K. Nonlinear atom interferometer surpasses classical precision limit. *Nature*, 464(7292):1165–1169, 4 2010. URL.

Gross (1961) - Gross, E. P. Structure of a quantized vortex in boson systems. *Il Nuovo Cimento (1955-1965)*, 20(3):454–477, 5 1961. URL.

Grygar et al. (2022) - Grygar, J., Hloušek, J., Fiurášek, J., and Ježek, M. Quantum non-Gaussianity certification of photon number-resolving detectors. *Optics Express*, 30(18):33097, 8 2022. URL.

Gühne and Tóth (2009) - Gühne, O. and Tóth, G. Entanglement detection. *Physics Reports*, 474(1-6): 1–75, 4 2009. URL.

Gupt et al. (2019) - Gupt, B., Izaac, J., and Quesada, N. The Walrus: a library for the calculation of hafnians, Hermite polynomials and Gaussian boson sampling. *Journal of Open Source Software*, 4 (44):1705, 12 2019. URL.

Guth (1981) - Guth, A. H. Inflationary universe: A possible solution to the horizon and flatness problems. *Physical Review D*, 23(2):347–356, 1 1981. URL.

Guth (1997) - Guth, A. H. Was cosmic inflation the bang of the big bang? *The Beam Line*, 27(3), 1997. URL.

Hercé (2023) - Hercé, G. Momentum correlations in strongly-depleted 4he* Bose-Einstein condensates. Université Paris-Saclay. 2023. URL.

Hercé et al. (2023) - Hercé, G., Bureik, J.-P., Ténart, A., Aspect, A., Dareau, A., and Clément, D. Full counting statistics of interacting lattice gases after an expansion: The role of condensate depletion in many-body coherence. *Physical Review Research*, 5(1):L012037, 3 2023. URL.

Hernández-Rajkov et al. (2021) - Hernández-Rajkov, D., Padilla-Castillo, J. E., Río-Lima, A. D., Gutiérrez-Valdés, A., Poveda-Cuevas, F. J., and Seman, J. A. Faraday waves in strongly interacting superfluids. *New Journal of Physics*, 23(10):103038, 10 2021. URL.

Hillery and Zubairy (2006) - Hillery, M. and Zubairy, M. S. Entanglement Conditions for Two-Mode States. *Physical Review Letters*, 96(5):050503, 2 2006. URL.

Hloušek et al. (2021) - Hloušek, J., Ježek, M., and Fiurášek, J. Direct Experimental Certification of Quantum Non-Gaussian Character and Wigner Function Negativity of Single-Photon Detectors. *Physical Review Letters*, 126(4):043601, 1 2021. URL.

Hodgman et al. (2009) - Hodgman, S. S., Dall, R. G., Byron, L. J., Baldwin, K. G. H., Buckman, S. J., and Truscott, A. G. Metastable Helium: A New Determination of the Longest Atomic Excited-State Lifetime. *Physical Review Letters*, 103(5):053002, 7 2009. URL.

Hodgman et al. (2017) - Hodgman, S. S., Khakimov, R. I., Lewis-Swan, R. J., Truscott, A. G., and Kheruntsyan, K. V. Solving the Quantum Many-Body Problem via Correlations Measured with a Momentum Microscope. *Physical Review Letters*, 118(24):240402, 6 2017. URL.

Hohenberg and Martin (1965) - Hohenberg, P. and Martin, P. Microscopic theory of superfluid helium. *Annals of Physics*, 34(2):291–359, 9 1965. URL.

Horn and Mathias (1990) - Horn, R. A. and Mathias, R. Cauchy-Schwarz inequalities associated with positive semidefinite matrices. *Linear Algebra and its Applications*, 142:63–82, 12 1990. URL.

Horodecki et al. (1996) - Horodecki, M., Horodecki, P., and Horodecki, R. Separability of mixed states: necessary and sufficient conditions. *Physics Letters A*, 223(1-2):1–8, 11 1996. URL.

Horodecki (1997) - Horodecki, P. Separability criterion and inseparable mixed states with positive partial transposition. *Physics Letters A*, 232(5):333–339, 8 1997. URL.

Horodecki et al. (2009) - Horodecki, R., Horodecki, P., Horodecki, M., and Horodecki, K. Quantum entanglement. *Reviews of Modern Physics*, 81(2):865–942, 6 2009. URL.

Hung et al. (2013) - Hung, C.-L., Gurarie, V., and Chin, C. From Cosmology to Cold Atoms: Observation of Sakharov Oscillations in a Quenched Atomic Superfluid. *Science*, 341(6151):1213–1215, 9 2013. URL.

Hyllus and Eisert (2006) - Hyllus, P. and Eisert, J. Optimal entanglement witnesses for continuous-variable systems. *New Journal of Physics*, 8(4):51–51, 4 2006. URL.

Hyllus et al. (2012) - Hyllus, P., Pezzé, L., Smerzi, A., and Tóth, G. Entanglement and extreme spin squeezing for a fluctuating number of indistinguishable particles. *Physical Review A*, 86(1):012337, 7 2012. URL.

Isoard et al. (2021) - Isoard, M., Milazzo, N., Pavloff, N., and Giraud, O. Bipartite and tripartite entanglement in a Bose-Einstein acoustic black hole. *Phys. Rev. A*, 104(6):063302, 12 2021. URL.

Isserlis (1918) - Isserlis, L. On a formula for the product-moment coefficient of any order of a normal frequency distribution in any number of variables. *Biometrika*, 12(1/2):134–139, 1918.

Jackson et al. (1998) - Jackson, A. D., Kavoulakis, G. M., and Pethick, C. J. Solitary waves in clouds of Bose-Einstein condensed atoms. *Phys. Rev. A*, 58(3):2417–2422, 9 1998. URL.

Jackson and Zaremba (2002) - Jackson, B. and Zaremba, E. Accidental Suppression of Landau Damping of the Transverse Breathing Mode in Elongated Bose-Einstein Condensates. *Physical Review Letters*, 89(15):150402, 9 2002. URL.

Jacquet et al. (2020) - Jacquet, M. J., Weinfurtner, S., and König, F. The next generation of analogue gravity experiments. *Philosophical Transactions of the Royal Society A: Mathematical, Physical and Engineering Sciences*, 378(2177):20190239, 8 2020. URL.

Jaskula (2010) - Jaskula, J.-C. Création et étude de sources d'états non classiques pour l'optique atomique quantique. Institut d'Optique Graduate School. 2010.

Jaskula et al. (2010) - Jaskula, J.-C., Bonneau, M., Partridge, G. B., Krachmalnicoff, V., Deuar, P., Kheruntsyan, K. V., Aspect, A., Boiron, D., and Westbrook, C. I. Sub-Poissonian Number Differences in Four-Wave Mixing of Matter Waves. *Physical Review Letters*, 105(19):190402, 11 2010. URL.

Jaskula et al. (2012) - Jaskula, J.-C., Partridge, G. B., Bonneau, M., Lopes, R., Ruaudel, J., Boiron, D., and Westbrook, C. I. Acoustic Analog to the Dynamical Casimir Effect in a Bose-Einstein Condensate. *Physical Review Letters*, 109(22):220401, 11 2012. URL.

Jeltes et al. (2007) - Jeltes, T., McNamara, J. M., Hogervorst, W., Vassen, W., Krachmalnicoff, V., Schellekens, M., Perrin, A., Chang, H., Boiron, D., Aspect, A., and Westbrook, C. I. Comparison of the Hanbury Brown–Twiss effect for bosons and fermions. *Nature*, 445(7126):402–405, 1 2007. URL.

Jin et al. (1997) - Jin, D. S., Matthews, M. R., Ensher, J. R., Wieman, C. E., and Cornell, E. A. Temperature-Dependent Damping and Frequency Shifts in Collective Excitations of a Dilute Bose-Einstein Condensate. *Physical Review Letters*, 78(5), 1997.

Kagan and Maksimov (2001) - Kagan, Y. and Maksimov, L. Damping of trapped Bose-Einstein condensate oscillations at zero temperature. *Physical Review A*, 64(5):053610, 2001.

Kagan et al. (1996) - Kagan, Y., Surkov, E. L., and Shlyapnikov, G. V. Evolution of a Bose-condensed gas under variations of the confining potential. *Physical Review A*, 54(3):R1753–R1756, 9 1996. URL.

Kanamori (1972) - Kanamori, H. Mechanism of tsunami earthquakes. *Physics of the Earth and Planetary Interiors*, 6(5):346–359, 1972. URL.

Keller et al. (2014) - Keller, M., Kotyrba, M., Leupold, F., Singh, M., Ebner, M., and Zeilinger, A. Bose-Einstein condensate of metastable helium for quantum correlation experiments. *Physical Review A*, 90(6):063607, 12 2014. URL.

Kelley and Kleiner (1964) - Kelley, P. L. and Kleiner, W. H. Theory of Electromagnetic Field Measurement and Photoelectron Counting. *Physical Review*, 136(2A):A316–A334, 10 1964. URL.

Keshet and Ketterle (2013) - Keshet, A. and Ketterle, W. A Distributed GUI-based Computer Control System for Atomic Physics Experiments. *Review of Scientific Instruments*, 84(1):015105, 1 2013. URL.

Kheruntsyan et al. (2012) - Kheruntsyan, K. V., Jaskula, J.-C., Deuar, P., Bonneau, M., Partridge, G. B., Ruaudel, J., Lopes, R., Boiron, D., and Westbrook, C. I. Violation of the Cauchy-Schwarz Inequality with Matter Waves. *Physical Review Letters*, 108(26):260401, 6 2012. URL.

Killoran et al. (2014) - Killoran, N., Cramer, M., and Plenio, M. B. Extracting Entanglement from Identical Particles. *Physical Review Letters*, 112(15):150501, 4 2014. URL.

Kofman et al. (1994) - Kofman, L., Linde, A., and Starobinsky, A. A. Reheating after Inflation. *Physical Review Letters*, 73(24):3195–3198, 12 1994. URL.

Kofman et al. (1997) - Kofman, L., Linde, A., and Starobinsky, A. Towards the Theory of Reheating After Inflation. *Physical Review D*, 56(6):3258–3295, 9 1997. URL.

Köhnke et al. (2021) - Köhnke, S., Agudelo, E., Schünemann, M., Schlettwein, O., Vogel, W., Sperling, J., and Hage, B. Quantum Correlations beyond Entanglement and Discord. *Physical Review Letters*, 126(17):170404, 4 2021. URL.

Kok and Braunstein (2001) - Kok, P. and Braunstein, S. L. Multi-dimensional Hermite polynomials in quantum optics. *Journal of Physics A: Mathematical and General*, 34(31):6185, 7 2001. URL.

Krämer et al. (2005) - Krämer, M., Tozzo, C., and Dalfovo, F. Parametric excitation of a Bose-Einstein condensate in a one-dimensional optical lattice. *Physical Review A*, 71(6):061602, 6 2005. URL.

Krešić et al. (2023) - Krešić, I., Robb, G. R. M., Oppo, G.-L., and Ackemann, T. Generating Multiparticle Entangled States by Self-Organization of Driven Ultracold Atoms. *Physical Review Letters*, 131(16):163602, 10 2023. URL.

Krishnaswamy et al. (2024) - Krishnaswamy, S., Schlue, F., Ares, L., Dyachuk, V., Stefszky, M., Brecht, B., Silberhorn, C., and Sperling, J. Experimental retrieval of photon statistics from click detection. *Phys. Rev. A*, 110(2):023717, 8 2024. URL.

Kunkel et al. (2018) - Kunkel, P., Prüfer, M., Strobel, H., Linnemann, D., Frölian, A., Gasenzer, T., Gärttner, M., and , M. K. O. Spatially distributed multipartite entanglement enables EPR steering of atomic clouds. *Science*, 360(6387):413–416, 2018. URL.

Kurtsiefer et al. (1997) - Kurtsiefer, C., Pfau, T., and Mlynek, J. Measurement of the Wigner function of an ensemble of helium atoms. *Nature*, 386(6621):150–153, 3 1997. URL.

Labeyrie (1998) - Labeyrie, G. Deux outils pour l'optique atomique: Jet intense d'hélium métastable et Miroir à onde évanescente exaltée. Université Paris Sud - Paris XI. 1998.

Labeyrie et al. (1999) - Labeyrie, G., Browaeys, A., Rooijakkers, W., Voelker, D., Grosperrin, J., Wanner, B., Westbrook, C., and Aspect, A. A focussing funnel for metastable helium. *The European Physical Journal D*, 7(3):341, 1999. URL.

Lahav et al. (2010) - Lahav, O., Itah, A., Blumkin, A., Gordon, C., Rinott, S., Zayats, A., and Steinhauer, J. Realization of a Sonic Black Hole Analog in a Bose-Einstein Condensate. *Phys. Rev. Lett.*, 105 (24):240401, 12 2010. URL.

Lähteenmäki et al. (2013) - Lähteenmäki, P., Paraoanu, G. S., Hassel, J., and Hakonen, P. J. Dynamical Casimir effect in a Josephson metamaterial. *Proceedings of the National Academy of Sciences*, 110 (11):4234–4238, 3 2013. URL.

Lambrecht et al. (1996) - Lambrecht, A., Jaekel, M.-T., and Reynaud, S. Motion Induced Radiation from a Vibrating Cavity. *Phys. Rev. Lett.*, 77(4):615–618, 7 1996. URL.

Lamirault (2023) - Lamirault, C. Détermination du nombre d'atomes d'un gaz d'hélium par imagerie d'absorption. Master's thesis, 2023.

Lange et al. (2018) - Lange, K., Peise, J., Lücke, B., Kruse, I., Vitagliano, G., Apellaniz, I., Kleinmann, M., Tóth, G., and Klempt, C. Entanglement between two spatially separated atomic modes. *Science*, 360(6387):416–418, 4 2018. URL.

Le Bellac (2007) - Le Bellac, M. *Physique quantique*. EDP Sciences - CNRS Editions, 2007.

Leach and Andriopoulos (2008) - Leach, P. G. L. and Andriopoulos, K. The Ermakov equation: a commentary. *Applicable Analysis and Discrete Mathematics*, 2(2):146–157, 2008. URL.

Leibfried et al. (1996) - Leibfried, D., Meekhof, D. M., King, B. E., Monroe, C., Itano, W. M., and Wineland, D. J. Experimental Determination of the Motional Quantum State of a Trapped Atom. *Physical Review Letters*, 77(21):4281–4285, 11 1996. URL.

Lellouch et al. (2017) - Lellouch, S., Bukov, M., Demler, E., and Goldman, N. Parametric Instability Rates in Periodically Driven Band Systems. *Phys. Rev. X*, 7(2):021015, 5 2017. URL.

Leonhardt (2010) - Leonhardt, U. *Essential Quantum Optics: from quantum measurements to black holes*. Cambridge University Press, 2010. ISBN 978-0-521-86978-2. URL.

Leprince (2024) - Leprince, C. Phase control and pulse shaping in Bragg diffraction for quantum atom optics: From matter-wave interferences to a Bell's inequality test. Université Paris-Saclay. 2024. URL.

Leprince et al. (2024) - Leprince, C., Gondret, V., Lamirault, C., Dias, R., Marolleau, Q., Boiron, D., and Westbrook, C. I. Coherent coupling of momentum states: selectivity and phase control, Submitted to Phys. Rev. A. 2024. URL.

Liebster et al. (2023) - Liebster, N., Sparn, M., Kath, E., Fujii, K., Görlitz, S., Enss, T., Strobel, H., and Oberthaler, M. K. Emergence of crystalline steady state in a driven superfluid, arXiv. 10 2023. URL.

Linde (1982) - Linde, A. Scalar field fluctuations in the expanding universe and the new inflationary universe scenario. *Physics Letters B*, 116(5):335–339, 10 1982. URL.

Lopes (2014) - Lopes, R. An atomic Hong-Ou-Mandel experiment. Institut d'Optique Graduate School. 2014. URL.

Lopes et al. (2015) - Lopes, R., Imanaliev, A., Aspect, A., Cheneau, M., Boiron, D., and Westbrook, C. I. Atomic Hong–Ou–Mandel experiment. *Nature*, 520(7545):66–68, 4 2015. URL.

Lücke et al. (2011) - Lücke, B., Scherer, M., Kruse, J., Pezzé, L., Deuretzbacher, F., Hyllus, P., Topic, O., Peise, J., Ertmer, W., Arlt, J., Santos, L., Smerzi, A., and Klempt, C. Twin Matter Waves for Interferometry Beyond the Classical Limit. *Science*, 334(6057):773–776, 11 2011. URL.

Luo et al. (2016) - Luo, Y., Yan, S., Hu, Q., Jia, A., Wei, C., and Yang, J. Contrast enhancement via shaped Raman pulses for thermal coldatom cloud interferometry. *The European Physical Journal D*, 70(12):262, 12 2016. URL.

Lvovsky et al. (2001) - Lvovsky, A. I., Hansen, H., Aichele, T., Benson, O., Mlynek, J., and Schiller, S. Quantum State Reconstruction of the Single-Photon Fock State. *Physical Review Letters*, 87(5): 050402, 7 2001. URL.

Lvovsky et al. (2020) - Lvovsky, A. I., Grangier, P., Ourjoumtsev, A., Parigi, V., Sasaki, M., and Tualle-Brouri, R. Production and applications of non-Gaussian quantum states of light. 6 2020. URL.

Macrì et al. (2018) - Macrì, V., Ridolfo, A., Di Stefano, O., Kockum, A. F., Nori, F., and Savasta, S. Nonperturbative Dynamical Casimir Effect in Optomechanical Systems: Vacuum Casimir-Rabi Splittings. *Physical Review X*, 8(1):011031, 2 2018. URL.

Marolleau (2019) - Marolleau, Q. Condensats d'helium métastable Violation d'inégalités de Bell. Master's thesis, 2019.

Marolleau (2022) - Marolleau, Q. Quantum atom optics with metastable helium atoms. Université Paris-Saclay. 12 2022.

Marolleau et al. (2024) - Marolleau, Q., Leprince, C., Gondret, V., Boiron, D., and Westbrook, C. I. Sub-shot-noise interferometry with two-mode quantum states. *Physical Review A*, 109(2):023701, 2 2024. URL.

Martin et al. (2023) - Martin, J., Micheli, A., and Vennin, V. Comparing quantumness criteria. *Europhysics Letters*, 142(1):18001, 4 2023. URL.

Martin et al. (1988) - Martin, P. J., Oldaker, B. G., Miklich, A. H., and Pritchard, D. E. Bragg scattering of atoms from a standing light wave. *Phys. Rev. Lett.*, 60(6):515–518, 2 1988. URL.

McDonald and Warren (1991) - McDonald, S. and Warren, W. S. Uses of shaped pulses in NMR: A primer. *Concepts Magn. Reson.*, 3(2):55–81, 4 1991. URL.

Menotti and Stringari (2002) - Menotti, C. and Stringari, S. Collective oscillations of a one-dimensional trapped Bose-Einstein gas. *Physical Review A*, 66(4):043610, 10 2002. URL.

Micheli (2023) - Micheli, A. Entanglement and decoherence in cosmology and in analogue gravity experiments. Université Paris-Saclay. 2023. URL.

Micheli (2024) - Micheli, A. Longitudinal profile and excitations of a Bose gas beyond Gerbier, Private communication. 6 2024.

Micheli and Robertson (2022) - Micheli, A. and Robertson, S. Phonon decay in 1d atomic Bose quasi-condensates via Beliaev-Landau damping. *Physical Review B*, 106(21):214528, 12 2022. URL.

Micheli and Robertson (2024) - Micheli, A. and Robertson, S. Extension of the decay rate to BECs: theory and numerics, Private communication. 9 2024.

Moal et al. (2006) - Moal, S., Portier, M., Kim, J., Dugué, J., Rapol, U. D., Leduc, M., and Cohen-Tannoudji, C. Accurate Determination of the Scattering Length of Metastable Helium Atoms Using Dark Resonances between Atoms and Exotic Molecules. *Physical Review Letters*, 96(2):023203, 1 2006. URL.

Modi et al. (2012) - Modi, K., Brodutch, A., Cable, H., Paterek, T., and Vedral, V. The classical-quantum boundary for correlations: Discord and related measures. *Reviews of Modern Physics*, 84 (4):1655–1707, 11 2012. URL.

Moore (1970) - Moore, G. T. Quantum Theory of the Electromagnetic Field in a VariableLength OneDimensional Cavity. *Journal of Mathematical Physics*, 11(9):2679–2691, 9 1970. URL.

Morris et al. (2020) - Morris, B., Yadin, B., Fadel, M., Zibold, T., Treutlein, P., and Adesso, G. Entanglement between Identical Particles Is a Useful and Consistent Resource. *Physical Review X*, 10(4): 041012, 10 2020. URL.

Muñoz Mateo and Delgado (2006) - Muñoz Mateo, A. and Delgado, V. Extension of the Thomas-Fermi approximation for trapped Bose-Einstein condensates with an arbitrary number of atoms. *Physical Review A*, 74(6):065602, 12 2006. URL.

NASA (2003) - NASA, J. Piezoelectrically Actuated Shutter for High Vacuum. 5 2003. URL.

Nguyen et al. (2015) - Nguyen, H. S., Gerace, D., Carusotto, I., Sanvitto, D., Galopin, E., Lemaı tre, A., Sagnes, I., Bloch, J., and Amo, A. Acoustic Black Hole in a Stationary Hydrodynamic Flow of Microcavity Polaritons. *Phys. Rev. Lett.*, 114(3):036402, 1 2015. URL.

Nguyen et al. (2019) - Nguyen, J. H. V., Tsatsos, M. C., Luo, D., Lode, A. U. J., Telles, G. D., Bagnato, V. S., and Hulet, R. G. Parametric Excitation of a Bose-Einstein Condensate: From Faraday Waves to Granulation. *Physical Review X*, 9(1):011052, 3 2019. URL.

Nicolin (2011) - Nicolin, A. I. Resonant wave formation in Bose-Einstein condensates. *Physical Review E*, 84(5):056202, 11 2011. URL.

Nicolin and Raportaru (2010) - Nicolin, A. I. and Raportaru, M. C. Faraday waves in high-density cigar-shaped Bose–Einstein condensates. *Physica A: Statistical Mechanics and its Applications*, 389(21):4663–4667, 11 2010. URL.

Nicolin et al. (2007) - Nicolin, A. I., Carretero-González, R., and Kevrekidis, P. G. Faraday waves in Bose-Einstein condensates. *Physical Review A*, 76(6):063609, 12 2007. URL.

Nogrette et al. (2015) - Nogrette, F., Heurteau, D., Chang, R., Bouton, Q., Westbrook, C. I., Sellem, R., and Clément, D. Characterization of a detector chain using a FPGA-based time-to-digital converter to reconstruct the three-dimensional coordinates of single particles at high flux. *Review of Scientific Instruments*, 86(11):113105, 11 2015. URL.

Nova et al. (2015) - Nova, J. R. M. D., Sols, F., and Zapata, I. Entanglement and violation of classical inequalities in the Hawking radiation of flowing atom condensates. *New Journal of Physics*, 17(10): 105003, 10 2015. URL.

Nowak et al. (2000) - Nowak, S., Browaeys, A., Poupard, J., Robert, A., Boiron, D., Westbrook, C., and Aspect, A. Magnetic trapping of metastable helium atoms. *Applied Physics B*, 70(3):455–457, 3 2000. URL.

O. Jagutzki et al. (2002) - O. Jagutzki, A. Cerezo, A. Czasch, R. Dorner, M. Hattas, Min Huang, V. Mergel, U. Spillmann, K. Ullmann-Pfleger, T. Weber, H. Schmidt-Bocking, and G. D. W. Smith. Multiple hit readout of a microchannel plate detector with a three-layer delay-line anode. *IEEE Transactions on Nuclear Science*, 49(5):2477–2483, 10 2002.

Orzel et al. (2001) - Orzel, C., Tuchman, A. K., Fenselau, M. L., Yasuda, M., and Kasevich, M. A. Squeezed States in a Bose-Einstein Condensate. *Science*, 291(5512):2386–2389, 3 2001. URL.

Ourjoumtsev (2007) - Ourjoumtsev, A. Étude théorique et expérimentale de superpositions quantiques cohérentes et d'états intriqués non-gaussiens de la lumière. Institut d'Optique, Université Paris XI. 2007. URL.

Ourjoumtsev et al. (2006a) - Ourjoumtsev, A., Tualle-Brouri, R., and Grangier, P. Quantum Homodyne Tomography of a Two-Photon Fock State. *Physical Review Letters*, 96(21):213601, 6 2006a. URL.

Ourjoumtsev et al. (2006b) - Ourjoumtsev, A., Tualle-Brouri, R., Laurat, J., and Grangier, P. Generating Optical Schrödinger Kittens for Quantum Information Processing. *Science*, 312(5770):83–86, 4 2006b. URL.

Parentani (2003) - Parentani, R. The inflationary paradigm: predictions for CMB. *Comptes Rendus Physique*, 4(8):935–943, 10 2003. URL.

Partridge et al. (2010) - Partridge, G. B., Jaskula, J.-C., Bonneau, M., Boiron, D., and Westbrook, C. I. Bose-Einstein condensation and spin mixtures of optically trapped metastable helium. *Physical Review A*, 81(5):053631, 5 2010. URL.

Peres (1996) - Peres, A. Separability Criterion for Density Matrices. *Physical Review Letters*, 77(8): 1413–1415, 8 1996. URL.

Perrier (2020) - Perrier, M. Interférences multiples avec atomes froids. Université Paris-Saclay. 2020.

Perrier et al. (2019) - Perrier, M., Amodjee, Z., Dussarrat, P., Dareau, A., Aspect, A., Cheneau, M., Boiron, D., and Westbrook, C. Thermal counting statistics in an atomic two-mode squeezed vacuum state. *SciPost Physics*, 7(1):002, 7 2019. URL.

Perrin (2008) - Perrin, A. Observation de paires d'atomes corrélés au travers de la collision de deux condensats de Bose-Einstein. Université Pierre et Marie Curie - Paris VI. 2008.

Perrin et al. (2007) - Perrin, A., Chang, H., Krachmalnicoff, V., Schellekens, M., Boiron, D., Aspect, A., and Westbrook, C. I. Observation of Atom Pairs in Spontaneous Four-Wave Mixing of Two Colliding Bose-Einstein Condensates. *Physical Review Letters*, 99(15):150405, 10 2007. URL.

Petrov et al. (2000) - Petrov, D. S., Shlyapnikov, G. V., and Walraven, J. T. M. Regimes of Quantum Degeneracy in Trapped 1d Gases. *Physical Review Letters*, 85(18):3745–3749, 10 2000. URL.

Philbin et al. (2008) - Philbin, T. G., Kuklewicz, C., Robertson, S., Hill, S., Konig, F., and Leonhardt, U. Fiber-optical analog of the event horizon. *Science*, 319(5868):1367–1370, 2008. URL.

Pirandola et al. (2009) - Pirandola, S., Serafini, A., and Lloyd, S. Correlation matrices of two-mode bosonic systems. *Physical Review A*, 79(5):052327, 5 2009. URL.

Pitaevskii and Stringari (1997) - Pitaevskii, L. and Stringari, S. Landau damping in dilute Bose gases. *Physics Letters A*, 235(4):398–402, 11 1997. URL.

Pitaevskii and Stringari (1998) - Pitaevskii, L. and Stringari, S. Elementary Excitations in Trapped Bose-Einstein Condensed Gases Beyond the Mean-Field Approximation. *Physical Review Letters*, 81(21):4541–4544, 11 1998. URL.

Pitaevskii (1961) - Pitaevskii, L. P. Vortex lines in an imperfect Bose gas. *Sov. Phys. JETP*, 13(2): 451–454, 1961.

Pitaevskiĭ and Stringari (2016) - Pitaevskiĭ, L. P. and Stringari, S. *Bose-Einstein condensation and superfluidity*. Number 164 in International series of monographs on physics. Oxford University Press, Oxford, United Kingdom, first edition edition, 2016. ISBN 978-0-19-875888-4 978-0-19-882443-5.

Plenio (2005) - Plenio, M. B. Logarithmic Negativity: A Full Entanglement Monotone That is not Convex. *Physical Review Letters*, 95(9):090503, 8 2005. URL.

Plenio and Virmani (2005) - Plenio, M. B. and Virmani, S. An introduction to entanglement measures. *arXiv preprint quant-ph/0504163*, 2005.

Popescu (1994) - Popescu, S. Bell's inequalities versus teleportation: What is nonlocality? *Physical Review Letters*, 72(6):797–799, 2 1994. URL.

Popov (1972) - Popov, V. N. Hydrodynamic Hamiltonian for a nonideal Bose gas. *Teoreticheskaya i Matematicheskaya Fizika*, 11(2):236–247, 1972.

Pylak and Zin (2018) - Pylak, M. and Zin, P. Influence of the interaction between quasiparticles on parametric resonance in Bose-Einstein quasicondensates. *Physical Review A*, 98(4):043603, 10 2018. URL.

Rarity and Tapster (1990) - Rarity, J. G. and Tapster, P. R. Experimental violation of Bell's inequality based on phase and momentum. *Phys. Rev. Lett.*, 64(21):2495–2498, 5 1990. URL.

Raven (2022) - Raven, H. v. A new Caesium quantum gas microscope with precise magnetic field control. Ludwig-Maximilians-Universität München. 2022.

Reid and Walls (1986) - Reid, M. D. and Walls, D. F. Violations of classical inequalities in quantum optics. *Physical Review A*, 34(2):1260–1276, 8 1986. URL.

Richard et al. (2003) - Richard, S., Gerbier, F., Thywissen, J. H., Hugbart, M., Bouyer, P., and Aspect, A. Momentum Spectroscopy of 1d Phase Fluctuations in Bose-Einstein Condensates. *Physical Review Letters*, 91(1):010405, 7 2003. URL.

Robert (2001) - Robert, A. Réalisation d'un condensat de Bose-Einstein d'atomes d'hélium métastable. Université Paris Sud - Paris XI. 2001.

Robert et al. (2001) - Robert, A., Sirjean, O., Browaeys, A., Poupard, J., Nowak, S., Boiron, D., Westbrook, C. I., and Aspect, A. A Bose-Einstein Condensate of Metastable Atoms. *Science*, 292(5516): 461–464, 4 2001. URL.

Robertson (2021) - Robertson, S. Notes on COSQUA: Separability, g2, all that stuff, Private communication. 6 2021.

Robertson et al. (2017a) - Robertson, S., Michel, F., and Parentani, R. Assessing degrees of entanglement of phonon states in atomic Bose gases through the measurement of commuting observables. *Physical Review D*, 96(4):045012, 8 2017a. URL.

Robertson et al. (2017b) - Robertson, S., Michel, F., and Parentani, R. Controlling and observing nonseparability of phonons created in time-dependent 1d atomic Bose condensates. *Physical Review D*, 95(6):065020, 3 2017b. URL.

Robertson et al. (2018) - Robertson, S., Michel, F., and Parentani, R. Nonlinearities induced by parametric resonance in effectively 1d atomic Bose condensates. *Physical Review D*, 98(5):056003, 9 2018. URL.

Rooijakkers et al. (1996) - Rooijakkers, W., Hogervorst, W., and Vassen, W. An intense collimated beam of metastable helium atoms by two-dimensional laser cooling. *Optics Communications*, 123 (1-3):321–330, 1 1996. URL.

Rousseaux et al. (2008) - Rousseaux, G., Mathis, C., Maı
ssa, P., Philbin, T. G., and Leonhardt, U. Observation of negative-frequency waves in a water tank: a classical analogue to the Hawking effect? *New Journal of Physics*, 10(5):053015, 2008.

Sahota and Quesada (2015) - Sahota, J. and Quesada, N. Quantum correlations in optical metrology: Heisenberg-limited phase estimation without mode entanglement. *Physical Review A*, 91(1):013808, 1 2015. URL.

Salasnich et al. (2002) - Salasnich, L., Parola, A., and Reatto, L. Effective wave equations for the dynamics of cigar-shaped and disk-shaped Bose condensates. *Physical Review A*, 65(4):043614, 4 2002. URL.

Sasaki and Suzuki (2006) - Sasaki, M. and Suzuki, S. Multimode theory of measurement-induced non-Gaussian operation on wideband squeezed light: Analytical formula. *Physical Review A*, 73(4): 043807, 4 2006. URL.

Sayrin et al. (2011) - Sayrin, C., Dotsenko, I., Zhou, X., Peaudecerf, B., Rybarczyk, T., Gleyzes, S., Rouchon, P., Mirrahimi, M., Amini, H., Brune, M., Raimond, J.-M., and Haroche, S. Real-time quantum feedback prepares and stabilizes photon number states. *Nature*, 477(7362):73–77, 9 2011. URL.

Schabbauer (2023) - Schabbauer, J. Experiment control for quantum simulation with non-local interactions. Vienna University of Technology. 2023. URL.

Scheel et al. (2001) - Scheel, S., Opatrny, T., and Welsch, D. G. Entanglement degradation of a two-mode squeezed vacuum in absorbing and amplifying optical fibers. *Optics and Spectroscopy*, 91(3): 411–417, 9 2001. URL.

Schellekens (2007) - Schellekens, M. The Hanbury Brown and Twiss Effet for Cold Atoms. Université Paris Sud - Paris XI. 2007.

Schellekens et al. (2005) - Schellekens, M., Hoppeler, R., Perrin, A., Gomes, J. V., Boiron, D., Aspect, A., and Westbrook, C. I. Hanbury Brown Twiss Effect for Ultracold Quantum Gases. *Science*, 310 (5748):648–651, 10 2005. URL.

Schemmer et al. (2018) - Schemmer, M., Johnson, A., and Bouchoule, I. Monitoring squeezed collective modes of a one-dimensional Bose gas after an interaction quench using density ripples analysis. *Physical Review A*, 98(4):043604, 10 2018. URL.

Schmidt et al. (2003) - Schmidt, P. O., Hensler, S., Werner, J., Binhammer, T., Görlitz, A., and Pfau, T. Doppler cooling of an optically dense cloud of magnetically trapped atoms. *Journal of the Optical Society of America B*, 20(5):960, 5 2003. URL.

Schrödinger (1935) - Schrödinger, E. Discussion of Probability Relations between Separated Systems. *Mathematical Proceedings of the Cambridge Philosophical Society*, 31(4):555–563, 10 1935. URL.

Schweigler et al. (2017) - Schweigler, T., Kasper, V., Erne, S., Mazets, I., Rauer, B., Cataldini, F., Langen, T., Gasenzer, T., Berges, J., and Schmiedmayer, J. Experimental characterization of a quantum many-body system via higher-order correlations. *Nature*, 545(7654):323–326, 5 2017. URL.

Seidelin et al. (2004) - Seidelin, S., Gomes, J. V., Hoppeler, R., Sirjean, O., Boiron, D., Aspect, A., and Westbrook, C. I. Getting the Elastic Scattering Length by Observing Inelastic Collisions in Ultracold Metastable Helium Atoms. *Physical Review Letters*, 93(9):090409, 8 2004. URL.

Serafini (2017) - Serafini, A. *Quantum continuous variables: a primer of theoretical methods*. CRC Press, Taylor, Boca Raton, 1 edition, 2017. ISBN 978-1-4822-4634-6. doi: 10.1201/9781315118727. URL.

Serafini et al. (2004a) - Serafini, A., Illuminati, F., Paris, M. G. A., and De Siena, S. Entanglement and purity of two-mode Gaussian states in noisy channels. *Physical Review A*, 69(2):022318, 2 2004a. URL.

Serafini et al. (2004b) - Serafini, A., Illuminati, F., and Siena, S. D. Symplectic invariants, entropic measures and correlations of Gaussian states. *Journal of Physics B: Atomic, Molecular and Optical Physics*, 37(2):L21–L28, 1 2004b. URL.

Shchukin and Vogel (2005) - Shchukin, E. and Vogel, W. Inseparability Criteria for Continuous Bipartite Quantum States. *Physical Review Letters*, 95(23):230502, 11 2005. URL.

Shlyapnikov et al. (1994) - Shlyapnikov, G. V., Walraven, J. T. M., Rahmanov, U. M., and Reynolds, M. W. Decay Kinetics and Bose Condensation in a Gas of Spin-Polarized Triplet Helium. *Physical Review Letters*, 73(24):3247–3250, 12 1994. URL.

Simon (2000) - Simon, R. Peres-Horodecki Separability Criterion for Continuous Variable Systems. *Physical Review Letters*, 84(12):2726–2729, 3 2000. URL.

Simon et al. (1987) - Simon, R., Sudarshan, E. C. G., and Mukunda, N. Gaussian-Wigner distributions in quantum mechanics and optics. *Physical Review A*, 36(8):3868–3880, 10 1987. URL.

Simon et al. (1994) - Simon, R., Mukunda, N., and Dutta, B. Quantum-noise matrix for multimode systems: U(*n*) invariance, squeezing, and normal forms. *Physical Review A*, 49(3):1567–1583, 3 1994. URL.

Smithey et al. (1993) - Smithey, D. T., Beck, M., Raymer, M. G., and Faridani, A. Measurement of the Wigner distribution and the density matrix of a light mode using optical homodyne tomography: Application to squeezed states and the vacuum. *Physical Review Letters*, 70(9):1244–1247, 3 1993. URL.

Sperling et al. (2012a) - Sperling, J., Vogel, W., and Agarwal, G. S. Sub-Binomial Light. *Physical Review Letters*, 109(9):093601, 8 2012a. URL.

Sperling et al. (2012b) - Sperling, J., Vogel, W., and Agarwal, G. S. True photocounting statistics of multiple on-off detectors. *Physical Review A*, 85(2):023820, 2 2012b. URL.

Sperling et al. (2019) - Sperling, J., Perez-Leija, A., Busch, K., and Silberhorn, C. Mode-independent quantum entanglement for light. *Phys. Rev. A*, 100(6):062129, 12 2019. URL.

Staliunas et al. (2002) - Staliunas, K., Longhi, S., and De Valcárcel, G. J. Faraday Patterns in Bose-Einstein Condensates. *Physical Review Letters*, 89(21):210406, 11 2002. URL.

Stamper-Kurn et al. (1998) - Stamper-Kurn, D. M., Miesner, H.-J., Inouye, S., Andrews, M. R., and Ketterle, W. Collisionless and Hydrodynamic Excitations of a Bose-Einstein Condensate. *Phys. Rev. Lett.*, 81(3):500–503, 7 1998. URL.

Stamper-Kurn et al. (1999) - Stamper-Kurn, D. M., Chikkatur, A. P., Görlitz, A., Inouye, S., Gupta, S., Pritchard, D. E., and Ketterle, W. Excitation of phonons in a Bose-Einstein condensate by light scattering. *Physical Review Letters*, 83(15):2876–2879, 10 1999. URL.

Stamper-Kurn et al. (2001) - Stamper-Kurn, D. M., Chikkatur, A. P., Görlitz, A., Gupta, S., Inouye, S., Stenger, J., Pritchard, D. E., and Ketterle, W. Probing Bose-Einstein Condensates with Optical Bragg Scattering. *International Journal of Modern Physics B*, 15(10n11):1621–1640, 5 2001. URL.

Starkey et al. (2013) - Starkey, P. T., Billington, C. J., Johnstone, S. P., Jasperse, M., Helmerson, K., Turner, L. D., and Anderson, R. P. A scripted control system for autonomous hardware timed experiments. *Review of Scientific Instruments*, 84(8):085111, 8 2013. URL.

Steinhauer (2014) - Steinhauer, J. Observation of self-amplifying Hawking radiation in an analogue black-hole laser. *Nature Physics*, 10(11):864–869, 11 2014. URL.

Steinhauer (2015) - Steinhauer, J. Measuring the entanglement of analogue Hawking radiation by the density-density correlation function. *Physical Review D*, 92(2):024043, 7 2015. URL.

Steinhauer (2016) - Steinhauer, J. Observation of quantum Hawking radiation and its entanglement in an analogue black hole. *Nature Physics*, 12(10):959–965, 10 2016. URL.

Steinhauer et al. (2002) - Steinhauer, J., Ozeri, R., Katz, N., and Davidson, N. The Excitation Spectrum of a Bose-Einstein Condensate. *Physical Review Letters*, 88(12):120407, 3 2002. URL.

Stenger et al. (1999) - Stenger, J., Inouye, S., Chikkatur, A. P., Stamper-Kurn, D. M., Pritchard, D. E., and Ketterle, W. Bragg Spectroscopy of a Bose-Einstein Condensate. *Physical Review Letters*, 82 (23):4569–4573, 6 1999. URL.

Stringari (1996) - Stringari, S. Collective Excitations of a Trapped Bose-Condensed Gas. *Phys. Rev. Lett.*, 77(12):2360–2363, 9 1996. URL.

Stringari (1998) - Stringari, S. Dynamics of Bose-Einstein condensed gases in highly deformed traps. *Physical Review A*, 58(3):2385–2388, 9 1998. URL.

Ténart (2021) - Ténart, A. Momentum-space correlations in the depletion of weakly interacting lattice Bose gases. Université Paris-Saclay. 2021. URL.

Tenart et al. (2021) - Tenart, A., Hercé, G., Bureik, J.-P., Dareau, A., and Clément, D. Observation of pairs of atoms at opposite momenta in an equilibrium interacting Bose gas. *Nature Physics*, 17(12): 1364–1368, 12 2021. URL.

The CREMA Collaboration et al. (2023) - The CREMA Collaboration, Schuhmann, K., Fernandes, L. M. P., Nez, F., Ahmed, M. A., Amaro, F. D., Amaro, P., Biraben, F., Chen, T.-L., Covita, D. S., Dax, A. J., Diepold, M., Franke, B., Galtier, S., Gouvea, A. L., Götzfried, J., Graf, T., Hänsch, T. W., Hildebrandt, M., Indelicato, P., Julien, L., Kirch, K., Knecht, A., Kottmann, F., Krauth, J. J., Liu, Y.-W., Machado, J., Monteiro, C. M. B., Mulhauser, F., Naar, B., Nebel, T., Santos, J. M. F. d., Santos, J. P., Szabo, C. I., Taqqu, D., Veloso, J. F. C. A., Voss, A., Weichelt, B., Antognini, A., and Pohl, R. The helion charge radius from laser spectroscopy of muonic helium-3 ions, arXiv. 2023. URL.

Thomas et al. (2022) - Thomas, K. F., Henson, B. M., Wang, Y., Lewis-Swan, R. J., Kheruntsyan, K. V., Hodgman, S. S., and Truscott, A. G. A matter-wave Rarity–Tapster interferometer to demonstrate non-locality. *The European Physical Journal D*, 76(12):244, 12 2022. URL.

Tóth et al. (2007) - Tóth, G., Knapp, C., Guhne, O., and Briegel, H. J. Optimal Spin Squeezing Inequalities Detect Bound Entanglement in Spin Models. *Physical Review Letters*, 2007.

Tozzo and Dalfovo (2004) - Tozzo, C. and Dalfovo, F. The fate of phonons in freely expanding Bose-Einstein condensates. *Physical Review A*, 69(5):053606, 5 2004. URL.

Tychkov et al. (2004) - Tychkov, A. S., Koelemeij, J. C. J., Jeltes, T., Hogervorst, W., and Vassen, W. Two-color magneto-optical trap for metastable helium. *Physical Review A*, 69(5):055401, 5 2004. URL.

UltimHeat (1962) - UltimHeat, M. Comportement du cuivre et ses alliages à température extrême. *Revue technique de vulgarisation*, 09-10(69), 1962.

Unruh (1981) - Unruh, W. G. Experimental Black-Hole Evaporation? *Physical Review Letters*, 46(21): 1351–1353, 5 1981. URL.

Van Der Beek et al. (2020) - Van Der Beek, R. F. H. J., Onishchenko, O., Vassen, W., Eikema, K. S. E., and Bethlem, H. L. Bloch oscillations with a metastable helium Bose-Einstein condensate. *Physical Review A*, 102(6):061302, 12 2020. URL.

van der Werf et al. (2023) - Werf, Y., Steinebach, K., Jannin, R., Bethlem, H. L., and Eikema, K. S. E. The alpha and helion particle charge radius difference from spectroscopy of quantum-degenerate helium, arXiv. 2023. URL.

Vassen et al. (2012) - Vassen, W., Cohen-Tannoudji, C., Leduc, M., Boiron, D., Westbrook, C. I., Truscott, A., Baldwin, K., Birkl, G., Cancio, P., and Trippenbach, M. Cold and trapped metastable noble gases. *Reviews of Modern Physics*, 84(1):175–210, 2 2012. URL.

Vezzoli et al. (2019) - Vezzoli, S., Mussot, A., Westerberg, N., Kudlinski, A., Dinparasti Saleh, H., Prain, A., Biancalana, F., Lantz, E., and Faccio, D. Optical analogue of the dynamical Casimir effect in a dispersion-oscillating fibre. *Communications Physics*, 2(1):84, 7 2019. URL.

Vidal and Werner (2002) - Vidal, G. and Werner, R. F. Computable measure of entanglement. *Physical Review A*, 65(3):032314, 2 2002. URL.

Viermann et al. (2022) - Viermann, C., Sparn, M., Liebster, N., Hans, M., Kath, E., Parra-López, Á., Tolosa-Simeón, M., Sánchez-Kuntz, N., Haas, T., Strobel, H., Floerchinger, S., and Oberthaler, M. K. Quantum field simulator for dynamics in curved spacetime. *Nature*, 611(7935):260–264, 11 2022. URL.

Vincent Liu (1997) - Vincent Liu, W. Theoretical Study of the Damping of Collective Excitations in a Bose-Einstein Condensate. *Physical Review Letters*, 79(21):4056–4059, 11 1997. URL.

Vogel and Risken (1989) - Vogel, K. and Risken, H. Determination of quasiprobability distributions in terms of probability distributions for the rotated quadrature phase. *Physical Review A*, 40(5): 2847–2849, 9 1989. URL.

Walls and Milburn (2008) - Walls, D. F. and Milburn, G. J. *Quantum optics*. Springer, Berlin, 2nd ed edition, 2008. ISBN 978-3-540-28573-1.

Wang et al. (2024) - Wang, A., Park, S. Y., Hartman, A., Hector Hernandez, P., Ng, K. B., Schlossberger, N., Wright, T., Kompella, R., Ye, J., and Cornell, E. Long coherence time of the JILA Generation III eEDM experiment. *Bulletin of the American Physical Society*, 2024.

Wang et al. (2021) - Wang, J. S., Ritterbusch, F., Dong, X.-Z., Gao, C., Li, H., Jiang, W., Liu, S.-Y., Lu, Z.-T., Wang, W.-H., Yang, G.-M., Zhang, Y.-S., and Zhang, Z.-Y. Optical Excitation and Trapping of 81kr. *Phys. Rev. Lett.*, 127(2):023201, 7 2021. URL.

Wang and Wilde (2020) - Wang, X. and Wilde, M. M. Cost of Quantum Entanglement Simplified. *Physical Review Letters*, 125(4):040502, 7 2020. URL.

Wasak et al. (2014) - Wasak, T., Szańkowski, P., Ziń, P., Trippenbach, M., and Chwedeńczuk, J. Cauchy-Schwarz inequality and particle entanglement. *Physical Review A*, 90(3):033616, 9 2014. URL.

Wasak et al. (2016) - Wasak, T., Szańkowski, P., Trippenbach, M., and Chwedeńczuk, J. Cauchy–Schwarz inequality for general measurements as an entanglement criterion. *Quantum Information Processing*, 15(1):269–278, 1 2016. URL.

Watson (2000) - Watson, S. An Exposition on Inflationary Cosmology. 5 2000. URL.

Weedbrook et al. (2012) - Weedbrook, C., Pirandola, S., García-Patrón, R., Cerf, N. J., Ralph, T. C., Shapiro, J. H., and Lloyd, S. Gaussian quantum information. *Reviews of Modern Physics*, 84(2): 621–669, 5 2012. URL.

Weinfurtner et al. (2011) - Weinfurtner, S., Tedford, E. W., Penrice, M. C. J., Unruh, W. G., and Lawrence, G. A. Measurement of stimulated Hawking emission in an analogue system. *Physical Review Letters*, 106(2):021302, 1 2011. URL.

Werner (1989) - Werner, R. F. Quantum states with Einstein-Podolsky-Rosen correlations admitting a hidden-variable model. *Physical Review A*, 40(8):4277–4281, 10 1989. URL.

Weyl (1950) - Weyl, H. *The Theory of Groups and Quantum Mechanics*. Dover Books on Mathematics. Dover Publications, 1950. ISBN 978-0-486-60269-1. URL.

Wick (1950) - Wick, G. C. The Evaluation of the Collision Matrix. *Physical Review*, 80(2):268–272, 10 1950. URL.

Wick et al. (1952) - Wick, G. C., Wightman, A. S., and Wigner, E. P. The Intrinsic Parity of Elementary Particles. *Physical Review*, 88(1):101–105, 10 1952. URL.

Wigner (1932) - Wigner, E. On the Quantum Correction For Thermodynamic Equilibrium. *Physical Review*, 40(5):749–759, 6 1932. URL.

Williamson (1936) - Williamson, J. On the Algebraic Problem Concerning the Normal Forms of Linear Dynamical Systems. *American Journal of Mathematics*, 58(1):141–163, 1936. URL.

Wilson et al. (2011) - Wilson, C. M., Johansson, G., Pourkabirian, A., Simoen, M., Johansson, J. R., Duty, T., Nori, F., and Delsing, P. Observation of the dynamical Casimir effect in a superconducting circuit. *Nature*, 479(7373):376–379, 11 2011. URL.

Wittemer et al. (2019) - Wittemer, M., Hakelberg, F., Kiefer, P., Schröder, J.-P., Fey, C., Schützhold, R., Warring, U., and Schaetz, T. Phonon Pair Creation by Inflating Quantum Fluctuations in an Ion Trap. *Physical Review Letters*, 123(18):180502, 10 2019. URL.

Yuen (1976) - Yuen, H. P. Two-photon coherent states of the radiation field. *Physical Review A*, 13(6): 2226–2243, 6 1976. URL.

Zambelli et al. (2000) - Zambelli, F., Pitaevskii, L., Stamper-Kurn, D. M., and Stringari, S. Dynamic structure factor and momentum distribution of a trapped Bose gas. *Physical Review A*, 61(6):063608, 5 2000. URL.

Zaremba (1998) - Zaremba, E. Sound propagation in a cylindrical Bose-condensed gas. *Physical Review A*, 57(1):518–521, 1 1998. URL.

Zener and Fowler (1932) - Zener, C. and Fowler, R. H. Non-adiabatic crossing of energy levels. *Proceedings of the Royal Society of London. Series A, Containing Papers of a Mathematical and Physical Character*, 137(833):696–702, 1932. URL.

Zenesini et al. (2024) - Zenesini, A., Berti, A., Cominotti, R., Rogora, C., Moss, I. G., Billam, T. P., Carusotto, I., Lamporesi, G., Recati, A., and Ferrari, G. False vacuum decay via bubble formation in ferromagnetic superfluids. *Nature Physics*, 20(4):558–563, 4 2024. URL.

Zhang et al. (2021) - Zhang, D., Barral, D., Cai, Y., Zhang, Y., Xiao, M., and Bencheikh, K. Hierarchy of Nonlinear Entanglement Dynamics for Continuous Variables. *Phys. Rev. Lett.*, 127(15):150502, 10 2021. URL.

université PARIS-SACLAY

ÉCOLE DOCTORALE
Ondes et matière (EDOM)

Titre : De l'intrication de quasi-particules dans un condensat de Bose-Einstein
Mots clés : Atomes froids ; Physique Quantique ; Simulations quantiques ; Gravité analogue ; Intrication d'états gaussiens ; Résonance paramétrique

Résumé : Ce mémoire de thèse traite de la non-séparabilité de paires de quasi-particules excitées par résonance paramétrique. Le dispositif expérimental utilisé pendant cette thèse permet de produire un condensat de Bose-Einstein d'hélium métastable. L'utilisation d'un gaz d'atomes ultra-froid permet d'atteindre des températures suffisamment basses afin de pouvoir observer des phénomènes intrinsèquement quantiques : la non-séparabilité de l'état. Dans ce travail, nous utilisons le condensat comme un réservoir cohérent permettant de peupler deux modes d'impulsions. L'avantage de l'hélium métastable est sa grande énergie interne, qui permet la détection électronique de particules uniques. Nous mesurons donc la position et le temps d'impact des particules après un temps de vol de 308 ms, ce qui permet de reconstruire la distribution en impulsion dans le piège. Dans la première contribution théorique de ce travail, nous démontrons que la mesure des fonctions de corrélation à deux et quatre corps permet de quantifier la non-séparabilité d'un état gaussien. Nous dérivons également un critère permettant d'attester la séparabilité de l'état via la seule mesure la fonction de corrélation à deux corps. Dans la partie expérimentale, nous améliorons la machine permettant de produire notre gaz ultra-froid, ainsi que sa stabilité. Par ailleurs, nous mettons en œuvre des techniques originales afin de dévier une partie des atomes et éviter la saturation de notre détecteur. Ces améliorations nous permettent ainsi d'observer la non-séparabilité de l'état.

Title : On the entanglement of quasi-particles in a Bose-Einstein Condensate
Keywords : Quantum Physics ; Quantum simulations ; Cold atoms ; Analog gravity ; Entanglement of Gaussian states ; Parametric resonance

Abstract : This thesis focuses on the non-separability of pairs of quasi-particles excited by parametric resonance. The experimental setup used here allows the production of a Bose-Einstein condensate of metastable helium. The use of an ultra-cold atomic gas makes it possible to reach sufficiently low temperatures to observe intrinsically quantum phenomena : the non-separability of the state. In this work, we use the condensate as a coherent reservoir to populate two momentum modes. The advantage of metastable helium is its high internal energy, which allows the electronic detection of single particles. We therefore measure the position and the time of impact of the particles after a time of flight of 308 ms, which allows us to reconstruct the in-trap momentum distribution. In the first theoretical contribution of this work, we demonstrate that measuring the two- and four-body correlation functions not only attests to, but also quantifies the non-separability of a Gaussian state. We also derive a new entanglement witness using only the two-body correlation function. In the experimental part, we improve the machine used to produce our ultra-cold gas and enhance its stability. We implement original techniques to deflect part of the atoms and avoid the saturation of our detector. These improvements allow us to observe the non-separability of the state.